

WASHINGTON UNIVERSITY
SEVER INSTITUTE
SCHOOL OF ENGINEERING AND APPLIED SCIENCE
DEPARTMENT OF ENERGY, ENVIRONMENTAL AND CHEMICAL
ENGINEERING

Hydrodynamics and Mixing in Single Phase and Liquid-Solid Stirred Tank
Reactors

by
Debangshu Guha

Prepared under the directions of
Professor M.P. Duduković and Professor P.A. Ramachandran

A thesis presented to the Sever Institute of
Washington University in partial fulfillment of the
requirements for the degree of
DOCTOR OF SCIENCE

August 2007
Saint Louis, Missouri

WASHINGTON UNIVERSITY
SEVER INSTITUTE
SCHOOL OF ENGINEERING AND APPLIED SCIENCE
DEPARTMENT OF ENERGY, ENVIRONMENTAL AND CHEMICAL
ENGINEERING

ABSTRACT

Hydrodynamics and Mixing in Single Phase and Liquid-Solid Stirred Tank Reactors

by

Debangshu Guha

ADVISORS:

Professor M.P. Duduković

Professor P.A. Ramachandran

August 2007

Saint Louis, Missouri

Traditional design of mechanically agitated reactors assumes perfect and instantaneous mixing, the validity of which depends on the relative magnitudes of the characteristic reaction and mixing times. Proper understanding of mixing effects can lead to reduction in waste production (undesired products) and increased profitability of operation. Although Computational Fluid Dynamics (CFD) can be used for this purpose, it suffers from the disadvantage of high computation cost when complex chemistries with large number of species are involved. A CFD-based compartmental approach is proposed in this work as a promising alternative under such constraints, which has been shown to provide reasonable predictions at reduced computation expense for single phase systems. A methodology for the a priori determination of the number of compartments has also been developed based on a time-scale analysis. However, extension of this approach to solid-liquid stirred tanks is

incumbent on the extensive evaluation of CFD predictions for such systems. The dearth of available experimental data necessitated the use of two non-intrusive techniques, namely, Computer Automated Radioactive Particle Tracking (CARPT) and Computed Tomography (CT) to obtain the solids dynamics and solids phase distribution in the reactor, which are eventually used to assess the predictability of existing CFD models. Moreover, CARPT data clearly show that the impeller speed for incipient solid suspension is over-predicted by the Zwietering's correlation (1958), resulting in increased energy requirement for the operation of these reactors. The Euler-Euler model and the large eddy simulation are the CFD models assessed in this study and several available models for interphase interactions are evaluated. Discrepancies can be observed close to the impeller while improved predictions are obtained in regions away from the impeller. Once CFD is standardized to obtain reliable flow predictions, the compartmental model can be extended to solid-liquid systems, and the methodology, approach and algorithm developed can be used for industrial reactors for any reaction type provided rate terms and kinetic constants are known.

To
My Mom and Dad

Contents

List of Tables	viii
List of Figures.....	ix
Nomenclature	xiv
Acknowledgements	xvii
Chapter 1	
Introduction.....	1
1.1. Motivation for Research	2
1.2. Research Objectives	4
1.3. Thesis Outline	5
Chapter 2	
Background	6
2.1. Single Phase Flow Modeling.....	7
2.2. Mixing Effect on Reactive Flows.....	11
2.3. Liquid-Solid Flows	14
2.3.1. Experimental Studies.....	14
2.3.2. Solids Flow Modeling.....	18
2.4. Summary	20
Chapter 3	
CFD-Based Compartmental Model for Single Phase Systems	22
3.1. Detailed Model for Turbulent Reactive Systems	23
3.2. Model Reduction and Compartment Level Equations	25

3.3. Compartmental Model Inputs from CFD.....	29
3.3.1. Compartment Discretization Scheme	30
3.3.2. Exchange Coefficients.....	34
3.4. Results and Discussion	35
3.4.1. The System.....	35
3.4.2. Flow Field.....	36
3.4.3. Inert Tracer Mixing.....	36
3.4.4. First and Second Order Kinetics	39
3.4.5. Effect of Mixing on Multiple Reactions	42
3.5. Summary	52
 Chapter 4	
Large Eddy Simulation of Single Phase Flow.....	53
4.1. Filtered Navier-Stokes Equations	54
4.2. Methodology	56
4.3. Tank Geometry and Simulated Operating Conditions	57
4.4. Results and Discussions	58
4.4.1. Radial Profiles	58
4.4.2. Axial Profiles.....	62
4.4.3. Impeller Flow Number	62
4.5. Summary	66
 Chapter 5	
Solids Flow Dynamics in a Solid-Liquid Stirred Tank	68
5.1. The Stirred Vessel.....	69

5.2. CARPT Setup	70
5.3. CARPT Technique.....	72
5.4. Experimental Conditions	73
5.5. Results and Discussions	74
5.5.1. Grid Independence of Computed Quantities	75
5.5.2. Overall Flow Pattern	77
5.5.3. Ensemble-Averaged Solids Radial Velocity	79
5.5.4. Ensemble-Averaged Solids Tangential Velocity.....	82
5.5.5. Ensemble-Averaged Solids Axial Velocities.....	85
5.5.6. Solids Turbulent Kinetic Energy	90
5.5.7. Solids Sojourn Time Distributions	95
5.6. Summary	104
 Chapter 6	
Solids Distribution in a Solid-Liquid Stirred Tank	105
6.1. The Stirred Vessel.....	106
6.2. CT Setup.....	106
6.3. CT Technique	108
6.4. Experimental Conditions	109
6.5. Results and Discussions	109
6.5.1. Solids Mass Balance	115
6.5.2. Probable Causes of Failure	116
6.6. Summary	120
 Chapter 7	
Evaluation of CFD Models for Solid-Liquid Stirred Tank	122

7.1. Tank Geometry and Simulation Condition.....	123
7.2. Euler-Euler Model	124
7.3. Large Eddy Simulation	127
7.4. Results and Discussions	130
7.4.1. Overall Flow Pattern	130
7.4.2. Solids Velocity Radial Profiles.....	131
7.4.3. Turbulent Kinetic Energy Profiles	137
7.4.4. Slip (Relative) Reynolds Number.....	142
7.4.5. Solids Volume Fraction.....	144
7.4.6. Influence of Baffles.....	144
7.4.7. Solids Sojourn Time Distributions	148
7.5. Influence of Drag and Lift Closures on the Euler-Euler Predictions of Solids Flow Field.....	153
7.5.1. Effect of Flow Properties on the Forces on a Solid Sphere – Literature Review.....	155
7.5.2. Closure Models Tested.....	163
7.5.3. Observations	165
7.6. Summary	171
 Chapter 8	
Conclusions and Future Work.....	173
8.1. Future Work.....	176
 References.....	 179
Vita.....	190

List of Tables

Table 1.1 Some industrial applications of stirred reactors.....	2
Table 5.1 Experimental conditions for CARPT study	74
Table 5.2 Number of compartments used to check grid independence of computed quantities from CARPT data.....	75
Table 6.1 Percentage solids mass balance errors	116
Table 7.1 Axial variation of solids fractional occurrence, mean sojourn time and standard deviation as obtained with CARPT and LES for 1% solids holdup at 1000 RPM.....	151
Table 7.2 Drag and lift closures evaluated with the Euler-Euler model.....	164

List of Figures

Figure 3.1 Configuration of a single backmixed compartment showing neighboring interconnected compartments	26
Figure 3.2 A discretized compartment in the compartmental framework	31
Figure 3.3 Discretization in the axial direction	33
Figure 3.4 Schematic diagram of the geometry used.....	36
Figure 3.5 Convergence of predicted mixing time with number of compartments	38
Figure 3.6 Comparison of predicted mixing time with literature correlations	39
Figure 3.7 Dimensionless mixing time (predicted) vs. Reynolds Number.....	40
Figure 3.8 Dimensionless standard deviation vs. conversion for a first order reaction.....	41
Figure 3.9 Conversion vs. time for a first order reaction	41
Figure 3.10 Dimensionless standard deviation vs. conversion for a second order reaction.....	43
Figure 3.11 Conversion vs. time for a second order reaction	43
Figure 3.12 Details of the geometry used for the simulation of multiple reactions (Paul and Treybal, 1971).....	45
Figure 3.13 Dimensionless standard deviation vs. time for a semi-batch second order, competitive-consecutive reaction scheme.....	46
Figure 3.14 Yield of R as a function of time for the multiple reaction scheme	47
Figure 3.15 Comparison between measured and predicted yield of R at the end of the reaction for the two feed locations	47
Figure 3.16 Sensitivity of the exchange term on the prediction of yield (f denotes the multiplication factor to the normal exchange coefficients obtained earlier, i.e. $f=0$ signifies no exchange term is used).....	49
Figure 3.17 Contours of reactant B concentration ($kmol/m^3$) for the bottom feed inlet at (a) 5 seconds, (b) 10 seconds, (c) 15 seconds and (d) 20 seconds	50
Figure 3.18 Contours of reactant B concentration ($kmol/m^3$) for the top feed inlet at (a) 5 seconds, (b) 10 seconds, (c) 15 seconds and (d) 20 seconds	50

Figure 3.19 Comparison between predicted yields of R at the end of the reaction obtained using compartmental model and full CFD simulation for the two feed locations.....	51
Figure 4.1 Radial profile of liquid radial velocity	59
Figure 4.2 Radial profile of liquid tangential velocity.....	59
Figure 4.3 Radial profile of liquid axial velocity.....	60
Figure 4.4 Radial profile of turbulent kinetic energy.....	61
Figure 4.5 Radial profile of kinetic energy dissipation rate	61
Figure 4.6 Axial profile of liquid radial velocity.....	63
Figure 4.7 Axial profile of liquid tangential velocity.....	63
Figure 4.8 Axial profile of liquid axial velocity.....	64
Figure 4.9 Axial profile of turbulent kinetic energy.....	64
Figure 4.10 Axial profile of kinetic energy dissipation rate	65
Figure 4.11 Radial profile of pumping flow number (Ri : Impeller Radius).....	65
Figure 5.1 Schematic of the tank used for CARPT/CT experiments.....	70
Figure 5.2 Schematic of CARPT experimental setup.....	71
Figure 5.3 Photograph of CARPT experimental setup with solid-liquid stirred tank.....	72
Figure 5.4 Comparison of (a) radial, (b) tangential and (c) axial solids velocities obtained with two grids for 1% solids holdup at 850 RPM (Ri = Impeller radius)	77
Figure 5.5 Velocity vector plots of solids velocity for overall solids holdup of (a) 1% at 1000 RPM and (b) 7% at 1200 RPM.....	78
Figure 5.6 Radial profiles of solids radial velocity for overall solids holdup of 1% at (a) 850 RPM and (b) 1000 RPM.....	80
Figure 5.7 Radial profiles of solids radial velocity for overall solids holdup of 7% at (a) 1050 RPM and (b) 1200 RPM.....	81
Figure 5.8 Axial profiles of solids radial velocity for overall solids holdup of 1% at (a) 850 RPM and (b) 1000 RPM.....	83
Figure 5.9 Axial profiles of solids radial velocity for overall solids holdup of 7% at (a) 1050 RPM and (b) 1200 RPM.....	84

Figure 5.10 Radial profiles of solids tangential velocity for overall solids holdup of 1% at (a) 850 RPM and (b) 1000 RPM	86
Figure 5.11 Radial profiles of solids tangential velocity for overall solids holdup of 7% at (a) 1050 RPM and (b) 1200 RPM	87
Figure 5.12 Axial profiles of solids tangential velocity for overall solids holdup of 1% at (a) 850 RPM and (b) 1000 RPM	88
Figure 5.13 Axial profiles of solids tangential velocity for overall solids holdup of 7% at (a) 1050 RPM and (b) 1200 RPM	89
Figure 5.14 Radial profiles of solids axial velocity for overall solids holdup of 1% at (a) 850 RPM and (b) 1000 RPM.....	91
Figure 5.15 Radial profiles of solids axial velocity for overall solids holdup of 7% at (a) 1050 RPM and (b) 1200 RPM.....	92
Figure 5.16 Axial profiles of solids axial velocity for overall solids holdup of 1% at (a) 850 RPM and (b) 1000 RPM.....	93
Figure 5.17 Axial profiles of solids axial velocity for overall solids holdup of 7% at (a) 1050 RPM and (b) 1200 RPM.....	94
Figure 5.18 Radial profiles of solids turbulent kinetic energy for overall solids holdup of 1% at (a) 850 RPM and (b) 1000 RPM.....	96
Figure 5.19 Radial profiles of solids turbulent kinetic energy for overall solids holdup of 7% at (a) 1050 RPM and (b) 1200 RPM	97
Figure 5.20 Axial profiles of solids turbulent kinetic energy for overall solids holdup of 1% at (a) 850 RPM and (b) 1000 RPM.....	98
Figure 5.21 Axial profiles of solids turbulent kinetic energy for overall solids holdup of 7% at (a) 1050 RPM and (b) 1200 RPM	99
Figure 5.22 Axial variations of (a) mean and (b) standard deviations of solids sojourn time distributions for overall solids holdup of 1% at 850 RPM and 1000 RPM	101
Figure 5.23 Axial variations of (a) mean and (b) standard deviations of solids sojourn time distributions for overall solids holdup of 7% at 1050 RPM and 1200 RPM	102

Figure 6.1 Photograph of CT experimental setup with stirred tank	107
Figure 6.2 Contour plots of solids holdup distribution for (a) 1% solids 850 RPM and (b) 7% solids 1200 RPM	110
Figure 6.3 Radial profiles of solids holdup at different axial locations for overall solids holdup of 1% at (a) 850 RPM and (b) 1000 RPM	112
Figure 6.4 Radial profiles of solids holdup at different axial locations for overall solids holdup of 7% at (a) 1050 RPM and (b) 1200 RPM	113
Figure 6.5 Comparison of solids distribution at $z/H = 0.65$ at different impeller speeds for overall solids holdup of 1%	114
Figure 6.6 Comparison of solids distribution at $z/H = 0.65$ at different impeller speeds for overall solids holdup of 7%	114
Figure 6.7 Solids holdup distribution in the phantom (a) actual and (b) simulated.....	118
Figure 6.8 Quantification of error in the phantom study (a) mean holdup, standard deviation and average error, and (b) dimensionless standard deviation	119
Figure 7.1 Impeller cross-section showing the grid used for the Euler-Euler simulation in Fluent 6.2	127
Figure 7.2 Impeller cross-section showing the grid used for the large eddy simulation, and the points defining the impeller and tank wall via the forcing method.....	129
Figure 7.3 Overall solids flow pattern in the tank as obtained from (a) CARPT, (b) Euler-Euler simulation and (c) Large eddy simulation (all figures in same scale)	131
Figure 7.4 Radial profiles of solids radial velocity at different axial locations in the tank	134
Figure 7.5 Radial profiles of solids tangential velocity at different axial locations in the tank.....	136
Figure 7.6 Radial profiles of solids axial velocity at different axial locations in the tank	139

Figure 7.7 Radial profiles of solids turbulent kinetic energy at different axial locations in the tank	141
Figure 7.8 Radial comparison of mixture TKE from the Euler-Euler model and liquid phase TKE from the large eddy simulation at the impeller cross-section ($z/T = 0.34$).....	143
Figure 7.9 Radial comparison of slip Reynolds number from the Euler-Euler model and the large eddy simulation at the impeller cross-section ($z/T = 0.34$).....	143
Figure 7.10 Radial comparison of solids holdup (v/v) from the Euler-Euler model and the large eddy simulation at the impeller cross-section ($z/T = 0.34$)	145
Figure 7.11 Comparison of CARPT and CFD predictions at planes containing the baffles for $z/T = 0.34$ (a) radial velocity, (b) axial velocity and (c) tangential velocity.....	146
Figure 7.12 Comparison of CARPT and CFD predictions at planes midway between the baffles for $z/T = 0.34$ (a) radial velocity, (b) axial velocity and (c) tangential velocity	148
Figure 7.13 Axial variation of the moments of the solids sojourn time distribution in the tank.....	152
Figure 7.14 Solids fractional occurrences in different axial regions of the tank.....	153
Figure 7.15 Solids sojourn time distributions at different axial slices in the tank	154
Figure 7.16 Distribution of liquid phase vorticity (s^{-1}) in the tank obtained from the Euler-Euler simulation (a) $r-\theta$ plane (b) $r-z$ plane.....	156
Figure 7.17 Influence of drag closure model on the Euler-Euler predictions of solids velocity components at $z/T = 0.34$	167
Figure 7.18 Influence of drag closure model on the Euler-Euler predictions of solids holdup	168
Figure 7.19 Influence of lift closure model on the Euler-Euler predictions of solids velocity components at $z/T = 0.34$	169
Figure 7.20 Influence of lift closure model on the Euler-Euler predictions of solids holdup	170

Nomenclature

A : Constant

B : Percentage solid loading

b : Blade height

C : Clearance of impeller from tank bottom

c_i : Concentration of component c

C_D, C_L : Drag and lift coefficient

$\langle c_{c,m} \rangle$: Cup-mixing concentration

c_c' : Fluctuating concentration

\bar{c}_c : Mean concentration of component c

$\langle c_c \rangle$: Volume averaged concentration

D : Impeller diameter

D_m : Molecular diffusivity

D_r : Turbulent dispersion coefficient

Da : Damkohler number

d_p, d_s : Particle diameter

E : Sojourn time distribution

H : Liquid height

k : Turbulent kinetic energy

k_{ex} : Exchange coefficient

l_e : Eddy length scale

l_K : Kolmogorov microscale

n : Number of occurrences

N : Number of compartments

n_b : Number of blades

N_{imp} : Impeller speed

N_{js} : Impeller speed for incipient solid suspension

N_R : Number of reactions

N_Q : Impeller flow number
 Pe : Peclet number
 Po : Power number
 p : Degree of homogeneity, i.e. local concentrations do not vary more than $(1-p)\%$ of the mean concentration
 Q : Volumetric flow rate
 R : Tank radius
 Re : Reynolds number
 Re_s : Relative Reynolds number
 R_i : Impeller radius
 S : Constant for Zwietering's correlation
 Sc : Schmidt number
 Sc_T : Turbulent Schmidt number
 $S_{rad}, S_\theta, S_{ax}$: Compartment surface areas in radial, angular and axial directions
 T : Tank diameter
 t : Time
 t_m : Mixing time
 t_s : Solids sojourn time
 u, u_s, U : Solids velocity
 u_l : Liquid velocity
 U_{tip} : Impeller tip speed
 u' : Fluctuating velocity
 \bar{u}_i : Mean velocity
 $\langle \bar{u}_m \rangle$: Surface average velocity
 V : Compartment volume
 V_T : Total fluid volume
 a : Volume fraction
 ε : Kinetic energy dissipation rate
 μ_i : Mean of sojourn time distribution at zone i
 μ_l : Liquid viscosity

ν : Kinematic viscosity

ρ_l, ρ_s : Liquid and solid density

σ : Concentration standard deviation

σ_i : Standard deviation of sojourn time distribution at zone i

ω : Vorticity

Acknowledgements

The seemingly long five years of graduate study is finally at the verge of completion. This is the most opportune moment to acknowledge all who crossed path during the journey and contributed directly or indirectly to reach the end of this tunnel. They have shown me light whenever darkness prevailed, motivated and encouraged me when depression was the order of the day and of course provided the necessary warmth and support during difficult times.

My advisors, Prof. M.P. Dudukovic and Prof. P.A. Ramachandran, undoubtedly deserve to start the list for reasons more than one. It was an excellent opportunity to work under the tutelage of two stalwarts of chemical reaction engineering. These five years had been instrumental for my academic development in close association with them. Further, it was an added privilege to work as a teaching assistant for their undergraduate and graduate reaction engineering courses for many semesters during this period, which always provided me an opportunity to revisit the basic nuances of reaction engineering. I sincerely thank them for showing me the way and helping me reach this destination through their words of motivation, encouragement and advice.

I express my deep sense of gratitude to all my committee members, Prof. M.H. Al-Dahhan, Prof. B. Subramaniam, Prof. R.V. Chaudhari and Dr. S. Mehta for finding the time to be on my thesis committee in spite of their busy schedules. Prof. Al-Dahhan has always been a constant support and has been extremely helpful during difficult times. It was a wonderful experience to work with Prof. Subramaniam on the modeling of hydroformylation reactors as a part of the Center for Environmentally Beneficial Catalysis (CEBC). The association was fruitful, productive and learning intensive. I thank him for being encouraging and helpful whenever necessary. I am thankful to Dr. Mehta for providing me the opportunity to work as a summer intern in Air Products and Chemicals Inc. during the summer of 2004. It was a rewarding experience to work with Dr. Mehta

and Javier Alvare on the development of the compartmental model during that stint. I also express my gratitude to Prof. R.A. Gardner for serving as a member on my proposal defense committee.

I would like to acknowledge Prof. Jos Derksen at the University of Delft for carrying out the solid-liquid large eddy simulation for my experimental condition and providing me the data for comparison with experimental results. It was fruitful working with him and I thank him for his thoughtful comments and suggestions. I am also thankful to Dr. Peter Spicka of Fluent for always having the time to address many Fluent-related issues over these years.

The Center for Environmentally Beneficial Catalysis (NSF engineering research center) needs to be acknowledged at this point for funding most of this work. It also provided an excellent and rare platform to work in cross-functional teams across different university campuses. It was a great experience to work with Dr. Hong Jin and Jing Fang from University of Kansas during my association with the center. I thank all the faculties and staff members of the center for being nice and supportive all through these years. I also express my gratitude to all CREL industrial members for providing their support through additional funding, and also for their comments, criticism and constructive suggestions during the CREL meeting every year.

It was a dream come true five years back when I had the opportunity to learn how to “make friends with chemical reactors” from the words of Prof. Octave Levenspiel in my very first CREL annual meeting. However, it was just a beginning and his hilarious and exciting post-dinner talk continued to be the cynosure of the meeting every year to follow. The annual CREL meeting and the concluding talk by Prof. Levenspiel will remain a memory to be cherished all through my life.

I would like to express my gratitude to the department secretaries, Rose, Mindy, Jean, Ruth and Angela for all their help whenever needed. They have always been supportive with warm greetings and ever-smiling face. I also thank Jim Linders for his help in fabrications

and modifications of the experimental setup time and again during the course of the graduate study.

I owe a lot to many of my fellow CREL members who made my work and life in graduate school a memorable experience. Although it is not possible to name everyone, few of them need special recognition. I enjoyed my association with RC and will cherish the frequent brain-storming sessions with him on different aspects of chemical engineering. It was also a pleasure to work with him as teaching assistant for the undergraduate reaction engineering course for four years in a row. Mehul had always been very supportive at difficult times and a great friend. I thank him for all his help during the particle tracking experiments. I also thank Rajneesh for his ever-enthusiastic help in any and every CT related issue. Radmila has been a good friend and I thank her for all the refreshing chit-chats and for her support.

I made a number of friends during this long journey that I never felt alone. My long term association with my roommates Shrinivas and Satyaki had been wonderful and worth cherishing. I will be missing them a lot. It was a real pleasure and good luck to have such caring friends like Dipanjanda, Anganadi, Saurabhda, Gargidi, Mrinmoyda, Gargidi, Abhijitda, Nilanjanadi, Suman, Poulomi and Swarnali around, who, apart from cooking sumptuous dinners, had always provided support and motivation whenever necessary. It would have been very difficult without all of them.

My list will remain incomplete without recognizing my mom and dad whose unbounded love and encouragement made this thesis possible. I dedicate this work to them and sincerely seek their blessings for the path ahead.

Debangshu Guha

Washington University in St. Louis

August 2007

Chapter 1

Introduction

Stirred tank reactors, in which one or more impellers are used to generate flow and mixing within the reactor, are widely used in variety of process industries. Some of the industrial processes carried out in stirred reactors are listed in Table 1.1 (Ranade, 2002). The classification presented here is based on the number of phases handled in the reactor. These reactors are often chosen for industrial applications instead of bubble columns, packed columns or staged tray columns when some of the following conditions are encountered (Mann, 1985),

- Gas flow is large relative to the liquid flow
- Liquid phase residence time needs to be varied over a wide range
- High level of backmixing is desirable in the fluid phases
- Good mass transfer for low solubility gases needs to be assured
- Good heat transfer properties are required (exothermic reactions)
- Liquid phase is highly viscous
- Solids are required and need to be suspended

The most obvious drawback of the stirred vessel is its greater mechanical complexity of construction in comparison to bubble, packed and staged columns. Rotating shafts and impellers confer their own difficulties from an operational perspective, especially for high pressure gas-liquid contacting, where efficient sealing is required to prevent leaks and contamination. Stirred vessels can also present difficulties at very large scales of operation due to the massiveness of the drive units and rotating parts, thereby resulting in enormous power requirement. Increased fundamental understanding of hydrodynamics and mixing in

such vessels would allow more compact and efficient designs, and will also lead to reduction in power requirement and waste generation.

Table 1.1 Some industrial applications of stirred reactors

Phases Handled	Applications
Liquid	Alkylations, Sulfonations, Esterifications, Bulk and Solution Polymerizations (styrene, acrylonitrile, ethylene, propylene)
Gas-Liquid	Oxidations (ethylene, paraffins), Chlorinations (acetic acid, dodecane), Carbonylations(methanol, propanol), Manufacture of sulfuric acid, adipic acid, oxamide, Esterifications
Gas-Liquid-Solid	Hydrogenations (olefins, edible oils, several chloro and nitro aromatics), Oxidations (p-xylene), Fermentations (alcohol, single cell proteins, antibiotics), Waste water treatment
Liquid-Liquid	Suspension and Emulsion Polymerizations (styrene, vinyl-chloride), Extractions
Liquid-Solid	Calcium Hydroxide (from calcium oxide), Regeneration of ion-exchange resins, Anaerobic Fermentations
Gas-Liquid-Liquid	Bi-phase hydroformylations, Carbonylations
Gas-Solid	Stirred fluidized beds (polyethylene, polypropylene)

1.1. Motivation for Research

The prediction of performance of stirred tank reactors still remains a challenging problem on account of the complex hydrodynamics generated by the rotating internals. The correct design and operation of these reactors can be crucial to the profitability of a process by virtue of its influence on the reaction yield or productivity. Traditionally this is based on empirical correlations describing macroscopic parameters such as power demand, overall average mass and heat transfer coefficients or dispersed phase hold-up. Many studies have

been published to describe the key parameters as functions of design variables such as impeller speed, diameter of tank and impeller or liquid height. It is, however, not uncommon that a reaction attractive on the laboratory scale fails to provide the desired performance on the production scale. The most common cause of such failure is an incomplete understanding and improper treatment of the interplay of mixing and complex reaction schemes with one or more fast reaction steps. To handle such interactions properly requires a complete understanding of the hydrodynamics of the system.

As can be seen in Table 1.1, most of the industrial processes involve more than one phase (gas-liquid, liquid-solid or gas-liquid-solid) and therefore, a better understanding of the hydrodynamics of multiphase systems is necessary before mixing effects in such systems can be investigated. Proper understanding of the mixing and hydrodynamic effects on reaction rates can lead to improved control over phase distributions and reaction selectivity, which essentially provides means for efficient design and operation leading to waste minimization, energy savings and increased profitability. This being the overall goal of the research efforts in the Center for Environmentally Beneficial Catalysis (CEBC) also provides motivation for this research work. Many of the CEBC envisioned processes use stirred tank reactors (hydroformylations, oxidations, alkylations etc.). Therefore, significant understanding of the hydrodynamics in these reactors is necessary in order to design and operate reactors for the processes envisioned in CEBC.

Mixing in a stirred tank reactor typically takes place through convection (at larger length scales in the inertial subrange; commonly referred to as macromixing), coarse-scale turbulent exchanges (at intermediate length scales larger than the Kolmogorov scale; commonly called mesomixing), as well as by deformation of fluid elements followed by molecular diffusion (at smaller length scales below the Batchelor scale; commonly described as micromixing) (Vicum et al., 2004). The effect of mixing on the reactor performance becomes important when the time scales of some of the reactions are small compared to time scale of mixing. In the completely turbulent regime ($Re_{imp} > 10^4$) the macromixing and mesomixing effects on the reactor performance depend highly on the

mean flow field and turbulence that exists within the reactor. Hence, the hydrodynamics needs to be studied before mixing and its influence on the reactor performance can be quantified.

1.2. Research Objectives

The overall objectives of this research can be summarized as follows:

(a) Development of a framework for CFD-based Compartmental Model for single phase systems to predict the effect of mixing on the performance of the reactor. To increase the generality of the model, a methodology needs to be devised to determine the number and size of the compartments necessary to represent a given reaction and impeller system provided the kinetics and operating conditions are known. With the location and size of the compartments being known, the next step involves the proper extraction of mean flow fields and turbulence quantities from the full CFD simulation to the compartmental framework in terms of averaged quantities. This framework, developed for single phase systems, can be extended to model turbulent reactive flows in two-phase systems (liquid-solid and gas-liquid), provided that the currently available CFD models are tested and validated extensively with experimental data.

(b) Quantification of solids distribution and solids flow fields in solid-liquid stirred tank reactors using two non-invasive specialized techniques namely, Computer Automated Radioactive Particle Tracking (CARPT) and Gamma-ray Computed Tomography (CT). These techniques had been developed in CREL (Devanathan, 1991; Kumar, 1994) and are useful tool to gain quantitative insights into hydrodynamics and phase distributions in multiphase reactors (Chaouki, Larachi and Dudukovic, 1997). CARPT will provide Lagrangian information regarding solids dynamics in the reactor which can be used to obtain the overall flow pattern and the Eulerian flow quantities, i.e. the ensemble-averaged velocity profiles and solids turbulent kinetic energies. The Lagrangian information can be processed to obtain the solids sojourn time distributions in the reactor as well, which will

provide insights into the solids suspension characteristics in the reactor. The other important aspect that governs the performance of a multiphase reactor and needs to be quantified is the distribution of phases inside the reactor. The time-averaged solid hold-up distribution at different cross-sections in the reactor can be obtained with the CT technique quantitatively.

(c) Evaluation of the ability of the available CFD models in predicting the solids dynamics and phase distributions in a stirred vessel. The experimental information that will be obtained using CARPT and CT can be efficiently used for this purpose. The models to be evaluated include the Large Eddy Simulation (LES) and the Euler-Euler model. Influence of different available drag and lift closures on the predictions of the Euler-Euler CFD model will also be investigated to understand which closure provides better prediction of experimental data in a solid-liquid stirred tank.

1.3. Thesis Outline

This thesis has been structured in the following manner. Chapter 2 provides a brief background and literature review of CFD and mixing models available for single phase and solid-liquid stirred tank reactors. The hydrodynamic information available in the open literature for solid-liquid stirred tanks is also discussed. The development and evaluation of the CFD-based compartmental model for single phase systems is presented in Chapter 3. Large eddy simulation of single phase flow obtained using Fluent 6.2 is assessed against CARPT and other literature data in Chapter 4. Chapter 5 outlines the experimental work carried out with the CARPT technique and the results obtained for the solids flow field in a stirred tank. Chapter 6 presents the use of the CT technique in quantifying the solids distribution in the tank, and the results obtained are critically evaluated. The assessment of the Large Eddy Simulation and the Euler-Euler model in predicting the solids dynamics in a stirred tank is discussed in Chapter 7. Finally, the work is summarized in Chapter 8 and the conclusions reached are reported. The areas that require future attention are also outlined.

Chapter 2

Background

The effects of flow and mixing on reactive systems have been recognized for many decades. Due to their importance in the field of process industries, the interplay of mixing and reaction in stirred vessels has been the subject of many investigations (Paul and Treybal, 1971; Middleton, Pierce and Lynch, 1986; Akiti and Armenante, 2004). The lack of scale-up reliability of these reactors is partly due to the fact that most investigations have attempted to set up correlations among spatially averaged parameters (lumped parameter models), such as average temperature and reagent concentrations (assumption of perfect mixing), average power dissipation per unit volume, average mass transfer coefficients, and so on. On the other hand, all these parameters may exhibit considerable variation within the stirred vessel and are considerably affected by the geometry of the impeller and of the mixing tank and, in general, scale up differently. All these in-homogeneities are wiped out by the lumping process, which is therefore bound to lead to uncertainties in the final result.

In order to avoid the limitations associated with the lumping process, distributed parameter models, based on the actual flow fields in the mixing tanks, are preferable. These require an accurate knowledge of the local properties of the flow field in the mixer, which can be obtained either through experimentation (Rammohan, 2002; Fishwick et al., 2005) or by numerical simulation of the relevant flow fields (Brucato et al., 2000; Ljungqvist and Rasmuson, 2001; Ranade et al., 2001b; Derksen, 2003). Understanding the hydrodynamics and phase distributions in the reactor is necessary before turbulent reactive flows can be modeled and the effect of mixing on reactor performance can be quantified.

2.1. Single Phase Flow Modeling

The hydrodynamics in stirred tanks of even single phase flow is extremely complex due to the presence of rotating internals and regions of large velocity gradients. The simulation of three-dimensional flow fields in these reactors is a complex, computation-intensive task. However, the continuing decrease of computing costs and the development of commercial codes for computational fluid dynamics (CFD) have prompted several studies aimed at its application to mixing tanks (Middleton, Pierce and Lynch, 1986; Brucato et al., 1994; Brucato et al., 2000; Bujalski et al., 2002). The quality of the computed results strongly depend on the spatial resolution (finer grid size improves the accuracy of the result but increases the computation time significantly) as well as on the turbulence model used.

Flow in baffled stirred reactors has been modeled by employing several different approaches, which can be mainly classified into four types (Ranade, 2002):

- Black Box approach (most publications before 1995)
- Sliding Mesh model
- Multiple Reference Frame or Inner-Outer approach
- Snapshot approach

The black box approach (Placek et al., 1986; Kresta and Wood, 1991) excludes the impeller region from the solution domain and replaces it with the boundary conditions on the surface swept by the impeller blades which are specified using either experimental data or simplified models. In most cases k - ε turbulence model has been used which requires boundary conditions for k and ε as well. The applicability of this approach is limited by the availability of experimental data and is not applicable to new operating conditions without corresponding experimental measurements. The extension to multiphase flows is not trivial since it is extremely difficult to obtain accurate boundary conditions at the impeller. More importantly, this approach does not capture the details of the flow in the impeller region, which is needed for realistic simulations of reactive mixing and multiphase flows in stirred reactors.

To eliminate the limitations of the black box approach, attempts have been made to simulate the flow within and outside the impeller region either with a combination of moving and deforming mesh or with a sliding mesh (Harris et al., 1996; Ng et al., 1998). In the sliding mesh approach, full transient simulations are carried out using two grid zones. One grid zone is attached to the stationary baffles and reactor wall while the other is attached to the rotating impeller. This approach is more general as it does not require any experimental input for the simulations. However, the computational requirements are significantly higher which make the sliding mesh model less attractive for modeling flows in industrial reactors. Also, it is not always necessary to have a full time varying flow field for most engineering calculations as the flow field becomes cyclical after a number of impeller rotations. This led to the development of the other two approaches to approximate unsteady flow in stirred vessels.

In the Multiple Reference Frame (MRF) or the inner-outer approach (Brucato et al., 1994; Marshall, Haidari and Subbiah, 1996) flow characteristics of the inner region are solved using a rotating framework. These results provide the boundary conditions for the outer region which is solved in a stationary framework. The outer region solution then provides the boundary conditions for the inner region. This is repeated in an iterative manner. The effect of rotation is accounted for by including the Coriolis acceleration term and the centrifugal force term.

The snapshot approach is based on taking a snapshot of flow in stirred vessels with a fixed relative position of the blades and baffles (Ranade et al., 2001b). In the snapshot approach, the flow is simulated using a stationary framework for a specific blade position. If necessary, simulations can be carried out at different blade positions to obtain ensemble-averaged results over different blade positions.

Apart from these four approaches for modeling the rotating impeller, the Immersed Boundary (IB) method (Peskin, 2002) has also been employed recently to model flows in stirred vessels (Verzicco et al., 2004; Tyagi et al., 2007). In this method, which was

originally introduced to study flow patterns around heart valves (Peskin, 1972), the complex geometrical features are incorporated by adding a forcing function in the governing equations (Tyagi et al., 2007). The forcing function is specified in such a way that the presence of a flow boundary within the computational domain can be simulated without altering the computational grid (Mohd-Yusof, 1998). This can reduce the computation cost significantly since grid restructuring is often time consuming and computationally expensive. The Immersed Boundary methodology and the detailed derivation of the governing equations are discussed by Peskin (2002).

The issues that still remain in the simulation of turbulent flows are the closures associated with the Reynolds averaged Navier-Stokes (RANS) equations. In the standard k - ε model the stresses are closed invoking the Boussinesq hypothesis which assumes that the Reynolds stresses are proportional to the mean velocity gradients with the constant of proportionality being turbulent viscosity. The turbulent viscosity is calculated based on the information from the k - ε model. The standard k - ε model, however, has the inherent disadvantage of lumping all the length scales associated with the turbulence process into a single scale, and as a result cannot resolve the turbulence appropriately. In fact, the equation for k is not exact and involves gradient-diffusion approximation to close the equation, while the equation for ε is almost pure invention (Davidson, 2004) where the model constants are tuned to capture certain well-documented flows. “In effect, the k - ε model is a highly sophisticated exercise in interpolating between data sets” (Davidson, 2004). As a result, even if the quantitative prediction of the mean flow field using this model for single phase flow in stirred tanks is accepted to be of engineering accuracy, the predictions for the turbulent kinetic energy are not reasonable (Rammohan, 2002). Similar observation can be made from the work of Jones et al. (2001) who compared the performance of six different two-equation turbulence models (k - ε , k - ω and their variants) in predicting the flow in an unbaffled stirred tank by comparing them with Laser Doppler Velocimetry (LDV) data. They conclude that discrepancies in predictions exist near the impeller shaft and the impeller discharge region where the flow is non-isotropic, and suggest that more sophisticated turbulence model is required to account for the non-

isotropy in the flow (Jones, Harvey III and Acharya, 2001). On the other hand, Deglon and Meyer (2006) mention that the poor predictions typically obtained using the k - ϵ turbulence model might be because of numerical errors rather than the shortcoming of the turbulence model itself. Although the mean flow field remains almost unaffected by the grid resolution or the discretization scheme, the turbulent kinetic energy predictions seem to be strongly dependent on them (Deglon and Meyer, 2006). In their study, a grid consisting of nearly two million cells to describe half of a tank 15cm in diameter along with a high-order discretization scheme was necessary to obtain reasonable prediction for the turbulent kinetic energies.

To resolve turbulence at all scales, Direct Numerical Simulation (DNS) is an option which essentially involves a full numerical simulation of the governing Navier-Stokes equation without any approximation. The effect of eddies on the mean flow are not modeled at any scale and eddies of all sizes from the largest (order of reactor length scale) to the smallest (Kolmogorov microscale, l_k) are computed directly. This requires the simulation to be performed using very fine grids (grid spacing of the order of Kolmogorov microscale, l_k) and very small time steps ($\Delta t \sim l_k/U$, where U is the characteristic velocity). It turns out that the computer time required for DNS simulation is proportional to the cube of the Reynolds number (Davidson, 2004), which essentially makes the DNS impossible for the simulation of industrial flows at high Reynolds numbers with currently available computational resources (Fox, 1996). However, as expected, more accurate predictions for both the mean and fluctuating flows can be obtained with DNS compared to RANS simulation at relatively low Reynolds number (Verzicco et al., 2004), and hence DNS can be efficiently used as a bench-marking tool by carrying out numerical experiments with the flow of interest (Davidson, 2004).

The more viable alternative to the Direct Numerical Simulation is the Large Eddy Simulation (LES). This approach resolves the large-scale structures but does not solve for the sub-grid scales directly. The influence of the small scale eddies on the flow is modeled using a suitable sub-grid scale (SGS) model. An example of such a model that is commonly

used is the Smagorinsky model (Smagorinsky, 1963), which assumes the SGS motion to be purely diffusive and represents it in terms of an eddy viscosity. The rationale behind LES is based on the fact that the smaller scales in the energy cascade are largely passive taking up whatever energy is passed on to them from the larger scales, which is justified since energy and information generally travel down to smaller scales but not in the reverse direction (Davidson, 2004). LES has been successfully applied to model single phase flows in stirred vessels (Revstedt, Fuchs and Tragardh, 1998; Derksen and Van den Akker, 1999; Alcamo et al., 2005) and comparison with RANS simulation (Hartmann et al., 2004) clearly demonstrates the superiority of LES in terms of predicting the turbulent quantities in the reactor. However, it should be noted that the improvement in the predictions obtained in a large eddy simulation is still at the expense of the computational cost associated with it. But considering the facts that often (though not always) it is the large scale eddies in a flow which are dominant, and that in DNS most of the computational effort is spent in resolving the small-to-intermediate scales (Davidson, 2004), the large eddy simulation becomes the more viable option compared to DNS in order to gain fundamental understanding on turbulent flows. Although LES is computationally much cheaper than the DNS, it is still extremely difficult to use for the simulation of large scale industrial reactors. As a result, for such cases, $k-\varepsilon$ is still the model of choice in spite of its limitations.

2.2. Mixing Effect on Reactive Flows

The reactants in a chemical reactor have to come into contact at the molecular level before the chemical reaction can take place. The course of chemical reactions, which is dictated by molecular events, is therefore directly affected by mixing within the reactor. This understanding of the importance of turbulent reactive mixing on reactor performance resulted in the development of many phenomenological models of different level of complexities to describe its effect in stirred tank reactors. Some examples include the Segregated Flow/ Maximum Mixedness models, the Interaction by Exchange with the Mean (IEM) model (David and Villermaux, 1987), the Engulfment Deformation Diffusion (EDD) model (Baladyga and Bourne, 1984a), and more recently the Population Balance

model (Madras and McCoy, 2004). These models primarily attempt to describe the effect of micromixing on the reactor performance. But none of them account for the detailed flow description within the reactor.

The other prevalent approach is the compartmental modeling approach which essentially attempts to describe the macromixing effects on reactor performance, but accounts for certain level of mesomixing as well (through the inclusion of the exchange terms in the conservation equation). An example of this approach is the Network of Zones model (Mann and Hackett, 1988; Mann and El-Hamouz, 1995; Holden and Mann, 1996), which divides the reactor into smaller perfectly mixed cells which are connected through typical flow patterns. This model, however, depends on the available literature correlations for the impeller pumping flow to map the flow field in the system. It has been shown that the uncertainties in the estimation of the flow number (which vary 30-50% depending on the different literature correlations used) can result in uncertainties in the model predictions (Boltersdorf, Deerberg and Schluter, 2000). Turbulence is mimicked in the Network of Zones model by the use of exchange flows which are taken as a fraction of the main flow through the compartment. These fractions and the number of compartments serve as the model parameters and are generally selected arbitrarily.

Mixing has a major influence on the product ratio in fast competitive reactions, as the product ratio in these reactions is determined by local concentrations (Middleton, Pierce and Lynch, 1986; El-Hamouz and Mann, 1998). Partial segregation of reagents occurs when reaction rates exceed mixing rates and frequently causes product distributions to be mixing dependent. This segregation of species has been shown to happen for dispersion of tracers and different reactions both experimentally and computationally by several authors (Paul and Treybal, 1971; Middleton, Pierce and Lynch, 1986; Mann and Hackett, 1988; Mann and El-Hamouz, 1995; El-Hamouz and Mann, 1998; Brucato et al., 2000; Boltersdorf, Deerberg and Schluter, 2000; Assirelli et al., 2002; Verschuren, Wijers and Keurentjes, 2002). Similar to concentration segregation, temperature segregation can also

occur within the reactor (Baladyga, Bourne and Walker, 1998), which can be of importance for exothermic reactions.

More recently, CFD has emerged as an alternative modeling tool, which can be used to solve the flow field as well as the concentration field simultaneously (or separately) in a stirred vessel (Smith, 1997; Brucato et al., 2000; Bujalski et al., 2002). In modeling of turbulent reactive flows using the Reynolds averaged equations, closing the scalar flux and the reaction terms is necessary to solve for the concentration field. Most often, the scalar flux term is closed using the gradient diffusion model (Fox, 1996) which assumes that the scalar flux is proportional to the gradient of the mean concentration and the constant of proportionality is defined as the turbulent diffusivity or the eddy dispersion coefficient. For slow reactions ($Da \ll 1$), the contribution from the fluctuating concentrations to the reaction term is small, since turbulent mixing occurs before the reaction can take place (Fox, 1996). In other cases the reaction term can be closed using a PDF description of the scalar field. The advantage of this method is that the total contribution to the reaction term can be directly calculated from the composition PDF (Fox, 1996; Fox, 2003). An approach based on the PDF method is the Turbulent Mixer model (Baladyga, 1989; Vicum et al., 2004) which characterizes the mixture structure by solving the mixture fraction and the variance (decomposed into different components) equations for an inert tracer. More fundamental simulations to investigate the mixing effects in chemical reactors can be carried out using large eddy simulation (LES), although feasibility of such an approach for industrial reactions that comprises of large number of species is still questionable. However, mixing time required for inert blending operations can be fundamentally investigated using this methodology and better predictions can be obtained compared to those obtained using the RANS model (Hartmann, Derksen and Van den Akker, 2006; Jian and Zhengming, 2006).

One of the limitations of CFD modeling of turbulent reactive flows is that it can become computationally intensive which might be of serious concern in prediction of product distribution for industrial reactions where the number of components involved might be

significantly large. An improved methodology (in terms of computational expenses) can be devised if flow and turbulence parameters obtained from CFD simulation (or experimental data) in the reactor are used along with the phenomenological models, thereby decoupling the flow and the kinetics of the system but still accounting for the effect of the hydrodynamics on the mixing behavior of the system. There have been many such modeling efforts over the last few years for different reactors like stirred tanks (Alexopoulos, Maggioris and Kiparissides, 2002; Bezzo, Macchietto and Pantelides, 2003; Akiti and Armenante, 2004), autoclaves (Wells and Harmon Ray, 2005), crystallizers (Kougoulos, Jones and Wood-Kaczmar, 2006), bubble columns (Rigopoulos and Jones, 2003) and slurry bubble column reactors (Degaleesan, 1997) and it has been shown that they produce reasonable predictions at much lower computational cost.

2.3. Liquid-Solid Flows

Turbulently agitated solid-liquid suspension is one of the most important unit operations in the chemical, biochemical and mineral processing industries, because of its ability to provide excellent mixing and contacting between the phases. This ensures good heat and mass transfer properties for the system, apart from providing good solid suspension because of the flow pattern and turbulence prevailing in the reactor. Relevant examples of solid-liquid systems include multiphase catalytic reactions, crystallization, precipitation, leaching, dissolution, coagulations and water treatment. Despite their widespread use, the design and operation of these tanks remain a challenging problem because of the complexity encountered due to the three dimensional circulating and turbulent multiphase flow in the reactor.

2.3.1. Experimental Studies

An important aspect in the design and operation of slurry reactors is the determination of the state of full suspension, at which point no particles reside on the vessel bottom for a long time. Such a determination is critical to enhance the performance of the reactor,

because until such a condition is achieved the total surface area of the particles is not efficiently utilized. Considerable research was directed to determine the minimum impeller speed N_{js} required to suspend all the particles from the bottom of the reactor. The pioneering work of Zwietering (1958) based on visual observations for the “just-suspended” condition (no particle settles at the tank bottom for more than 1 second) is still the most widely used criterion in operation of solid-liquid stirred tank reactors. Numerous papers on “just-suspended” speed for different operating conditions and different impellers have been published since then (Nienow, 1968; Takahashi and Fujita, 1995; Armenante, Nagamine and Susanto, 1998; Wu, Zhu and Pullum, 2001), which are all similar to the Zwietering’s correlation, except that variations in the exponents of different terms can be observed. Baldi et al. (1978) took a semi-empirical approach and derived an expression for the “just-suspended” speed using turbulent scaling arguments. Their derivation is based on the assumption that the suspension of particles in the tank is mainly due to eddies of a certain critical scale, which is of the order of the particle size. Their analysis leads to a similar expression as the one obtained by Zwietering. Quantification of the unsuspended mass of solid particles experimentally (Brucato and Brucato, 1998), however, show that at speeds of about 80% of Zwietering’s ‘complete suspension’ speed practically all particles get suspended. This can have significant impact on the energy savings with respect to current design practices.

Although the available correlations in the literature are of great importance from an operational point of view, they do not provide a clear understanding of the physics underlying the system. From a physical standpoint, the state of suspension of solid particles in the reactor is completely governed by the hydrodynamics and turbulence prevailing in the reactor. The interaction of the particles with the liquid flow field (in terms of lift, drag, buoyancy and gravity forces) and also the interactions with other particles (significant for dense systems) determine the motion of the solid particles within the reactor. Although many experimental efforts have been focused on developing correlations for “just-suspension speed”, a systematic experimental study to characterize the solids hydrodynamics in slurry reactors can hardly be found in the literature. Nouri and Whitelaw

(1992) used the laser-Doppler velocimetry (LDV) to measure the mean velocities and turbulent quantities of the solid phase in a fully baffled stirred tank reactor driven by a Rushton turbine. But their experiments were carried out predominantly for very dilute suspensions (0.02 vol %) which is well below 0.3% suggested by Lumley (1978) for particle-particle interaction to be significant, and hence, the reported solids dynamics does not show very significant deviation from the measurements obtained in single phase flow (Nouri and Whitelaw, 1992). Wittmer et al. (1997) reported the Lagrangian tracking of a solid particle inside a stirred tank using two synchronized video cameras. Their technique, however, cannot be considered versatile because of the associated drawbacks: the fluid has to be optically transparent and the particle has to be large so that it is visible. Also, such optical method is likely to fail in case of dense suspensions where the system tends to become more and more opaque. Wu et al. (2000) used a dense suspension (22.5 vol %) in their study to investigate the pumping performance of axial flow impellers and its influence on solids suspension. Using LDV they reported only the time-averaged axial velocity distribution at a distance 10% of the impeller diameter below the center line. The other velocity components as well as turbulent parameters are not measured in this work because of the fact that their objective was to relate the impeller pumping capacity to the “ S ” parameter in the Zwietering’s correlation. Recently, Fishwick et al. (2005) used the positron emission particle tracking (PEPT) to study the fluid dynamics in solid-liquid stirred tanks. They successfully demonstrated that PEPT can provide Lagrangian description of solids dynamics in the reactor, but their study is limited to a very dilute system as well (1% w/w). Hence a systematic experimental characterization at higher solids loading is still lacking in the literature and needs to be addressed in order to have a better understanding of solids flows in dense slurry reactors.

The other important aspect of solid-liquid flow, apart from the solids flow dynamics, is the quantification of solids distribution in the stirred vessel. The condition for the critical impeller speed for incipient solid suspension ensures that the solids do not stay at the tank bottom for a long time, which essentially provides the lower bound of the operational speed for a geometrical arrangement and solids loading in the reactor. The upper bound,

on the other hand, is actually given by the speed at which nearly homogeneous suspension is achieved in the reactor, but in reality will be dictated by the power requirement since the power is proportional to the cube of the impeller speed. An optimum, from an operational point of view, exists between these two bounds where significant suspension can be achieved with a reasonable power input.

There have been few attempts to experimentally study the solids dispersion and suspension in a stirred vessel (Yamazaki et al., 1986; Barresi and Baldi, 1987; Shamlou and Koutsakos, 1989; Godfrey and Zhu, 1994; Spidla et al., 2005) in a systematic manner. Many of these investigations report only the axial variations of the solids concentration in the reactor (Shamlou and Koutsakos, 1989; Godfrey and Zhu, 1994). The measured solids concentration in such cases is believed to be representative of the mean concentration in the entire cross section. This would be the case if there are no radial solids concentration gradients. Yamazaki et al. (1986) and Barresi and Baldi (1987), on the other hand, measured the radial solids concentration profiles in a stirred vessel but observed that significant radial gradients did not exist for the conditions of their experiments. The experimental measurements presented by Barresi and Baldi (1987) were for dilute suspension with overall solids loading of 1.5% and solids particle diameter in the range of 100-177 μm . This probably led to the observation of the flat radial profiles for the solids concentration in the tank when operated at speeds around the “just-suspension” speed predicted by the Zwietering’s correlation (1958), which has been shown to over-predict the speed for incipient solid suspension in the reactor (Brucato and Brucato, 1998). The observation of Yamazaki et al. (1986) is rather surprising since they used a dense suspension of 15% (v/v) with particle diameters of 135 μm . The operational speed was somewhere between 300 to 1200 RPM, but the impeller speed at which the radial measurements were made is not reported in the paper. Small particle size might have led to the suspension quality observed in their work. Also it should be noted that most of these studies are either carried out using intrusive techniques like optical-fiber probe (Yamazaki et al., 1986), conductivity probe (Spidla et al., 2005), by drawing samples from the reactor (Barresi and Baldi, 1987), or are performed using various optical measurement techniques (Shamlou and Koutsakos, 1989;

Godfrey and Zhu, 1994). The intrusive techniques have the disadvantage that the probe itself will have some effect on the flow dynamics and solids suspension, while the optical techniques suffer from the limitation that such techniques are not applicable to dense 'opaque' systems.

2.3.2. Solids Flow Modeling

With the improvement in computational capabilities, Computational Fluid Dynamics (CFD) has emerged as a viable option to study turbulent multiphase flows and gain insights on the hydrodynamic behavior of complex systems. Several such attempts have been made to investigate the solids flow dynamics in stirred tank reactor as well, starting from the 'black-box' approach to describe the impeller (Gosman et al., 1992; Barrue et al., 2001), where experimental data provides the boundary conditions at the impeller region to perform the simulation. The 'black-box' approach is obviously not entirely predictive in nature and requires experimental information at all conditions that are simulated. The increase in computational power further led to the use of the Algebraic Slip Mixture model (Altway et al., 2001) which assumes that both the phases exist at all points in space in the form of interpenetrating continua, and the equations solved comprise of the continuity and momentum equations for the mixture, volume fraction equation for the secondary phase and an algebraic equation for the slip velocity between the phases which then allows the two phases to move at different velocities. The Euler-Euler approach also invokes the concept of interpenetrating continua, but solves the continuity and momentum balances for each phase separately which results in simultaneous determination of the flow fields of the two phases (Montante et al., 2001; Sha et al., 2001; Micale et al., 2004; Montante and Magelli, 2005; Spidla et al., 2005; Khopkar et al., 2006). The Euler-Lagrange approach, on the other hand, considers each particle individually and tracks their trajectories by solving the equations of motions for each of them (Decker and Sommerfeld, 1996; Zhang and Ahmadi, 2005). As a result, this approach is considerably more expensive compared to the Euler-Euler approach and is mostly limited to simulations of solids volume fraction less than about 5%. Derksen (2003) used the large eddy simulation (LES) to model the solids

dynamics in a turbulently agitated stirred tank. As discussed earlier, the LES methodology is much more fundamentally based compared to that of the standard RANS based models since it directly solves for the large scale eddies while the influence of the small scale eddies on the flow are modeled. The improved predictions obtained for single phase flows using LES (Derksen and Van den Akker, 1999; Hartmann et al., 2004) also motivated the use of LES to model solid-liquid flows. However, because of the large computational cost associated with it, these simulations are still limited to smaller reactor sizes and relatively lower volume fractions of solids (Derksen, 2003). Similar to single phase systems, the most fundamental simulation that can be carried out for two-phase flow is the direct numerical simulation (DNS), where all the length scales of turbulence (integral scale to the Kolmogorov microscale) are directly resolved by performing the simulation with very fine grid and solving the Navier-Stokes equations at very small time step. Sbrizzai et al. (2006) attempted to carry out a direct numerical simulation of the solids dispersion in an unbaffled stirred tank reactor, where the Lagrangian tracking of the solids were performed for a period of three impeller revolutions. This was limited by the computational resources available. However, the authors observed that this time window was not long enough to obtain a fully developed field for the solids phase, and hence they used their preliminary study only to derive an understanding of the transient of dispersion dynamics. The huge computation expense for DNS and the fact that resolving the microscales might be often unnecessary (Davidson, 2004), therefore, makes the large eddy simulation a more realistic alternative in order to gain fundamental understanding on two-phase turbulent flows.

Although Computational Fluid Dynamics (CFD) does provide a platform that can be used to obtain significant insights into complex multiphase flow problems, it is necessary to validate the model predictions extensively with experimental data before they can be confidently used for the design and operation of industrial reactors. However, as mentioned before, most of the experimental work carried out for solid-liquid stirred tanks focus on the determination of the minimum impeller speed for incipient particle suspension (Nienow, 1968; Takahashi and Fujita, 1995; Armenante et al., 1998; Wu et al., 2001) resulting in correlations which are similar to that of Zwietering's (1958) except that

variations in the exponents of different terms can be observed. These correlations do not provide any insight into the solid-liquid flows in the tank and, in reality, have only operational importance. The experimental studies reported in the literature mostly consist of the axial measurement of concentration profiles in the vessel (Yamazaki et al., 1986; Barresi and Baldi, 1987; Shamlou and Koutsakos, 1989; Godfrey and Zhu, 1994; Spidla et al., 2005), which ignore the radial gradients that exist in the reactor. As a result, the majority of the CFD studies for solid-liquid stirred tanks are either devoted to the improved prediction of axial solid concentration profiles only (Micale et al., 2000; Barrue et al., 2001; Altway et al., 2001; Montante and Magelli, 2005; Spidla et al., 2005; Khopkar et al., 2006), or are focused on the prediction of particle suspension height in a stirred vessel (Micale et al., 2004). The predictions for the solids flow and solids distributions in the tank have not been extensively validated yet, but are necessary in order to use CFD for the design, optimization and scale-up of solid-liquid stirred tank reactors.

2.4. Summary

The review of the open literature presented here clearly shows that single phase and multiphase flow dynamics and mixing have an important role to play on the performance of stirred tank reactors. The local concentrations in the reactor govern the product distribution and the reactor performance when time scales of some of the reactions are small compared to the time scale of mixing. The convective flow generated by the impeller rotation determines the macromixing behavior of the system, while mesomixing occurs due to the dispersion due to turbulence. As a result, it is imperative to account for the flow field and turbulence in the reactor in order to predict and quantify the effects of mixing in the system. CFD turns out to be a promising approach in this regard, but can be still limited by the computational cost required for the simulation of large scale industrial reactors with large number of reactions taking place in the system. An efficient and cost-effective approach can be a combination of CFD and compartmental model to tackle the turbulent reactive flow problem of industrial importance. But, unlike the existing Network of Zones model, the number and location of the compartments to be used should be

determined from the flow and kinetic information based on a time-scale analysis in order to make the model more general and adaptable to various reaction systems.

The CFD-based compartmental approach can be expanded to two-phase solid-liquid systems as well, when the CFD predictions in such systems are thoroughly tested and validated. Currently available experimental studies are either focused towards the development of correlations for critical impeller speed to achieve incipient solid suspension, or report axial variations of solids concentration in the tank while ignoring the radial variations that can often exist. As a result, most of the literature on CFD simulations of solid-liquid stirred vessels attempts to provide improved prediction of axial solids concentration profiles only, rather than providing detailed comparison of the flow and phase distribution predictions in the tank. Experimental data on solids hydrodynamics at reasonable solids loading is sparse and needs to be obtained. Solids distribution in the reactor should also be studied and both axial and radial variations of solids distribution should be reported. Such information, if obtained, will provide the opportunity to evaluate and assess the ability of available CFD models in predicting the solids dynamics and solids distribution in a solid-liquid stirred tank extensively and critically. This is essential before turbulent reactive flows in these complex systems can be modeled and mixing effects on the reactor performance can be quantified.

Chapter 3

CFD-Based Compartmental Model for Single Phase Systems

The impact of flow and mixing on the reactor performance has been recognized for several decades (Paul and Treybal, 1971; Middleton, Pierce and Lynch, 1986; Mann and Hackett, 1988; Mann and El-Hamouz, 1995; El-Hamouz and Mann, 1998; Brucato et al., 2000; Boltersdorf, Deerberg and Schluter, 2000; Assirelli et al., 2002; Verschuren, Wijers and Keurentjes, 2002). Quantification of such effects is important for the design and scale-up of stirred tank reactors. Understanding the interplay of hydrodynamics and mixing in these reactors provides better control over product selectivity, which in turn leads to reduction in waste generation (undesired products) and to increased profitability of operation. Computational Fluid Dynamics (CFD) provides a promising platform for modeling turbulent reactive flows by solving the flow and kinetics in the reactor either simultaneously or sequentially. However, CFD simulations can become computationally very expensive when the number of species in the reactor is large, which is common for many of the industrial processes. The CFD-based compartmental approach provides a more viable and realistic alternative to model such systems at a lower computational cost by using a length scale significantly larger than typical CFD grids. This length scale of the compartment is, however, very important and should be determined based on the flow and kinetics in the system. Such a methodology can provide reasonable predictions for the mixing effects in the stirred vessels at a reduced cost. This chapter describes the development of the CFD-based compartmental model for single phase turbulent reactive flows in stirred tank reactors. A scheme has been developed to determine the number and locations of the compartments based on the detailed flow simulation data provided the

kinetics of the system is known. The results have been tested against experimental data available in the literature and comparison has been made with the predictions of full blown CFD simulation as well.

3.1. Detailed Model for Turbulent Reactive Systems

The mass balance equation for any component c in the reactor is given by (Bird, Stewart and Lightfoot, 1994)

$$\frac{\partial c_c}{\partial t} + u_i \frac{\partial c_c}{\partial x_i} = D_m \frac{\partial^2 c_c}{\partial x_i^2} + R_c \quad (3.1)$$

Note that the repeated index i implies summation. Reynolds averaging of equation (3.1) by decomposing the concentration as $c_c = \bar{c}_c + c_c'$ and the velocity as $u_i = \bar{u}_i + u_i'$ results in

$$\frac{\partial \bar{c}_c}{\partial t} + \bar{u}_i \frac{\partial \bar{c}_c}{\partial x_i} + \overline{\frac{\partial u_i' c_c'}{\partial x_i}} = D_m \frac{\partial^2 \bar{c}_c}{\partial x_i^2} + \bar{R}_c + \overline{R_c'} \quad (3.2)$$

Rendering equation (3.2) dimensionless by using a characteristic length scale L , velocity scale U_0 and concentration scale C_0 we get (* indicates dimensionless quantities),

$$\frac{\partial \bar{c}_c^*}{\partial t^*} + \bar{u}_i^* \frac{\partial \bar{c}_c^*}{\partial x_i^*} + \overline{\frac{\partial u_i'^* c_c'^*}{\partial x_i^*}} = \frac{D_m}{LU_0} \frac{\partial^2 \bar{c}_c^*}{\partial x_i^{*2}} + Da \bar{R}_c^* + Da \overline{R_c'^*} \quad (3.3)$$

The second term on the LHS of equation (3.3) accounts for convection due to the mean flow. The third term accounts for dispersion caused by the fluctuations. The Reynolds averaged reaction term contains the contributions from the mean reactant concentrations (\bar{R}_c^*) and the mean of the cross terms of the fluctuating concentrations ($\overline{R_c'^*}$). Damkohler number, Da , is the ratio of the convection time scale to the reaction time scale ($Da = (L/U_0)/(C_0/R(C_0))$). The first term on the RHS accounts for the contribution from molecular diffusion. $\frac{D_m}{LU_0}$ is the ratio of the convection time scale to the diffusion

time scale, i.e. inverse of the Peclet number, Pe . For completely turbulent flows at high Reynolds number for liquid phase systems $Pe \gg 1$ (since $Re \gg 1$ and $Sc \gg 1$) and the contribution of molecular diffusion can be safely neglected. However, the scalar-flux term (dispersion) and the second part of the reaction term ($\overline{R_c^*}$) need to be closed to solve the system of equations.

The scalar flux term is commonly closed using the gradient diffusion model (Fox, 1996) which can be written as

$$\overline{u_i c_c} = -D_t \frac{\partial \overline{c_c}}{\partial x_i} \quad \text{or,} \quad \overline{u_i^* c_c^*} = -\frac{D_t}{LU_0} \frac{\partial \overline{c_c^*}}{\partial x_i} \quad (3.4)$$

where D_t is defined as the turbulent diffusivity, or the eddy dispersion coefficient, which varies from region to region within the reactor. $\frac{D_t}{LU_0}$ is the ratio of the convection time scale to the dispersion time scale (inverse of the dispersion Peclet number), i.e. a product of the Sc_T^{-1} (turbulent Schmidt number) and Re_t^{-1} ($Re_t = \frac{LU_0}{\nu_t}$).

The contribution from the fluctuating concentrations in the reaction term ($\overline{R_c^*}$) is small for slow reactions ($Da \ll 1$), where the turbulent mixing will occur before the reaction can take place (Fox, 1996). In the limit of infinitely fast reaction this term is equal in magnitude and opposite in sign to the mean reaction term, where sub-grid scale mixing or micromixing limits the rate (Fox, 2003). In case when micromixing is fast compared to the reaction time scale, the composition variable can be approximated by their mean values and the contribution from the fluctuating concentration can be neglected (Fox, 2003). In other cases the reaction term can be closed using a PDF description of the scalar field. The advantage of this method is that the total contribution to the reaction term can be directly calculated from the composition PDF (Fox, 1996). An example which uses the presumed PDF method is the Turbulent Mixer model (Baldyga, 1989; Vicum et al., 2004) which characterizes the mixture structure by solving the mixture fraction and the variance

(decomposed into different components to characterize concentration fluctuations on different scales) transport equations for an inert tracer. The real shape of the PDF is approximated with a beta-function that depends on time and position through the mean and variance of the local mixture fraction. The non-linear reaction rate can then be computed using the beta-function assumed. The details of the different closures available for the reaction term can be found in Fox (2003).

This differential model (equation 3.3) for the distribution of scalar (e.g. concentration) can be solved along with the Navier-Stokes equations to compute the concentration field within the reactor. Commercially available CFD packages like FLUENT have codes to solve these equations based on the finite volume approach. However, as mentioned earlier, this can become computationally intensive for multiple reactions with complex chemistries. In such cases model reduction into compartments can be useful.

3.2. Model Reduction and Compartment Level Equations

The compartmental modeling approach divides the entire reactor into a number of connected, well-mixed compartments as shown in Figure 3.1. Model reduction for this work is then obtained by volume averaging equation (3.3) over a defined compartment (a finite control volume V), which yields

$$\frac{d}{dt^*} \int_V \bar{c}_c dV + \int_V \bar{u}_i \frac{\partial \bar{c}_c}{\partial x_i} dV + \int_V \frac{\partial \bar{u}_i \bar{c}_c}{\partial x_i} dV = \int_V Da \bar{R}_c dV + \int_V Da \bar{R}_c^* dV \quad (3.5)$$

Using the Divergence Theorem and substituting equation (3.4) for $\bar{u}_i \bar{c}_c^*$, equation (3.5) is modified to,

$$\frac{dV \langle \bar{c}_c^* \rangle}{dt^*} + \int_S n_i \bar{u}_i \bar{c}_c^* dS = \int_S \frac{D_t}{LU_0} n_i \frac{\partial \bar{c}_c^*}{\partial x_i} dS + \int_V Da \bar{R}_c dV + \int_V Da \bar{R}_c^* dV \quad (3.6)$$

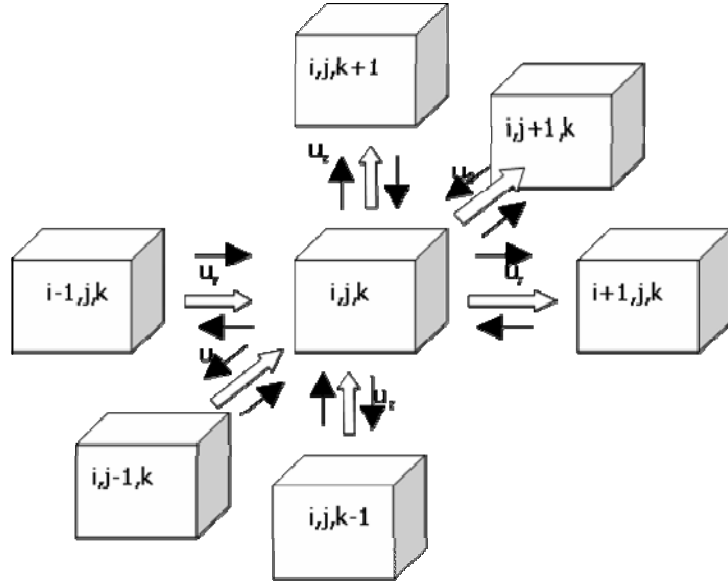


Figure 3.1 Configuration of a single backmixed compartment showing neighboring interconnected compartments

where $\langle c_c^* \rangle$ is the volume averaged concentration in the control volume defined as $\langle c_c^* \rangle = \int_V c_c^* dV / V$. The second term on the LHS of equation (3.6) can be written as $\int_S n_i \langle \bar{u}_i c_c^* \rangle dS = \sum_{k=1}^6 \langle \bar{u}_m \rangle_k \langle \bar{c}_{c,m} \rangle_k S_k$, where, $\langle \bar{u}_m \rangle_k$ is the surface average velocity and $\langle \bar{c}_{c,m} \rangle_k$ is the mixing-cup average (or volumetric flow rate average) concentration on surface k of the compartment defined as

$$\langle \bar{u}_m \rangle_k = \frac{\int_{S_k} n_i \bar{u}_i dS_k}{\int_{S_k} dS_k} \quad \text{and} \quad \langle \bar{c}_{c,m} \rangle_k = \frac{\int_{S_k} n_i \langle \bar{u}_i c_c^* \rangle dS_k}{\int_{S_k} n_i \bar{u}_i dS_k}$$

Note that the mixing-cup average concentration ($\langle \bar{c}_{c,m}^* \rangle_k$, for all k) is equal to the volume averaged concentration ($\langle c_c^* \rangle$) only when there is no concentration gradient in the volume element.

The first term on the RHS (dispersion term) of equation (3.6) denotes mixing due to eddy transport (mesomixing) across the cell faces. This can be written as

$$\int_S \frac{D_t}{LU_0} n_i \frac{\partial \bar{c}_c^*}{\partial x_i} dS = \sum_{k=1}^6 \frac{\langle D_t \rangle_k}{LU_0} \langle \frac{\partial \bar{c}_c^*}{\partial x_i} \rangle_k S_k, \text{ where, } \langle D_t \rangle_k \text{ is the surface average turbulent}$$

diffusivity and $\langle \frac{\partial \bar{c}_c^*}{\partial x_i} \rangle_k$ is the surface average gradient of the concentration on surface k of

the compartment defined as

$$\langle D_t \rangle_k = \frac{\int_{S_k} D_t dS_k}{\int_{S_k} dS_k} \quad \text{and} \quad \langle \frac{\partial \bar{c}_c^*}{\partial x_i} \rangle_k = \frac{\int_{S_k} n_i D_t \frac{\partial \bar{c}_c^*}{\partial x_i} dS_k}{\int_{S_k} D_t dS_k}$$

Note that $\langle \frac{\partial \bar{c}_c^*}{\partial x_i} \rangle_k = \left. \frac{\partial \langle \bar{c}_{c,m}^* \rangle}{\partial x_i} \right|_k$ only when there is no concentration gradient on the surface

of the compartment and $\left. \frac{\partial \langle \bar{c}_{c,m}^* \rangle}{\partial x_i} \right|_k = \left. \frac{\partial \langle c_c^* \rangle}{\partial x_i} \right|_k = \frac{\Delta \langle c_c^* \rangle}{\Delta x_i} \Big|_k$ when there is no concentration

gradient within the compartment volume as well. In this work, the compartments are assumed to be perfectly mixed which can be justified when the size of the compartments is small and the local Da in each compartment is kept smaller than 1 as discussed later in this chapter. With this assumption, equation (3.6) becomes,

$$\frac{dV \langle c_c^* \rangle}{dt^*} + \sum_{k=1}^6 \langle \bar{u}_m \rangle_k \langle c_c^* \rangle_k S_k = \sum_{k=1}^6 \frac{\langle D_t \rangle_k}{LU_0} \frac{\Delta \langle c_c^* \rangle}{\Delta x_i} \Big|_k S_k + \int_V Da \bar{R}_c^* dV + \int_V Da \bar{R}_c^* dV \quad (3.7)$$

Some comments on the role of the dispersion term are warranted here. Note that the inverse of the dispersion Peclet number appearing in equation (3.7) can be written as

$$\frac{\langle D_t \rangle_k}{LU_0} = Sc_T^{-1} Re_t^{-1} = Sc_T^{-1} Re_{local}^{-1} \frac{U_{local}}{U_0}$$

where U_{local} is the characteristic velocity defined for a particular compartment and Re_{local} is the local Reynolds number based on that velocity ($Re_{local} = \frac{LU_{local}}{\nu_t}$). Turbulent Schmidt number, Sc_T , is taken as 0.8 (Section 3.3.2) for all cases, as it is widely accepted in the literature (Yakhot, Orszag and Yakhot, 1987; Brucato et al., 2000). In the regions far from the impeller, Re_{local} and U_{local} are both small and the product $Sc_T^{-1} Re_{local}^{-1} \frac{U_{local}}{U_0}$ can be of $O(1)$. In such a case, dispersion will play a significant role on the predicted results. On the other hand, near the impeller, the local Reynolds number is large ($Re_{local}^{-1} \ll 1$) and the ratio $\frac{U_{local}}{U_0}$ is of $O(1)$. In those regions the relative importance of this term is small and convection dominates the mixing behavior of the system. This has been shown in the results as well (Section 3.4.5), where the inclusion of the dispersion term is important when the reactant feed point is far from the impeller but is not necessary when reactant feeding is close to the impeller.

The second term on the RHS of equation (3.6) is the reaction term due to the mean concentration, where $\bar{R}_c^* = f(\bar{c}_c^*)$. When no concentration gradients exist within a compartment, i.e. micromixing is not limiting, this can be written as $\int_V \bar{R}_c^*(\bar{c}_c^*) dV = \bar{R}_c^*(\langle c_c^* \rangle) V$. The third term on the RHS (contribution from the mean of the cross terms) is neglected in this work based on the fact that the local Da in each compartment is also kept smaller than 1 when the reactor is discretized into compartments (Section 3.3.1). Equation (3.7) then gets modified to

$$\frac{dV \langle c_c^* \rangle}{dt^*} + \sum_{k=1}^6 \langle \bar{u}_m \rangle_k \langle c_c^* \rangle_k S_k = \sum_{k=1}^6 \frac{\langle D_t \rangle}{LU_0} \frac{\Delta \langle c_c^* \rangle}{\Delta x_i} \Big|_k S_k + \bar{R}_c^*(\langle c_c^* \rangle) V \quad (3.8)$$

Equation (3.8) represents the mass balance for any component c in a compartment in dimensionless form. In terms of dimensional variables equation (3.8) can be represented as

$$\begin{aligned}
V_{i,j,k} \frac{dc_c^{i,j,k}}{dt} = & c_c^{i-1,j,k} S_{rad}^{i-1} u_{rad}^{i-1,j,k} + c_c^{i,j-1,k} S_{\theta} u_{\theta}^{i,j-1,k} + c_c^{i,j,k-1} S_{ax} u_{ax}^{i,j,k-1} - c_c^{i,j,k} S_{rad}^i u_{rad}^{i,j,k} \\
& - c_c^{i,j,k} S_{\theta} u_{\theta}^{i,j,k} - c_c^{i,j,k} S_{ax} u_{ax}^{i,j,k} - k_{ex}^{(i-1)} S_{rad}^{i-1} (c_c^{i,j,k} - c_c^{i-1,j,k}) - k_{ex}^{(i+1)} S_{rad}^i (c_c^{i,j,k} - c_c^{i+1,j,k}) \\
& - k_{ex}^{(j-1)} S_{\theta} (c_c^{i,j,k} - c_c^{i,j-1,k}) - k_{ex}^{(j+1)} S_{\theta} (c_c^{i,j,k} - c_c^{i,j+1,k}) - k_{ex}^{(k-1)} S_{ax} (c_c^{i,j,k} - c_c^{i,j,k-1}) \\
& - k_{ex}^{(k+1)} S_{ax} (c_c^{i,j,k} - c_c^{i,j,k+1}) + R_c V_{i,j,k}
\end{aligned} \tag{3.9}$$

where, $R_c = \sum_{m=1}^{N_R} \nu_{mc} r_m$; N_R = number of reactions; r_m = intrinsic rate of the m -th reaction;

ν_{mc} = stoichiometric coefficient and $k_{ex}^{(i-1)}$ = exchange coefficient at the $(i-1)$ face of the compartment (i,j,k) which is related to D_i as shown later. Equation (3.9) is the final compartment level model equation used in this work. It is important to recognize at this point that this model can only account for macromixing and mixing due to turbulent dispersion but ignores micromixing effects on reactor performance. The condition for which micromixing effects can be ignored depends on micromixing time scale compared to reaction time scale as discussed later in the text.

3.3. Compartmental Model Inputs from CFD

The CFD-based compartmental model consists of the following steps. The complete CFD solution of the flow field is first obtained in the entire tank. The next step is to determine the required number of compartments depending on the time scales of the reactions studied. This is discussed in Section 3.3.1. The first six terms on the RHS of equation (3.9) account for the transfer of component c by the bulk mean flows which are obtained by averaging the complete CFD solution over the faces of the defined compartments. The next six terms in the equation account for the transfer of mass due to turbulent dispersion. The exchange coefficient is estimated from the turbulent diffusivity averaged over the faces of the compartment as indicated in Section 3.3.2.

3.3.1. Compartment Discretization Scheme

The discretization scheme followed in this work has the following objective. Given the kinetics of a reactive system, the compartments are created in such a way that the overall local residence time of the liquid in a compartment is less than the characteristic reaction time scale, i.e.

$$\frac{V_i}{Q_{in,i}} < t_{rxn} \quad (3.10)$$

where V_i is the volume of the i -th compartment, $Q_{in,i}$ is the sum of all the inlet flows to the i -th compartment and t_{rxn} is the characteristic reaction time scale. This ensures that significant concentration gradients do not develop within a compartment due to reaction (ensures that in each compartment $Da < 1$) and hence compartments can be assumed to be macroscopically well-mixed in cases when micromixing is fast enough compared to reaction.

To achieve the overall objective, discretization is done independently in each coordinate direction by choosing a velocity profile along that direction. The scheme involves the following steps:

- Selecting an appropriate velocity profile for discretization in each of the coordinate direction, i.e. axial, radial and angular.
- Discretization along each coordinate direction is performed so that in each direction the individual criterion is met, i.e.

$$\frac{\Delta x_i}{v_{avg}} < t_{rxn} \quad (3.11)$$

where v_{avg} is the average velocity between locations i and $i+1$.

Note that independent discretization in each coordinate direction essentially ensures that equation (3.10) is satisfied for about one-third of the actual reaction time scale. This follows from the scaling argument presented below. Figure 3.2 shows a compartment of dimensions x_r , x_z and x_θ , and three characteristic velocity components v_r , v_z and v_θ through

the compartment in the three co-ordinate directions, respectively. For the given compartment

$$V \sim x_r x_z x_\theta \quad (3.12)$$

$$Q \sim |v_r| x_z x_\theta + |v_z| x_r x_\theta + |v_\theta| x_r x_z \quad (3.13)$$

$$\frac{Q}{V} \sim \frac{|v_r| x_z x_\theta + |v_z| x_r x_\theta + |v_\theta| x_r x_z}{x_r x_z x_\theta} = \frac{|v_r|}{x_r} + \frac{|v_z|}{x_z} + \frac{|v_\theta|}{x_\theta} \quad (3.14)$$

Now, if the discretization is carried out in each direction independently (without accounting for the contribution of the flow from the other two directions) we have

$$\frac{x_r}{|v_r|} < t_{rxn}, \quad \frac{x_z}{|v_z|} < t_{rxn} \quad \text{and} \quad \frac{x_\theta}{|v_\theta|} < t_{rxn}$$

which then implies that

$$\frac{Q}{V} > \frac{3}{t_{rxn}}$$

or, $\frac{V}{Q} < \frac{t_{rxn}}{3}$ (3.15)

Therefore, a reaction time scale $t'_{rxn} \sim 3t_{rxn}$ can be used for discretization, still satisfying the overall criterion given by equation (3.10).

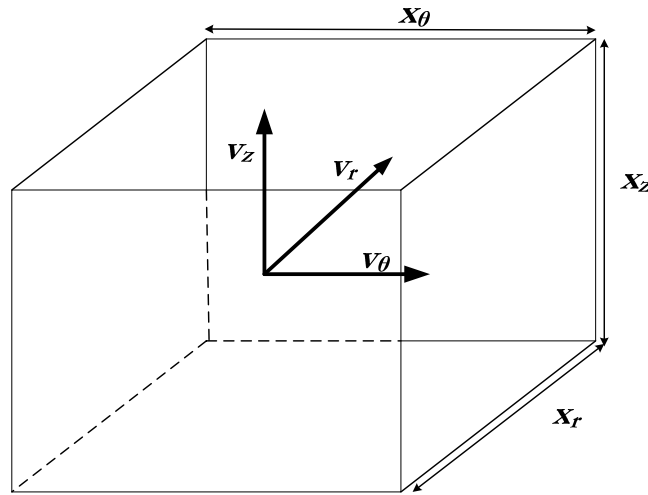


Figure 3.2 A discretized compartment in the compartmental framework

Selecting the velocity profile

To select the axial velocity profile for discretization, circumferentially-averaged axial velocity plots (v_z vs. z) are obtained at different radial positions in the reactor. An average axial velocity is calculated for each of the profiles as

$$\overline{v_z}|_{r_i} = \frac{\sum |v_{z_i}|}{N_p} \quad (3.16)$$

where v_{z_i} is the velocity at any given point in the profile and N_p is the total number of points. The average velocity obtained using equation (3.16) at each of the radial locations is compared and the profile that has the smallest value of the mean velocity is chosen for discretization. If equation (3.11) can be satisfied for a plane which has the smallest average flow, it would satisfy the criterion at other planes also where the average flows are larger (the compartment length Δx_i remaining same).

The same procedure is followed to select the radial and tangential velocity profiles by obtaining circumferentially-averaged radial and tangential velocity plots (v_r vs. r & v_θ vs. r) at different axial locations. The profiles with the smallest averages are chosen for discretization.

Discretization

The number and location of the axial compartments is obtained using the selected axial velocity profile. Given an axial location z_i (Figure 3.3) and the corresponding velocity $v_{z,i}$, we need to find a location z_{i+1} such that

$$\frac{z_{i+1} - z_i}{\frac{1}{2} |v_{z,i+1} + v_{z,i}|} < t_{rxn} \quad (3.17)$$

Since the velocity profile is known, z_{i+1} can be obtained by iteration so that the above criterion is satisfied.

The same procedure is followed to determine the number and location of the radial compartments using the radial velocity profile. The angular direction is divided evenly and the number of compartments can be obtained as

$$N_{\theta} = \max \left[\frac{2\pi r_i}{|v_{\theta,i}| t_{rxn}} \right] \quad (3.18)$$

where $v_{\theta,i}$ is the tangential velocity at r_i in the selected velocity profile.

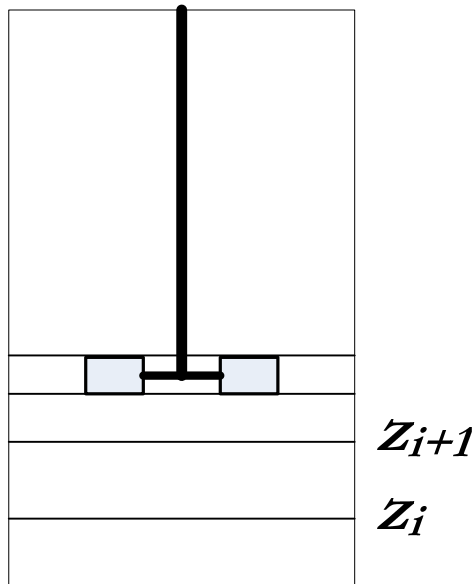


Figure 3.3 Discretization in the axial direction

This methodology is, however, conservative and creates too many compartments in the regions where velocities are very small (near the walls and near the bottom) and in the angular direction. This is avoided by neglecting regions of smaller velocities and dumping them into a neighboring larger compartment. The minimum velocity used in the discretization is determined from the corresponding velocity distribution (axial or radial or tangential) over the entire reactor. About 5-10% of the distribution around zero is

neglected and velocities larger than that are used for discretization. Also to obtain a more realistic number of compartments, the discretization in the axial and radial direction is carried out using a larger time scale (compared to the actual reaction time scale as described earlier). The number of compartments in the angular direction is taken as a multiple of the number of impeller blades (either 6 or 12 for the cases shown). After the compartments are created it is checked if the overall objective (equation 3.10) is met.

3.3.2. Exchange Coefficients

In earlier studies (Mann and Hackett, 1988; Holden and Mann, 1996) the dispersion due to turbulence had been described by exchange flows between compartments which were taken as a fraction of the mean flow through the compartment. In a recent work (Boltersdorf, Deerberg and Schluter, 2000) this fraction has been estimated from the normalized energy dissipation rate. The dispersion term, however, accounts for a larger length scale than the length scale at which energy dissipation occurs. Using this approach to calculate the exchange parameter the exchange term near the impeller is overestimated where most of the energy dissipation occurs (Boltersdorf, Deerberg and Schluter, 2000). In this work, the exchange coefficient at each face of each compartment is represented through the turbulent diffusivity, which in turn was estimated from the kinetic energy and dissipation rates obtained from the detailed CFD simulation.

The standard k - ε model assumes isotropic turbulence and the kinetic energy of fluctuations is described as

$$k = \frac{3}{2} u'^2 \quad (3.19)$$

Also, the fluctuating velocity based on the same assumption of homogeneous, isotropic turbulence (Kolmogorov's Universal Equilibrium theory) can be written as

$$u' \sim (\varepsilon l_e)^{1/3} \quad (3.20)$$

where, ε is the dissipation rate and l_e is the characteristic length scale.

The above two relationships (equations 3.19 and 3.20) give an estimate of the length scale of the large eddies that account for dispersion due to turbulence. The turbulent diffusivity, which can be described as the product of the characteristic velocity and the characteristic length scale, therefore, becomes

$$D_t \sim u'l_e = A\left(\frac{k^2}{\varepsilon}\right) \quad (3.21)$$

The constant A can be calculated using the standard k - ε model constant ($C_\mu = 0.09$) and assuming turbulent $S_{c_T} = 0.8$, which gives $A=0.1125$. The surface-averaged values of the turbulent diffusivity, $\langle D_t \rangle$, are obtained for each face of the compartments and the exchange coefficient is estimated as

$$k_{ex} = \frac{\langle D_t \rangle}{\Delta x_i} \quad (3.22)$$

where Δx_i is the distance between the centers of two neighboring compartments in the i -direction.

3.4. Results and Discussion

The above described model has been used first to predict the mixing of an inert tracer in a stirred tank. The model is then applied to single reaction schemes with linear and non-linear kinetics to test whether it shows the effect of mixing on the performance of the reactor. The flow fields are simulated at three different impeller speeds (150, 250 and 350 RPM) with $Re_{imp} \sim 11,000 - 26,000$. Finally a second order competitive-consecutive kinetic scheme is studied.

3.4.1. The System

The system used to simulate the flow is a cylindrical, flat-bottomed tank with diameter $T=0.2$ m. The height of the liquid (H) is equal to the tank diameter. The tank has four

baffles of width $T/10$ and is agitated by a six-bladed Rushton turbine of diameter $D=T/3$. The length of each blade is $T/12$ and the height is $T/15$. The impeller clearance (distance from the bottom of the tank) is equal to the impeller diameter. The schematic of the geometry is shown in Figure 3.4.

3.4.2. Flow Field

The single phase flow field is simulated using FLUENT 6.0 for the geometry defined in Section 3.4.1 and Figure 3.4. The Multiple Reference Frame (MRF) approach (Ranade, 2002) is used with the standard $k-\varepsilon$ model for turbulence. The top surface of the liquid is modeled as a free surface. The physical properties of the liquid are taken as that of water.

3.4.3. Inert Tracer Mixing

The inert tracer is injected at the top free surface of the liquid near the wall as a pulse injection. The mixing time to achieve 99% homogeneity in the tank (when the

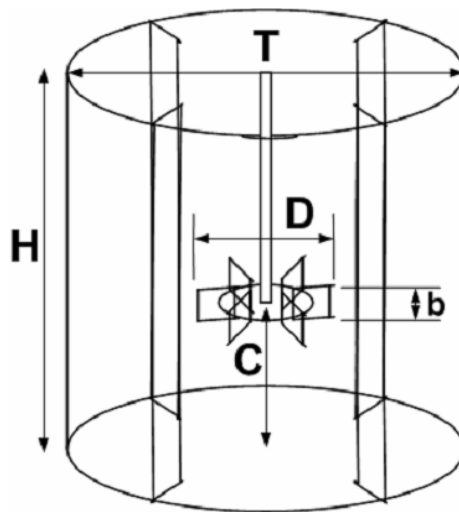


Figure 3.4 Schematic diagram of the geometry used

concentration in each compartment is not varying more than 1% of the mean concentration) is predicted. The level of mixing achieved is monitored through the standard deviation of the tracer concentration in the tank. Based on this, the criterion used to assure the desired level of homogeneity in the entire tank is given by

$$\sigma \leq (1-p)\bar{c}\left(\frac{N}{N-1}\right)^{1/2} \quad (3.23)$$

where σ is the standard deviation defined as $\sigma = \left[\frac{\sum_{i=1}^N (c_i - \bar{c})^2}{N-1} \right]^{1/2}$, p is the desired degree

of homogeneity, \bar{c} is the mean tracer concentration when complete mixing is achieved and N is the total number of compartments. The total number of compartments used for the simulations were varied from 120 ($5 \times 4 \times 6$:axial \times radial \times angular) to 720 ($12 \times 10 \times 6$:axial \times radial \times angular) where each of the coordinate directions is divided equally in length into the number of compartments in that direction, i.e. the center to center distance between any two neighboring compartments in a given direction is same throughout the domain. The predicted mixing time decreases as the number of compartments is increased and approaches at each RPM an asymptotic value as shown in Figure 3.5. The convergence, when the predicted mixing time is within $\pm 5\%$ of the asymptotic value, is achieved with 480 ($10 \times 8 \times 6$) compartments for 150 RPM and with 432 ($9 \times 8 \times 6$) compartments for 250 and 350 RPM. Further results presented in this section have been simulated using these numbers of compartments for which mixing time convergence was achieved.

The mixing times predicted by the model at different impeller speeds for 99% homogeneity ($p=0.99$) are compared with two correlations from the literature (Sano and Usui, 1985; Fasano, Bakker and Penney, 1994). These correlations from Fasano, Bakker and Penney (1994) and Sano and Usui (1985) are respectively given by

$$t_m = \frac{-\ln(1-p)}{1.06N_{imp} \left(\frac{D}{T}\right)^{2.17} \left(\frac{T}{H}\right)^{0.5}} \quad (3.24)$$

$$t_m = \frac{3.8 \left(\frac{D}{T}\right)^{-1.80} \left(\frac{b}{T}\right)^{-0.51} n_b^{-0.47}}{N_{imp}} \quad (3.25)$$

The constants for equation (3.24) are valid for fully turbulent regime ($Re_{imp} > 10,000$). At lower Reynolds Number the mixing time would be greater than that predicted by this equation. For equation (3.25), all the measurements were done for $Re_{imp} > 5000$ and the constants are valid only for 99% homogeneity in the tank.

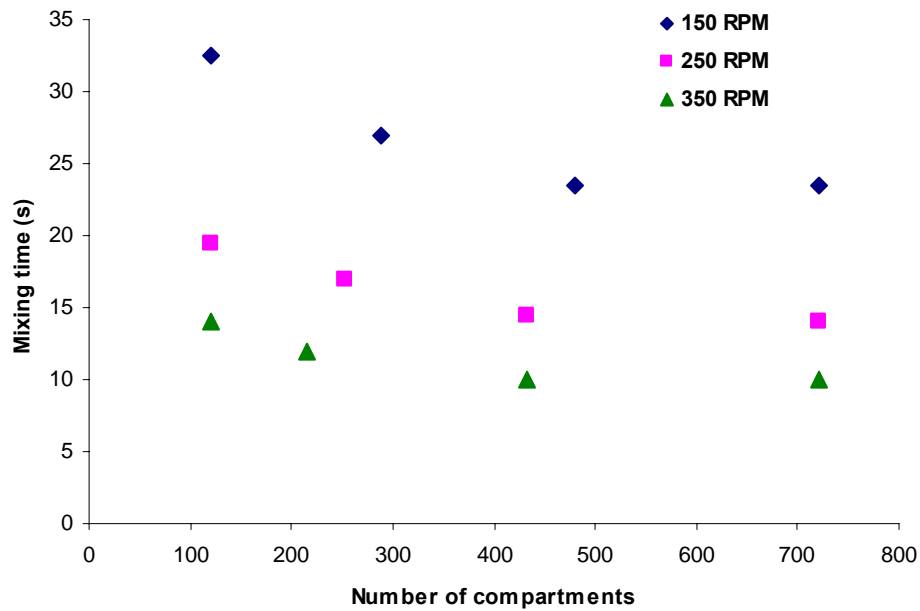


Figure 3.5 Convergence of predicted mixing time with number of compartments

Comparison of the predicted mixing times at different impeller speeds with the two correlations is shown in Figure 3.6. The model predictions compared reasonably well with

the correlation values to achieve 99% homogeneity in mixing. Studies on mixing in stirred tank reactors also show that in the completely turbulent regime, the dimensionless mixing time defined as $N_{imp}t_m$ becomes constant when plotted against the impeller Reynolds number. Such a plot based on the predicted mixing time in Figure 3.7 also exhibits essentially a constant value. The average value of the dimensionless mixing time as predicted by the compartmental model is about 59.

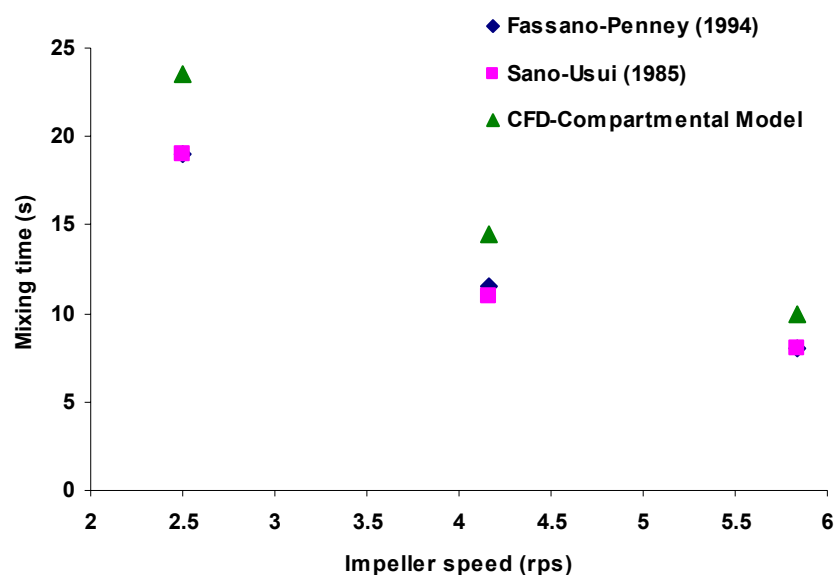


Figure 3.6 Comparison of predicted mixing time with literature correlations

3.4.4. First and Second Order Kinetics

In order to test the model developed, single reactions of first and second order kinetics are studied at two different impeller speeds (150 and 350 RPM) for a batch system. The reaction time scale is taken as 1 second. It has to be noted that the inert mixing times at 150 and 350 RPM are around 19 seconds and 9 seconds, respectively, i.e. the reaction time

scale is kept small compared to the time scale of mixing. It is therefore expected that mixing should have an influence on reactor performance under these conditions.

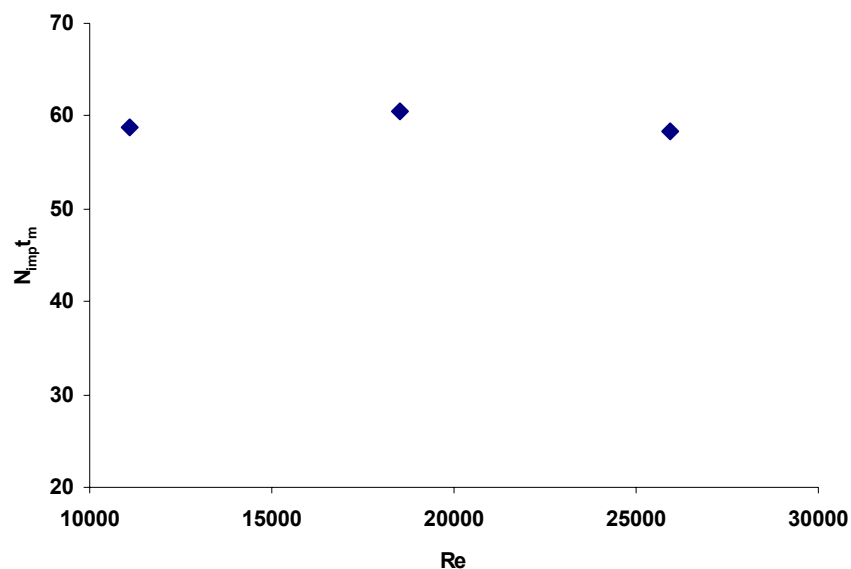


Figure 3.7 Dimensionless mixing time (predicted) vs. Reynolds Number

First Order Kinetics

The reaction stoichiometry for this case is given by $B \rightarrow Products$. The reactant B is added as a pulse to solvent A present in the reactor. The concentration of the reactant B in the pulse is 100 mol/m^3 , which would result in a mean B concentration of 10 mol/m^3 . The ratio of the added volume of reactant B to the total liquid volume in the reactor is ~ 0.1 . It is assumed that the reactor volume and the flow field do not change significantly due to the addition of reactant B . The number of compartments used for simulation is 594 ($11 \times 9 \times 6$: axial \times radial \times angular) at 150 RPM and 216 ($6 \times 6 \times 6$: axial \times radial \times angular) at 350 RPM.

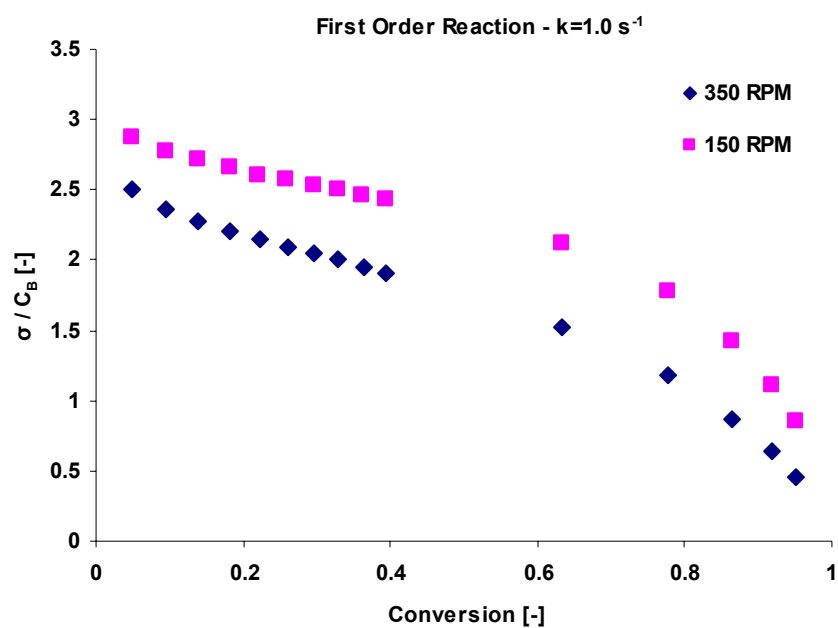


Figure 3.8 Dimensionless standard deviation vs. conversion for a first order reaction

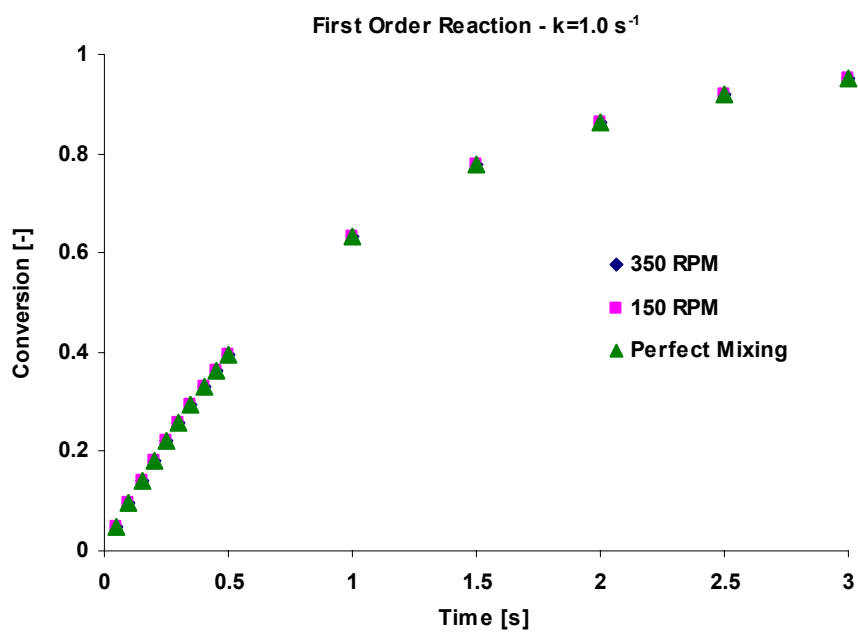


Figure 3.9 Conversion vs. time for a first order reaction

The difference in the mixing behavior of the system at different impeller speeds is visible in Figure 3.8 which shows a plot of the dimensionless standard deviation of the concentration of B in the reactor vs. conversion. The conversion is calculated based on the volume averaged mean concentration of the reactant in the reactor, while the standard deviation is non-dimensionalized with the mean concentration of reactant B at a given time. The standard deviation is larger at lower impeller speed, i.e. as expected mixing is poorer under this condition. On the other hand, Figure 3.9 shows a comparison of the reactor performance at the two speeds and that predicted by the classical perfectly mixed stirred tank model (instantaneous mixing at all length scales). The plots can be seen to overlap each other. This confirms the fact that conversion for a first order reaction is independent of the mixing behavior in the batch system and depends only on the reaction time.

Second Order Kinetics

The reaction stoichiometry for this case is $A+B \rightarrow Products$, and the reaction is first order in each reactant and is second order overall. The conditions are the same as stated for the first order reaction. The mean concentration of reactant A already present in the reactor is 10 mol/ m^3 so that the molar ratio of the two reactants fed to the system is equal to 1.

As before, the difference in the mixing behavior at the two conditions can be observed in Figure 3.10. However, now the reaction kinetics being non-linear, mixing has an effect on reactor performance. This is shown in Figure 3.11. Since this is a batch process, the slower the mixing the larger is the time needed to achieve a desired level of conversion (up to 90% conversion is shown in the plot).

3.4.5. Effect of Mixing on Multiple Reactions

Mixing effects on the performance of chemical reactors become much more significant when there are multiple reactions taking place in the system with widely varying time scales.

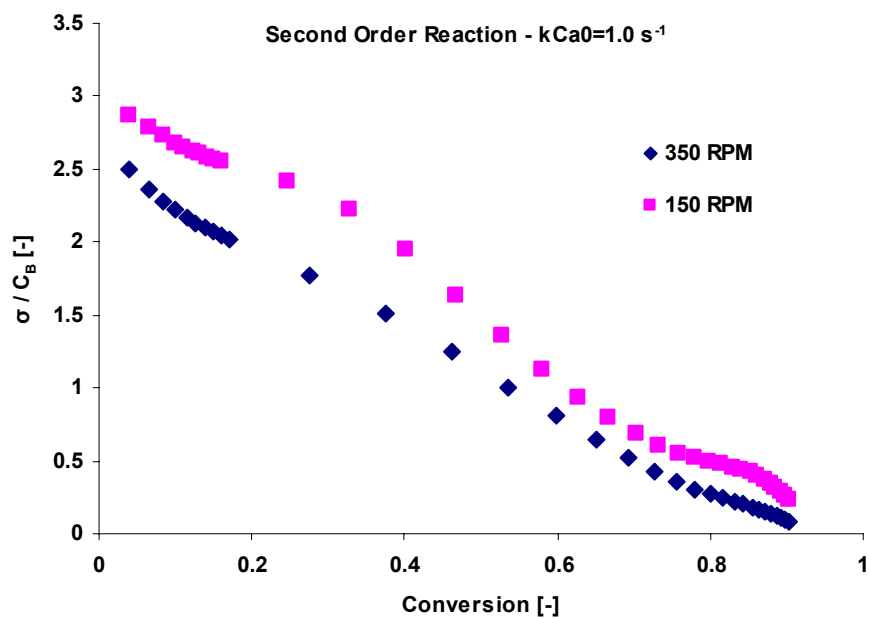


Figure 3.10 Dimensionless standard deviation vs. conversion for a second order reaction

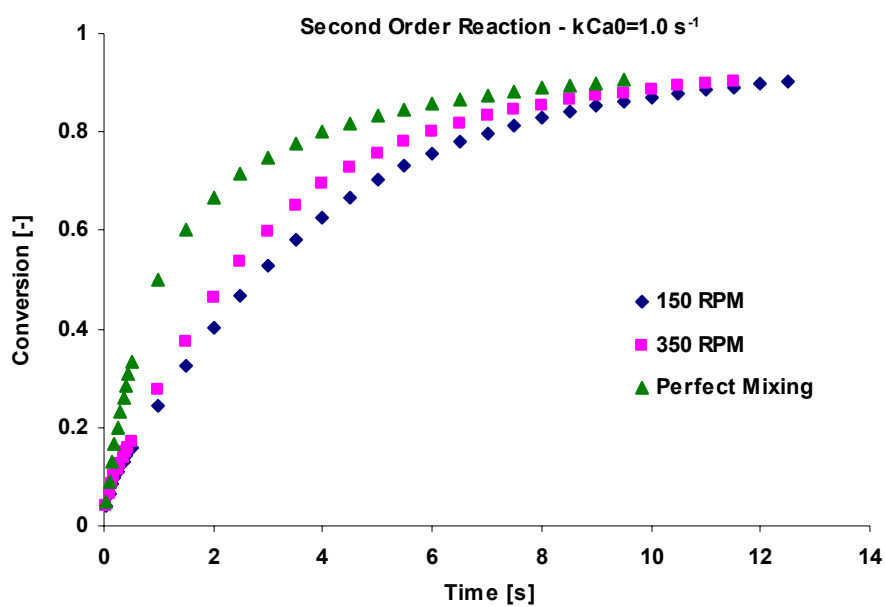
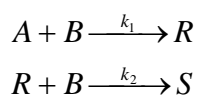


Figure 3.11 Conversion vs. time for a second order reaction

The formation of the desired products can be increased if mixing effects in such reactions can be predicted. From an environmental point of view, this can lead to the minimization of waste generation as well.

Paul and Treybal (1971) performed experiments with a second order, competitive-consecutive reaction scheme and showed the effect of feed location and mixing for a homogeneous, multiple-reaction system. The reaction used in that study was the iodination (B) of L-tyrosine (A) to produce 3-iodo-L-tyrosine (R) and 3,5-diiodo-L-tyrosine (S). The reaction scheme can be written as



The component R is the desired product of the reaction. The kinetic constants for the two reactions, as obtained from their study at 298K, are $k_1 = 0.035 m^3 mol^{-1} s^{-1}$ and $k_2 = 0.0038 m^3 mol^{-1} s^{-1}$. The first reaction is an order of magnitude faster than the second reaction.

The system comprises of semi-batch addition of reactant B (iodine) into pre-charged A (L-tyrosine) which has an initial concentration of $200 mol m^{-3}$. The concentration of reactant B in the feed is $2000 mol m^{-3}$. The volumetric feed rate of reactant B is such that the feeding time for B is 15 seconds and the molar ratio of reactant A to the total amount of B fed to the system is 1. The impeller speed is 1600 RPM. The number of compartments used for simulation is 1560 (13×10×12: axial×radial×angular). A schematic of the geometry used for the experimental study is shown in Figure 3.12. Two feed lines were used for the addition of reactant B , one at the top and the other below the impeller. The semi-batch injection of B is modeled as a series of discretized feeds at small intervals of time. The time interval between two feeds is taken as 0.5 seconds. No significant difference is observed by decreasing the time interval further.

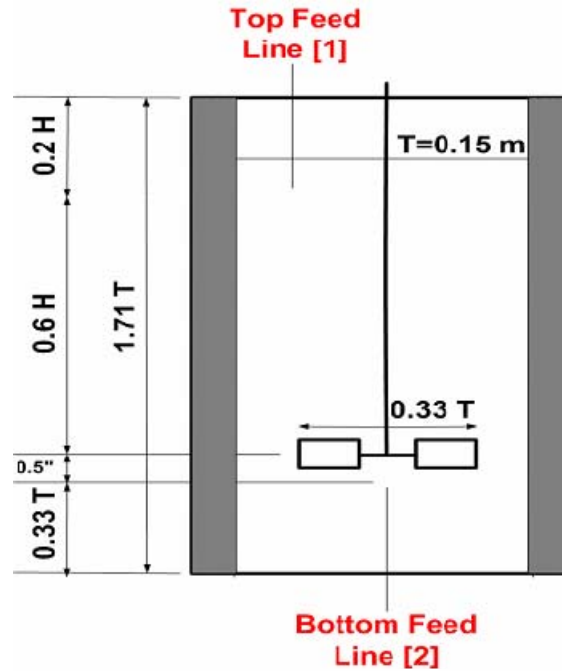


Figure 3.12 Details of the geometry used for the simulation of multiple reactions (Paul and Treybal, 1971)

An estimate of the micromixing time scale can be obtained as (Assirelli et al., 2002)

$$t_{micro} = 17.24 \sqrt{\frac{\nu}{\bar{\varepsilon}}} \quad (3.26)$$

where ν is the kinematic viscosity and $\bar{\varepsilon}$ is the average kinetic energy dissipation rate given by

$$\bar{\varepsilon} = P_o N_{imp}^3 D^5 V_T^{-1} \quad (3.27)$$

Assuming P_o as 5 for a Rushton turbine operating in the completely turbulent regime, the estimated micromixing time scale for the condition simulated turns out to be ~ 0.007 s. The reaction time scale based on the fastest reaction can be estimated as

$$t_{rxn} = \frac{1}{k_1 C_{A0}} \quad (3.28)$$

which is ~ 0.143 s. Since the micromixing time scale is much smaller than the time scale of the fastest reaction, performance will be limited by macromixing, and micromixing effects can be neglected.

The effect of the feed location on the mixing behavior of the system is shown in Figure 3.13. Mixing is poorer when the feeding of B is done from the top as evidenced by a much higher standard deviation of concentration of B compared to the bottom feed. The standard deviation starts to drop sharply after $t=15$ secs when the feeding of reactant B is stopped. Figure 3.14 shows the yield of R (defined as C_R/C_{A0}) as a function of time. The yield is lower when the top feed-line is used, thereby producing more of the undesired product S due to local over-reaction.

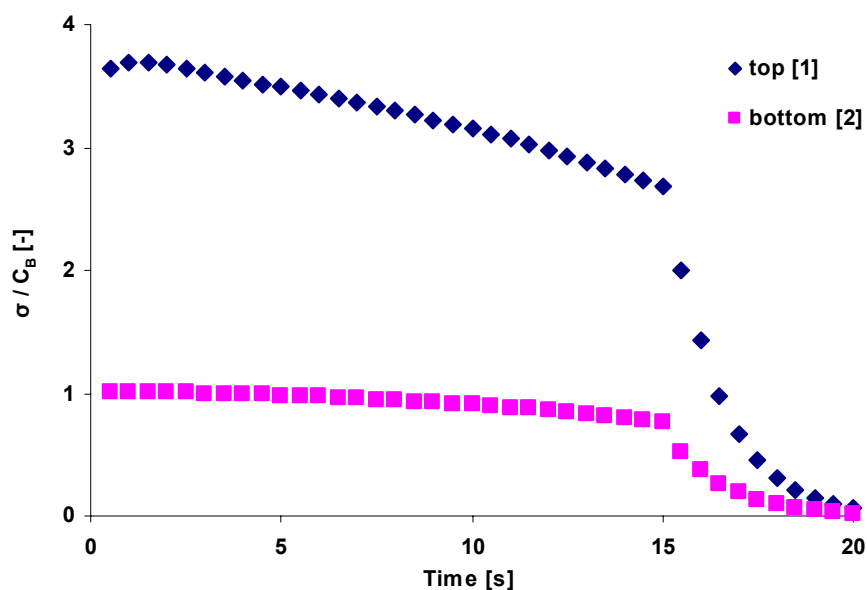


Figure 3.13 Dimensionless standard deviation vs. time for a semi-batch second order, competitive-consecutive reaction scheme

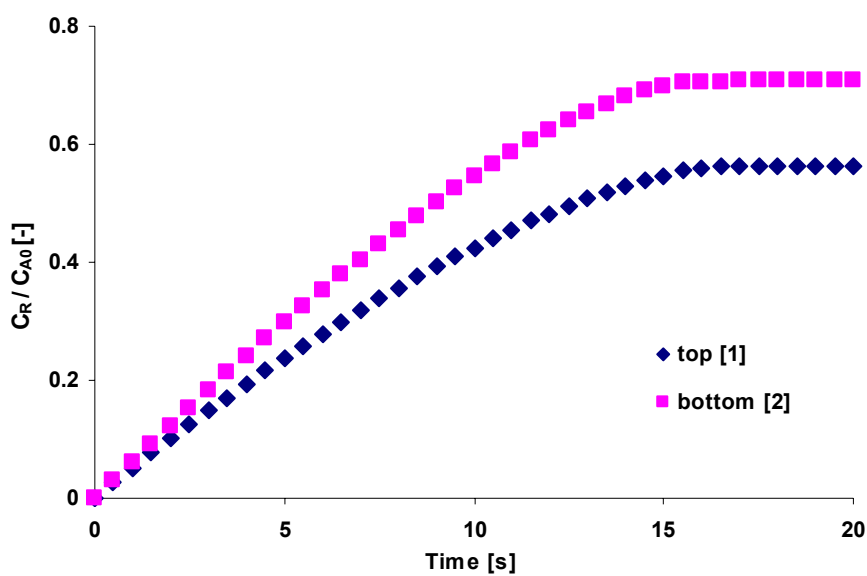


Figure 3.14 Yield of R as a function of time for the multiple reaction scheme

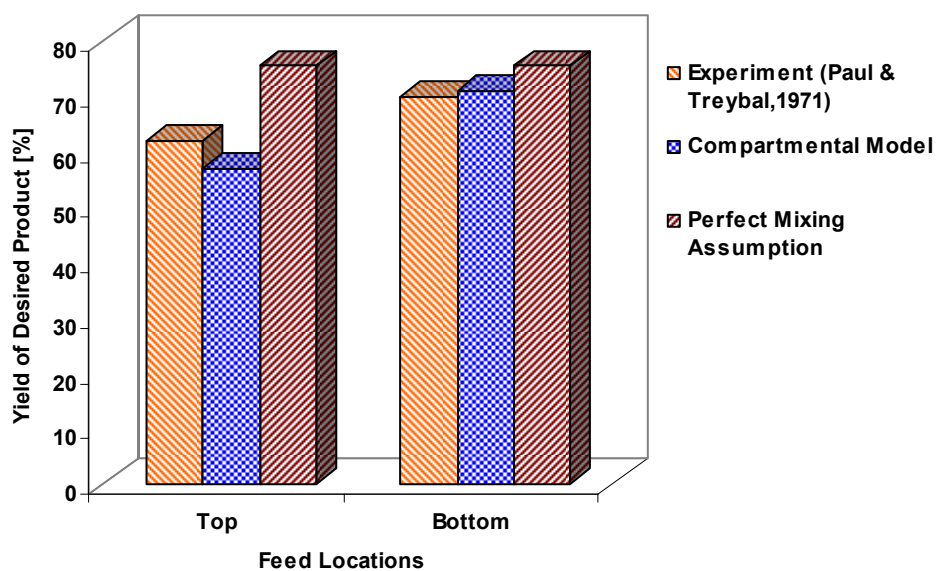


Figure 3.15 Comparison between measured and predicted yield of R at the end of the reaction for the two feed locations

In their experimental study, Paul and Treybal measured the yield of the product R when the reaction reached completion. Figure 3.15 shows a quantitative comparison of the measured yield of R and the yield predicted by the compartmental model and the perfectly mixed model at the end of the reaction for the two feed points. The conventional perfectly mixed model would predict a yield of 75.5% when there is no mixing limitation (Paul and Treybal, 1971). The compartmental model does a better job in predicting the product yield for different feed locations. The agreement between the experimental result and model prediction is reasonable (within 7-8%), though the performance is slightly under-predicted for the top feed-line. Under-predicting the yield of R implies that mixing is under-predicted for that case (since poorer mixing produces less R). One of the reasons for this could be the under-estimation of the exchange coefficient term in the model equation. To check the sensitivity of the predictions to this term, simulations were done by dropping the exchange terms completely (retaining only the mean flow) and also by increasing the exchange coefficients by a factor of 2. The results are shown in Figure 3.16. The top-feeding turns out to be quite sensitive to the exchange term, while the bottom one is almost independent of the exchange term. This is in line with the discussion presented earlier (Section 3.2).

Full CFD Simulation

It is of interest to compare the predictions of the compartmental model with those obtained using a full blown CFD simulation for the experimental study reported by Paul and Treybal (1971). For the full CFD simulation, the flow field in the reactor is solved using a Multiple Reference Frame approach (Ranade, 2002) for the geometry shown in Figure 3.12 at the operating condition described earlier. Water is used as the liquid phase for the simulation carried out. The species conservation equations are then solved with a frozen flow field in the reactor. All the components in the reactor are assumed to have the physical properties same as that of water so that the mass balance is conserved. The volumes of the injection zones at the top and bottom feed locations are made equal to the corresponding compartment volumes used in the compartmental model. The semi-batch

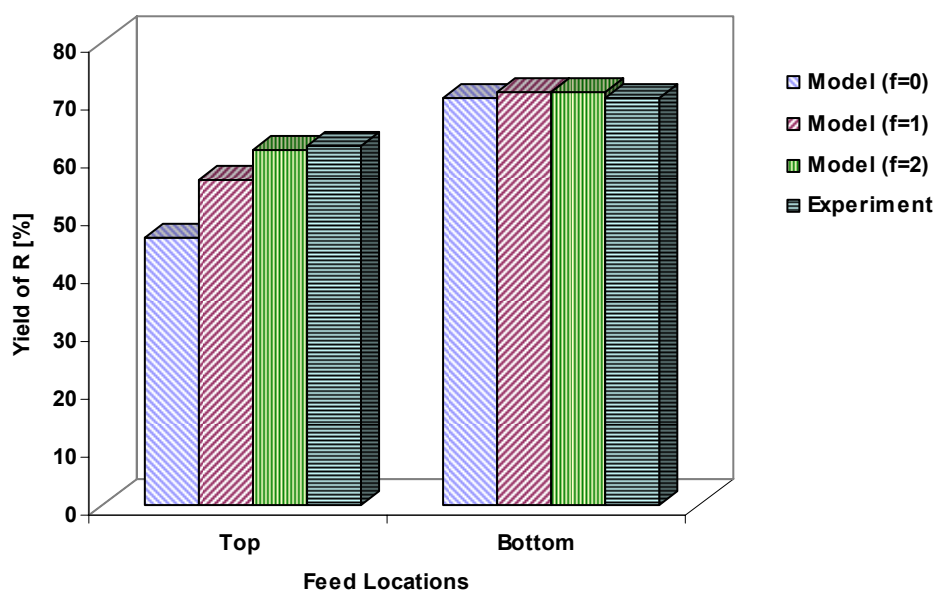


Figure 3.16 Sensitivity of the exchange term on the prediction of yield (f denotes the multiplication factor to the normal exchange coefficients obtained earlier, i.e. $f=0$ signifies no exchange term is used)

addition of reactant B is modeled as a constant source term in the injection zone such that the moles of B fed in 15 seconds is equal to the moles of reactant A initially present in the reactor. The time step used for the simulation is 0.01 second, which is an order of magnitude smaller than the characteristic reaction time scale (0.143 second). The source term is switched off at 15 seconds and the simulation is carried out till 20 seconds as was done for the compartmental model.

The significant segregation of reactant B in the system can be observed from the contours of B concentration shown in Figures 3.17 and 3.18 for the bottom and top feed locations respectively. Contour plots are presented in the $r-\theta$ plane at z value corresponding to the feed injection location. As time progresses and more and more B comes into the reactor, segregation of reactant qualitatively increases in both the cases. However, higher localized

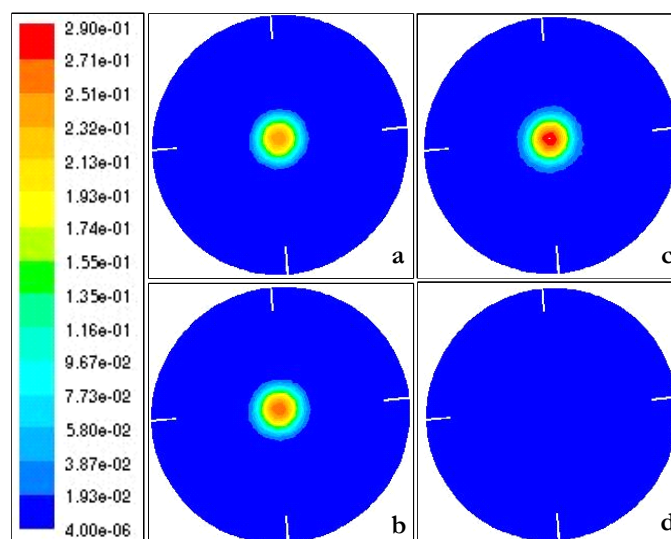


Figure 3.17 Contours of reactant B concentration ($kmol/m^3$) for the bottom feed inlet at (a) 5 seconds, (b) 10 seconds, (c) 15 seconds and (d) 20 seconds

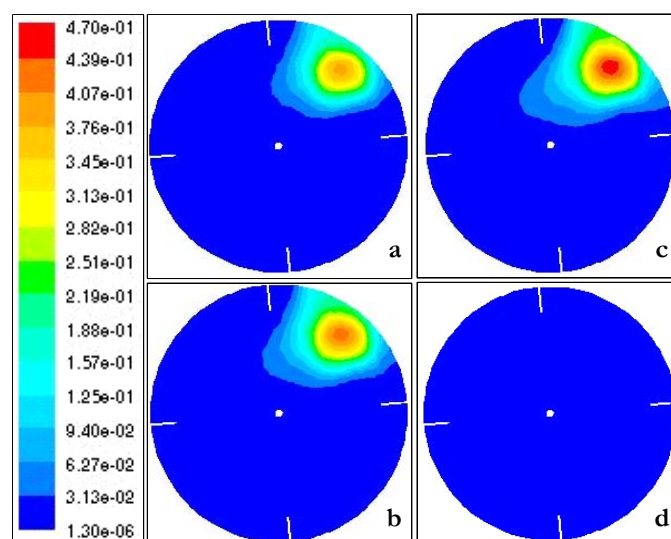


Figure 3.18 Contours of reactant B concentration ($kmol/m^3$) for the top feed inlet at (a) 5 seconds, (b) 10 seconds, (c) 15 seconds and (d) 20 seconds

concentration is observed when feeding is at the top resulting in a maximum observed value of about $4.7 \times 10^{-1} \text{ kmol/m}^3$ as opposed to $2.9 \times 10^{-1} \text{ kmol/m}^3$ when feeding is close to the impeller. After the feeding is stopped at 15 seconds, segregation starts to decrease in the reactor because of mixing, resulting in the observation of a completely mixed state at 20 seconds when the simulation is stopped.

The predictions obtained for the final yield of product R using the full CFD simulation are compared in Figure 3.19 with those obtained from the compartmental model and those observed in the original experiments (Paul and Treybal, 1971). It can be seen that the full blown CFD simulation for the turbulent reactive flow problem did not provide any major improvement in the predicted yields of R compared to the compartmental model, in spite of the fact that the computational time required for the CFD simulation was significantly larger.

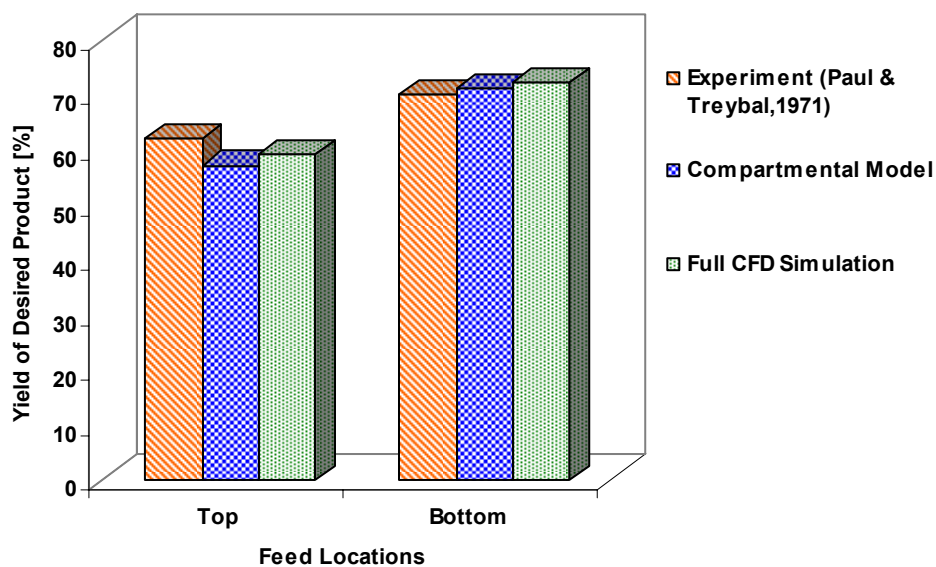


Figure 3.19 Comparison between predicted yields of R at the end of the reaction obtained using compartmental model and full CFD simulation for the two feed locations

3.5. Summary

The CFD-based compartmental model for single phase system is developed and employed to predict the effect of mixing on the performance of stirred tank reactors. In this approach, the flow field is solved using CFD and the averaged flow and turbulence (in terms of eddy diffusivity) information is transferred to the compartmental framework in order to solve the reactive flow problem. In the current stage of development the model can only account for macromixing and mixing due to turbulent dispersion (mesomixing), and ignores the micromixing effects on reactor performance. The condition for which micromixing effects can be ignored depends on the micromixing time scale compared to the reaction time scale. The number and locations of the compartments necessary to represent a given system depend on the flow and kinetics of the system, and a methodology for the a priori determination of the same is developed in this work based on a time-scale analysis of the two processes. The model has been tested both for inert mixing (blending) and for mixing with multiple chemical reactions using information available in the open literature. The results are in reasonable agreement and the effects of varying feed locations are nicely captured (Guha et al., 2006). Comparison with a full blown CFD simulation is also carried out and it is demonstrated that such a simulation did not provide any significant improvement in the predicted yields. Thus, the compartmental model is a promising alternative for the modeling of large-scale industrial reactors, considering the large computation requirement of a full CFD simulation. However, it should be noted that the discrepancy in the compartmental model prediction from data is larger when the reactant feeding is far from the impeller where the dispersion term (mesomixing) in the model equation becomes important. This term is closed through the turbulent eddy diffusivity using the k and ε values obtained from the CFD simulation of the flow with the standard k - ε model. The discrepancy observed might be related to the predictions of the turbulence quantities by the standard k - ε model, and therefore, it is worthwhile to see if the k and ε values obtained from the more fundamental large eddy simulation (LES) results in improved predictions of the reactor performance. Some of these issues are addressed in the next chapter.

Chapter 4

Large Eddy Simulation of Single Phase Flow

The CFD-based compartmental model developed in Chapter 3 for single phase flows in stirred tanks is promising considering the reasonable agreement obtained with the experimental data at a reduced computation cost. The only concern that remains is the importance of the dispersion term in regions far away from the impeller where the convective flows are weak. Since this term is closed using the turbulent kinetic energy (k) and energy dissipation rate (ε) predicted locally in the CFD simulation of the flow, it is important to obtain reasonably accurate predictions of these quantities in order to increase the generality and applicability of the model. The standard k - ε model is the most popular turbulence model, but has been shown to provide incorrect predictions of the turbulent quantities by several authors (Ng et al., 1998; Hartmann et al., 2004; Yeoh et al., 2004). This might have caused the observed difference of about 7-8% in the compartmental model predictions when feeding is at the top of the reactor where mixing due to turbulent dispersion (mesomixing) is important. The imperfect prediction of turbulence by the k - ε model is, however, not surprising knowing the limitations of the model as discussed in detail in Chapter 2.

The increase in computational resources led to the emergence of the Large Eddy Simulation (LES) as an alternative tool to gain more fundamental insights into flow and turbulence in stirred tanks (Revstedt, Fuchs and Tragardh, 1998; Derksen and Van den Akker, 1999; Yoon et al., 2003; Hartmann et al., 2004; Bakker and Oshinowo, 2004; Yeoh et al., 2004; Alcamo et al., 2005; Zhang, Yang and Mao, 2006; Tyagi et al., 2007). In large

eddy simulation the large scale eddies in the flow are directly resolved while the small scale structures (below grid resolution) are modeled using a sub-grid scale model. The rationale behind such an approach is the fact that energies typically cascade down to the smaller scales from the larger ones, but not in the opposite direction. The small scale structures in the flow are somewhat passive and take up whatever energy is passed on to them (Davidson, 2004). Also, large eddies are highly anisotropic and depend on the geometry and boundary conditions of the flow, while small scale eddies are more isotropic, independent of geometry and universal (Bakker and Oshinowo, 2004) thus improving the chances of finding an universal model when only the small eddies are modeled. LES has been shown to provide improved predictions of turbulent quantities in a stirred vessel (Hartmann et al., 2004; Yeoh et al., 2004), which in turn should lead to improved predictions from the compartmental model for the reactor performance. Although LES is significantly more computationally intensive than the standard k - ε model and cannot be used for the modeling of large-scale industrial reactors, this can be efficiently used as a bench-marking tool in order to understand clearly if the discrepancy in the compartmental model arises because of the discrepancy in predictions of the k - ε model. The LES model available with the commercial code Fluent 6.2 can be used for this purpose, but the predictions need to be evaluated first using CARPT (Rammohan, 2002) and LDV (Wu and Patterson, 1989) data from the literature. Whenever improved predictions are observed for the turbulent quantities compared to experimental data this can be used to provide improved flow information to the compartmental model for the test example of multiple reactions (Chapter 3) and the results obtained can be bench-marked.

4.1. Filtered Navier-Stokes Equations

The governing equations for a large eddy simulation consist of the filtered Navier-Stokes equations in the physical space obtained using a suitable filter function. This filtering process wipes out the fluctuations whose sizes are smaller than the resolved length scale (grid spacing used) and hence, the resulting equations essentially govern the dynamics of large scale eddies. Some of the key concepts associated with LES are summarized in the

paragraphs to follow, but a more detailed discussion on the filter functions and derivation of the filtered equations are provided by Davidson (2004).

A filtered variable $\bar{\phi}(x)$ is defined as

$$\bar{\phi}(x) = \int_D \phi(x') G(x, x') dx' \quad (4.1)$$

D is the fluid domain and G is the filter function used. In the Fluent 6.2 framework, the finite volume discretization implicitly provides a box-filter operation where the filter function is given by

$$\begin{aligned} G(x, x') &= \frac{1}{V}, \quad x' \in V \\ &= 0, \quad \textit{otherwise} \end{aligned} \quad (4.2)$$

V is the volume of the computational cell. The filtered variable then becomes

$$\bar{\phi}(x) = \frac{1}{V} \int_V \phi(x') dx', \quad x' \in V \quad (4.3)$$

Applying the filtering operation to the Navier-Stokes equation and noting that the operations of filtering and differentiation commute ($\frac{\partial \bar{\phi}}{\partial t} = \overline{\left(\frac{\partial \phi}{\partial t}\right)}$ and $\frac{\partial \bar{\phi}}{\partial x} = \overline{\left(\frac{\partial \phi}{\partial x}\right)}$;

Davidson, 2004), the resulting equations can be written as

$$\frac{\partial \bar{\rho}}{\partial t} + \frac{\partial}{\partial x_i} (\bar{\rho} \bar{u}_i) = 0 \quad (4.4)$$

$$\frac{\partial}{\partial t} (\bar{\rho} \bar{u}_i) + \frac{\partial}{\partial x_j} (\bar{\rho} \bar{u}_i \bar{u}_j) = \frac{\partial}{\partial x_j} \left(\mu \frac{\partial \bar{u}_i}{\partial x_j} \right) - \frac{\partial \bar{p}}{\partial x_i} - \frac{\partial \tau_{ij}^R}{\partial x_j} \quad (4.5)$$

$$\tau_{ij}^R = \overline{\rho u_i u_j} - \bar{\rho} \bar{u}_i \bar{u}_j \quad (4.6)$$

Thus, the filtering process introduces residual stresses, τ_{ij}^R , which are analogous to the Reynolds stresses introduced by time averaging. The commonly used approach to model the residual stress is by introducing the eddy-viscosity as

$$\tau_{ij} - \frac{1}{3} \tau_{kk} \delta_{ij} = -2\mu_t \bar{S}_{ij} \quad (4.7)$$

μ_t is the subgrid scale turbulent viscosity and $\overline{S_{ij}}$ is the rate of strain tensor for the resolved scale written as $\overline{S_{ij}} = \frac{1}{2} \left(\frac{\partial \overline{u}_i}{\partial x_j} + \frac{\partial \overline{u}_j}{\partial x_i} \right)$. The subgrid scale turbulent viscosity is

closed using the Smagorinsky model (Smagorinsky, 1963) that gives

$$\mu_t = \rho L_s^2 |\overline{S}| \quad (4.8)$$

L_s is the mixing length for the subgrid scale and $|\overline{S}| = \sqrt{2\overline{S_{ij}}\overline{S_{ij}}}$. The mixing length scale is calculated as $L_s = \min(\kappa d, C_s V^{1/3})$, where κ is the von Karman constant, d is the distance to the closest wall, V is the volume of the computational cell and C_s is the Smagorinsky constant which is usually given a value of 0.1. In Fluent 6.2, the filtered Navier-Stokes equations (4.4 and 4.5) are solved along with the eddy-viscosity model for the residual stresses (4.7) and with the Smagorinsky model for the subgrid viscosity (4.8).

4.2. Methodology

In order to assess the predictability of the large eddy simulation model in Fluent 6.2, an extensive comparison of the flow quantities are made against those obtained experimentally using CARPT (Rammohan, 2002) and laser-doppler velocimetry (Wu and Patterson, 1989). Also, comparison is made with the predictions of the standard k - ε model to quantify any improvement that is obtained using the LES model.

The Multiple Reference Frame (MRF) model (Ranade, 2002) is used to model the rotating impeller when the standard k - ε model is used. Two different meshes are employed – a coarser grid with about 174000 cells (G1) and a refined mesh with about 589000 cells (G2). A significantly finer mesh with about 946000 cells (G3) is used to perform the large eddy simulation along with the Sliding Mesh (SM) approach (Ranade, 2002) for the rotating impeller (Yeoh et al., 2004). The transient simulation is carried out for 35 impeller revolutions and the time averaging is done over the last five revolutions. The time step

used for the LES simulation is 0.002s, and hence, 200 time steps correspond to one impeller revolution. A User Defined Function (UDF) is developed and employed to perform the time-averaging of the data obtained with the sliding mesh model in Fluent 6.2. The time-averaged velocity components are computed from the filtered variables as

$$\bar{u}_i = \frac{\sum_{j=1}^{N_{time}} u_i \Delta t}{T} \quad (4.9)$$

where N_{time} is the number of time steps and T is the total time over which the time-averaging is performed.

The turbulent kinetic energy k is calculated from the time averaged quantities as (Derksen and Van den Akker, 1999)

$$k = \frac{1}{2} \sum_{i=1}^3 \left(\bar{u}_i^2 - \bar{u}_i^2 \right) \quad (4.10)$$

The energy dissipation rate ε is coupled to the local deformation rate and is computed as (Hartmann et al., 2004)

$$\varepsilon = (\nu + \nu_t) \left| \bar{S} \right|^2 \quad (4.11)$$

4.3. Tank Geometry and Simulated Operating Conditions

The schematic of the reactor is the same as that shown in Figure 3.4. The impeller geometry consists of a tank of diameter 0.2m (T), equipped with a standard six-bladed Rushton turbine. The height of the liquid (H) in the tank is equal to the diameter. The impeller diameter (D) and the clearance of the impeller (C) from the bottom of the tank are one-third of the tank diameter. The simulations are carried out with water in the tank for an impeller speed of 150 RPM ($Re \sim 11,000$) at which the single-phase CARPT experiment was previously conducted (Rammohan, 2002) in a tank of similar dimensions. On the other hand, the LDV data (Wu and Patterson, 1989) is obtained for a geometrically similar tank

of diameter 0.27m at 200 RPM ($Re \sim 29,000$). Since the data is taken at fully turbulent condition, the dimensionless quantities reported from the LDV study are also used for assessment.

4.4. Results and Discussions

The predicted results with the two grids using the standard k - ε model and those obtained with the LES-Sliding Mesh formulation are compared with the results obtained experimentally using CARPT (Rammohan, 2002) or LDV (Wu and Patterson, 1989). The LDV data is obtained at The time-averaged velocities are azimuthally averaged and compared with the experimental data. The radial profiles of the various flow quantities presented here are obtained at $z = T/3$ plane characterized by the presence of the impeller. On the other hand, the axial profiles are shown at $r = T/6$ plane which corresponds to the tip of the impeller blades. The radial distance is non-dimensionalized with the tank radius (R). The mean velocities and the turbulent kinetic energies are rendered dimensionless with U_{ip} and U_{ip}^2 respectively, where U_{ip} is the impeller tip speed. The kinetic energy dissipation rate is non-dimensionalized with the average dissipation rate calculated as $\varepsilon = \frac{Po N_{imp}^3 D^5}{V_T}$, where Po is the dimensionless power number (5 for Rushton turbine), N_{imp} is the impeller speed, D is the impeller diameter and V_T is the volume of the tank.

4.4.1. Radial Profiles

The radial profiles of the azimuthally averaged radial, tangential and axial liquid velocities are shown in Figures 4.1, 4.2 and 4.3 respectively. The prediction for the radial velocity shows some improvement with large eddy simulation especially close to the impeller where k - ε model slightly over-predicts CARPT data. Similar prediction of tangential velocity is observed from both models resulting in significant over-prediction of data near the

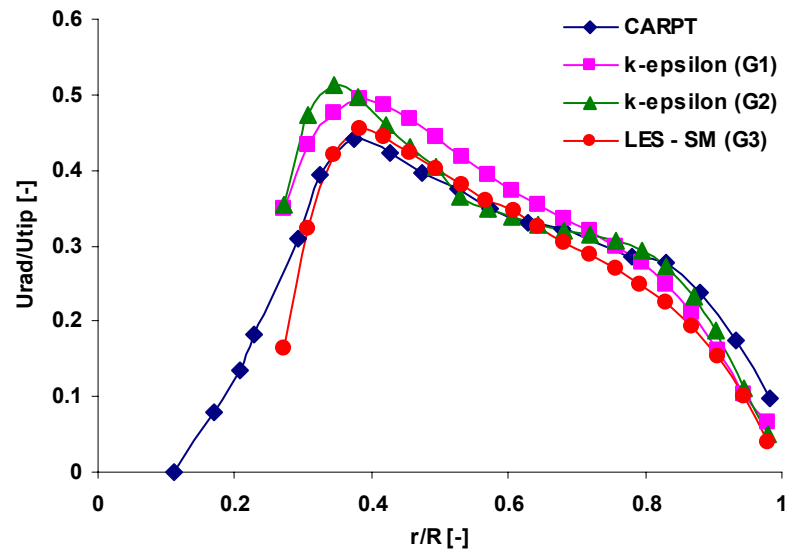


Figure 4.1 Radial profile of liquid radial velocity

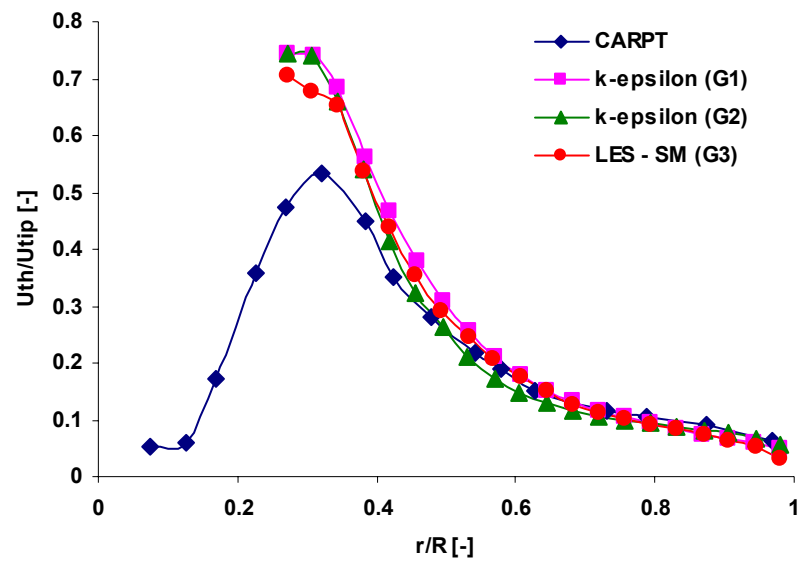


Figure 4.2 Radial profile of liquid tangential velocity

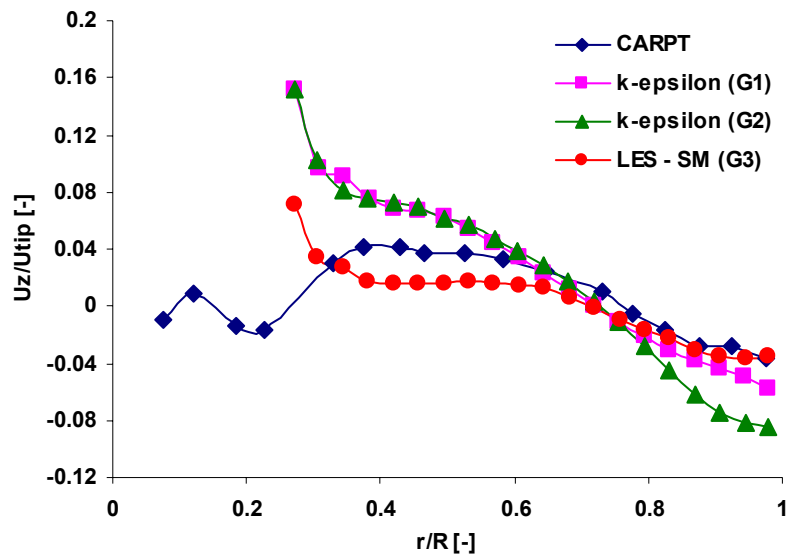


Figure 4.3 Radial profile of liquid axial velocity

impeller. The axial liquid velocity obtained with LES is in better agreement with the CARPT results as observed in Figure 4.3. As for the other velocity components, the axial liquid velocity is also over-predicted by the standard k - ε model close to the impeller. It is interesting to note that the refinement of the grid has hardly any influence on the k - ε model predictions of the mean flow quantities. This is in agreement with the results of Deglon and Meyer (2006) who concluded that the grid resolution does not impact the mean flow but can have strong effect on the turbulent quantities predicted. The radial profiles of the turbulent kinetic energy and the energy dissipation rate are depicted in Figures 4.4 and 4.5, respectively. The turbulent kinetic energy predictions are compared with those obtained from CARPT, while the energy dissipation rates are evaluated against LDV measurements. The turbulent kinetic energy obtained with the k - ε model agrees very well with values obtained using CARPT, and a significant effect of grid resolution is not observed in the present study. This is different from the observation of Deglon and Meyer (2006), although it should be noted that the meshes used in this work are not as fine as those used in their study to investigate the effect of grid resolution on the prediction of

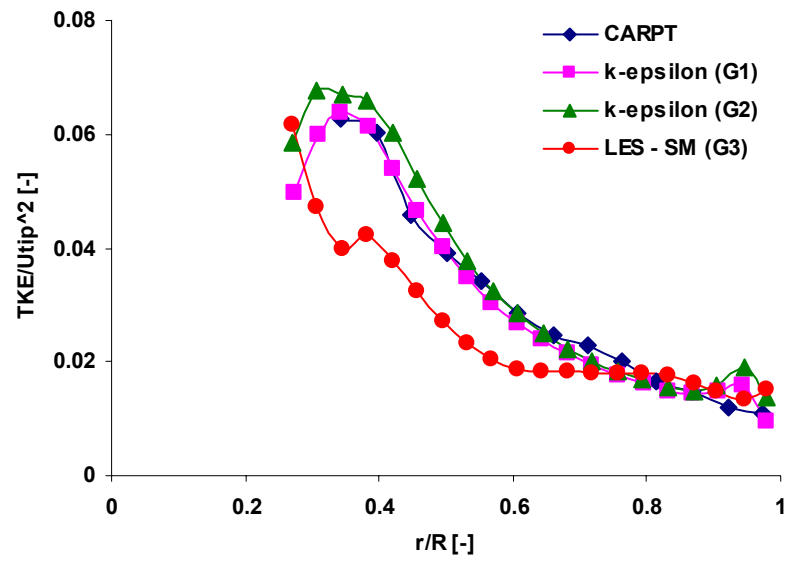


Figure 4.4 Radial profile of turbulent kinetic energy

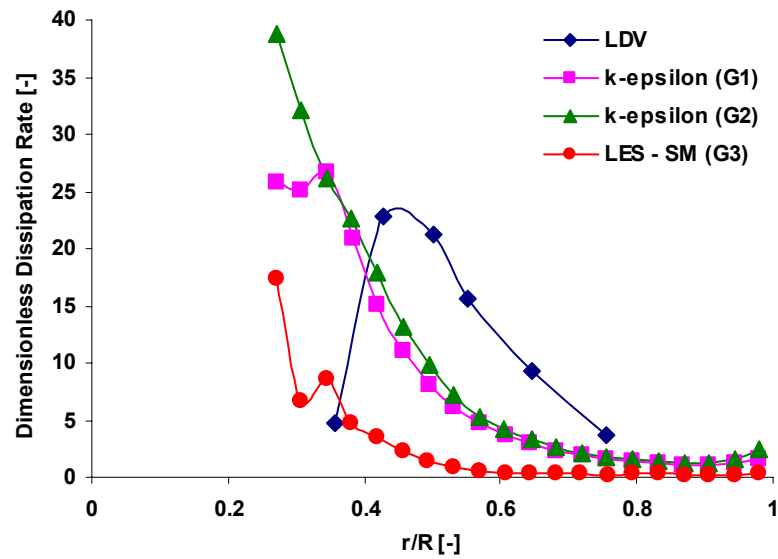


Figure 4.5 Radial profile of kinetic energy dissipation rate

turbulent quantities (Chapter 2). The dissipation rate is, however, severely over-predicted near the impeller and under-predicted elsewhere with the standard k - ε model when compared with LDV measurements. On the other hand, the LES simulation performed in this work was not able to capture the turbulent kinetic energies and energy dissipation rates, resulting in significant under-prediction of both the quantities.

4.4.2. Axial Profiles

Figures 4.6, 4.7 and 4.8 show the axial profiles of the liquid radial, tangential and axial velocities, respectively, as obtained with the k - ε model and large eddy simulation. The model predictions are compared with the CARPT data as before. The radial velocities obtained with the two models are more or less equivalent and no significant improvement is observed using LES. Both models predict similar trends for the liquid tangential velocity and the trend agrees well with the CARPT results. However, quantitatively k - ε model under-predicts and LES over-predicts the tangential velocity at most of the axial locations in the tank. Significant improvement in the prediction of axial velocity is obtained, especially below the impeller, when LES is used. The axial profiles for the turbulent kinetic energy and energy dissipation rate are depicted in Figures 4.9 and 4.10 respectively, where severe discrepancies can be observed between the simulations and experimental results obtained using LDV. The kinetic energy is considerably under-predicted both by the k - ε model and LES, while the dissipation rates are over-predicted by the k - ε model. The magnitudes of the dissipation rates predicted by LES are relatively in better agreement with LDV data, although LES qualitatively did not predict the bimodal profile observed experimentally. As discussed in the preceding section, the effect of grid resolution is minimal on the predictions of most of the flow quantities.

4.4.3. Impeller Flow Number

A characteristic of the rotating impeller is the amount of fluid discharged by the impeller,

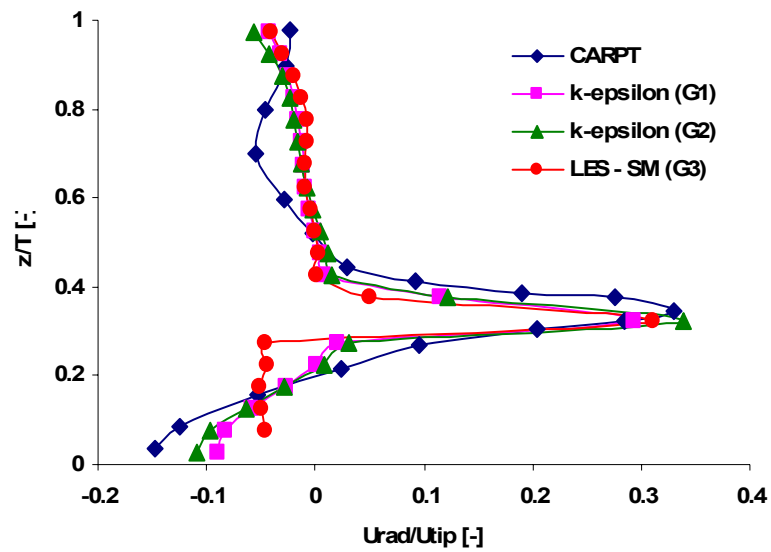


Figure 4.6 Axial profile of liquid radial velocity

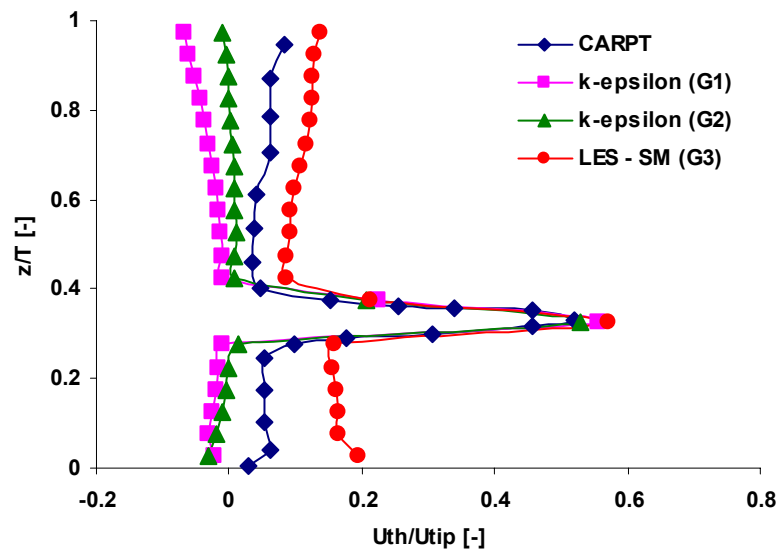


Figure 4.7 Axial profile of liquid tangential velocity

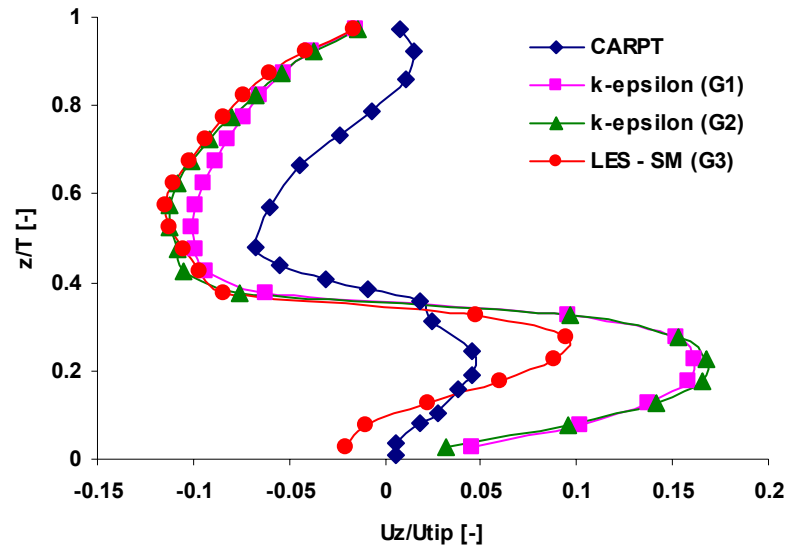


Figure 4.8 Axial profile of liquid axial velocity

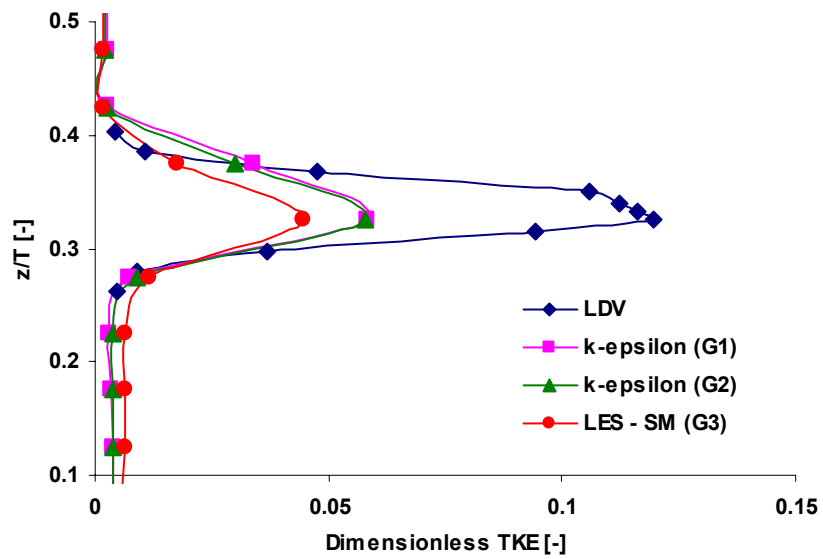


Figure 4.9 Axial profile of turbulent kinetic energy

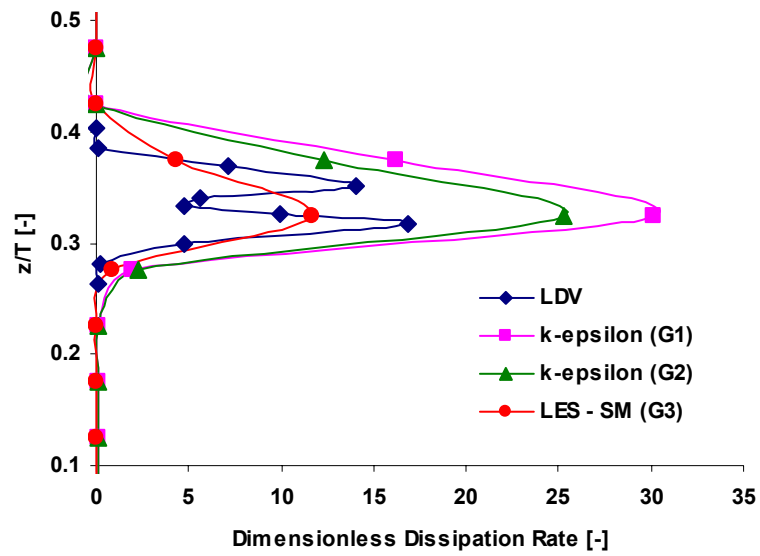


Figure 4.10 Axial profile of kinetic energy dissipation rate

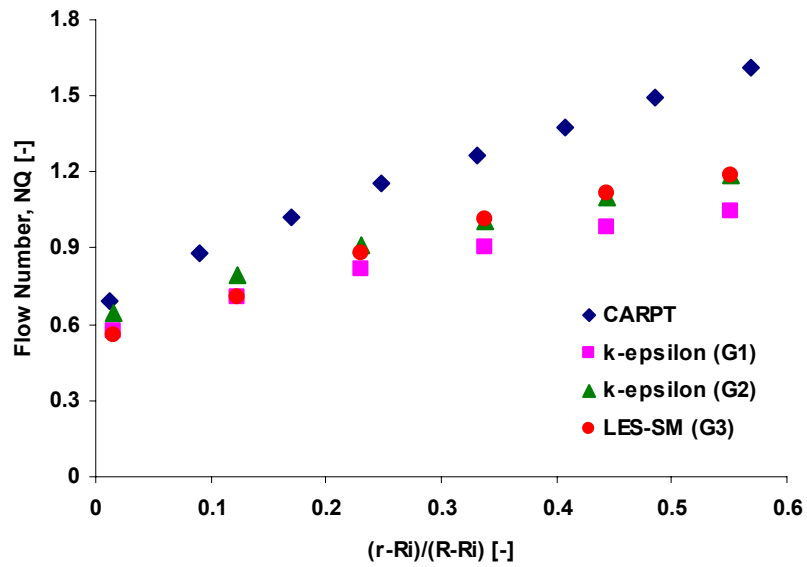


Figure 4.11 Radial profile of pumping flow number (R_i : Impeller Radius)

which depends on the type and geometry of the impeller and the rotational speed. The dimensionless quantity representing the discharged flow is the impeller flow number, N_Q defined as

$$N_Q = \frac{Q_p}{N_{imp} D^3} \quad (4.12)$$

Q_p is the flow pumped by the impeller calculated as $Q_p = \int_0^{2\pi} \int_{-b/2}^{b/2} U_{rad}(r, \theta, z) r d\theta dz$, where

b is the blade height. Typically, the flow number increases as Reynolds number increases and in the completely turbulent regime approaches a constant value depending on the type and geometry of the impeller (Paul, Atiemo-Obeng and Kresta, 2004).

The radial profile of the flow number, as obtained from the simulations using the $k-\varepsilon$ model and LES, are compared with those calculated from CARPT data in Figure 4.11. Both simulations significantly under-predict the flow number as the radial location of the surface of the impeller swept volume increases. However, predictions are in reasonable agreement in the vicinity of the impeller. Also marginal improvement in the predictions can be observed when a finer grid is used along with the standard $k-\varepsilon$ model.

4.5. Summary

Large eddy simulation for single phase flow in a stirred tank is carried out in this work using the commercial code Fluent 6.2. Simulations are performed at the same condition with the standard $k-\varepsilon$ model as well. The model predictions for the mean and turbulent flow quantities are compared with experimental data obtained using CARPT (Rammohan, 2002) and LDV (Wu and Patterson, 1989). Although the large eddy simulation with the sliding mesh formulation shows some improvement in the quantification of the mean flow field, the turbulent quantities are not captured well in the present simulation and are severely under-predicted compared to the experimental data. Since LES solves the filtered Navier-Stokes Equation instead of the RANS equations, LES solution is likely to depend

on the grid size used, and therefore, on the length scale captured. A rough estimate of the Kolmogorov length scale l_K for the case simulated with $\text{Re} \sim 10^4$, based on the scaling rule $l_K / L \sim \text{Re}^{-3/4}$ with the integral length scale L taken to be the reactor diameter T , provides $l_K \sim 10^{-3}T$ (Derksen, 2003). To obtain a full resolution of the flow a grid size of the order of 10^9 cells is at least required whereas the grid size used in the current simulation is of the order of 10^6 , which might have some impact on the flow properties that are captured. Also, the time step resolution used in the current work (200 time steps for one impeller revolution) is lot coarser than some of the studies in the literature. For example, Derksen and Van den Akker (1999) used 1600 time steps, while Hartmann et al. used 2900 time steps to describe one impeller rotation and both these studies show improved predictions of the mean flow and turbulent quantities using LES. So, further refinement in the grid and time step resolution should result in better predictions of the turbulent kinetic energies and energy dissipation rates. However, the computational expense being extremely large, with the current simulation requiring a computer time of at least 15 to 20 times more than the standard k - ε model, simulations with finer grids and time steps are not carried out in this work. As a result, the use of large eddy simulation to bench-mark the compartmental model prediction could not be successfully performed at present.

Chapter 5

Solids Flow Dynamics in a Solid-Liquid Stirred Tank

The compartmental mixing model developed for single phase systems depends on the flow and turbulence information obtained from CFD. This approach can be extended to model two-phase turbulent reactive flows as well. However, that will require more inputs from the CFD simulation in terms of flows and phase distributions for each of the phases present in the reactor. The predicted results will be obviously strongly dependent on the predictability of the computational model used to simulate the flow. It should be noted that for two-phase flows the compartmental model will require the closure of more terms in the volume averaged equations. Typical Boussinesq approximation can be used, but can result in some amount of error when those terms are important as shown for the single phase system. In multiphase systems, the error due to these approximations will add to the error in flow and turbulence predictions, and can lead to significant discrepancy in the final result. Hence, it is important to evaluate the CFD predictions for the flow and turbulence parameters before they are used to model the reactive flow problem in a stirred vessel. The solid-liquid flow in an agitated tank is the two-phase flow of interest in this work. The dearth of literature data at reasonable solids loading (as discussed in Chapter 2) motivates the experimental investigation of the solids flow dynamics in a solid-liquid stirred tank.

Computer Automated Radioactive Particle Tracking (CARPT), is a powerful non-invasive monitoring technique capable of providing the actual trajectories of a tracer particle in “opaque” multiphase flows (Chaouki, Larachi and Dudukovic, 1997). This yields the Lagrangian information about the velocity vector along the particle trajectory from which

the complete three dimensional velocity distributions and turbulence parameters can be obtained. Over the last two decades, CARPT has been used extensively and successfully to characterize both single phase and multiphase flows at high volume fractions in a variety of multiphase reactors such as bubble column (Devanathan, 1990; Yang, 1993; Degaleesan, 1997; Degaleesan, 2001), slurry bubble column (Rados et al., 2005), liquid-solid riser (Roy et al., 1997; Roy et al., 2005), gas-solid riser (Bhusarapu et al., 2005; Bhusarapu et al., 2006), liquid fluidized bed (Limtrakul et al., 2005), bio-digester (Karim et al., 2004), photo bioreactor (Luo et al., 2003) and stirred tank (Rammohan et al., 2001, Rammohan, 2002). This work aims to use the CARPT technique to study the solids hydrodynamics in a solid-liquid stirred tank reactor with relatively dense suspensions with overall solid hold-up ranging from 1% to 7% by volume. The extensive information obtained at varying impeller speeds and varying solids holdup can be used to validate available Computational Fluid Dynamics (CFD) predictions and will also provide insight into the complex solids dynamics and solids suspension in a solid-liquid stirred tank reactor.

5.1. The Stirred Vessel

The stirred vessel used to carry out the experiments is a cylindrical, flat-bottomed tank with diameter $T=0.2\text{ m}$. The height of the liquid (H) is equal to the tank diameter. The tank has four vertical baffles mounted on the wall, of width $T/10$ and $T/125$ in thickness. Agitation is provided by a six-bladed Rushton turbine of diameter $D=T/3$. The length of each blade is $T/12$ and the height is $T/15$. The impeller clearance, C (distance from the bottom of the tank), is equal to the impeller diameter. The schematic of the vessel geometry is shown in Figure 5.1.

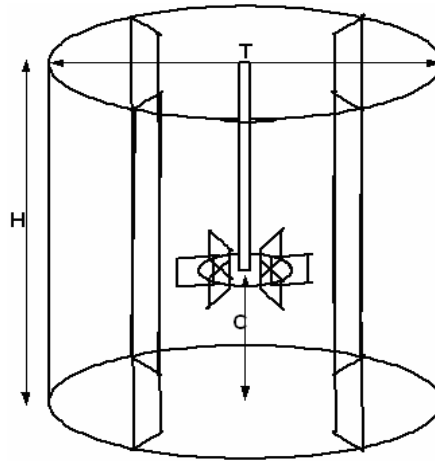


Figure 5.1 Schematic of the tank used for CARPT/CT experiments

5.2. CARPT Setup

The CARPT set-up comprises of 16 scintillation detectors mounted on aluminium supports, which are arranged on an octagonal base as shown by the schematic in Figure 5.2. There are eight aluminium supports positioned around the tank at 45° to each other. Each support has two holes of diameter 5.6 cm. The axial locations of the center of these holes are as follows: the lowest hole is at a distance of $Z1 = 2.42$ cm, followed by $Z2 = 7.5$ cm, $Z3 = 12.58$ cm and $Z4 = 17.66$ cm. Each aluminium support has the hole placed, either at $Z1$ and $Z4$ or at $Z2$ and $Z3$. Every successive support has alternate locations of the holes. Each detector unit consists of a cylinder 5.4 cm in diameter and 26.0 cm in length, and contains an active cylindrical sodium iodide crystal ($5.08\text{cm} \times 5.08\text{cm}$). These detectors are placed at the above-mentioned four axial levels. Every axial level has four detectors, each at right angles with the others. A photograph of the actual CARPT experimental set-up is provided in Figure 5.3. The radioactive tracer particle, the position of which is being tracked, is 0.3 mm in diameter and has a density of around 2500 kg/m^3 . These are the same as the diameter and density of the solids (glass beads) being tracked in

the current experiment. This particle is made of Sc-46 and is coated with a pre-calculated thickness of Parylene-N to match the density of the solid phase used for the experiments.

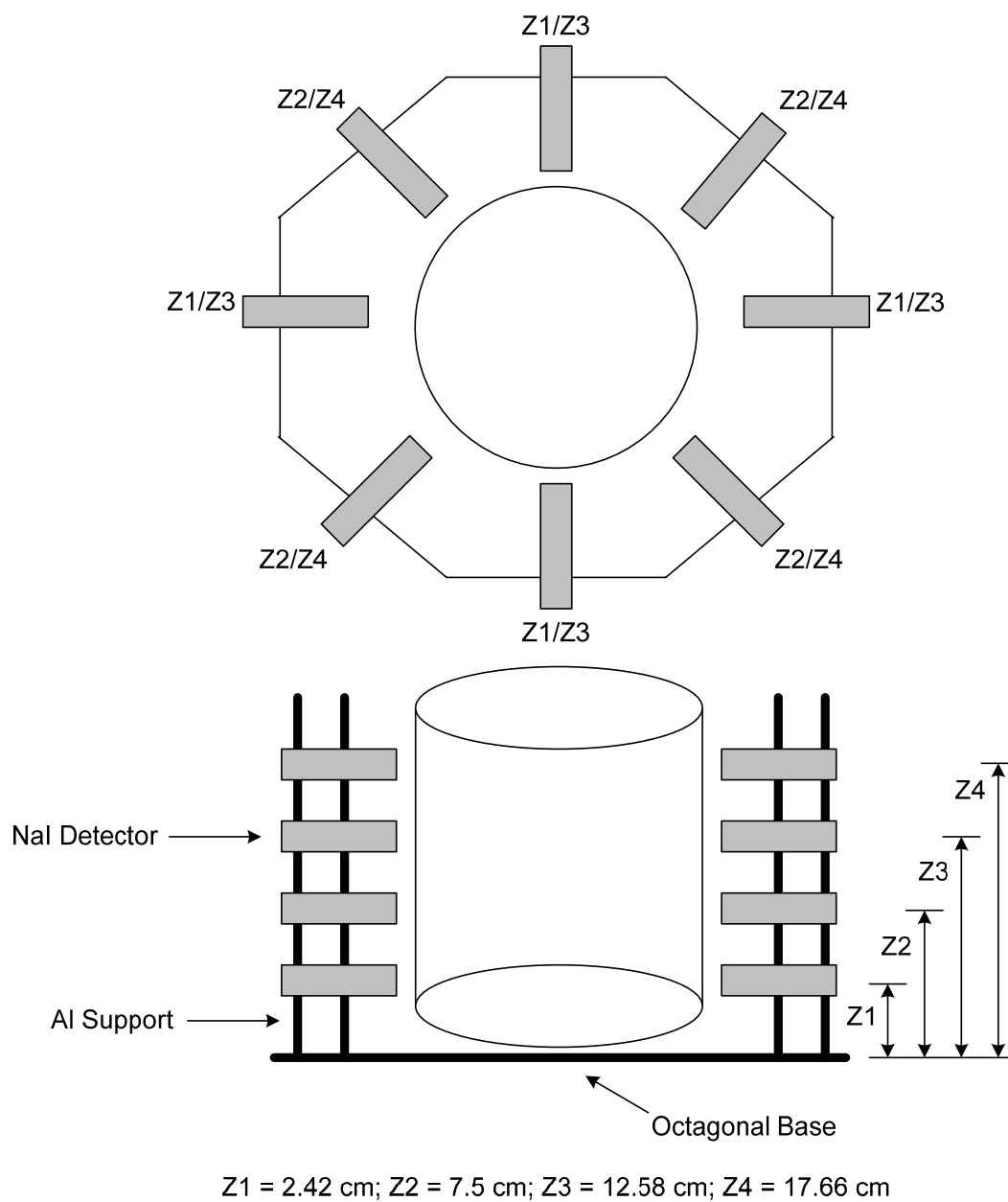


Figure 5.2 Schematic of CARPT experimental setup

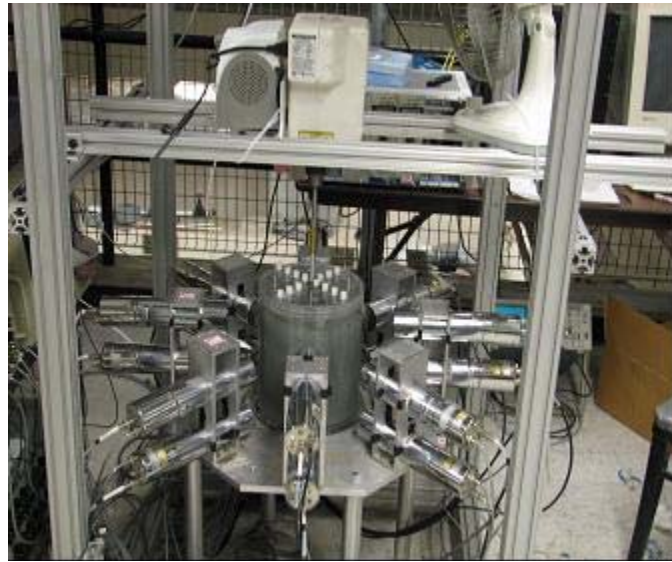


Figure 5.3 Photograph of CARPT experimental setup with solid-liquid stirred tank

5.3. CARPT Technique

The CARPT technique maps the flow of solids in the reactor by tracking a single radioactive particle (^{46}Sc) having the same size and density as the solids used for the experiments. As the particle moves about in the vessel, the location of the particle is determined by an array of scintillation detectors that monitor the gamma radiation emitted by the particle. In order to estimate the position of the particle from the radiation intensities measured by the detectors, calibration has to be performed before each experiment by placing the particle at various known locations and monitoring the radiation recorded by each detector. Thus a sequence of instantaneous position data is obtained for the particle at successive sampling instants. Time differentiation of the successive particle positions yields the instantaneous Lagrangian velocities of the particle. Ensemble averaging of the instantaneous Lagrangian particle velocities recorded at each location in the reactor has to be carried out to calculate the time-average Eulerian velocities of the solids in the system. Fluctuating velocities and solids kinetic energies are also obtained using the mean

and instantaneous velocities in the reactor. More details about the CARPT technique can be found elsewhere (Chaouki et al., 1997; Larachi et al., 1997).

In the current experimental study calibration curves are obtained for each detector by placing the tracer particle at about 500 known locations in different regions of the reactor. The sampling frequency used is 50 Hz, which is chosen such that the dynamic bias in particle position measurement (Rammohan et al., 2001) is kept within acceptable limits while the data acquisition time scale is of similar order of magnitude as the characteristic process time scale ($1/N_{imp}$) of the experiments, where N_{imp} is the impeller speed. For each of the experiment, data is obtained for 12 hours and every experiment is performed in duplicate in order to quantify the reproducibility of the measurements obtained. All the experiments are carried out by strictly following the safety protocols outlined in the CARPT user manual (2007).

5.4. Experimental Conditions

For this experimental study, water ($\rho = 1000 \text{ kg-m}^{-3}$) is used as the liquid phase and glass beads ($\rho = 2500 \text{ kg-m}^{-3}$) of mean diameter 0.3 mm are used as the solids phase. Experiments are carried out for two different solids hold-ups of 1% and 7% which correspond to 2.5 and 19% solid loading (wt/wt), respectively. For each hold-up, two different impeller speeds are studied, which are selected such that one is above and one is below the “just suspension speed” predicted by the Zwietering correlation given in (5.1).

$$N_{js} = S \frac{d_p^{0.2} \nu^{0.1} (|g|\Delta\rho)^{0.45}}{\rho_l^{0.45} T^{0.85}} B^{0.13} \quad (5.1)$$

where, S is a constant that depends on agitator type and geometric arrangement and

$$B = 100 \times \frac{\text{weight of solid}}{\text{weight of liquid}}$$

For a tank having the dimensions stated in the earlier section and equipped with a Rushton turbine, the parameter S is equal to about 8 (Zwietering, 1958). The details of the experimental conditions are summarized in Table 5.1.

Table 5.1 Experimental conditions for CARPT study

Overall Solid Hold-up (%)	N_{js}^* (RPM)	Expt. Set-1 (RPM)	Expt. Set-2 (RPM)
1	900	850	1000
7	1168	1050	1200

N_{js}^* = Just suspension speed predicted by Zwietering's correlation

5.5. Results and Discussions

As described in the previous section, the CARPT technique provides information about the solids flow dynamics in the reactor. The ensemble-averaged velocity components and turbulent kinetic energy of the solids at different location within the reactor are obtained and the results are azimuthally averaged and presented here. A weighted mean (weighted by the number of occurrences in each compartment) is used for the azimuthal averaging of all the quantities. For example, the azimuthally averaged m -th component of velocity is given by:

$$\overline{u_m}(i, k) = \frac{1}{T_{dim} \overline{n}(i, k)} \sum_{j=1}^{T_{dim}} \overline{u_m}(i, j, k) n(i, j, k) \quad (5.2)$$

where $\overline{u_m}(i, k)$ is the azimuthally averaged m -th component of velocity in compartment (i, k) , $\overline{u_m}(i, j, k)$ is the ensemble averaged corresponding component of the 3-D velocity vector in the (i, j, k) compartment, T_{dim} is the number of compartments in the azimuthal

direction, $n(i, j, k)$ is the number of occurrences in the (i, j, k) compartment and $\bar{n}(i, k)$ is the average number of occurrences in compartment (i, k) given by

$$\bar{n}(i, k) = \frac{1}{T_{\text{dim}}} \sum_{j=1}^{T_{\text{dim}}} n(i, j, k) \quad (5.3)$$

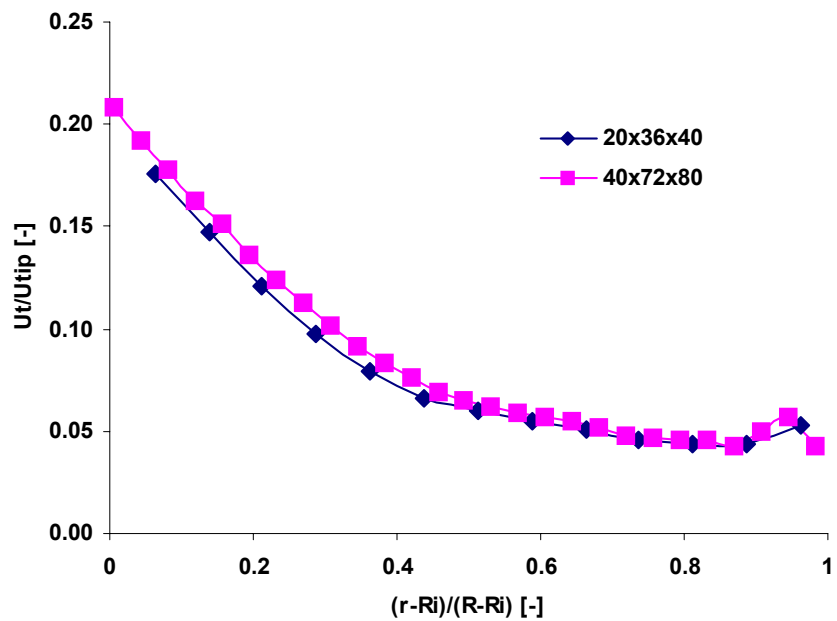
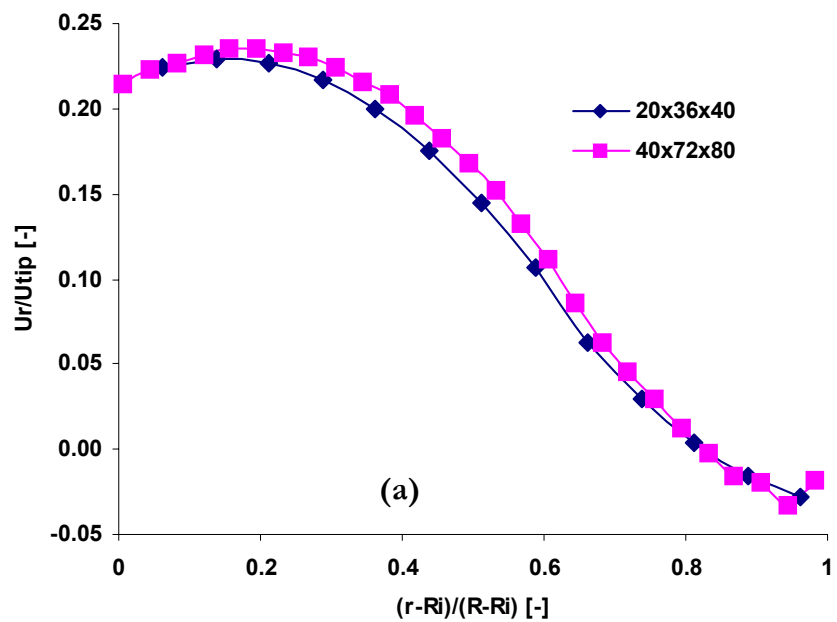
The velocities and turbulent kinetic energies reported here are non-dimensionalized with U_{ip} and U_{ip}^2 respectively, where U_{ip} is the impeller tip velocity given by $U_{ip} = \pi ND$. Solids sojourn time distributions (Rammohan et al., 2001) at different axial locations are also calculated using the data obtained and are reported here. The variations in the mean and standard deviation of the distributions provide some insight into the flow characteristic and solids suspension in the reactor. Each experiment has been reproduced twice and the error bars based on two data sets obtained are reported for all the quantities presented. The observed standard deviations for the ensemble averaged quantities are less than 10% of the mean value for most of the data points, which confirm the reproducibility of the results obtained.

5.5.1. Grid Independence of Computed Quantities

The grid independence of computed mean flow quantities is confirmed using the two different grids listed in Table 5.2. The number of compartments used in the second grid is twice that of those in the first grid in each direction (radial, axial and angular). The CARPT

Table 5.2 Number of compartments used to check grid independence of computed quantities from CARPT data

	Radial	Angular	Axial
Grid 1	20	36	40
Grid 2	40	72	80



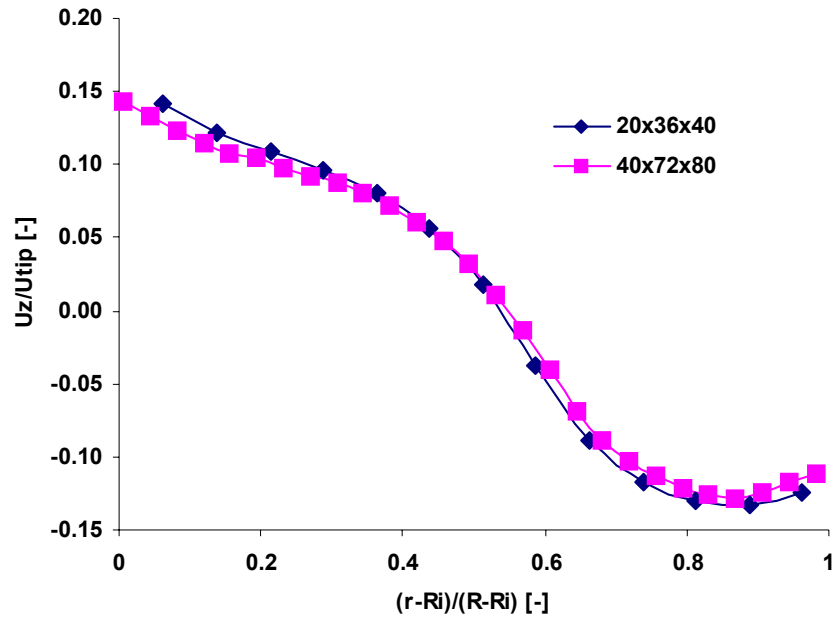


Figure 5.4 Comparison of (a) radial, (b) tangential and (c) axial solids velocities obtained with two grids for 1% solids holdup at 850 RPM (R_i = Impeller radius)

data for the overall solids holdup of 1% at impeller speed of 850 RPM is processed with the two grids, and the azimuthally averaged radial, tangential and axial solids velocities obtained are compared in Figures 5.4 (a) to 5.4 (c) respectively. Since the observed differences are minimal, the first grid with $20 \times 36 \times 40$ (radial \times angular \times axial) compartments is eventually used for all further post-processing of CARPT data.

5.5.2. Overall Flow Pattern

The 2-D velocity vector plots in one half of the tank showing the overall solids flow pattern are displayed in Figures 5.5(a) and 5.5(b) for overall solids holdup of 1% and 7% respectively. The two circulation loops above and below the impeller and the radial jet of solids in the impeller stream can be clearly seen in the figures. The radial jet from the

impeller slightly moves upward as it approaches the wall before it breaks up and creates the two characteristic loops. Close to the wall, the solids move upward above the impeller and downward below the impeller. On the other hand, the solids move downward above the the impeller and upward below the impeller near the center of the tank. However, the lower circulation loop seems to be significantly stronger than the upper one particularly in the case of 1% solids holdup.

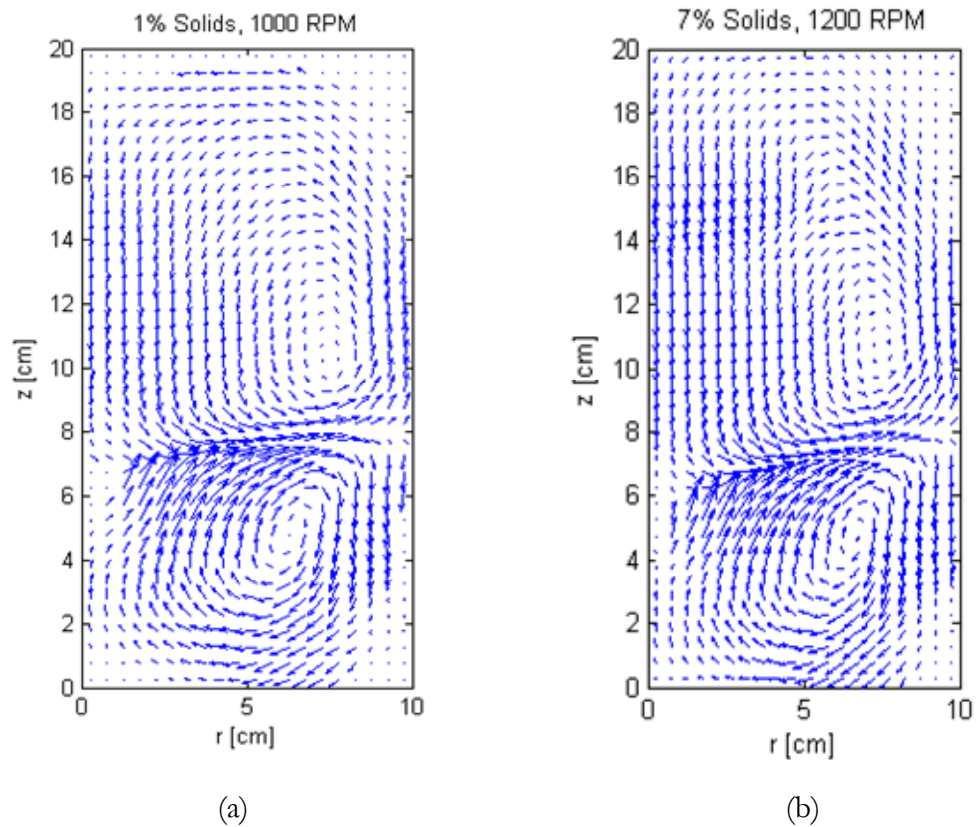


Figure 5.5 Velocity vector plots of solids velocity for overall solids holdup of (a) 1% at 1000 RPM and (b) 7% at 1200 RPM

5.5.3. Ensemble-Averaged Solids Radial Velocity

Figures 5.6 (a) and 5.6 (b) show the radial distributions of solids radial velocity for overall holdup of 1% in the reactor. The range of values obtained from repeated runs seldom exceeds the size of the data points and when it does it is shown by little bars around the points in Figures 5.6 (a), 5.6 (b) and all subsequent figures. The impeller speeds are 850 RPM and 1000 RPM respectively. Velocity distributions are reported at four axial levels – $z/T = 0.075$ (close to the bottom), 0.25 (just below the impeller), 0.34 (impeller plane) and 0.65 (midway between impeller and top free surface). The impeller plane, as expected, is characterized by the highest radial solids velocities compared to those at other axial locations. The maximum observed solids radial velocity at the impeller plane is about 22% of the impeller tip speed which is significantly different from the liquid velocity obtained for single phase flow (48% of tip speed) by Rammohan et al. (2001, 2002) in an earlier CARPT study carried out in a reactor of same dimensions. The difference between the two is an indication of the apparent relative velocity which is of the order of 26% of the impeller tip speed. This observation is different from that reported by Nouri and Whitelaw (1992) in their LDV study with very dilute suspension. Their measured value for the apparent relative velocity is about 6 to 13% of the tip speed. This provides clear indication that at larger solids loading, solid-solid interactions becomes increasingly important and affect the solids dynamics in the reactor. The observed solids radial velocity is negative at $z/T = 0.075$ because of the characteristic flow pattern observed with radial impellers that has two re-circulating loops one above and one below the impeller plane. The topmost plane studied ($z/T = 0.65$) is characterized by very small radial velocities. Similar distribution of solids radial velocities can be seen in Figures 5.7 (a) and (b) at overall solids holdup of 7% in the reactor at impeller speeds of 1050 RPM and 1200 RPM respectively. It can be observed that the dimensionless radial velocity follows the same trend at all the axial locations irrespective of the solid holdup and impeller speed used.

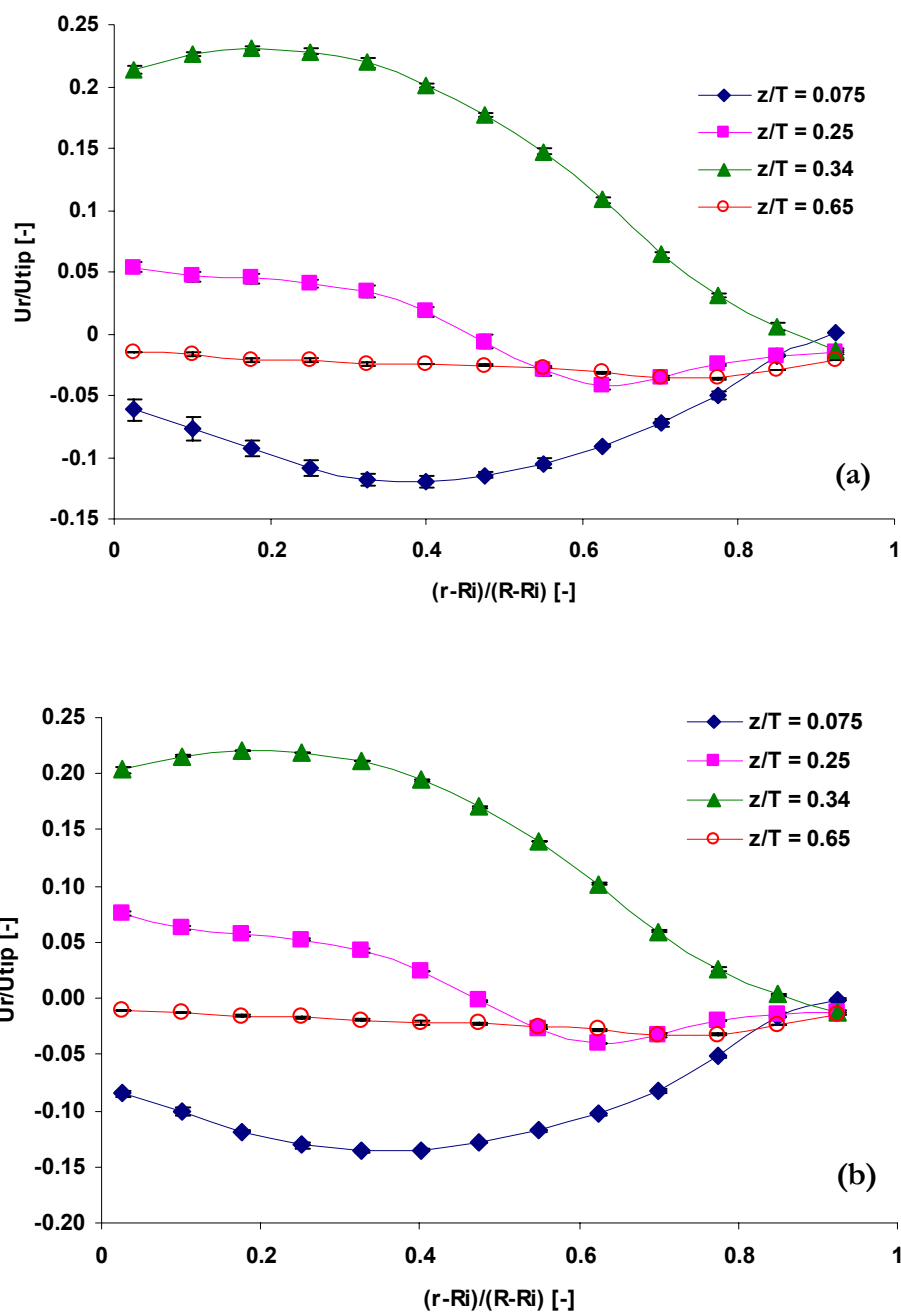


Figure 5.6 Radial profiles of solids radial velocity for overall solids holdup of 1% at (a) 850 RPM and (b) 1000 RPM

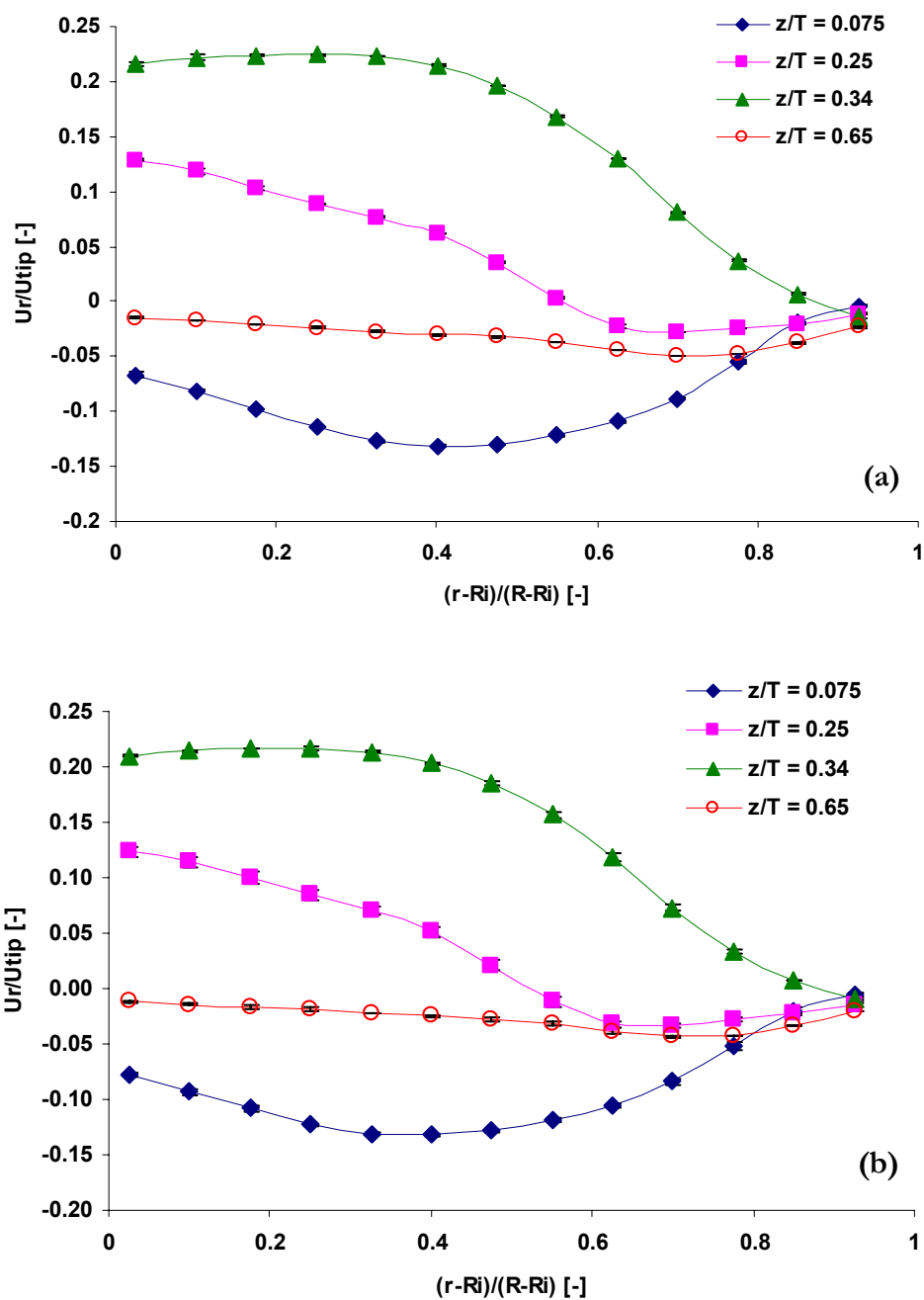


Figure 5.7 Radial profiles of solids radial velocity for overall solids holdup of 7% at (a) 1050 RPM and (b) 1200 RPM

The axial distributions of the solids radial velocity for overall solids holdup of 1% at impeller speeds of 850 RPM and 1000 RPM are presented in Figures 5.8 (a) and (b) respectively. Plots are shown at three radial locations in the tank where $r/R = 0.33, 0.5$ and 0.75 . The profile looks more or less similar at the first two radial locations, although slightly larger velocity is observed at the impeller plane at $r/R = 0.5$. The solids radial velocity decays as it approaches the wall and the peak of the curve appears at higher axial location indicating that the axis of the radial jet is slightly inclined upward. Such an observation has been reported by Sbrizzai et al. (2006) in their direct numerical simulation (DNS) of particle dispersion in an un-baffled stirred tank. The authors attributed this to the different boundary conditions imposed at the bottom (no-slip wall) and at the top (free-slip wall) of the vessel. Similar axial distributions can be observed for solids holdup of 7% in Figures 5.9 (a) and (b). All the trends for the dimensionless radial velocity observed with the lower solids loading can be noticed for the higher loading as well.

5.5.4. Ensemble-Averaged Solids Tangential Velocity

Figures 5.10 (a) and (b) display the radial distributions of solids tangential velocity for overall solids holdup of 1% in the tank at impeller speeds of 850 RPM and 1000 RPM respectively. Plots are shown at all the four axial locations defined earlier. The impeller plane is characterized by strong tangential velocity near the impeller tip that decreases rapidly as the solids move towards the stationary wall. Similar to the radial velocity, the maximum observed tangential velocity at the impeller plane is about 20% of the impeller tip speed in comparison to that obtained for single phase flow (52%) by Rammohan et al. (2001, 2002). The tangential velocities are more or less weak in the regions other than the impeller plane, the minimum being observed at the bottom plane ($z/T = 0.075$). Also radial gradients of the tangential velocity are very small at all axial locations other than the impeller plane where strong gradient exist. At the top ($z/T = 0.65$), the tangential flow can be observed to be larger compared to the radial flow at the same location. The radial

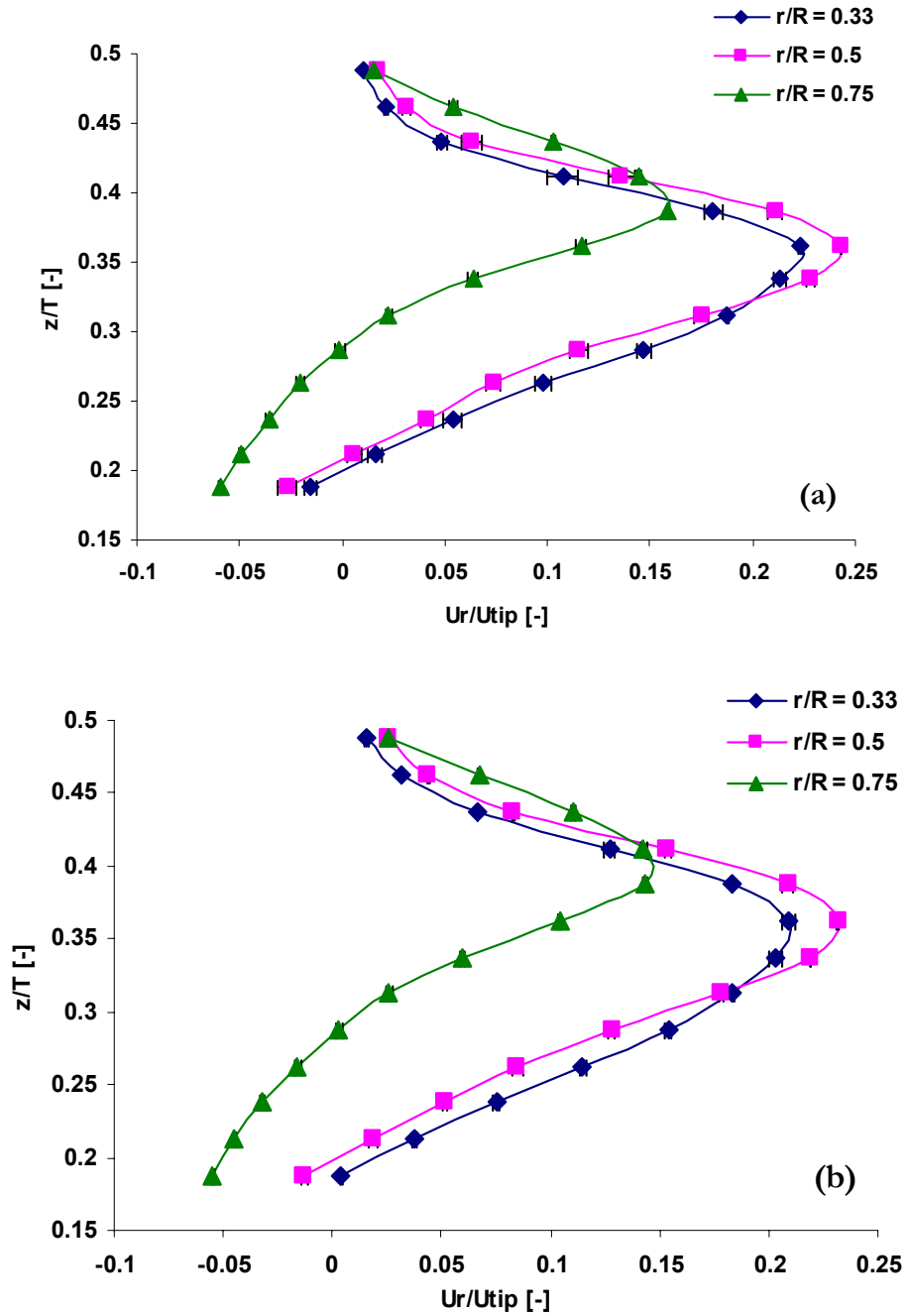


Figure 5.8 Axial profiles of solids radial velocity for overall solids holdup of 1% at (a) 850 RPM and (b) 1000 RPM

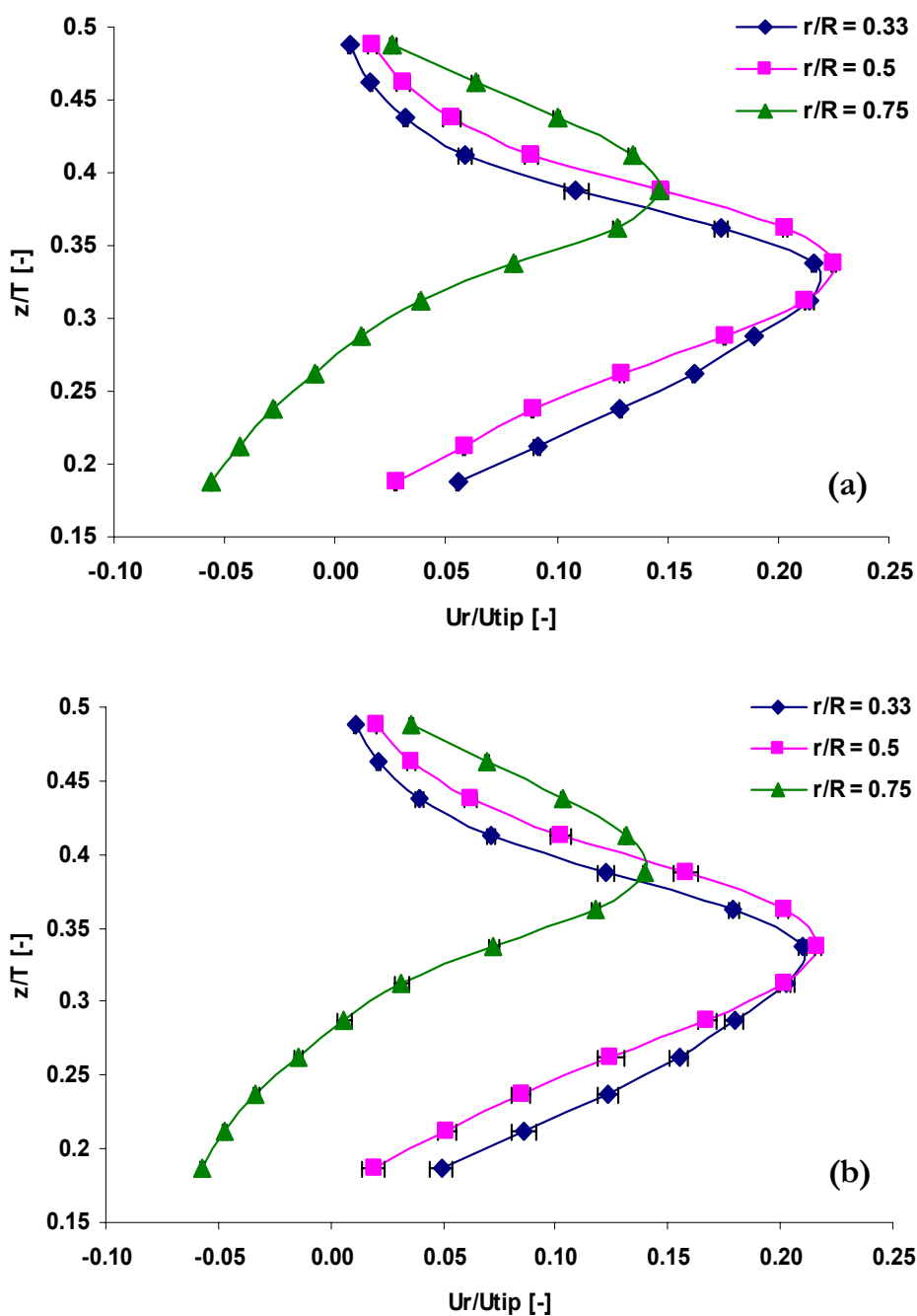


Figure 5.9 Axial profiles of solids radial velocity for overall solids holdup of 7% at (a) 1050 RPM and (b) 1200 RPM

distributions of solids tangential velocities are presented in Figures 5.11 (a) and (b) for overall holdup of 7% in the tank at impeller speeds of 1050 RPM and 1200 RPM, respectively. Increased tangential velocities are observed in these cases close to the radial location of the impeller tip at $z/T = 0.25$ compared to those for 1% holdup. Such an observation is reproducible with small error bars and seems to be caused by the higher solids loading, although the reason behind it cannot be explained explicitly at this point. The characteristic flow features discussed for the lower solids loading are also observed for the higher loading.

The axial distributions of the solids tangential velocity for overall solids holdup of 1% at impeller speeds of 850 RPM and 1000 RPM, respectively, are presented in Figures 5.12 (a) and (b). The maximum tangential velocity is observed at the impeller plane and the velocity decreases as the solids move away from the impeller. As observed in the radial velocity plots, the solids tangential velocity also peaks at a higher axial location close to the wall, confirming that the axis of the solid jet in the impeller stream is slightly inclined upward. Tangential velocity axial distribution plots for solids holdup of 7%, shown at impeller speeds of 1050 RPM and 1200 RPM in Figures 5.13 (a) and (b), respectively, reveal identical qualitative trends.

5.5.5. Ensemble-Averaged Solids Axial Velocities

The radial distributions of solids axial velocities are plotted in Figures 5.14 (a) and (b) at impeller speeds of 850 RPM and 1000 RPM, respectively, for overall solids holdup of 1%. The quantitative results for the axial velocities follow the qualitative trends discussed earlier. The axial velocity is minimum near the bottom ($z/T = 0.075$) depicting the tendency of the solids to settle down at the bottom of the reactor. At the top plane ($z/T = 0.65$), observed axial velocities are larger than the radial and tangential velocities at the same location. Figures 5.15 (a) and (b) display the radial distributions of solids axial velocity for overall holdup of 7% in the reactor at impeller speeds of 1050 RPM and 1200 RPM,

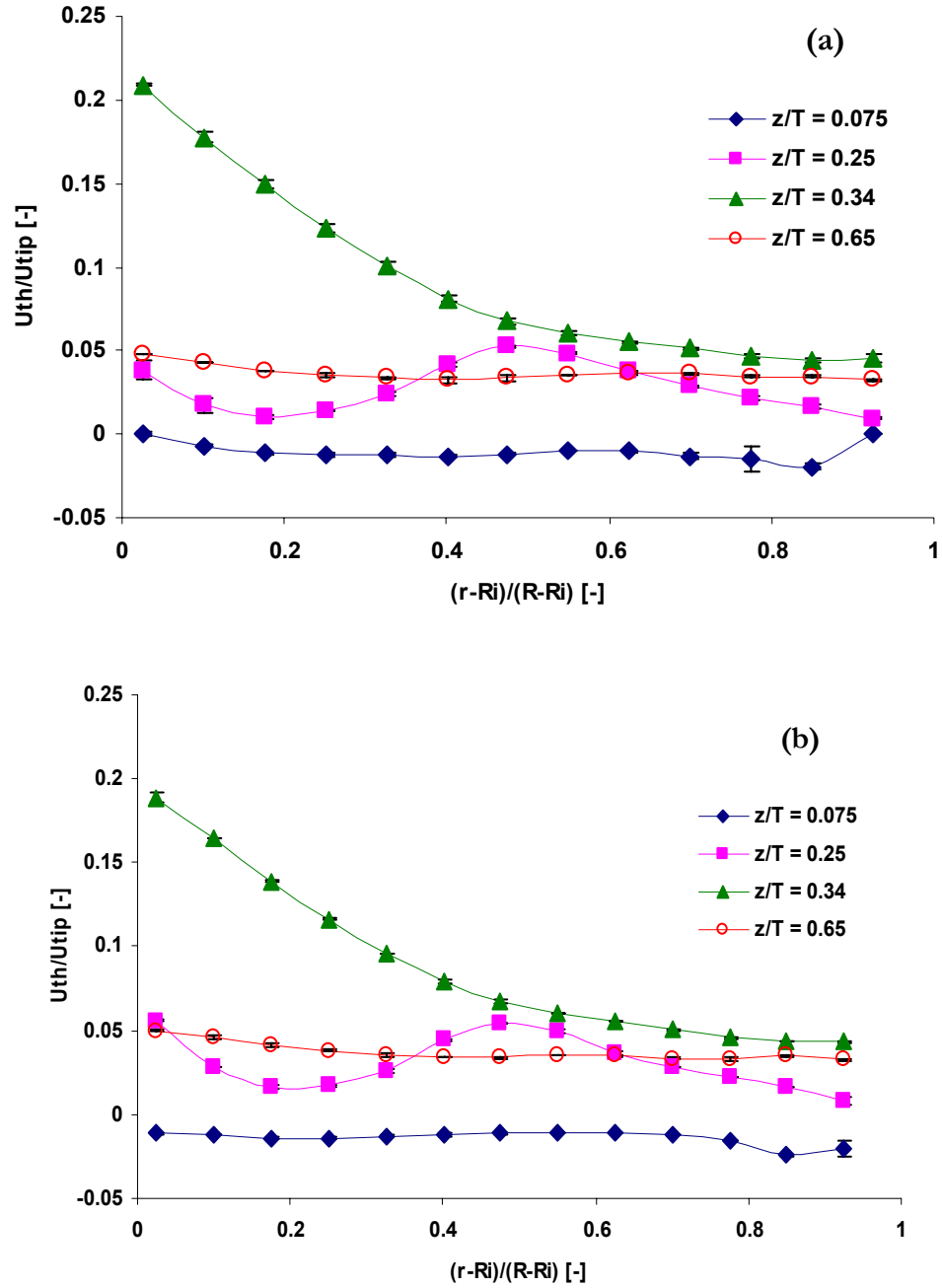


Figure 5.10 Radial profiles of solids tangential velocity for overall solids holdup of 1% at
(a) 850 RPM and (b) 1000 RPM

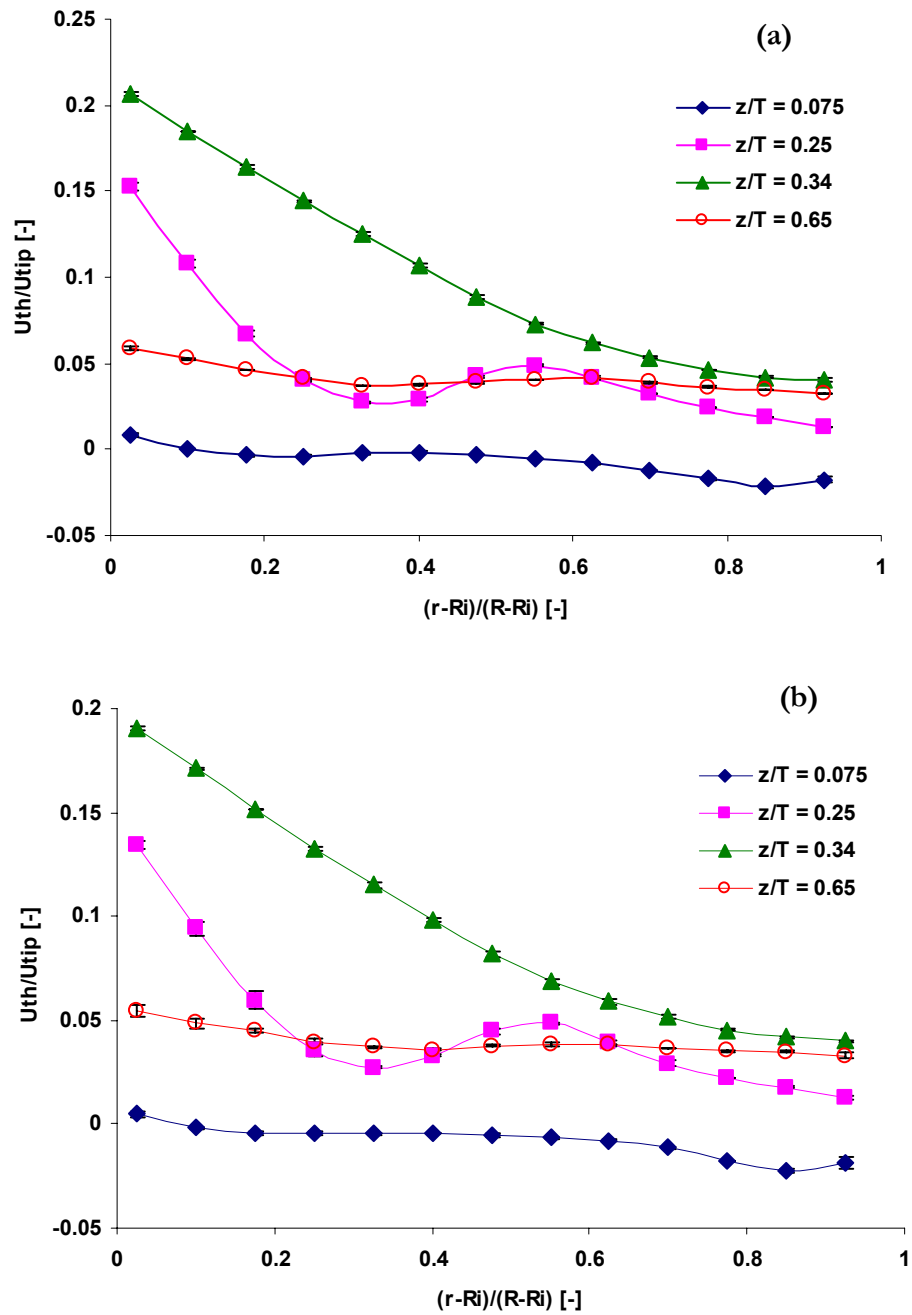


Figure 5.11 Radial profiles of solids tangential velocity for overall solids holdup of 7% at
(a) 1050 RPM and (b) 1200 RPM

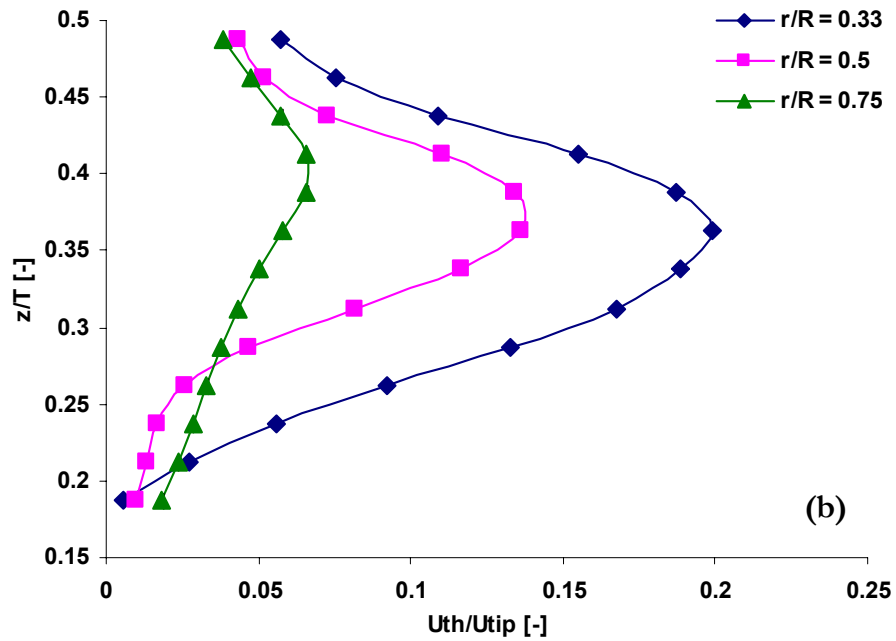
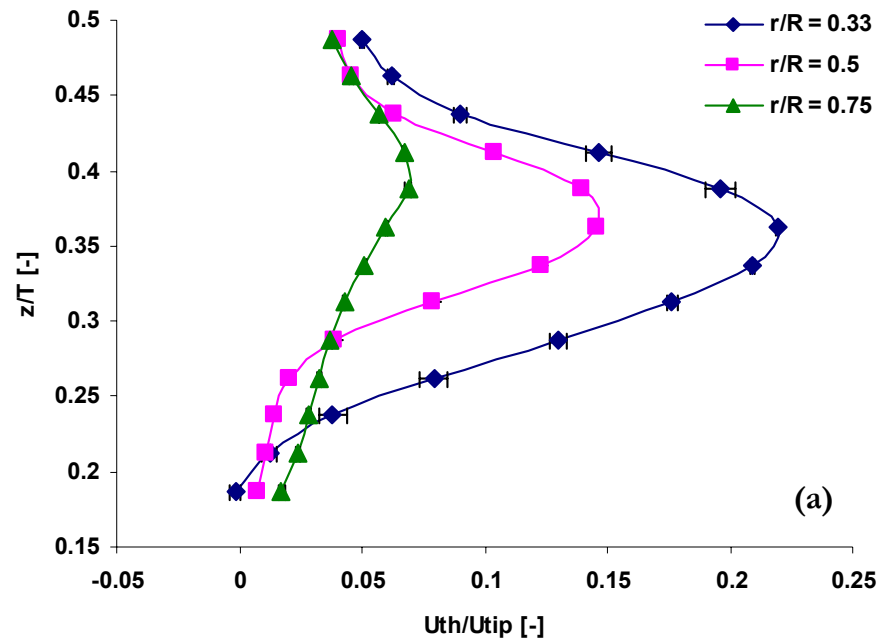


Figure 5.12 Axial profiles of solids tangential velocity for overall solids holdup of 1% at (a) 850 RPM and (b) 1000 RPM

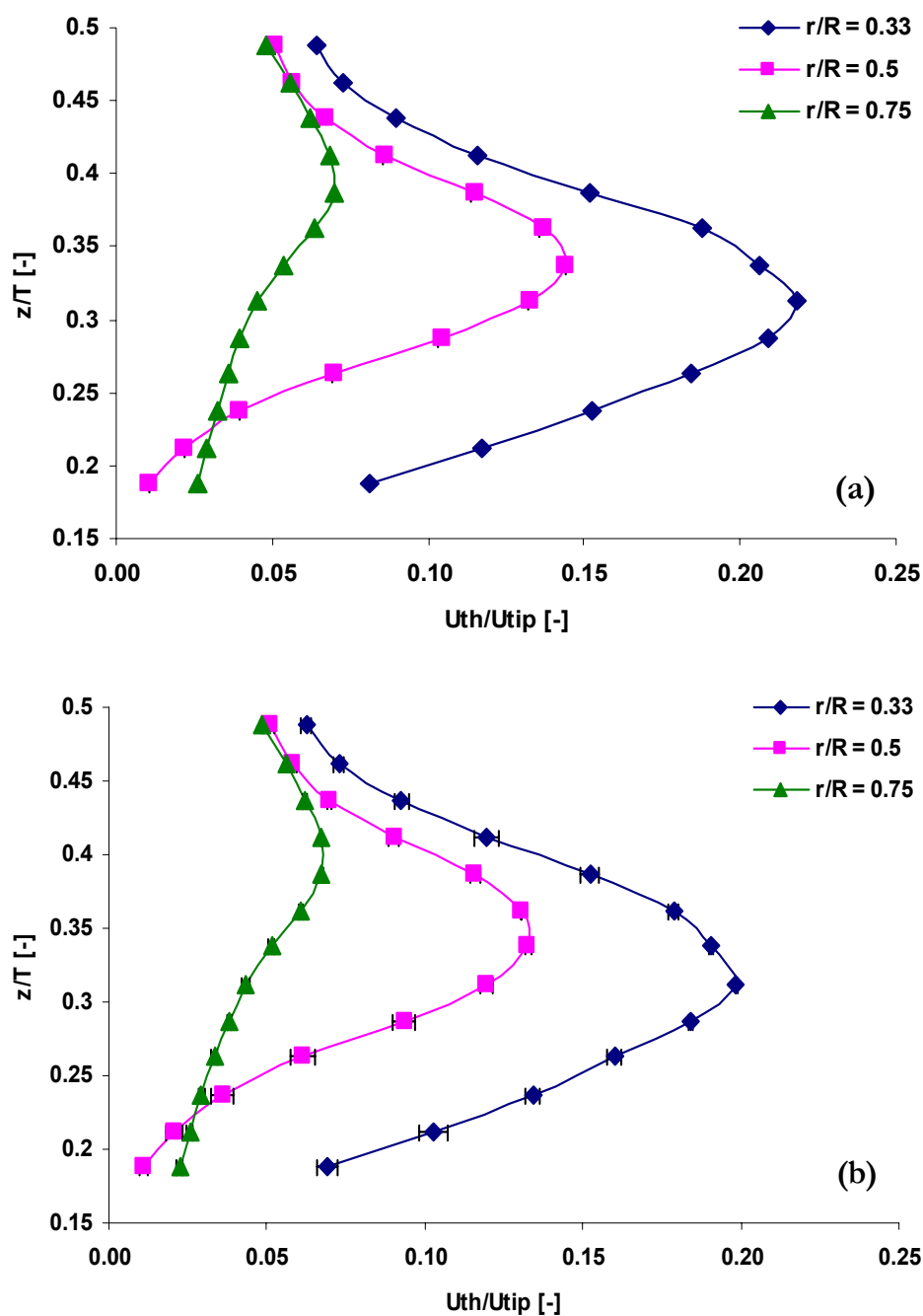


Figure 5.13 Axial profiles of solids tangential velocity for overall solids holdup of 7% at (a) 1050 RPM and (b) 1200 RPM

respectively. The overall flow pattern qualitatively remains the same as at 1% solids holdup and the qualitative features of the flow are retained, although significant difference can be observed quantitatively particularly at the impeller plane. The dimensionless axial velocity in these cases is much smaller close to the impeller tip at $z/T = 0.34$, than that measured for overall solids holdup of 1%.

The axial profiles of solids axial velocities shown in Figures 5.16 (a) and (b) for overall solids holdup of 1% confirm the flow pattern for a radial impeller. Below the impeller solids move upwards near the center and downwards near the wall, while above the impeller solids move downwards near the center and upwards near the wall. The absolute values of the axial velocities observed below the impeller are significantly larger compared to those above the impeller, which indicates that the flow gets weaker as it approaches the top of the reactor. The axial distributions at overall solids holdup of 7% presented in Figures 5.17 (a) and (b) have the same trend as those observed with 1% holdup.

5.5.6. Solids Turbulent Kinetic Energy

In Figures 5.18 (a) and (b), the radial variation of the solids turbulent kinetic energy is presented for solids holdup of 1% at impeller speeds of 850 RPM and 1000 RPM, respectively. The kinetic energy is small at both the top ($z/T = 0.65$) and bottom ($z/T = 0.075$) planes and is the largest in the planes close to the impeller ($z/T = 0.25$ and 0.34). The radial gradients in turbulent kinetic energy seem to be very small and no drastic changes are observed radially in a given plane. Such a trend is different from that observed typically for single phase flow where the turbulent kinetic energy decreases as we move radially towards the wall (Rammohan et al., 2001; Rammohan, 2002). The radial variations in turbulent kinetic energy at the higher solids holdup of 7% are reported in Figures 5.19 (a) and (b) at the two impeller speeds studied. The observed trends are similar to those in case of the lower solids loading. The axial distributions of solids turbulent kinetic energy for overall solids holdup of 1% are shown in Figures 5.20 (a) and (b). The maximum

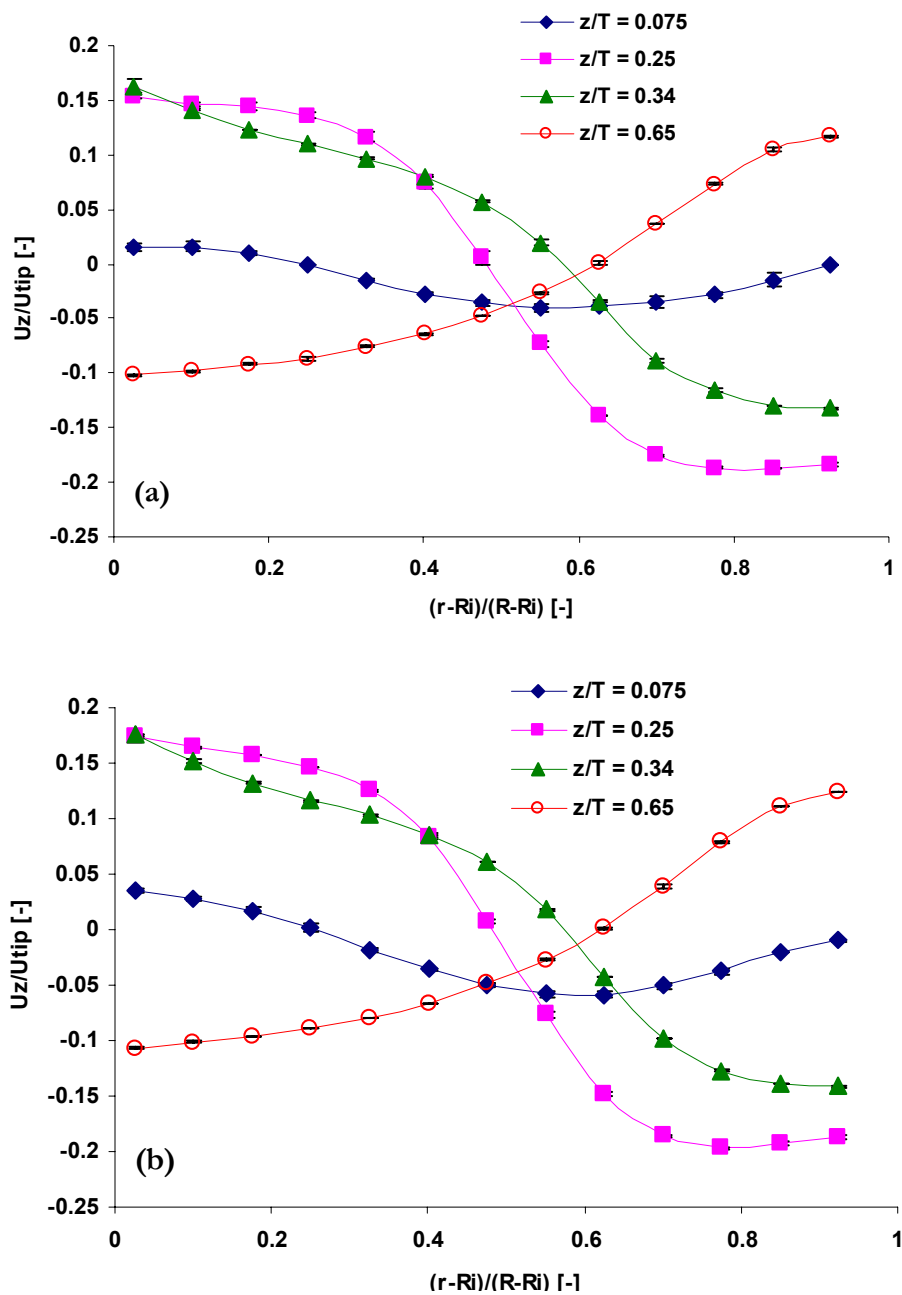


Figure 5.14 Radial profiles of solids axial velocity for overall solids holdup of 1% at (a) 850 RPM and (b) 1000 RPM

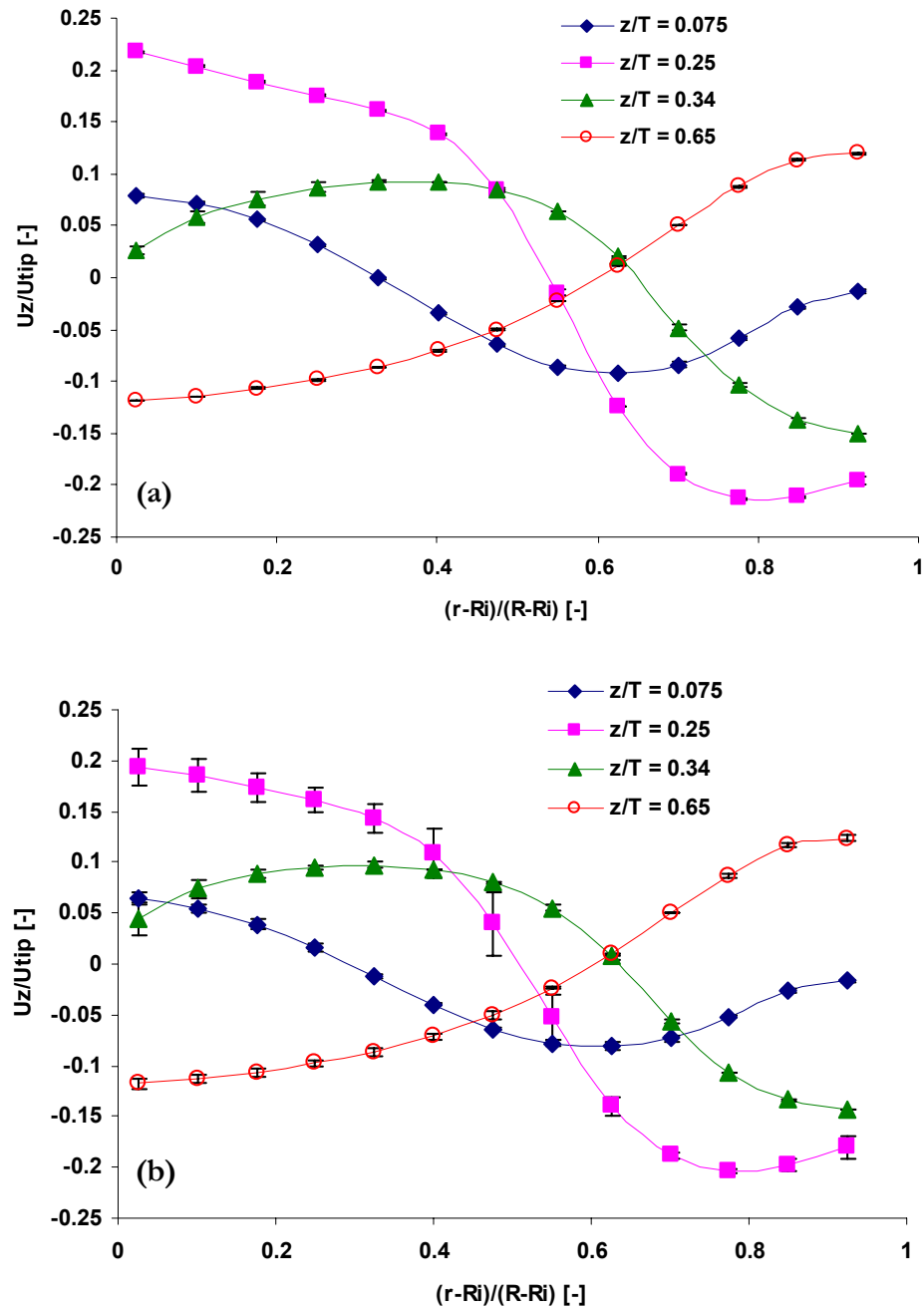


Figure 5.15 Radial profiles of solids axial velocity for overall solids holdup of 7% at (a) 1050 RPM and (b) 1200 RPM

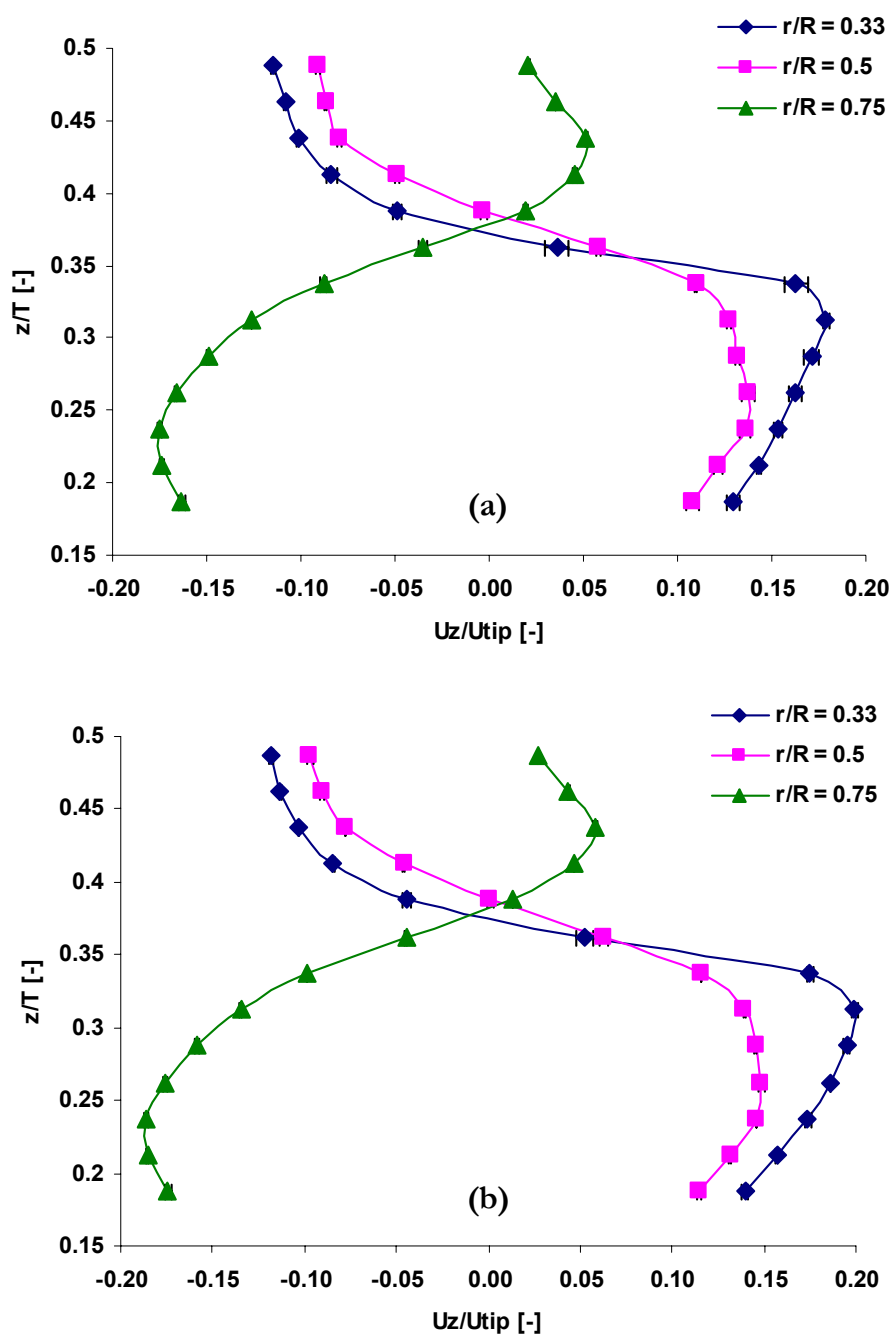


Figure 5.16 Axial profiles of solids axial velocity for overall solids holdup of 1% at (a) 850 RPM and (b) 1000 RPM

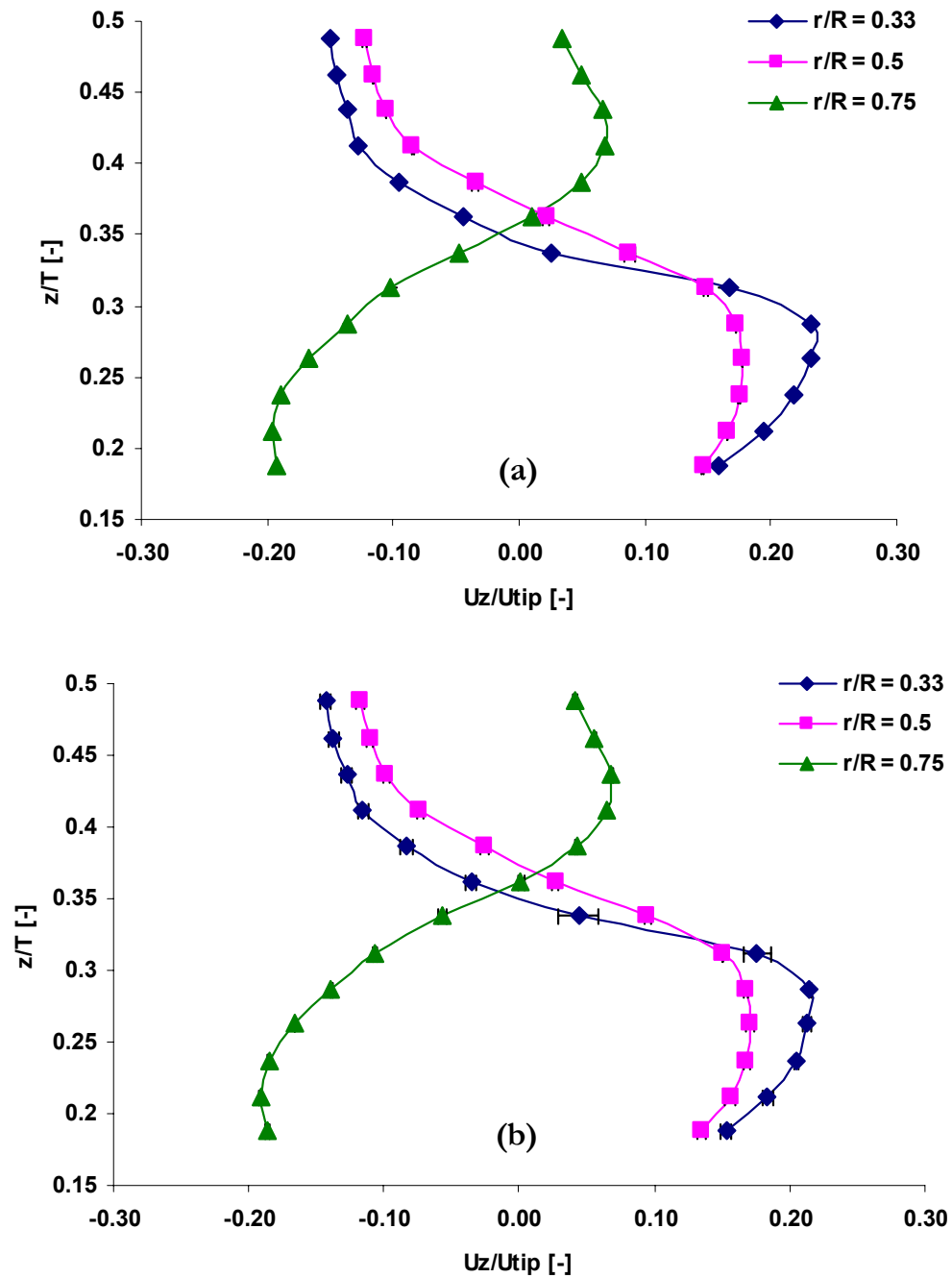


Figure 5.17 Axial profiles of solids axial velocity for overall solids holdup of 7% at (a) 1050 RPM and (b) 1200 RPM

kinetic energies are again observed in and around the impeller plane. Axial Profiles for overall solids holdup of 7% are given in Figures 5.21 (a) and (b).

5.5.7. Solids Sojourn Time Distributions

The instantaneous position data obtained from the CARPT runs are used to calculate the probability density function (PDF) of solids sojourn times in different axial regions in the reactor. The concept of sojourn time distribution (STD) has been discussed in detail by Rammohan et al. (2001), where the authors attempt to partially quantify the existence of dead zones in a single phase stirred tank flow using the STDs obtained from the CARPT data. These distributions can provide useful insights into the qualitative and quantitative features of the flow being studied.

Similar to the approach followed by Rammohan et al. (2001), the total height of the tank is divided into 10 equal axial regions each 2cm in height. From the CARPT experimental record the particle trajectory as a function of time is available (with the time beginning at zero and with every succeeding particle location recorded at intervals of $\Delta t = 0.02$ second corresponding to sampling frequency of 50 Hz used). To generate the STD curve for each zone, the records of the particle locations are scanned until the particle is found again in the zone of interest, i.e. the axial position of the tracer particle is between Z_{min} and Z_{max} of that zone. Now the particle is tracked until the tracer exits the zone of interest. The time the tracer particle spends in the axial zone under consideration from entry to exit is obtained. This yields the sojourn time of the tracer particle through the zone of interest during that pass. This process is repeated every time the particle enters and leaves the zone under consideration. For a CARPT run of 12 hours, the particle enters and exits a given axial zone several thousand times and a distribution of sojourn time of the particle in that axial region is obtained. Thus, the sojourn time distribution (STD) in any axial location i can be defined as

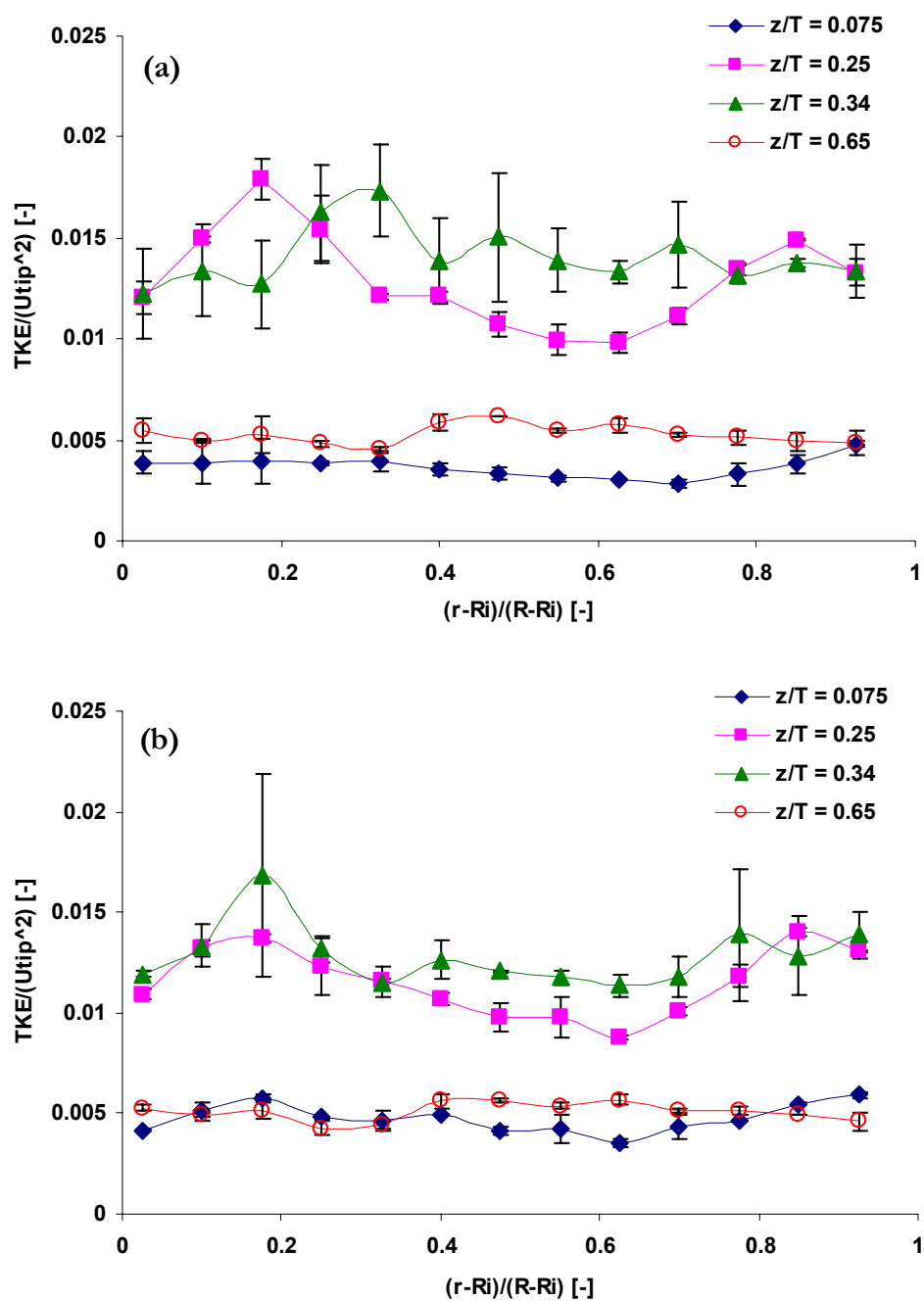


Figure 5.18 Radial profiles of solids turbulent kinetic energy for overall solids holdup of 1% at (a) 850 RPM and (b) 1000 RPM

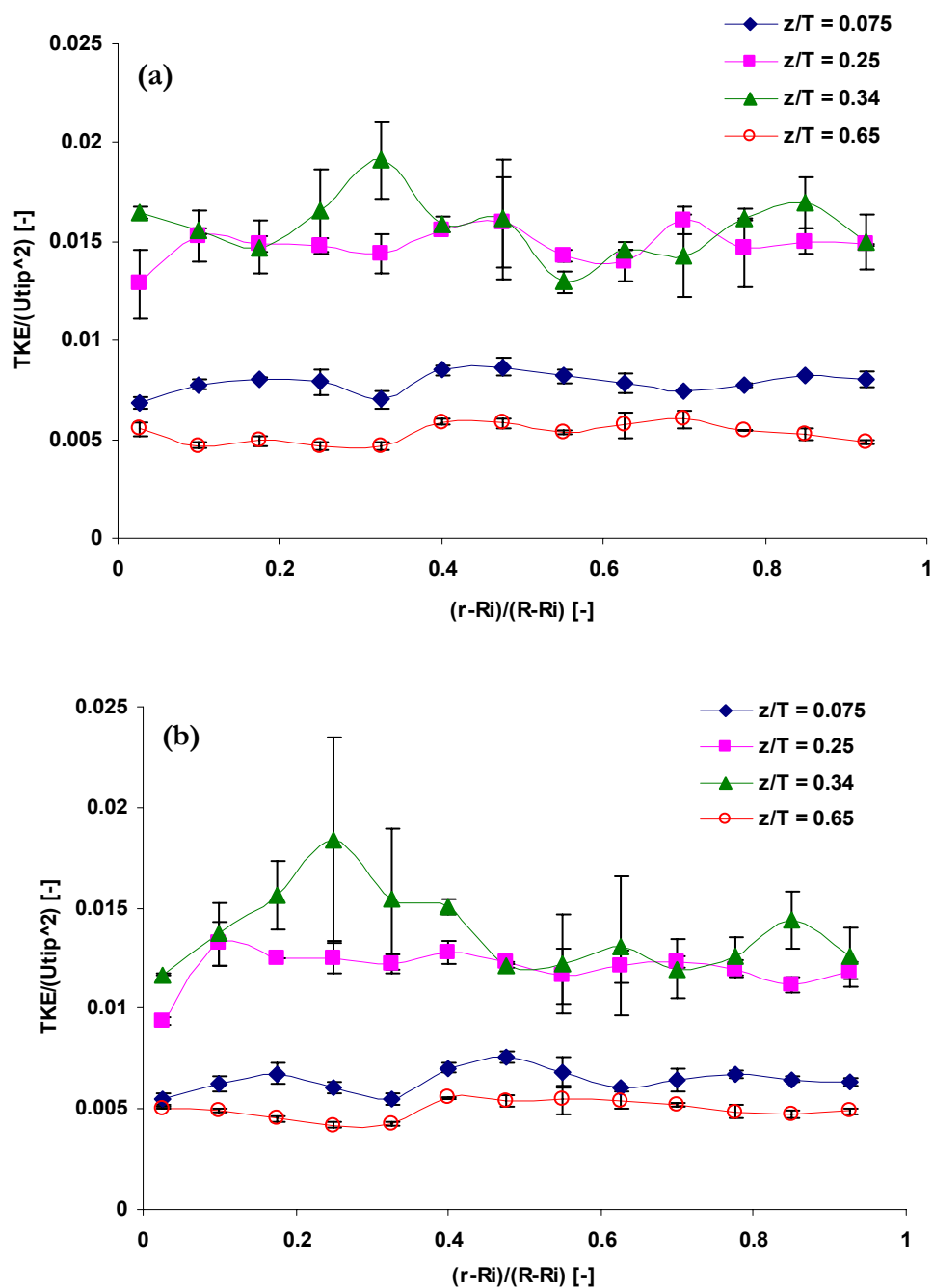


Figure 5.19 Radial profiles of solids turbulent kinetic energy for overall solids holdup of 7% at (a) 1050 RPM and (b) 1200 RPM

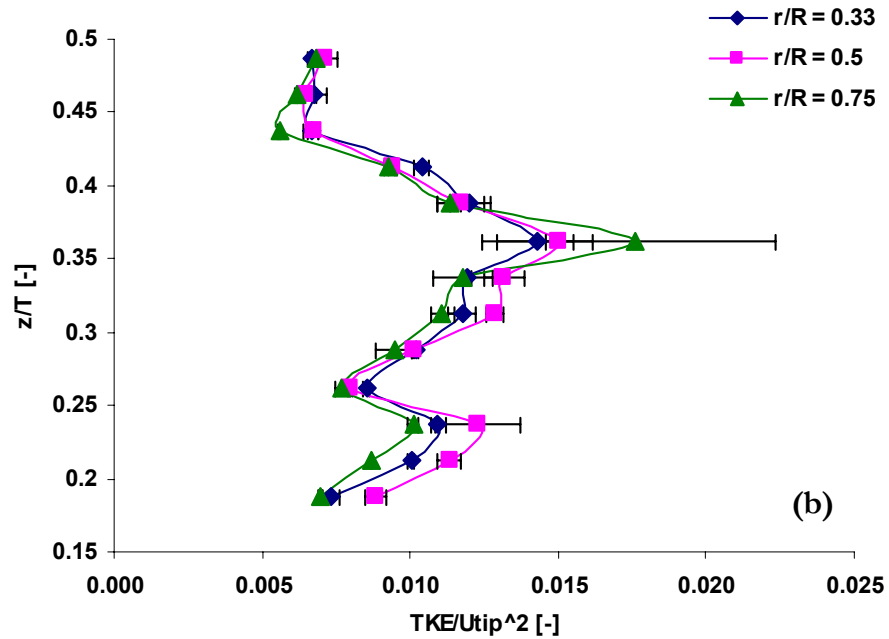
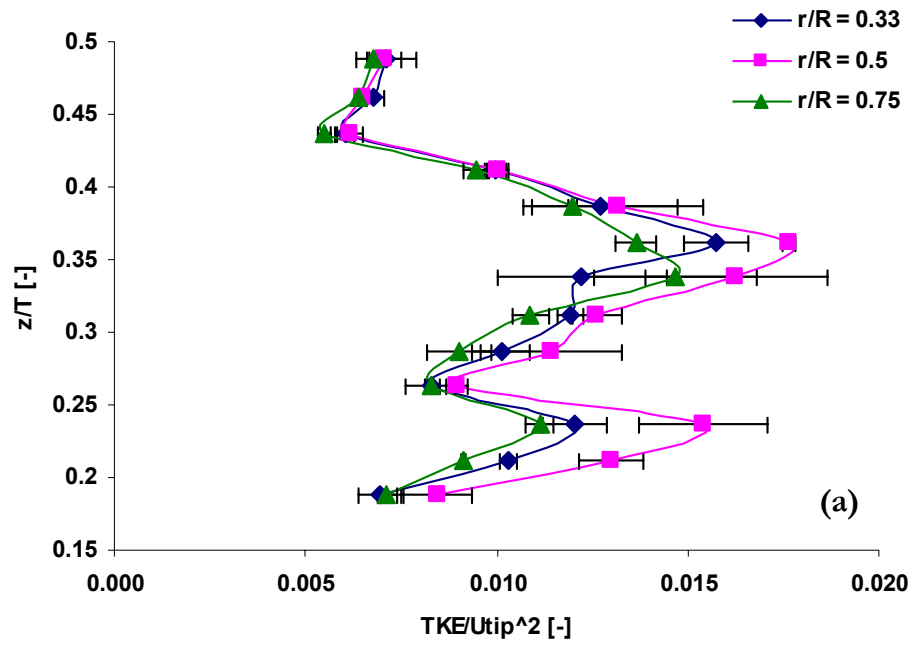


Figure 5.20 Axial profiles of solids turbulent kinetic energy for overall solids holdup of 1% at (a) 850 RPM and (b) 1000 RPM

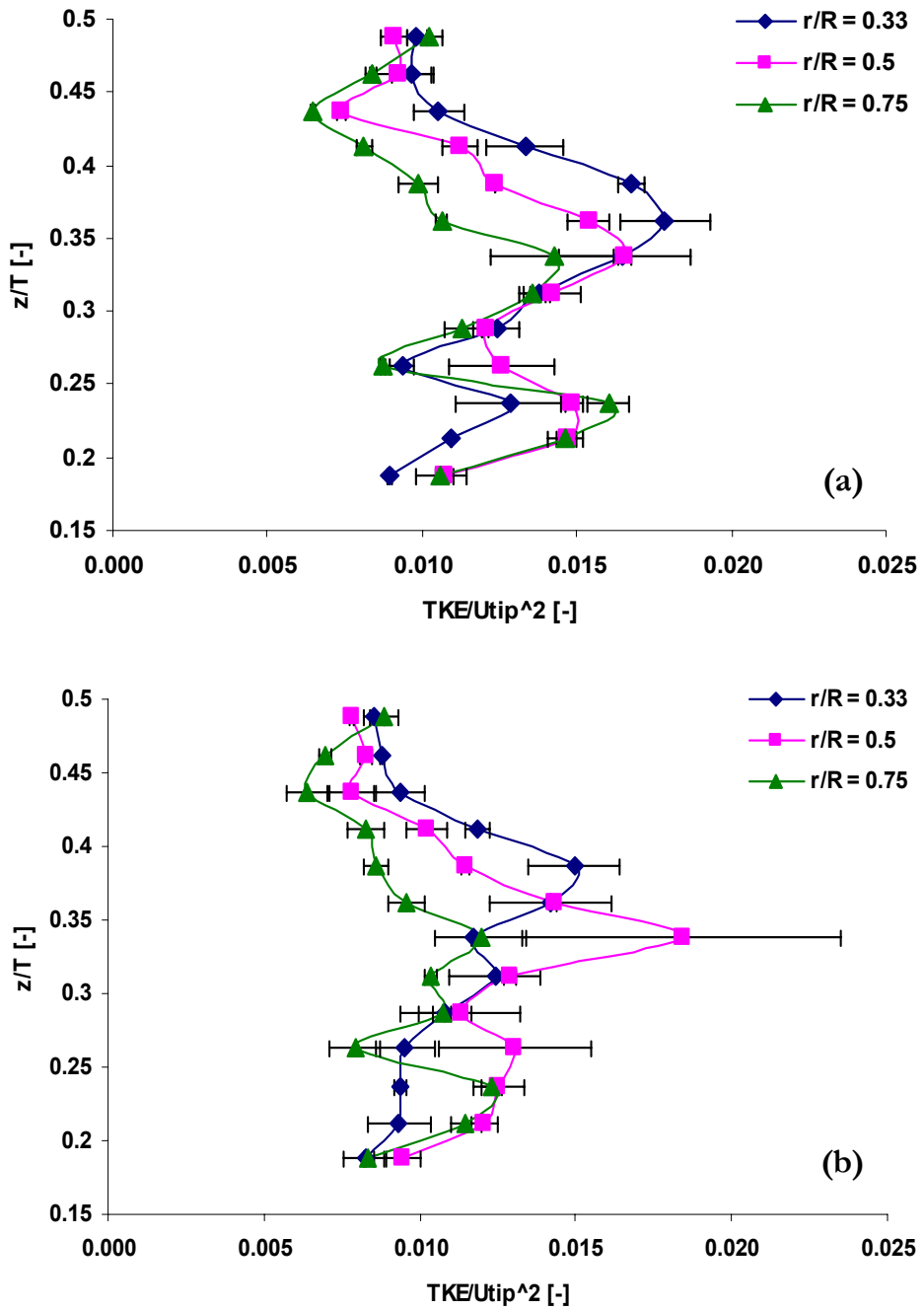


Figure 5.21 Axial profiles of solids turbulent kinetic energy for overall solids holdup of 7% at (a) 1050 RPM and (b) 1200 RPM

$E_i(t_s)\Delta t_s$ = fraction of occurrences in the location i that has sojourn times between t_s and $t_s + \Delta t_s$

Like any standard probability density function, STDs can also be characterized in terms of its moments. The zero-th moment is the integral of the fractional occurrences which becomes unity as required by the definition of a probability density function. The first moment provides the mean of the distribution μ_i , which is then defined as

$$\mu_i = \sum_{t_s=0}^{\infty} t_s E_i(t_s) \Delta t_s \quad (5.4)$$

The second central moment gives the variance of the distribution σ_i^2 , which is defined as

$$\sigma_i^2 = \sum_{t_s=0}^{\infty} (t_s - \mu_i)^2 E_i(t_s) \Delta t_s \quad (5.5)$$

The positive square-root of the variance is the standard deviation of the distribution, which depicts how much the distribution spreads out with respect to the mean value. It is important to note at this point that any other compartmentalization in the angular and radial direction is possible and STD can be obtained for any defined region of interest in the reactor using the CARPT data obtained (Rammohan, 2001).

The CARPT data has been processed as discussed above to generate the STD curves, and the moments of the distributions in all the axial regions are calculated. Figures 5.22 (a) and (b) show the axial variations of the mean and the standard deviation of the STD curves for overall solids holdup of 1% at impeller speeds of 850 RPM and 1000 RPM, respectively. The mean sojourn time in most axial locations is larger at lower impeller speed clearly indicating slower solids motion under such conditions. The trend is completely reversed at the highest axial level where the mean sojourn time is larger for the higher impeller speed. This indicates that at the lower impeller speed most solids do not get suspended to such heights (lower occurrence rate as shown in chapter 7) and those solids that reach this highest height tend to settle down immediately. However, at both impeller speeds the mean sojourn time has the minimum value at the impeller plane where solids move the fastest.

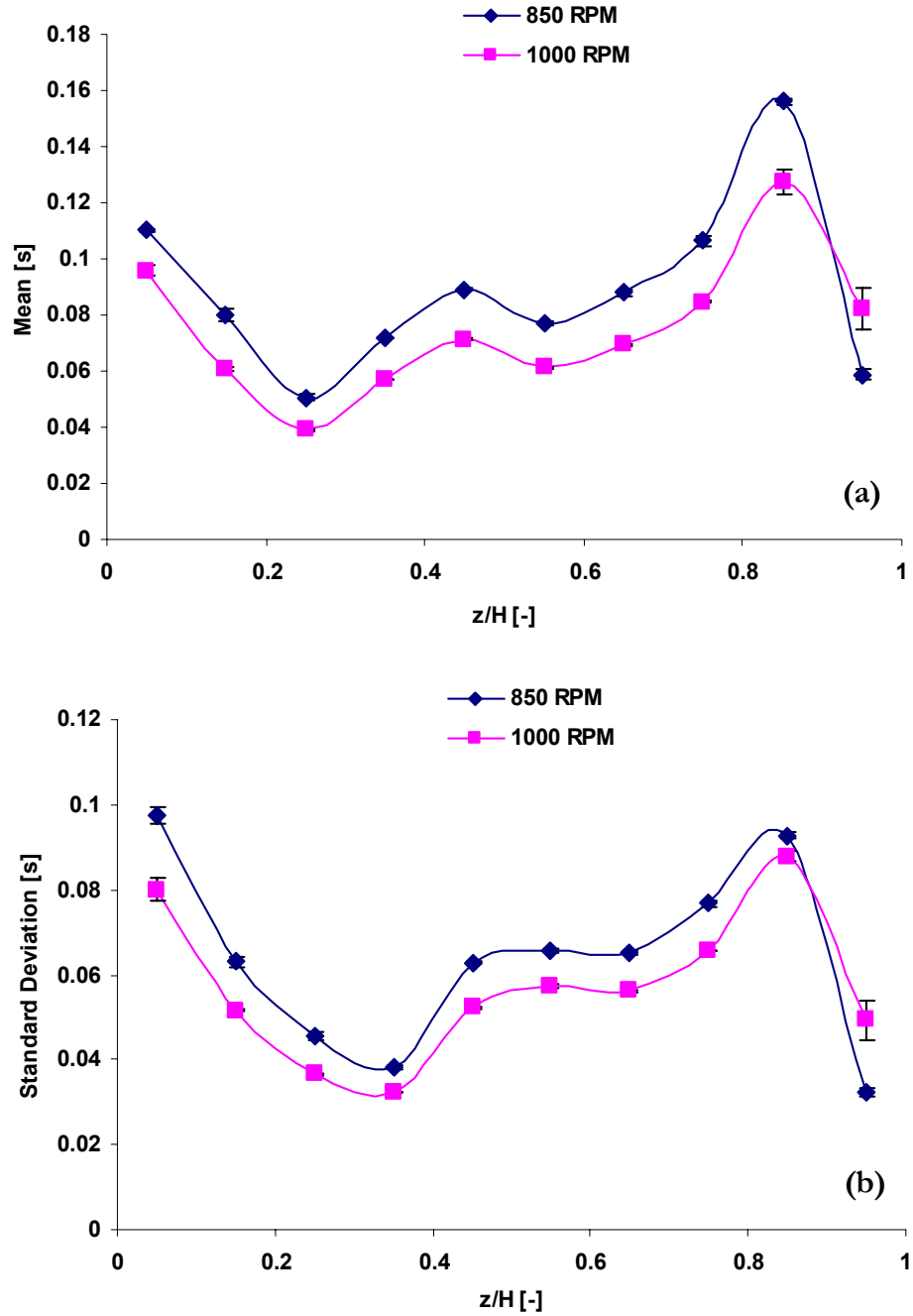


Figure 5.22 Axial variations of (a) mean and (b) standard deviations of solids sojourn time distributions for overall solids holdup of 1% at 850 RPM and 1000 RPM

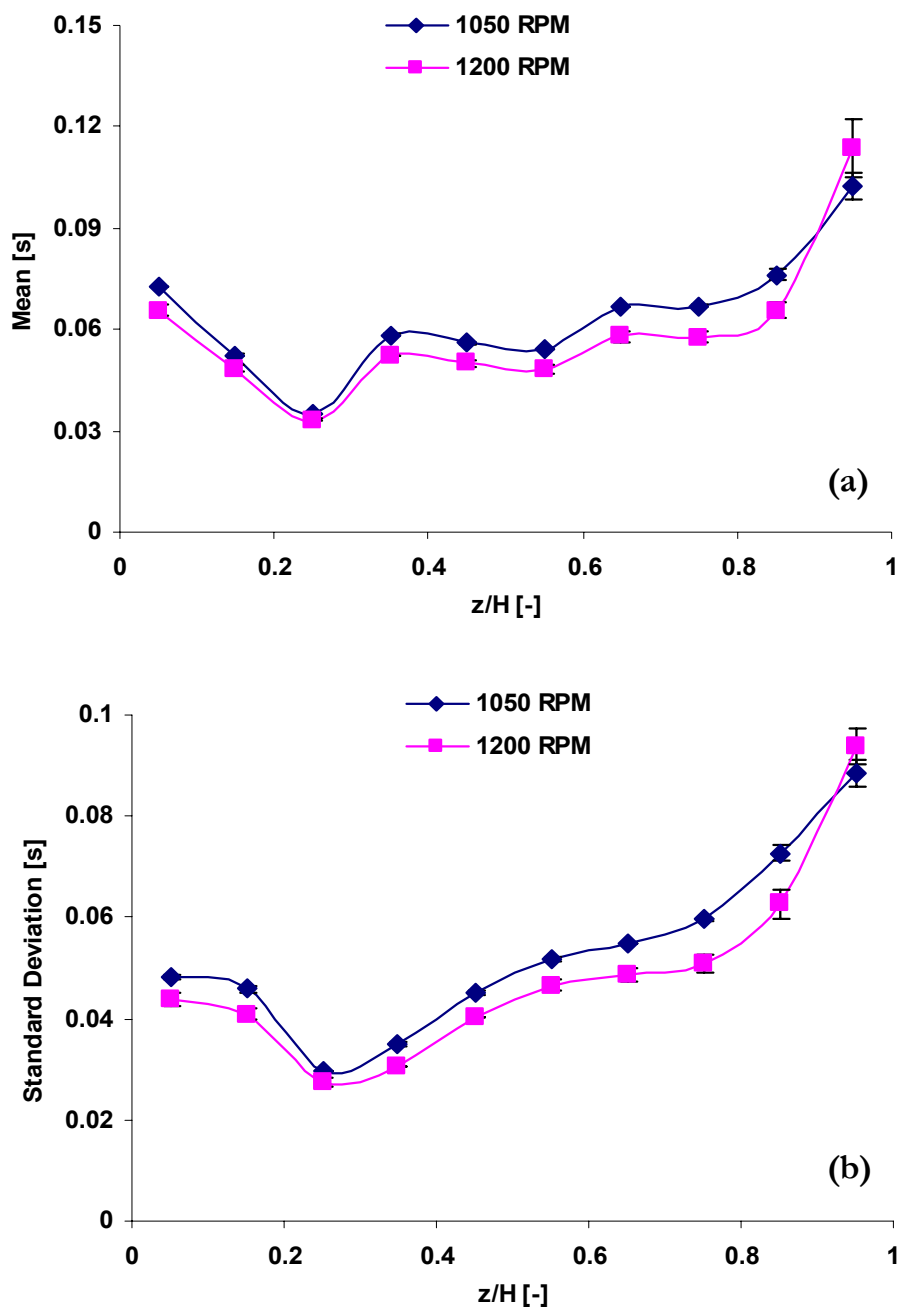


Figure 5.23 Axial variations of (a) mean and (b) standard deviations of solids sojourn time distributions for overall solids holdup of 7% at 1050 RPM and 1200 RPM

Similar trend is observed for the axial variation of the standard deviation as well. The minimum standard deviation in the impeller plane at both impeller speeds clearly suggests that the flow in this axial slice is closest to plug flow with the deviation from plug flow increasing as we move away from this region. This confirms the presence of the radial jet in the impeller zone. In Figures 5.23 (a) and (b), axial variations of the mean and the standard deviation of the STD curves for overall solids holdup of 7% at impeller speeds of 1050 RPM and 1200 RPM are presented, respectively. The mean sojourn times are again larger at lower impeller speed at most axial locations while in the topmost region it is reversed. But unlike for 1% solids holdup, in this case the mean sojourn time does not decrease drastically at the top. In fact, the mean sojourn time keeps increasing with height which seems to suggest that solids suspension to the top of the tank is achieved at both impeller speeds but the tendency of the solids to settle down is larger at lower speed, which then decreases the mean sojourn time at 1050 RPM compared to that at 1200 RPM. The standard deviation has the same trend as the mean and the minimum is observed at the impeller plane as discussed before.

The mean solids sojourn time at the bottom of the tank (0 to 2 cm) can provide further insight into the “just suspension” condition for the solids in the reactor. The conditions used for the current experimental study is chosen based on the prediction of the “just suspension” speed using the Zwietering’s correlation, which defines the condition of just suspension as the speed at which no particle settles at the tank bottom for more than one second. Impeller speeds above and below this predicted suspension speed are used here. The mean solids sojourn time at the bottom of the tank obtained from the CARPT data can be used to confirm the just suspension condition based on Zwietering’s one second rule, because of the fact that this time represents the mean time a solid particle spends at the bottom of the tank. It can be seen that the mean sojourn times at the tank bottom is way below one second for all the experimental conditions studied in this work, suggesting that “just suspension” according to Zwietering’s criterion is achieved at the lower impeller speeds as well. This observation confirms the results reported by Brucato and Brucato (1998) which concluded that the Zwietering’s correlation significantly over-predicts the just

suspension speed and practically all particles get suspended at speeds of about 80% of that predicted by the correlation.

5.6. Summary

An extensive quantification of the solids flow dynamics in solid-liquid stirred tank with dense suspensions is obtained using the Computer Automated Radioactive Tracking (CARPT). CARPT is a completely non-intrusive technique for the investigation of dense multiphase flows and provides Lagrangian description of the flow being studied. Such information is extremely valuable to gain fundamental insights into the hydrodynamics of the system, and also for the assessment and validation of the available CFD models. Various Eulerian measures of the flow in terms of ensemble-averaged solids velocity components and solids turbulent kinetic energy are calculated from the Lagrangian information obtained from the CARPT experiments. The solids hydrodynamics at high solids loading show significant difference compared to those observed at low solids loading in the existing literature studies indicating the importance of solid-solid interactions in dense slurry flows. The dimensionless profiles of each of the ensemble-averaged quantities calculated follow similar trends at different solids loadings and different impeller speeds at which measurements are carried out in the current work. The solids sojourn time distributions in various axial regions in the reactor are calculated from the CARPT data, and the mean and standard deviations of the distributions are computed. The mean sojourn time at the bottom of the reactor at the conditions of the experiments clearly indicate that incipient solids suspension based on Zwietering's "one second" rule is achieved even at the lower impeller speeds. This is in line with the study published by Brucato and Brucato (1998) which concludes that Zwietering's correlation leads to over-prediction of solids "just suspension" speed. Reduction of the operating impeller speed necessary for solids suspension can lead to significant energy savings for large scale industrial processes.

Chapter 6

Solids Distribution in a Solid-Liquid Stirred Tank

The performance of a multiphase reactor is not only governed by the hydrodynamics, but also depends on the distribution of the phases in the reactor. The presence of the dispersed phase in all regions within the vessel is important for the reaction to take place over the whole reactor and hence, utilize the entire reaction volume that is designed for it. As mentioned in Chapter 2, some attempts can be found in the open literature regarding the solids phase distribution in a solid-liquid stirred tank (Yamazaki et al., 1986; Barresi and Baldi, 1987; Shamlou and Koutsakos, 1989; Godfrey and Zhu, 1994; Spidla et al., 2005). But most of these investigations are limited to the axial variations of the solids concentration in the reactor, thereby ignoring the radial gradients that might actually prevail in the reactor (Shamlou and Koutsakos, 1989; Godfrey and Zhu, 1994) unless the system is homogeneously mixed. It is also worth mentioning that these studies are often carried out using intrusive techniques like the optical-fiber probe (Yamazaki et al., 1986), conductivity probe (Spidla et al., 2005) or by drawing samples from the reactor (Barresi and Baldi, 1987), or are performed through optical measurement techniques (Shamlou and Koutsakos, 1989; Godfrey and Zhu, 1994). The intrusive techniques have the inherent disadvantage of the probe itself having some effect on the flow dynamics and solids suspension, while the optical techniques suffer from the limitation that they cannot be applied to dense 'opaque' systems.

Considering the limitations of the available techniques, the gamma-ray Computed Tomography (CT) can be effectively used to measure the solids distribution in a solid-

liquid stirred tank. The CT technique (Chaouki et al., 1997) is completely non-intrusive and can be used for dense systems as well. Both the radial and axial solids distribution can be obtained and quantified using this technique. The scanner consists of an array of collimated NaI detectors and a gamma ray source (Cs-137). The total attenuation of the intensity of a beam of gamma ray as it passes through the system is given by the Beer-Lambert's law, and the density distribution in the cross section can be reconstructed from the measurements that are made along a number of beam paths across the reactor using a suitable reconstruction algorithm. The gamma-ray Computed Tomography (CT) has been applied to numerous reactor systems in order to gain insight into the phase distributions in those reactors and also to provide useful data for the verification of available CFD models. Some of the reactors that have been investigated include a gas-solid riser (Bhusarapu et al., 2006), liquid-solid riser (Roy et al., 2005), trickle bed (Boyer et al., 2005), liquid-solid fluidized bed (Limtrakul et al., 2005), packed/ebullated bed (Chen et al., 2001), bubble column (Kemoun et al., 2001; Shaikh and Al-Dahhan, 2005), trayed bubble column (Kemoun et al., 2001), monolith reactor (Roy and Al-Dahhan, 2005; Bauer et al., 2005) and gas-liquid stirred tank (Rammohan, 2002).

6.1. The Stirred Vessel

The stirred vessel used to carry out the experiments in this study is a cylindrical, flat-bottomed tank with same dimensions as the one used for the CARPT experiments. The detail of the geometry is described in section 5.1. The schematic of the vessel geometry is presented in Figure 5.1.

6.2. CT Setup

The single source CT setup used for this work consist of an array of seven NaI detectors and a 100 mCi Cs-137 gamma-ray source, as shown in the photograph in Figure 6.1. The plate containing the detectors and the sealed radioactive source can be rotated around the



Figure 6.1 Photograph of CT experimental setup with stirred tank

axis of the column by a stepping motor. The axial levels of the tank to be scanned can be reached by moving the entire assembly in the axial direction. A fan beam of 40° is provided by the source collimator and gets further collimated with a central slit of $5 \times 5 \text{ mm}^2$ placed in front of each detector, resulting in a set of beams along which radiation travels and get attenuated. This is known as a projection. The movement of the collimators along with the detectors is controlled using another stepping motor which, together with the rotation of the gamma-ray source, provide 17,500 projections in a typical CT experiment. In this work, the distribution of phase holdup is then reconstructed by dividing the scanned cross-section into 80×80 pixels and applying the estimation-maximization (E-M) algorithm (Kumar, 1994) for the counts received during the 17,500 projections.

6.3. CT Technique

The CT technique (Chaouki et al., 1997) provides the distribution of solids at different axial cross-sections of the reactor. As mentioned previously, the scanner consists of an array of collimated NaI detectors and a gamma ray source (Cs-137). The total attenuation of the intensity of a beam of gamma ray as it passes through the system is given by the Beer-Lambert's law, which essentially is equal to the integral sum of the attenuation through the system along the beam path. This can be written as

$$-\ln\left(\frac{I}{I_0}\right) = \sum_l (\rho\mu)_{eff,ij} l_{ij} \quad (6.1)$$

$(\rho\mu)_{eff,ij}$ is the effective volumetric attenuation coefficient in the pixel ij along the path l . The effective volumetric attenuation coefficient in pixel ij depends on the local phase distribution, which, for k phases in the system, is given by

$$(\rho\mu)_{eff,ij} = \sum_k (\rho\mu)_{k,ij} \varepsilon_{k,ij} \quad (6.2)$$

$(\rho\mu)_{k,ij}$ is the volumetric attenuation coefficient of the phase k , and $\varepsilon_{k,ij}$ is the holdup of phase k in pixel ij .

In the CT experiments, attenuations are measured along a number of such beam paths through the system from different directions around it. Given a set of attenuation measurements, the density distribution is reconstructed using the estimation-maximization (E-M) algorithm (Kumar, 1994). The solids hold-up distribution can then be azimuthally averaged to obtain the azimuthally-averaged radial profile for the hold-up at the axial location scanned. For the solid-liquid system considered in this work, equation (6.2) for pixel ij can be re-written as

$$(\rho\mu)_{LS,ij} = (\rho\mu)_{S,ij} \varepsilon_{S,ij} + (\rho\mu)_{L,ij} \varepsilon_{L,ij} \quad (6.3)$$

To determine the solids holdup $\varepsilon_{S,ij}$ in each pixel, the following cross-sectional scans and measurements need to be carried out for the estimation of the other parameters involved:

- Scan of the tank filled with water to estimate $(\rho\mu)_{L,ij}$.

- Scan of the tank filled with solids (solids-gas) and scan of the empty tank (gas) to estimate $(\rho\mu)_{s,ij}$. This also requires the measurement of the maximum solids holdup (packing fraction), ε_{s0} , when the entire cross-section is packed with the solid.

6.4. Experimental Conditions

The experimental conditions are the same as that of the CARPT experiments which were summarized in Table 5.1. At each of the conditions shown, scans are performed at three axial locations in the reactor given by $z/H = 0.075$ (close to the bottom), $z/H = 0.25$ (just below the impeller) and $z/H = 0.65$ (midway between the impeller and the top free surface). All scans are performed in duplicate to quantify the reproducibility of the measurements obtained by computing the error (standard deviation) in the experimental data.

6.5. Results and Discussions

The solids holdup distributions across the cross-section of the tank at $z/H = 0.075$ are shown qualitatively in Figures 6.2 (a) and (b) for two representative conditions from the scans taken. The bottom plane is chosen since it is expected to have significantly higher solids loading compared to other parts of the tank. Figure 6.2 (a) is for overall solids holdup of 1% at 850 RPM, while 6.2 (b) is for 7% solids holdup at 1200 RPM. Two of the four baffles can be clearly seen (around pixel number 40 in x and y directions) while the other two are not captured in both the scans. Large accumulation of solids is typically observed near the impeller shaft at the center of the tank. Upon careful observation of these solids distribution contour plots, a circular domain between the impeller and the tank wall can be seen where solids are almost absent. This is clearer in Figure 6.2 (b) where the overall solids holdup is larger, but is visible in Figure 6.2 (a) as well. Most of the solids are contained within the region between this circular ring and the impeller, while the presence of solids is scant outside the region.

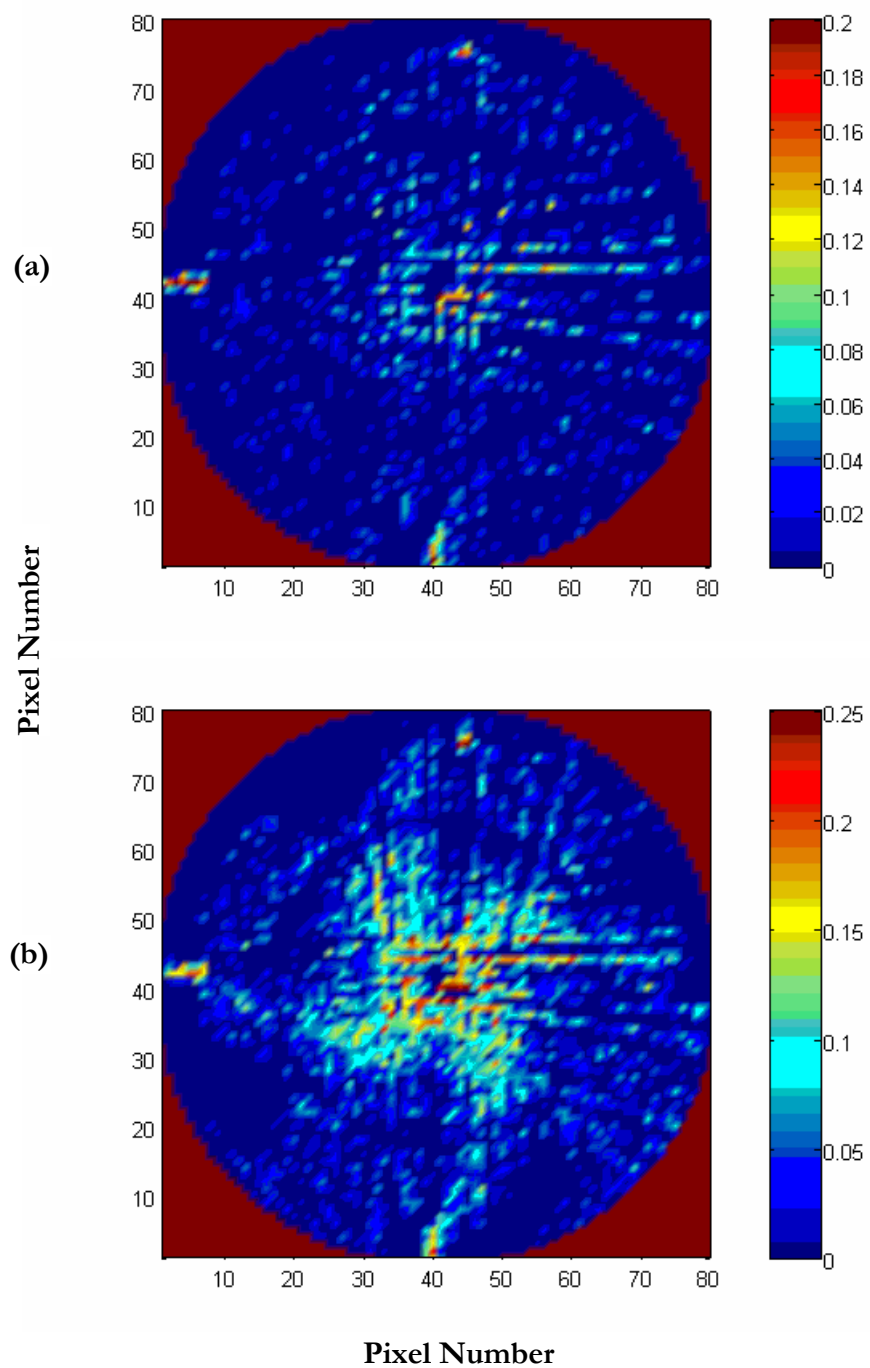


Figure 6.2 Contour plots of solids holdup distribution for (a) 1% solids 850 RPM and (b) 7% solids 1200 RPM

The azimuthally averaged radial profiles of the solids hold-up at the three axial locations mentioned in the preceding section is presented in Figures 6.3 (a) and (b) for the two different impeller speeds at overall solids holdup of 1%. The radial location in this plot and also in subsequent figures is non-dimensionalized with the tank radius, R . The region near the impeller shaft is characterized by high solids holdup at both the impeller speeds as observed qualitatively in Figure 6.2. The solids hold-ups at the bottom and middle planes are higher compared to the top planes showing the presence of solids mostly below the impeller even at the higher impeller speed. The circular ring observed in the contour plots where solids are almost absent results in the dip in the solids holdup around $r/R = 0.6$. The data obtained, however, is marked by significantly large error bars at some of the radial locations. Similar plots for overall solids holdup of 7% are presented in Figures 6.4 (a) and (b) for the two impeller speeds at which scans were performed. The qualitative features remain similar to those discussed for the lower loading, but reduction in the error bars and hence, improvement in the reproducibility of the data can be observed.

Two more observations regarding the obtained data need careful consideration. The first one is the anomalous behavior displayed by the top scan data ($z/H = 0.65$) at the lower solids holdup of 1%. The radial profiles for the solids holdup obtained at the two impeller speeds for that condition are compared in Figure 6.5. The data indicates that the solids hold-ups at the top surface are larger at 850 RPM compared to those at 1000 RPM, thereby showing a better solid suspension at the lower impeller speed. This is unrealistic since the higher power input and the larger characteristic velocity (impeller tip speed) at the higher impeller speed should provide improved solids suspension. Such an anomaly is, however, not observed for the overall solids hold-up of 7% for which case the top scans at the two impeller speeds are compared in Figure 6.6.

The other feature observed in the data is the absence of large solids holdups in regions close to the tank wall in most of the cases. The presence of solids near the wall is expected by virtue of the characteristic flow pattern obtained with a radial flow impeller, where the

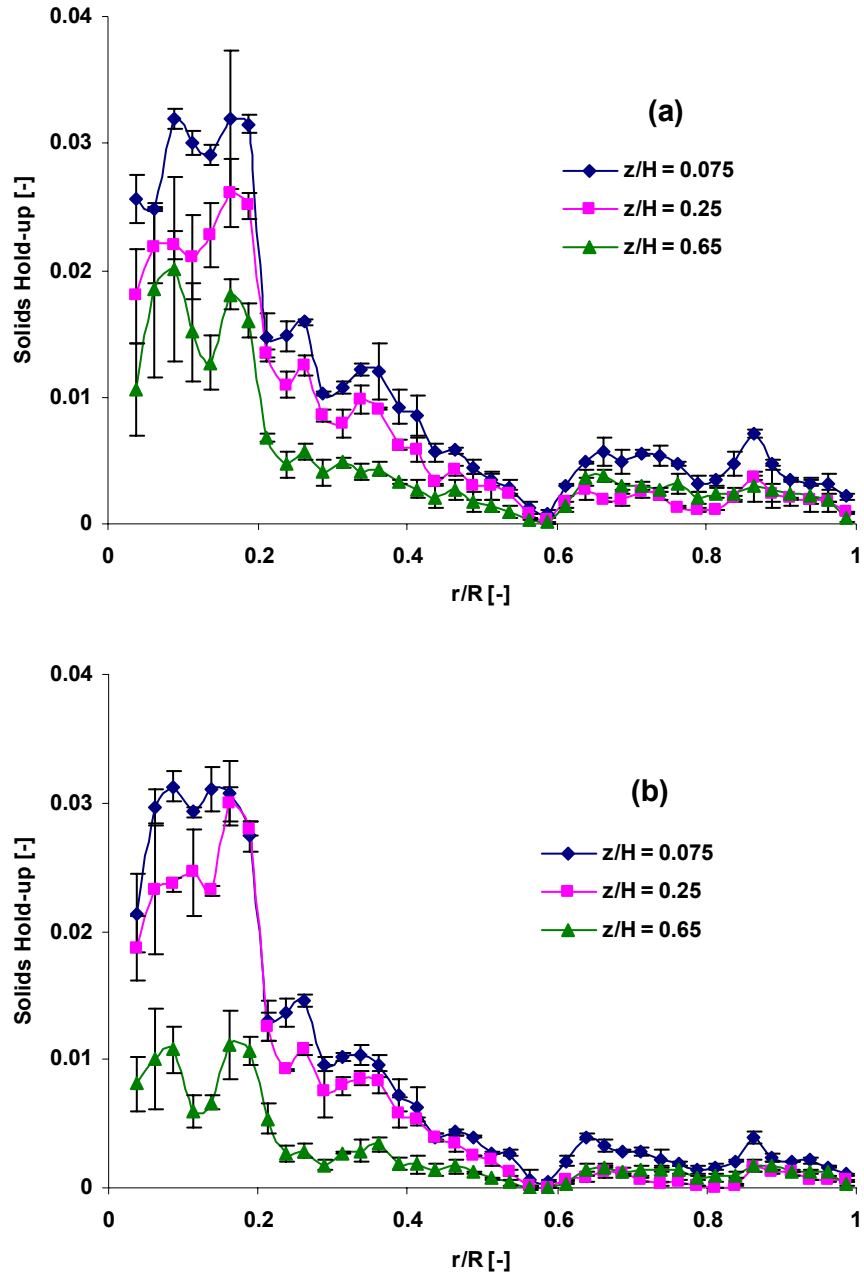


Figure 6.3 Radial profiles of solids holdup at different axial locations for overall solids holdup of 1% at (a) 850 RPM and (b) 1000 RPM

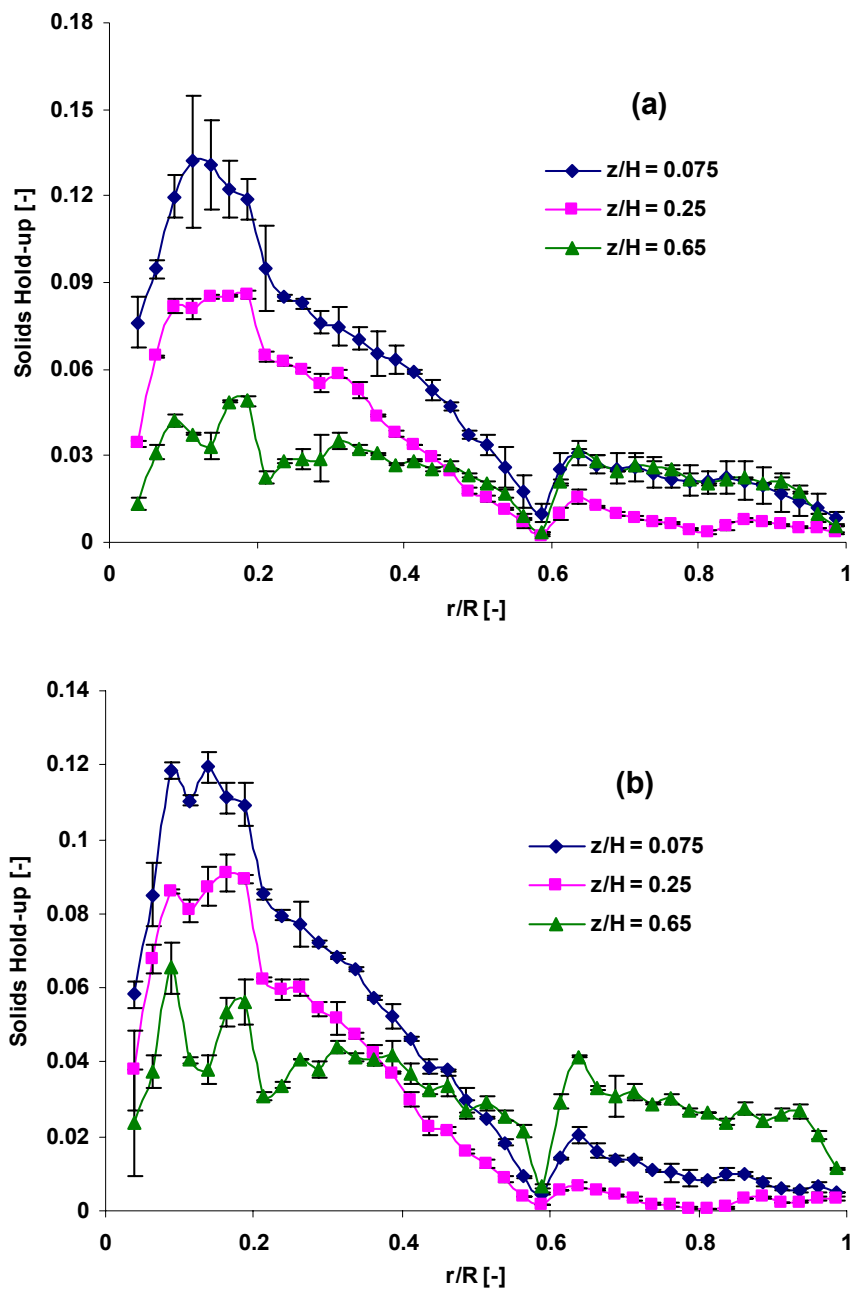


Figure 6.4 Radial profiles of solids holdup at different axial locations for overall solids holdup of 7% at (a) 1050 RPM and (b) 1200 RPM

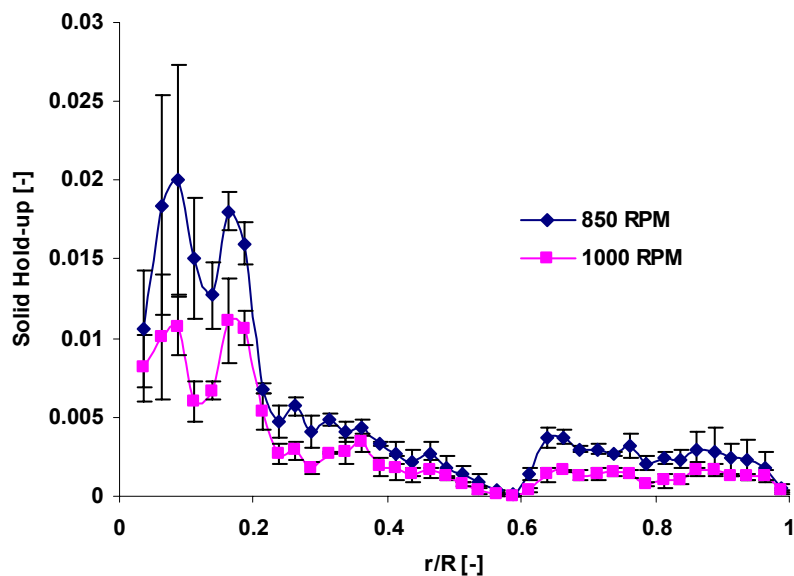


Figure 6.5 Comparison of solids distribution at $z/H = 0.65$ at different impeller speeds for overall solids holdup of 1%

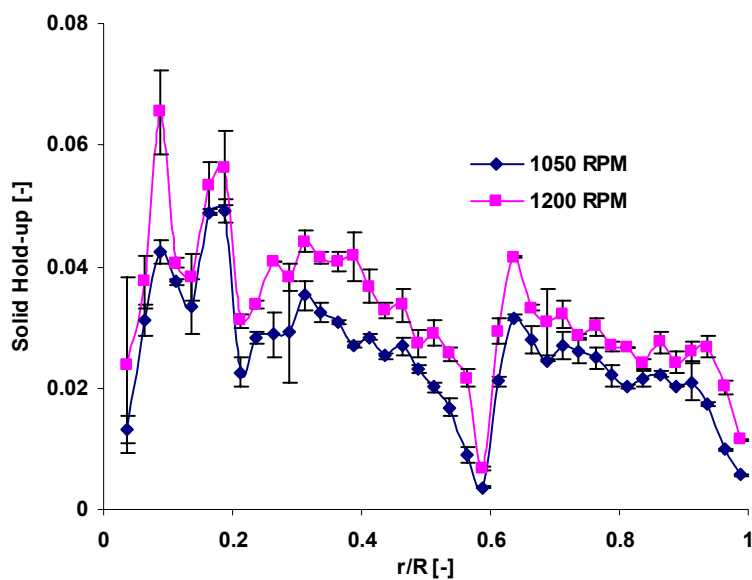


Figure 6.6 Comparison of solids distribution at $z/H = 0.65$ at different impeller speeds for overall solids holdup of 7%

solids flow down near the wall and move up near the center below the impeller and vice versa above the impeller. Both the regions close to the impeller shaft and the tank wall should be characterized by large solids holdup. While the large solids holdups near the impeller shaft can be observed in the results currently obtained, presence of solids near the wall is not captured. Hence, more analysis of the data obtained needs to be carried out before using it for the evaluation of CFD models confidently.

6.5.1. Solids Mass Balance

The most fundamental test for the data is to check if the solids mass balance in the tank is satisfied. To perform the mass balance, the solids holdup (ε_s) in the entire tank is generated from the three scans obtained experimentally by CT. The data interpolation is carried out using the *CSIEZ* routine available in the IMSL libraries. The mass of solids present in the tank (m_{cal}) can be estimated from the holdups obtained by the interpolation technique, which is then given by

$$m_{cal} = \rho_s \int_0^H \int_0^R 2\pi r dr dz \varepsilon_s \quad (6.4)$$

where ρ_s is the density of the solids used in the experiment. As the actual mass of solids being charged to the tank for the experiments is known (m_{ex}), the solids mass balance error can be defined as the ratio of the absolute difference between the mass of solids charged and the mass of solids estimated to the mass of solids charged, which can be written as

$$\% \text{ Solids Mass Balance Error} = \frac{|m_{ex} - m_{cal}|}{m_{ex}} \times 100 \quad (6.5)$$

Also, a similar exercise is performed using the CFD simulation data obtained at the same three axial levels as the experiments. Since solids mass balance is conserved while the CFD simulations are carried out, this provides an estimation of the error caused due to the interpolation. The results are summarized in Table 6.1, which shows that the interpolation error is about 10% for both the solids loading at which experiments are done. On the other

hand, the CT data led to errors of 60-70% at all the experimental conditions. It should be noted that the maximum error of 73% is obtained for the overall solids holdup of 1% at 1000 RPM, at which condition the anomaly discussed earlier can be observed.

Table 6.1 Percentage solids mass balance errors

Experimental Conditions	CFD (Test)	CT Data
1% - 850 RPM		58%
1% - 1000 RPM	9%	73%
7% - 1050 RPM		59%
7% - 1200 RPM	10%	56%

6.5.2. Probable Causes of Failure

At this point, it cannot be stated with certainty what led to the significant errors in the data obtained with CT, but certain speculations can be made that might have contributed to the failure in capturing the solids distribution in the tank. The E-M algorithm used for the reconstruction essentially calculates the effective volumetric attenuation coefficient $(\rho\mu)_{eff}$ in each pixel within the domain using the measured attenuation data obtained along various chord lengths through the tank during the experiment. The phase holdup in each pixel can be then calculated using the volumetric attenuation coefficient of each the phases as shown in equation (6.3). The volumetric gamma attenuation coefficient for water is 0.086 cm^{-1} , while that for glass is 0.193 cm^{-1} as obtained from the NIST database. The magnitudes of the volumetric attenuation coefficients for the two phases can be considered to be reasonably close in view of the fact that for standard air-water system almost three orders of magnitude difference in this quantity exists. This might have caused significant error in distinguishing between the solids and liquid phases particularly at low solids holdup. Also, it should be mentioned that low gamma counts were observed for many of the projections when the current experiments were carried out, which clearly implies the low signal to noise ratio for the data obtained.

To have a better understanding of the causes of failure, a numerical simulation is carried out to investigate if the close values of the volumetric attenuation coefficients caused the large errors observed. The gamma counts data are simulated following the methodology described in detail by Varma et al. (2007), such that they are Poisson random numbers with mean equal to the variance. A synthetic phantom having four square blocks of 20×20 pixels is used to generate the transmission data. Each of the four blocks is characterized by a different solids holdup with all the pixels within a given block having the same holdup. The rest of the domain is occupied by water having zero solids holdup. The four solids holdups used are 1%, 4%, 7% and 10%. The solids holdup distribution in the phantom is then reconstructed using the simulated transmission data, and the comparison between the actual and simulated phase distribution contours are presented in Figure 6.7 (a) and (b) respectively. The domain with 1% solids holdup is not clearly visible and is almost masked with the surrounding water. This clearly show that holdups lower than 1%, which can occur locally when the overall solids holdup is 1%, will never be observed in the scans and will be marked as water. However, regions with higher solids holdup of 4 to 10% are captured in the simulation, and qualitatively the image seems to have improved as the solids holdup increases.

The errors in each of the four blocks in the domain are then quantified by calculating the mean holdup, standard deviation from the true holdup value, average error and the dimensionless standard deviation in each block. These quantities are computed as follows:

$$\text{Mean holdup: } \bar{\varepsilon}_s = \frac{1}{N_{pix}} \sum_{i=1}^{N_{pix}} \varepsilon_s(i) \quad (6.6)$$

$$\text{Standard Deviation: } \sigma_s = \sqrt{\frac{1}{(N_{pix} - 1)} \sum_{i=1}^{N_{pix}} [\varepsilon_s(i) - \varepsilon_{true}]^2} \quad (6.7)$$

$$\text{Average Error: } \mu_{err} = \frac{1}{N_{pix}} \sum_{i=1}^{N_{pix}} |\varepsilon_s(i) - \varepsilon_{true}| \quad (6.8)$$

$$\text{Dimensionless Standard Deviation: } \bar{\sigma} = \frac{\sigma_s}{\varepsilon_{true}} \quad (6.9)$$

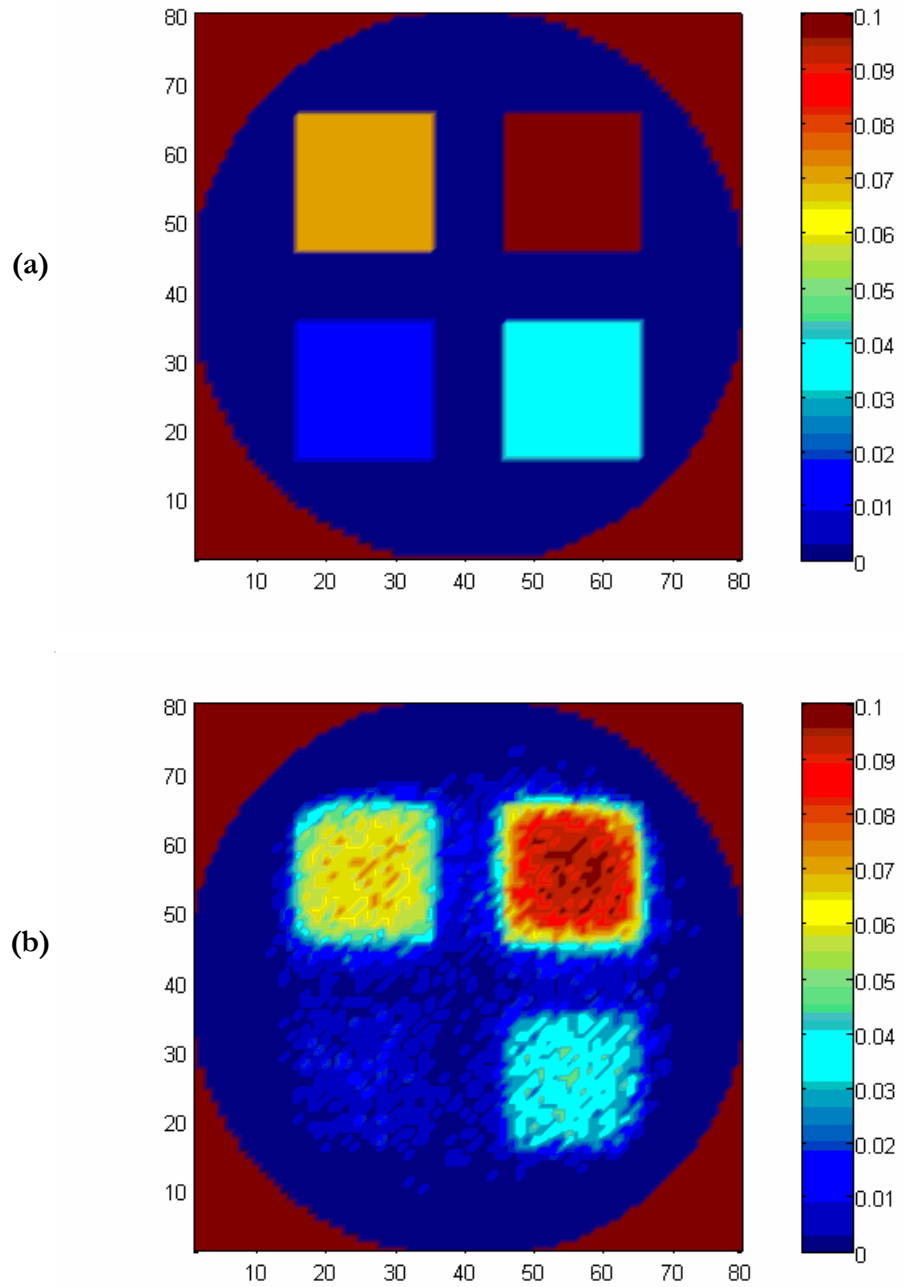


Figure 6.7 Solids holdup distribution in the phantom (a) actual and (b) simulated

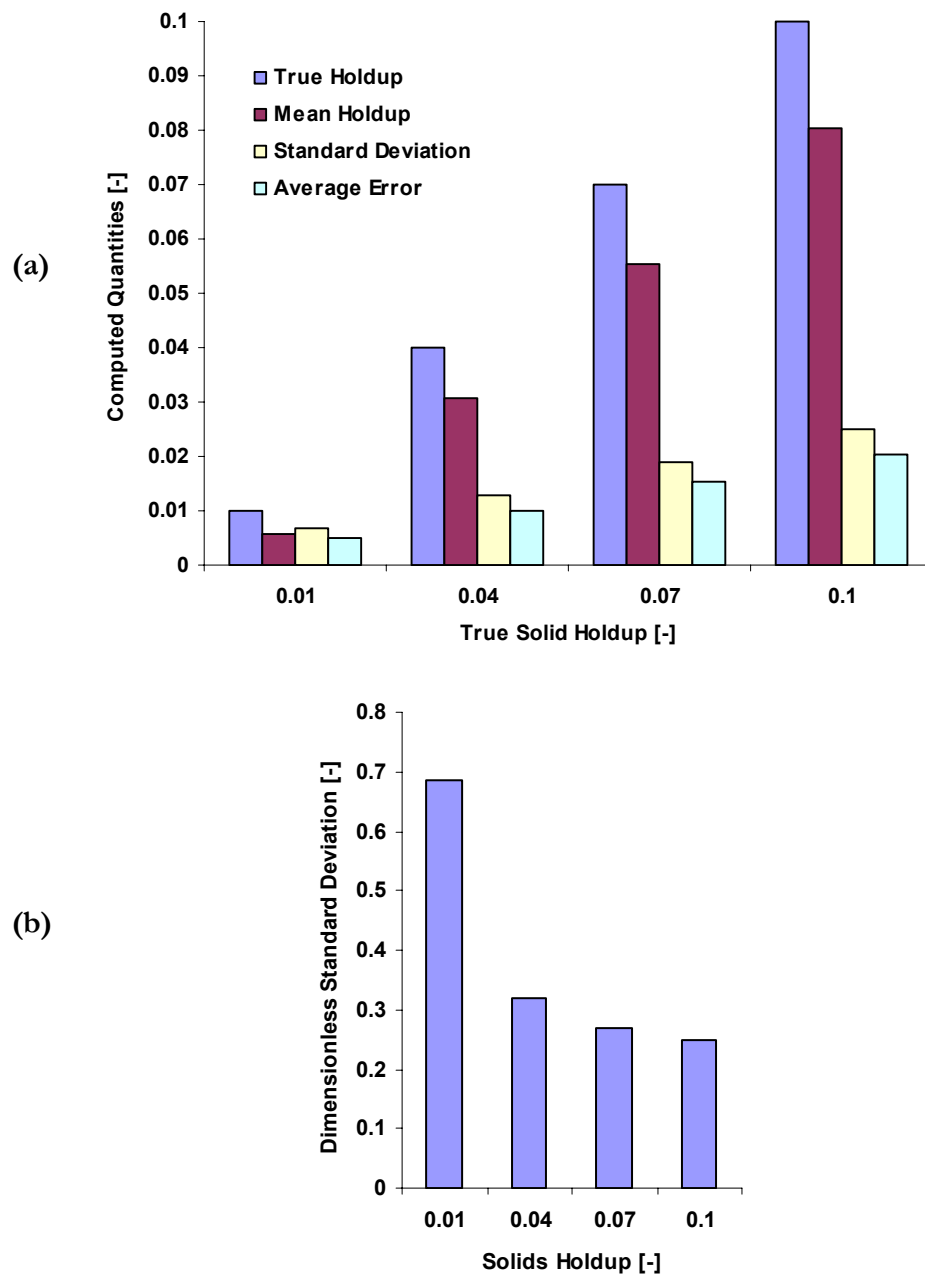


Figure 6.8 Quantification of error in the phantom study (a) mean holdup, standard deviation and average error, and (b) dimensionless standard deviation

N_{pix} is the number of pixels in a given block for which all the above quantities are computed, $\varepsilon_s(i)$ is the simulated solids holdup for the i -th pixel in the block and ε_{true} is the true value of solids holdup for that block in the phantom.

Figure 6.8 (a) shows comparison between the mean holdup, standard deviation and average error for the four solids holdup of 1%, 4%, 7% and 10%. Bars representing the true holdup values are also included on the plot to compare the computed mean holdup with the true value. Although the zones with higher solids holdups seem to be captured better qualitatively (Figure 6.7), quantitatively both the standard deviation and the average error increases as the solids holdup increases. However, the dimensionless standard deviation decreases as the solids holdup increases as observed in Figure 6.8 (b). Therefore, it seems likely that for the range of solids holdup studied in this work, the phases are not distinguished clearly at low solids holdups while the results are associated with increased errors at higher solids holdups.

6.6. Summary

The gamma-ray computed tomography (CT) technique is used in this work to obtain the solids distribution at different axial locations in a solid-liquid stirred tank. The experimental conditions are the same as those at which CARPT experiments are performed, so that complete characterization of the system at these conditions in terms of hydrodynamics and phase distribution are obtained. The evaluation of CFD models can then be performed for the predictability of the solids flow field as well as the solids distribution in the tank.

The data obtained using CT, however, shows an anomaly for overall solids holdup of 1% where improved solids suspension is observed at 850 RPM compared to that at 1000 RPM. Such an anomaly is not observed for the overall solids holdup of 7%. Also, the current data do not show the presence of solids close to the tank wall, although the high solids concentration near the impeller shaft is captured. Higher solids holdup near the wall is

expected because of the characteristic flow pattern with a radial flow impeller in a stirred vessel. To evaluate the data further, a solids mass balance in the tank is carried out by interpolating the solids holdup in the entire tank based on the experimental data at the three axial levels obtained using CT. The interpolation error is quantified by performing the same exercise using CFD data at the three axial levels. Although the interpolation error is of the order of 10%, a mass balance error of about 60-70% is observed with the current CT data at all the experimental conditions. A numerical investigation for the causes of error has been done with a synthetic phantom having solids holdup in the range 1% to 10%, which suggests that solids are not distinguished clearly from water at low solids holdup (1% or less) while the reconstruction result is associated with increased errors as the solids holdup increases. Hence, knowing the shortcoming of the current CT data, these solids distribution results will not be used for the assessment of CFD models in this work.

Chapter 7

Evaluation of CFD Models for Solid-Liquid Stirred Tank

The improvement of computational capabilities has led to the development and usage of computational fluid dynamics (CFD) based models to gain insight into complex multiphase flows in chemical reactors. The popularity of this approach is primarily due to the possibility that it can lead to large savings in experimentation time and cost. Also, assuming that computation cost is not going to be an issue in the future, such models can be used for the design, optimization and scale-up of industrial reactors. However, these models can be really useful only when their predictability in capturing the flow behavior is ascertained through extensive comparison with reliable experimental data. Therefore, using the model predictions for multiphase flows for design and scale-up without the necessary evaluation and assessment can be disastrous.

As discussed previously in Chapter 2, most of the CFD effort for solid-liquid stirred tanks that are available in the open literature are either devoted to the improved prediction of axial solid concentration profiles only (Micale et al., 2000; Barrue et al., 2001; Altway et al., 2001; Montante and Magelli, 2005; Spidla et al., 2005; Khopkar et al., 2006), or are focused on the prediction of particle suspension height in a stirred vessel (Micale et al., 2004). The predictions for the solids flow dynamics have not been evaluated yet because of the dearth of experimental data, and the Computer Automated Radioactive Particle Tracking (CARPT) experimental studies can be efficiently used for this purpose.

The objective of this chapter is to assess the quality of predictions obtained from numerical simulations of a complex, turbulent solid-liquid flow in a stirred tank by comparing model predictions with results from the CARPT experiment. The focus here is on the dynamic behavior of the dispersed solids phase in terms of solids velocities, turbulent kinetic energy and solids sojourn times in various parts of the tank. The Euler-Euler model available commercially in Fluent 6.2 and the large eddy simulation (LES) developed by Prof. Derksen (Derksen, 2003) at the University of Delft in Netherlands are evaluated in the current work for a solid suspension having overall solids volume fraction of 1% (v/v).

7.1. Tank Geometry and Simulation Condition

The geometry used to carry out the simulations is a cylindrical, flat-bottomed tank having the same dimensions as the one used for the CARPT experiments. The diameter of the tank is 0.2 m , and the liquid height in the tank is equal to the diameter of the tank. The impeller used is a six-bladed Rushton turbine having diameter equal to one-third of the tank diameter. The distance of the impeller disc from the bottom of the tank is also one-third of the tank diameter. The tank has four baffles mounted on the walls. Further detail of the dimensions is provided in section 5.1 and the schematic of the vessel geometry is presented in Figure 5.1.

The large eddy simulation and the Euler-Euler model simulation are performed for overall solids loading of 2.5% w/w (1% v/v). The rotational speed of the impeller is 1000 RPM resulting in a Reynolds number ($\text{Re} = \frac{N_{imp} D^2}{\nu}$) of about 74,000. The liquid phase is water and the solids phase is glass beads having a mean diameter of 0.3mm. At 2.5% solids loading, the just-suspension speed predicted by Zwietering's criterion (1958) is about 900 RPM for a Rushton turbine impeller.

7.2. Euler-Euler Model

In the Euler-Euler approach each phase is assumed to coexist at every point in space in the form of interpenetrating continua. The continuity and momentum equations are solved for all the phases present and the coupling between the phases is obtained through pressure and interphase exchange coefficients. For each phase q , the conservation equation is written as a function of the volume fraction of the phase α_q . The continuity equation for phase q without mass transfer between phases is written as

$$\frac{\partial}{\partial t}(\alpha_q \rho_q) + \nabla \cdot (\alpha_q \rho_q \vec{u}_q - \rho_q D_t \nabla \alpha_q) = 0 \quad (7.1)$$

\vec{u}_q is the velocity of phase q .

The momentum balances for the liquid and solid phases are given by equations (7.2) and (7.3) respectively as

$$\frac{\partial}{\partial t}(\alpha_l \rho_l \vec{u}_l) + \nabla \cdot (\alpha_l \rho_l \vec{u}_l \vec{u}_l) = -\alpha_l \nabla p + \nabla \cdot \overline{\overline{\tau}}_l + \alpha_l \rho_l \vec{g} + K_{sl}(\vec{u}_s - \vec{u}_l) + \vec{F}_{lift} \quad (7.2)$$

$$\frac{\partial}{\partial t}(\alpha_s \rho_s \vec{u}_s) + \nabla \cdot (\alpha_s \rho_s \vec{u}_s \vec{u}_s) = -\alpha_s \nabla p - \nabla p_s + \nabla \cdot \overline{\overline{\tau}}_s + \alpha_s \rho_s \vec{g} + K_{sl}(\vec{u}_l - \vec{u}_s) - \vec{F}_{lift} \quad (7.3)$$

The turbulent dispersion of the secondary phase (solids) is accounted in equation 7.1 through the turbulent diffusivity D_r . The default value of 0.75 in Fluent for the dispersion Prandtl number is used in this work to compute the turbulent diffusivity. K_{sl} is the momentum exchange coefficient to account for the interphase drag, while \vec{F}_{lift} accounts for the lift force between the liquid and the solid phases. The term p_s in equation (7.3) represents the solids pressure which accounts for the force due to particle interactions. This term is closed applying the kinetic theory of granular flow and is composed of a kinetic term and a second term due to particle collisions. The solids pressure is a function of the coefficient of restitution for particle collisions, the granular temperature and the radial distribution function which corrects for the probability of collisions between grains when the solids phase becomes dense (Fluent User Manual). The granular temperature is

proportional to the kinetic energy of the fluctuating particle and is obtained by solving the transport equation derived from the kinetic theory. The default values provided for the granular model constants in the Fluent 6.2 framework are used in the present study, more detailed discussion on which can be found in the Fluent User Manual.

The standard $k - \varepsilon$ model with mixture properties is used as the turbulence model. This is based on the observation reported by Montante and Magelli (2005) that the mixture model leads to similar results obtained using a $k - \varepsilon$ model for each phase while requiring significantly lower computation time. The Multiple Reference Frame (MRF) approach is used to model the rotating impeller (Ranade, 2002), where the flow in the impeller region is solved in a rotating framework while the outer region is solved in a stationary framework. This algorithm assumes the flow to be steady and the impeller-baffle interactions are accounted by suitable coupling at the interface between the two regions where the continuity of the absolute velocity is enforced. The MRF boundary is located at $r/R = 0.5$ and is in agreement with the work of Oshinowo et al. (2000), which states that when the impeller diameter is smaller than half of the tank diameter (which happens to be the case here) the optimal radial position of the boundary between the two zones is roughly midway between the impeller blade tip and the inner radius of the baffle.

The interface exchange coefficient to account for the drag force in equations (7.2) and (7.3) involves the drag coefficient C_D and is given by

$$K_{sl} = \frac{3}{4} C_D \frac{\alpha_s \rho_l |\vec{u}_s - \vec{u}_l|}{d_s} \quad (7.4)$$

In this work, the drag coefficient is quantified using the Schiller-Neumann (1933) model, where C_D is obtained as

$$C_D = \begin{cases} 24(1 + 0.15 \text{Re}_s^{0.687}) / \text{Re}_s & \text{Re}_s \leq 1000 \\ 0.44 & \text{Re}_s > 1000 \end{cases} \quad (7.5)$$

Re_s is the relative Reynolds number defined as $\text{Re}_s = \frac{\rho_l d_s |\vec{u}_s - \vec{u}_l|}{\mu_l}$. The lift force has

been shown to have minor influence on the Euler-Euler predictions of solid-liquid flow in a stirred vessel (Ljungqvist and Rasmuson, 2001) and has been eventually neglected by several authors in their simulations (Montante and Magelli, 2005; Spidla et al., 2005; Khopkar et al., 2006). However, it is retained in this work since it is included in the large eddy simulation and is quantified through the lift coefficient C_L , which is kept at the default constant value of 0.5 for the current simulation.

The grid consists of about 589000 cells consisting of hexahedron and tetrahedron elements as shown in Figure 7.1 to simulate the full geometry of the tank. This grid size is chosen based on a recent study by Khopkar et al. (2006) who performed an Euler-Euler simulation in a geometrically similar solid-liquid stirred tank of 0.3m diameter agitated by a Rushton turbine. They used 287875 cells to obtain the grid independent solution for the flow in half of the tank. The grid size used in this work is more than twice of that, which is necessary since simulation is performed for the full tank, and considering that the diameter of the tank in this case is smaller than the one simulated by Khopkar et al. (2006), the grid density here is higher than that used in their work. Also, the recent work of Deglon and Meyer (2006) for single phase flows in stirred vessels concludes that the mean flow is unaffected by the grid resolution while the turbulent kinetic energy is influenced by the grid density used for the simulation. However, the solids turbulent kinetic energies predicted by the Euler-Euler simulation in this work is compared with those predicted by the large eddy simulation which is significantly more fundamentally based and computed with very high grid resolution (240^3 cells or 13.8 million cells). Since differences in the solids kinetic energy predictions by the two models is minimal throughout the solution domain as shown in section 7.4.3, further Euler-Euler simulations with finer grid is not carried out in this work. The Euler-Euler simulation is considered converged when the residuals dropped below 10^{-5} . Also, the overall solids balance is monitored after every iteration to ensure that the solids mass balance is not violated.

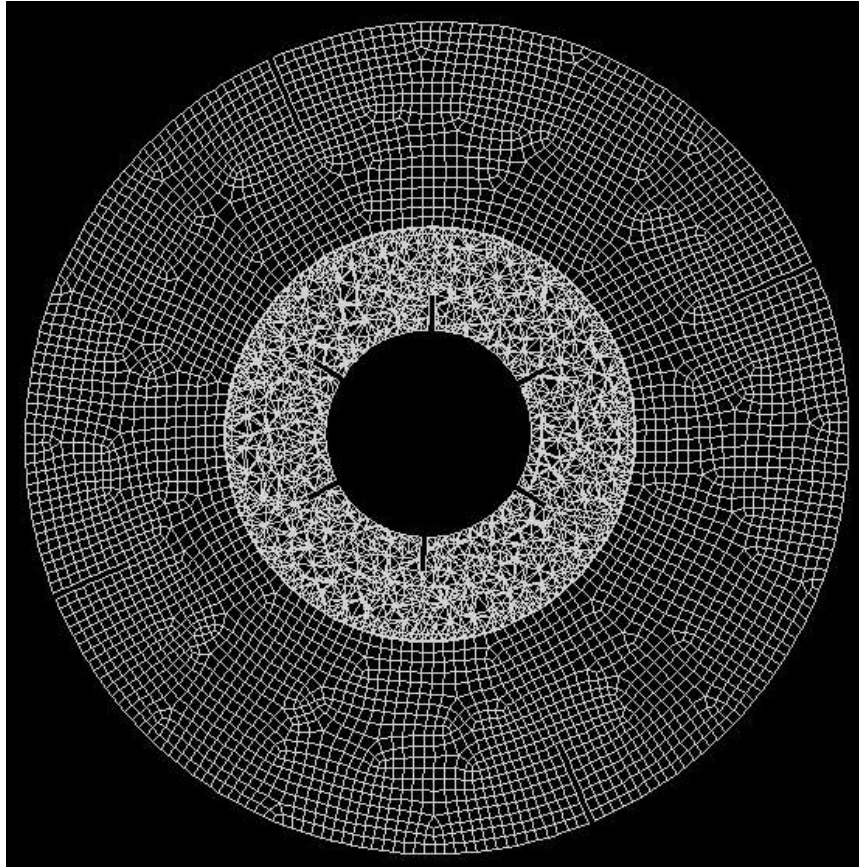


Figure 7.1 Impeller cross-section showing the grid used for the Euler-Euler simulation in Fluent 6.2

7.3. Large Eddy Simulation

The large eddy simulation (LES) is the other model evaluated which is based on an Eulerian-Lagrangian approach. The three-dimensional, unsteady continuous phase flow is solved by means of the lattice-Boltzmann method (Chen and Doolen, 1998) on a uniform, cubic grid. The grid spacing is such that the diameter of the tank T is spanned by 240 cells as shown in Figure 7.2. The total number of cells considered in the LES is 240^3 or 13.8 million cells. The full, three-dimensional geometry of the tank is considered (no

assumptions regarding the flow's symmetry have been made). The impeller moves relative to the fixed grid and the effect of this motion is represented by body forces acting on the fluid. These body forces are adapted dynamically such that at all times the no-slip condition on the impeller surface (shaft, disk, and blades) defined as a collection of closely spaced forcing points not necessarily coinciding with the lattice is satisfied. These forcing points have also been indicated in Figure 7.2. A detailed description of this forcing approach can be found in Derksen and Van den Akker (1999). The Smagorinsky subgrid-scale model (Smagorinsky, 1963) has been used for representing the effect of the unresolved (subgrid) scales on the resolved scales. The Smagorinsky constant C_s was set to 0.1 throughout the flow.

In this flow, spherical solid particles (diameter $d_f = 0.3$ mm) are dispersed. The desired solids volume fraction of 1% requires about 7 million spheres to be inserted to the system. The procedure for setting up and solving the equations of motion of the particles has been elaborately explained in Derksen (2003). The key features are that for each sphere the equations of linear and rotational motion taking into account drag, (net) gravity, lift forces (being able to determine the Magnus force is the main reason for considering rotational motion of the particles), stress-gradient forces, and added mass are solved. To determine the drag force on the particles, the subgrid-scale motion is also considered next to the resolved fluid motion. The unresolved scale motion is estimated by a Gaussian random process with standard deviation $u_{sgs} = \sqrt{2/3 k_{sgs}}$, where the subgrid-scale kinetic energy k_{sgs} is estimated via an equilibrium assumption. A new random velocity is picked after each eddy lifetime to mimic the fluid motion at the unresolved scales. Further detail for the solids particle dynamics can be found in Derksen (2003). As in the Euler-Euler approach a non-linear drag coefficient according to the Schiller-Neumann model is considered.

At the solids volume fractions simulated, particle-particle collisions have great impact on the distribution of solids over the volume of the mixing tank (Derksen, 2003). For this reason, a time-step-driven collision algorithm (Chen et al., 1998) has been implemented. It

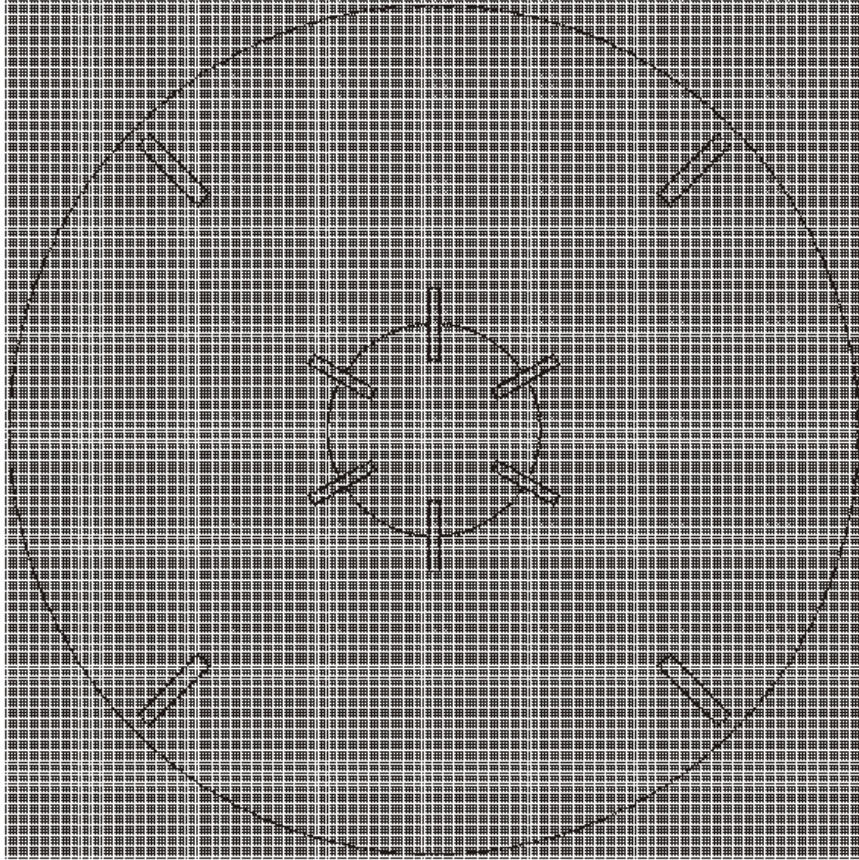


Figure 7.2 Impeller cross-section showing the grid used for the large eddy simulation, and the points defining the impeller and tank wall via the forcing method

keeps track of each individual particle-particle collision in the tank with the restriction (for computational reasons) that one particle can only experience one collision during one time step. Given the small time step that is used (2800 time steps per impeller revolution), and the (tank-averaged) solids volume fraction of 1%, the number of collisions that are missed as a result of this restriction is very limited (Derksen, 2003). All the collisions are considered to be fully elastic and frictionless.

The LES results that are presented here are all time averaged. After reaching a quasi steady state, the LES was run for a period comprising 16 impeller revolutions to collect sufficient flow information such that converged statistical results could be presented.

7.4. Results and Discussions

This section compares the results obtained with the large eddy simulation (LES) and the Euler-Euler model with those obtained from the CARPT experiment. Quantitative comparisons are shown for the mean solids velocity profiles and solids turbulent kinetic energy profiles at four axial regions of the tank that are given by $z/T = 0.075$ (close to the bottom), 0.25 (just below impeller), 0.34 (impeller plane) and 0.65 (midway between impeller and the top free surface). Also, comparison between the predictions of the two models for the liquid phase turbulent kinetic energy, the slip (or relative) Reynolds number (Re_s) and the solids holdup distribution in the tank are presented discussed. The mean velocities are made dimensionless with the impeller tip speed, U_{ip} . The turbulent kinetic energy is made dimensionless with U_{ip}^2 . The radial location in the tank is non-dimensionalized with the tank radius R ($R=T/2$). An extensive review of the literature is also presented to understand the influence of flow features on the drag and lift forces acting on a solid sphere, and several drag and lift closures commonly used in the literature are evaluated with the Euler-Euler model.

7.4.1. Overall Flow Pattern

Figures 7.3 (a) to 7.3 (c) show the ensemble averaged solids velocity field in a vertical plane in the tank as observed in the CARPT experiment and those predicted by the Euler-Euler model and the large eddy simulation, respectively. Clearly, in the experimental result the lower recirculation loop below the impeller is significantly stronger than the one above the impeller. This is not observed in either the large eddy simulation or the Euler-Euler prediction, where qualitatively both loops appear to be equally strong. Also it should be

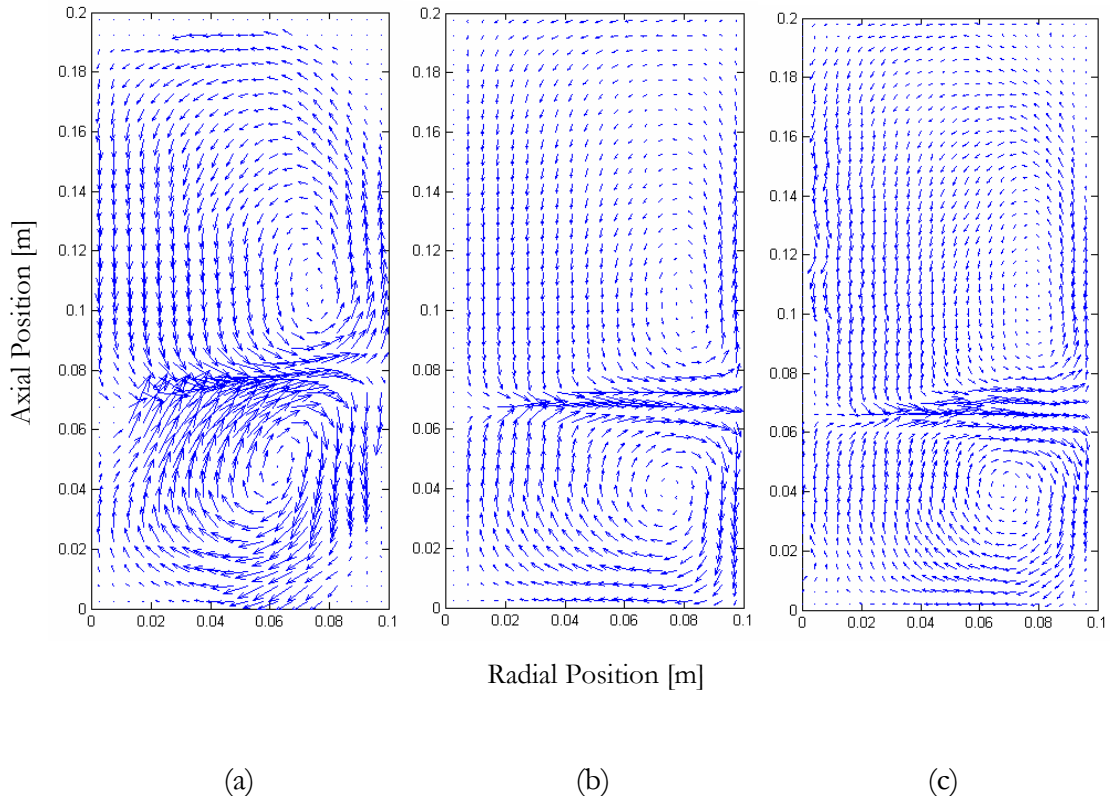


Figure 7.3 Overall solids flow pattern in the tank as obtained from (a) CARPT, (b) Euler-Euler simulation and (c) Large eddy simulation (all figures in same scale)

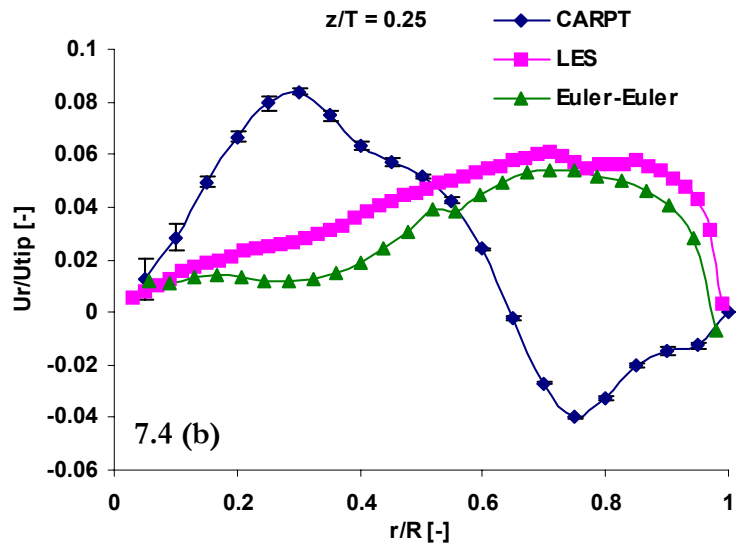
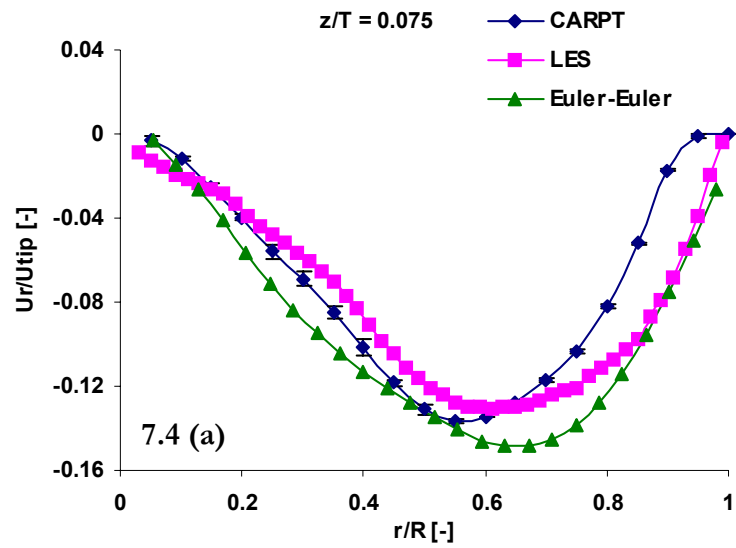
noted that below the impeller near the center where solids flow upwards (characteristic flow pattern for radial flow impellers) there is a significant contribution of the radial velocity apart from the strong axial velocity. This is not predicted in the numerical results, where the velocities at those locations are almost completely dominated by the axial component.

7.4.2. Solids Velocity Radial Profiles

The radial profiles of the time (ensemble) averaged solids radial velocity as obtained from the CARPT experiment and the two numerical models at the four axial locations in the

reactor are compared in Figures 7.4 (a) to 7.4 (d). The Euler-Euler predictions of time-averaged solids radial velocity are quite comparable with those obtained from the LES simulation, except at the impeller plane ($z/T = 0.34$) where improved predictions compared to CARPT data are observed with LES. However, both models still over-predict the solids velocity in the impeller outstream region. The numerical predictions are reasonably good in the regions far from the impeller and discrepancies are mostly observed in and around the impeller. Just below the impeller, at $z/T = 0.25$ (Figure 7.4b), both the simulations predict completely different trends from those observed experimentally. A much stronger radial flow stream at radial positions of $r/R < \sim 0.6$ is indicated by the data compared to simulation. This is in line with the observation that was made based on the overall flow pattern discussed earlier. The solids flowing upward near the center below the impeller have a stronger radial component as observed in the experimental study than that predicted by the models.

Figures 7.5 (a) to 7.5 (d) depict the radial profiles of time (ensemble) averaged solids tangential velocity as obtained from the CARPT experiment and the two numerical models at the four axial locations in the reactor. At the impeller plane ($z/T = 0.34$), the tangential velocity is over-predicted by both the models close to the impeller, but the LES predictions are improved in the region $r/R > \sim 0.4$. At the planes away from the impeller ($z/T = 0.075$ and 0.65), LES predictions of the tangential velocity is far superior to those obtained from the Euler-Euler model particularly in the region $r/R < \sim 0.5$. Although the strong swirl below the impeller plane ($z/t = 0.25$) observed in the experimental data is not captured by any of the models, LES predictions show improved trends compared to its Euler-Euler counterparts throughout the radial domain. Overall, the LES results for the solids tangential velocity compare much better with the CARPT experimental findings as opposed to the Euler-Euler predictions, at least in terms of capturing the right trends at all the axial locations presented here.



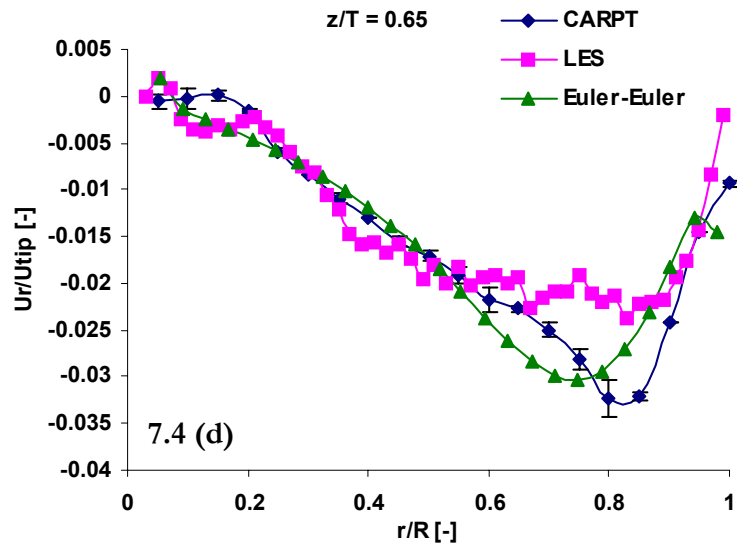
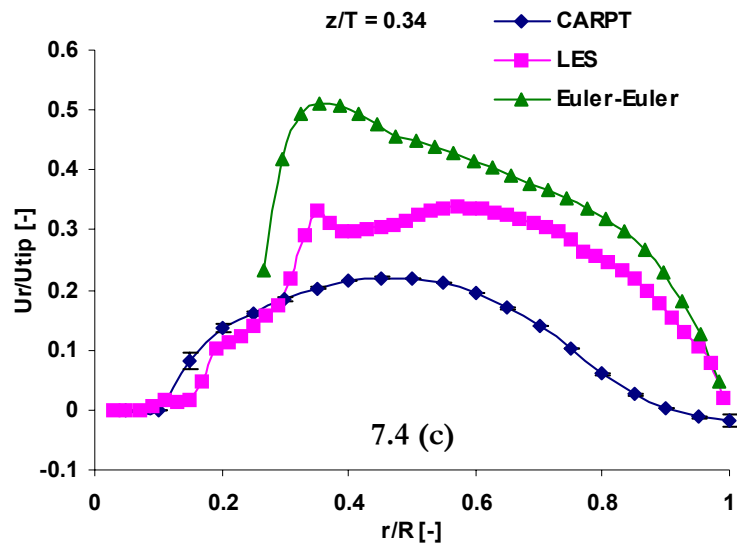
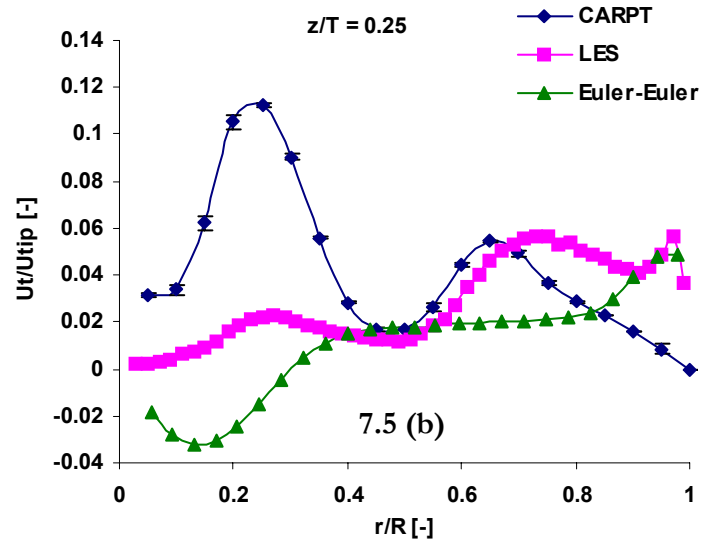
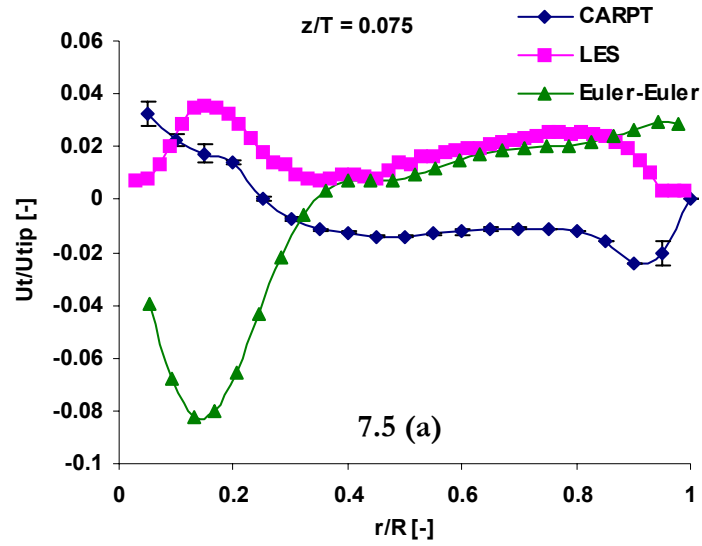


Figure 7.4 Radial profiles of solids radial velocity at different axial locations in the tank



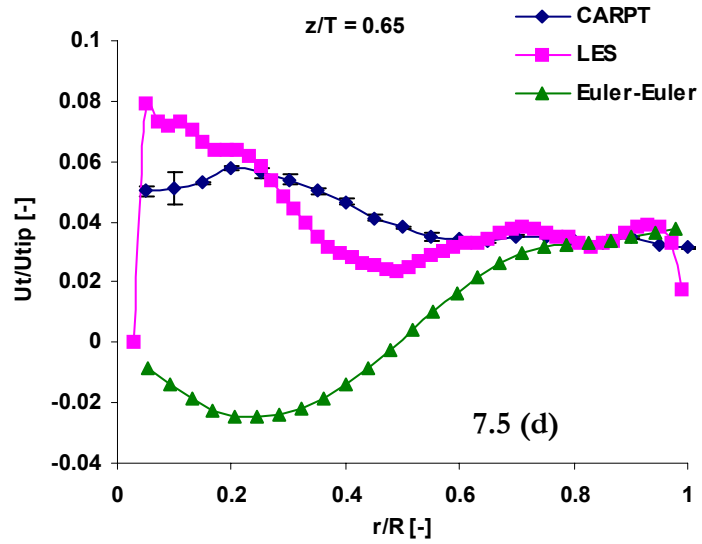
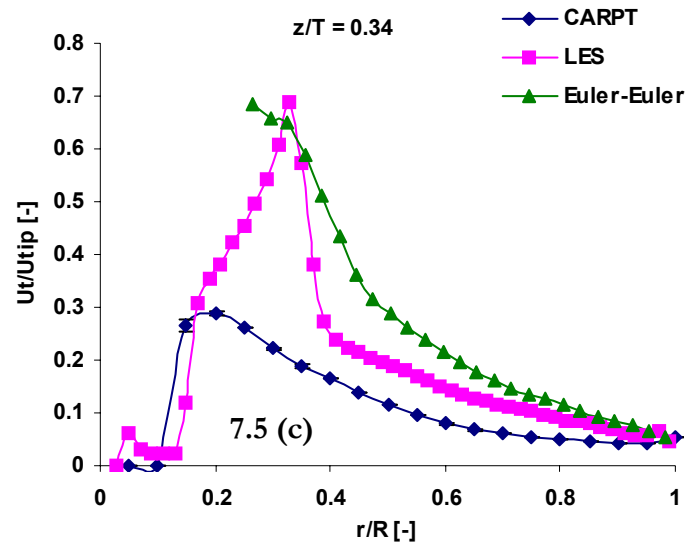
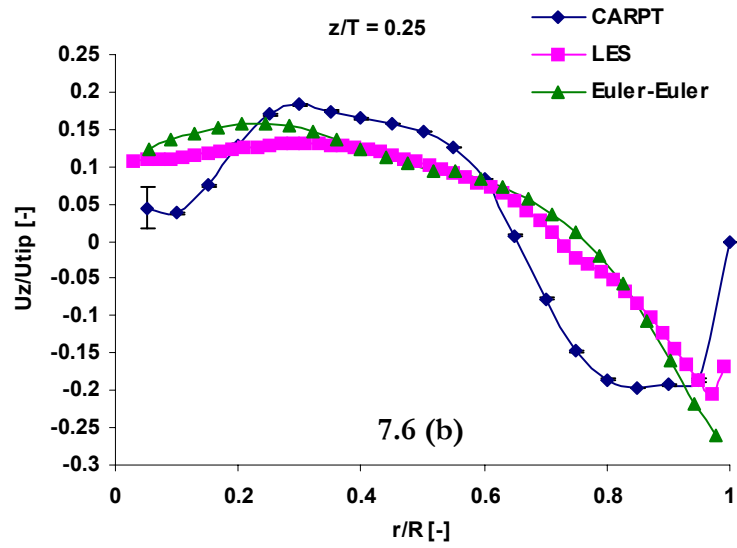
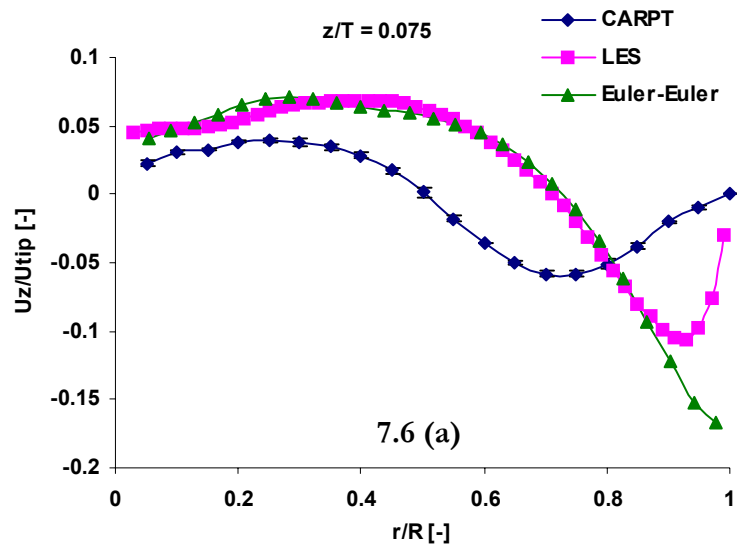


Figure 7.5 Radial profiles of solids tangential velocity at different axial locations in the tank

The radial profiles of time (ensemble) averaged solids axial velocity as obtained from the CARPT experiment and the two numerical models at the four axial locations in the reactor are compared in Figures 7.6 (a) to 7.6 (d). The predictions obtained with the large eddy simulation and the Euler-Euler model are more or less comparable for the solids axial velocities at most of the axial locations, but improved trend can be observed with the Euler-Euler model in the impeller plane. A strong upward velocity is indicated by the experimental data at radial positions of $r/R \sim 0.7$, which is not predicted by the numerical models. The Euler-Euler predicts velocities close to zero at all radial positions, while LES shows a strong downward velocity for $r/R < \sim 0.6$ and almost zero velocity thereafter. But it should be mentioned that in the processing of CARPT data the sampling size of the compartment where velocities are evaluated and averaged is larger and hence, the perfect demarcation of the axial planes is difficult. The number of compartments used for the data processing is $20 \times 36 \times 40$ (radial \times angular \times axial) resulting in a sampling size of 0.5cm in the axial direction. However, the numerical results are semi-quantitatively in line with the CARPT data at all the axial planes other than the plane containing the impeller. The solids in the radial jet from the impeller stream, as obtained from the experiment, has a significant axial velocity associated with it because of which the axis of the solids stream as a whole slightly moves upward as it approaches the wall. Similar observation is reported numerically by Sbrizzai et al. (2006) in their direct numerical simulation (DNS) of solids dispersion in an unbaffled stirred vessel. The authors attributed the upward inclination of the axis of the jet to the different boundary conditions that are imposed at the bottom (no-slip) and at the top (free-slip) of the tank. However, this cannot be observed in the numerical results obtained in this work using large eddy simulation and the Euler-Euler model.

7.4.3. Turbulent Kinetic Energy Profiles

Figures 7.7 (a) to 7.7 (d) represent the radial profiles of solids turbulent kinetic energy as obtained from the CARPT experiment and the two numerical models at the four axial locations in the tank. It is interesting to note that the numerical predictions obtained using



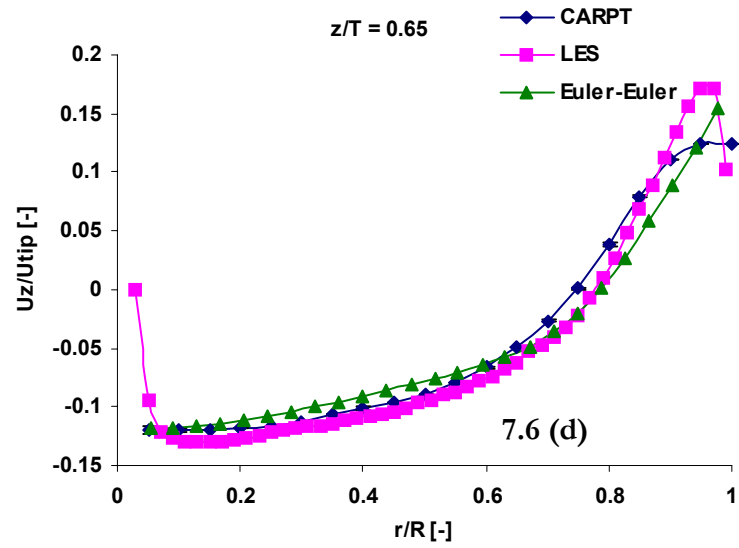
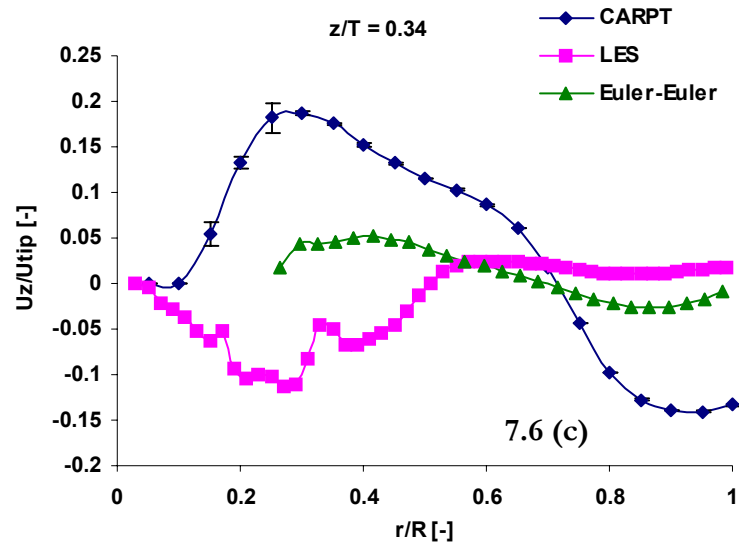
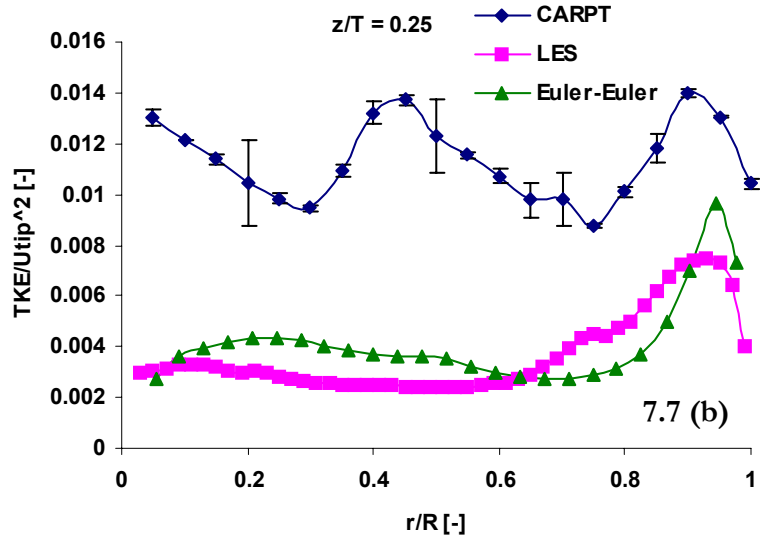
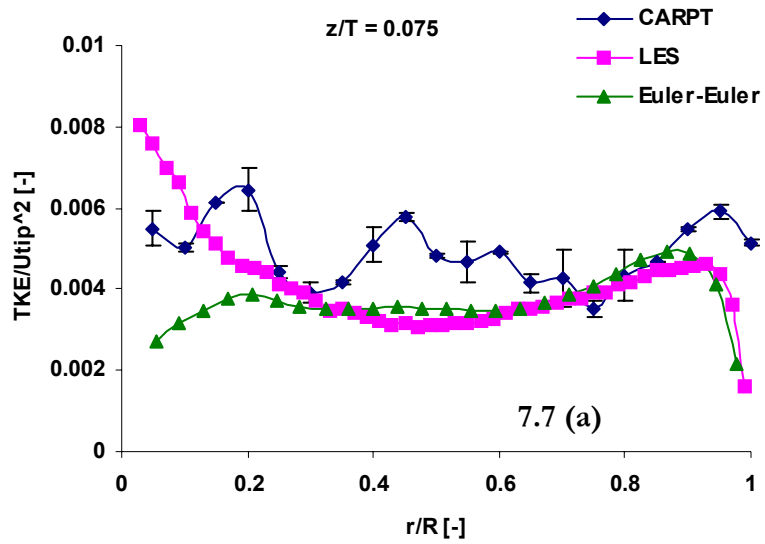


Figure 7.6 Radial profiles of solids axial velocity at different axial locations in the tank



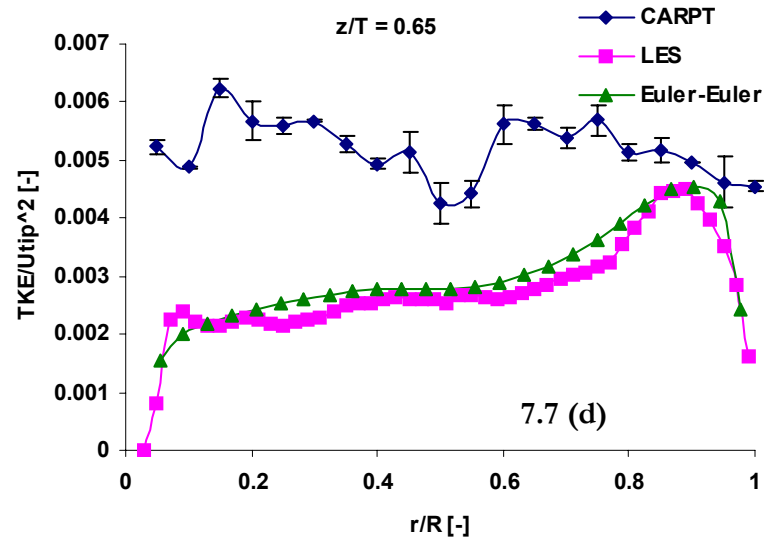
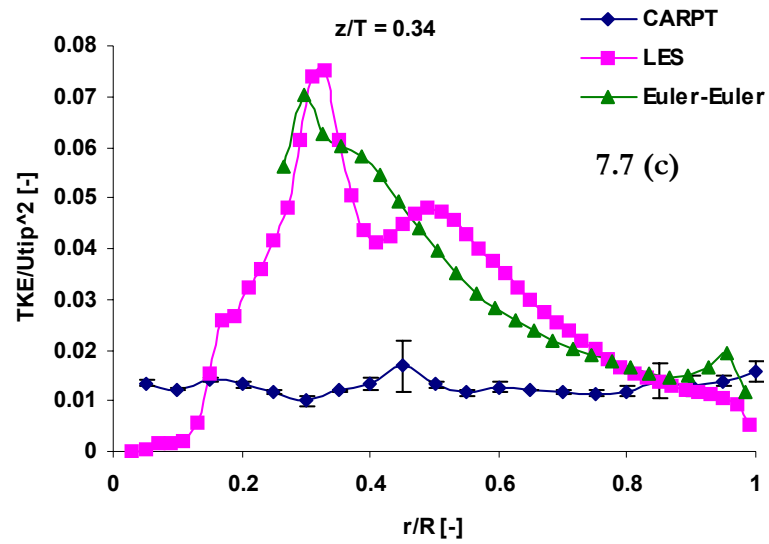


Figure 7.7 Radial profiles of solids turbulent kinetic energy at different axial locations in the tank

the large eddy simulation and the Euler-Euler model are in good agreement at all the four axial locations reported here and no additional improvement in prediction of the solids kinetic energy is observed with the LES model throughout the tank. This is quite surprising since it is well known that LES provides significantly improved predictions of turbulent kinetic energies for single phase flow compared to RANS model (Hartmann et al., 2004). When compared to the CARPT experimental data, it can be observed that the solids turbulent kinetic energies are over-predicted by both the models at the impeller plane and under-predicted at all other axial locations. This limits the ability to utilize the current CFD results for the extension of the compartmental model to solid-liquid system. The under-prediction of the turbulent kinetic energies in regions away from the impeller will lead to under-prediction of the turbulent dispersion term similar to that observed for the single phase system. This term being proportional to the square of the turbulent kinetic energy can have a significant impact on the model predictions.

It will be of interest to compare the liquid phase turbulent kinetic energies predicted by the two models and to see if both the models provide similar performance. Although the LES model solves for the liquid phase turbulence separately, the Euler-Euler simulation solves for the k - ε model with mixture properties and assumes that the same turbulence field is shared by the two phases. As a result, the mixture turbulent kinetic energy profile obtained from the Euler-Euler model is compared with the liquid phase turbulent kinetic energy obtained from LES at the plane of the impeller ($z/T = 0.34$) in Figure 7.8. It can be observed that this comparison reveals significant under-prediction of the turbulent kinetic energy from the RANS model compared to those predicted by LES. It seems that the solids phase turbulence might be less sensitive to the model being used while an improved model performs better to resolve the continuous phase turbulence.

7.4.4. Slip (Relative) Reynolds Number

The slip (or relative) Reynolds number (Re_s) quantifies the magnitude of the slip velocity between the two phases in the tank, and is computed as defined earlier in section 7.2

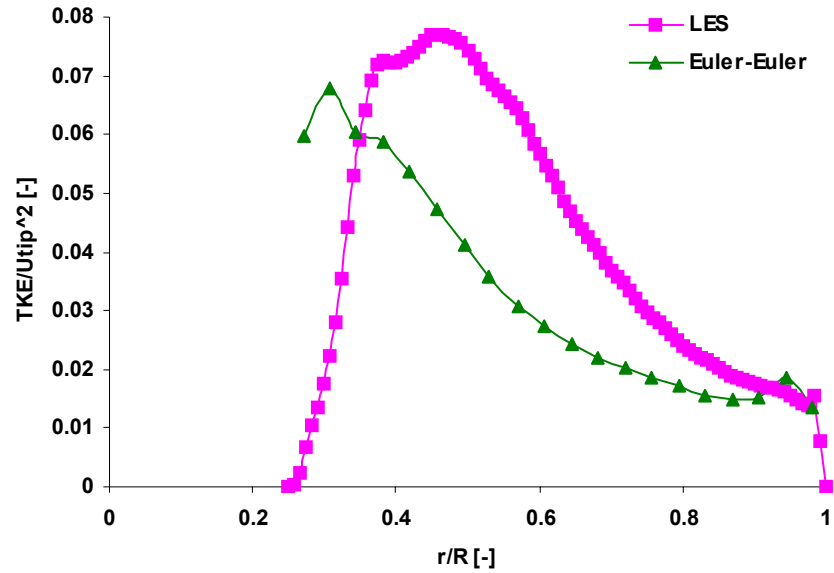


Figure 7.8 Radial comparison of mixture TKE from the Euler-Euler model and liquid phase TKE from the large eddy simulation at the impeller cross-section ($z/T = 0.34$)

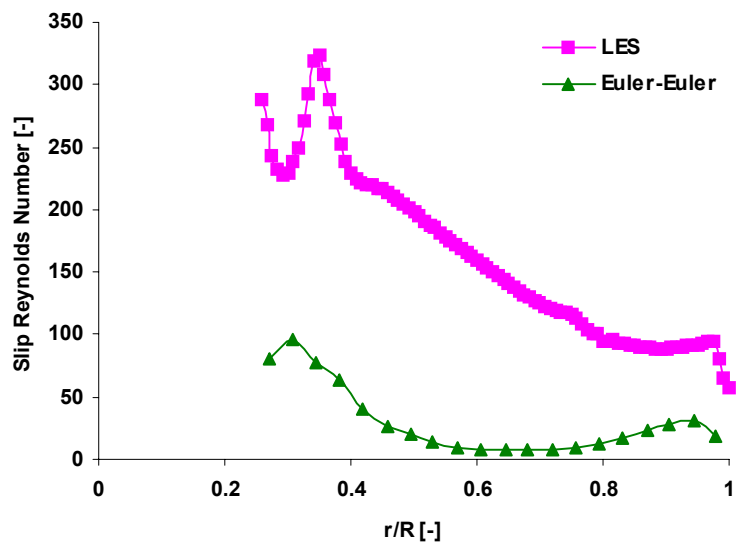


Figure 7.9 Radial comparison of slip Reynolds number from the Euler-Euler model and the large eddy simulation at the impeller cross-section ($z/T = 0.34$)

(below equation 7.5). The lower the value of slip, the more the dispersed phase (solids) tends to follow the continuous phase and vice versa. The radial profiles of the slip Reynolds number predicted by the two models at the impeller plane ($z/T = 0.34$) are presented in Figure 7.9. The slip velocity computed from the Eulerian simulation are significantly lower than those from the large eddy simulation, the difference being more than an order of magnitude at many of the radial locations. The closures used for the inter-phase interactions depend on the computed slip Reynolds number, and incorrect quantification of this quantity can impact the simulated flow field significantly.

7.4.5. Solids Volume Fraction

The radial profiles of the solids holdup (v/v) distribution obtained from the two models are plotted in Figure 7.10 at the plane containing the impeller ($z/T = 0.34$). Although the qualitative trends are similar, quantitatively LES predicts lower solids holdup compared to Euler-Euler model at most of the radial locations. This is, however, not surprising considering the significantly higher slip Reynolds number predicted by LES (Figure 7.9). Increased slip leads to more solids to settle down resulting in a lower prediction of solids holdup.

7.4.6. Influence of Baffles

In order to get insight into the local effect of baffles on the solids flow field, the radial, axial and tangential velocities at the impeller plane ($z/T = 0.34$) obtained from the CARPT data are averaged separately over the four angular planes containing the baffles and over the four angular planes midway between the baffles. The results of the CFD models are also averaged similar to the CARPT data. The CARPT-CFD comparison for the planes containing the baffles is shown in Figure 7.11 (a) to 7.11 (c), while those for the planes midway between two baffles is presented in Figures 7.12 (a) to 7.12 (c). The CARPT data for any velocity component does not show significant difference between the two cases, which is again because of the larger sampling size of the compartments used for data

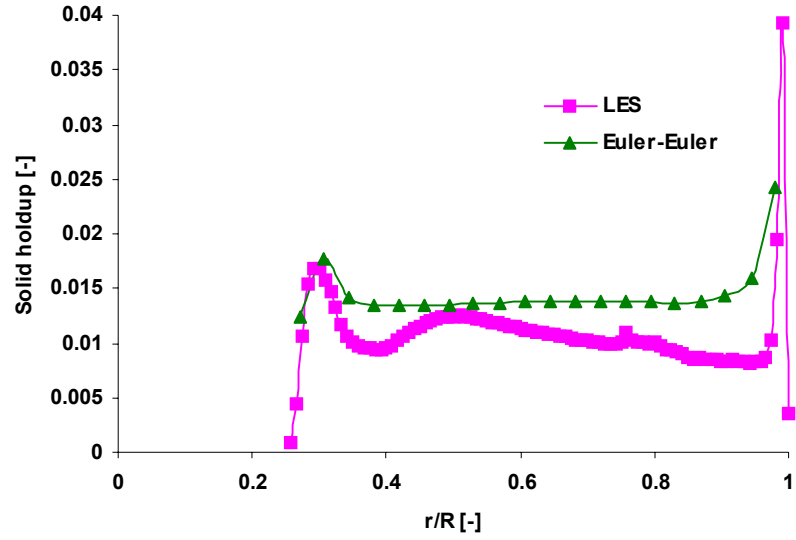
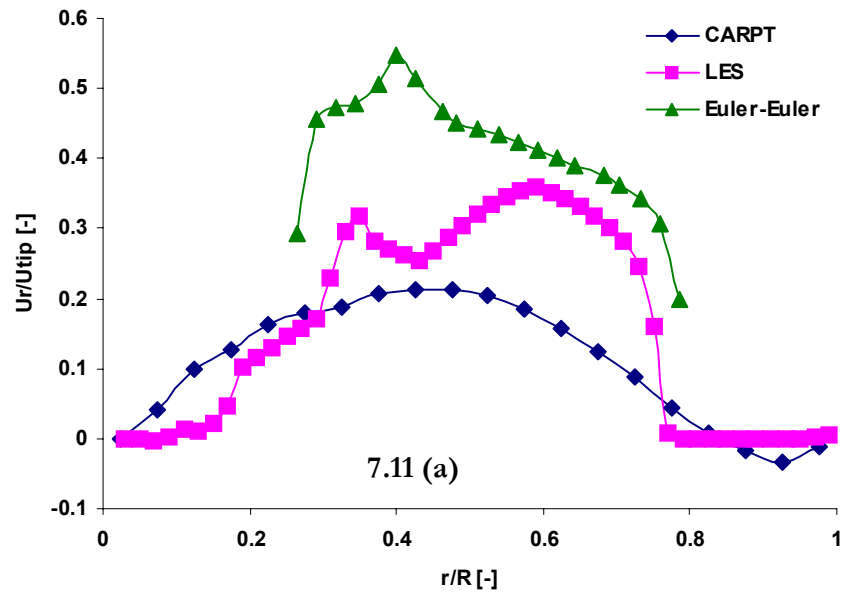


Figure 7.10 Radial comparison of solids holdup (v/v) from the Euler-Euler model and the large eddy simulation at the impeller cross-section ($z/T = 0.34$)



7.11 (a)

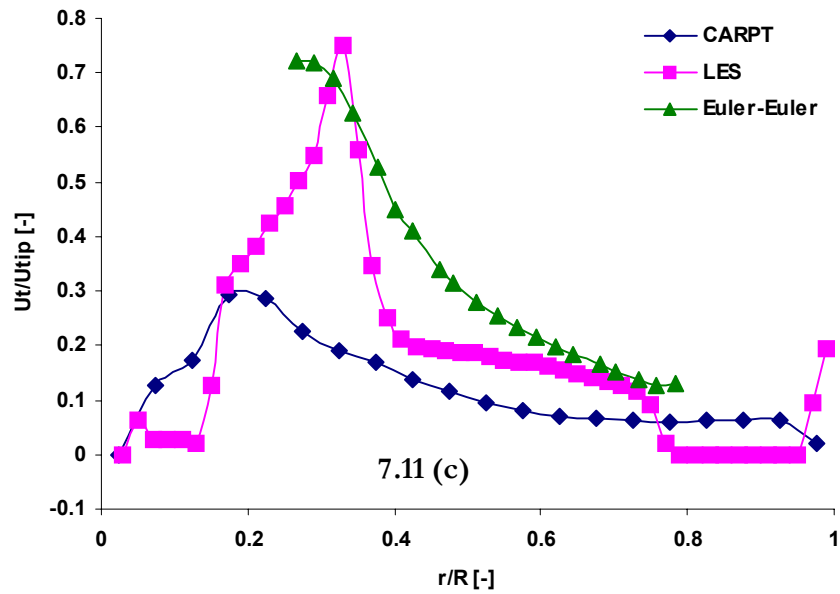
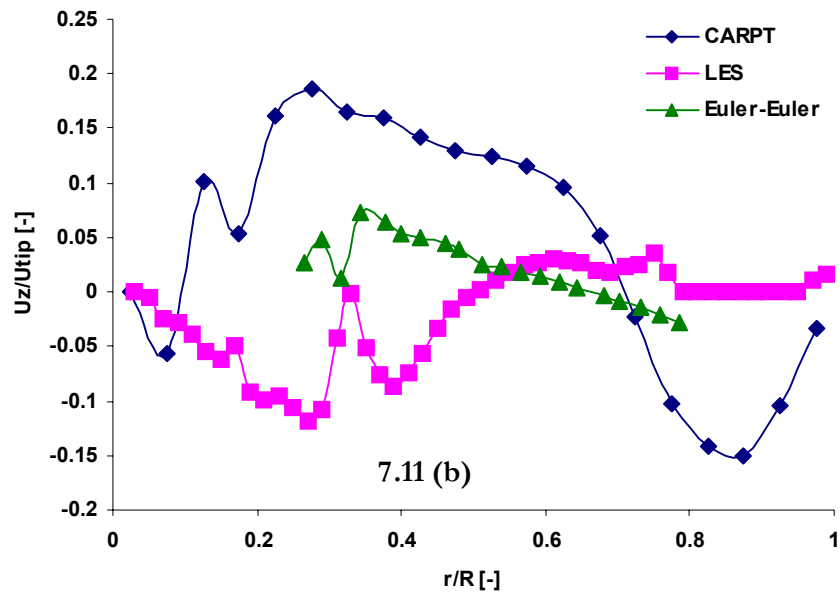
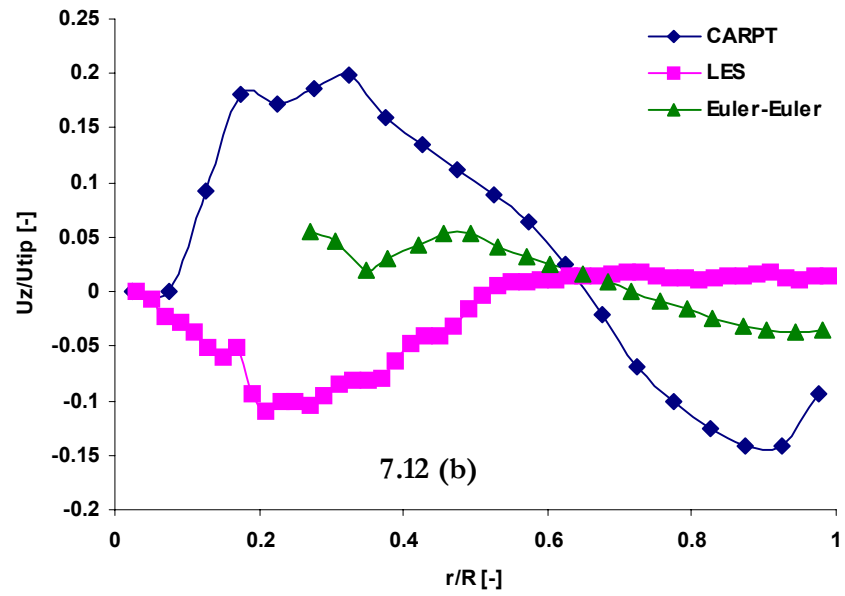
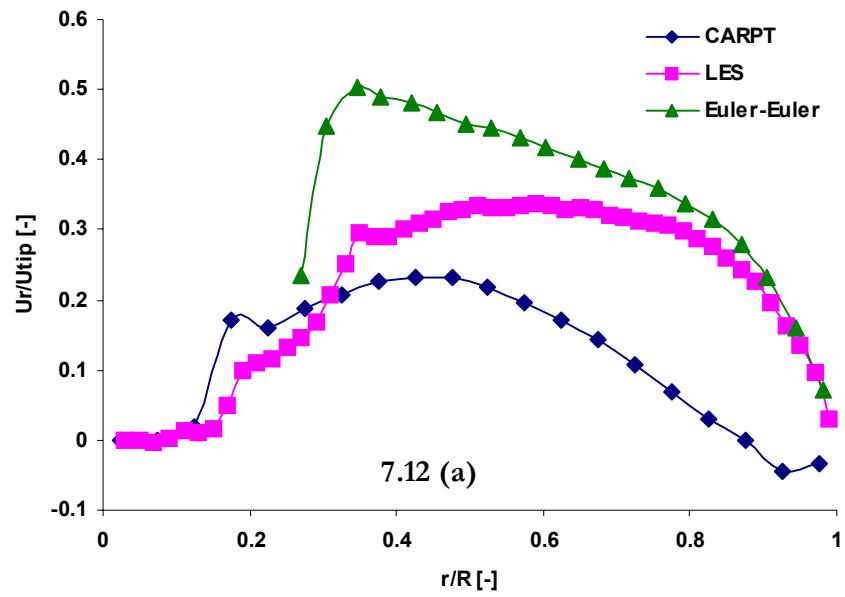


Figure 7.11 Comparison of CARPT and CFD predictions at planes containing the baffles for $z/T = 0.34$ (a) radial velocity, (b) axial velocity and (c) tangential velocity



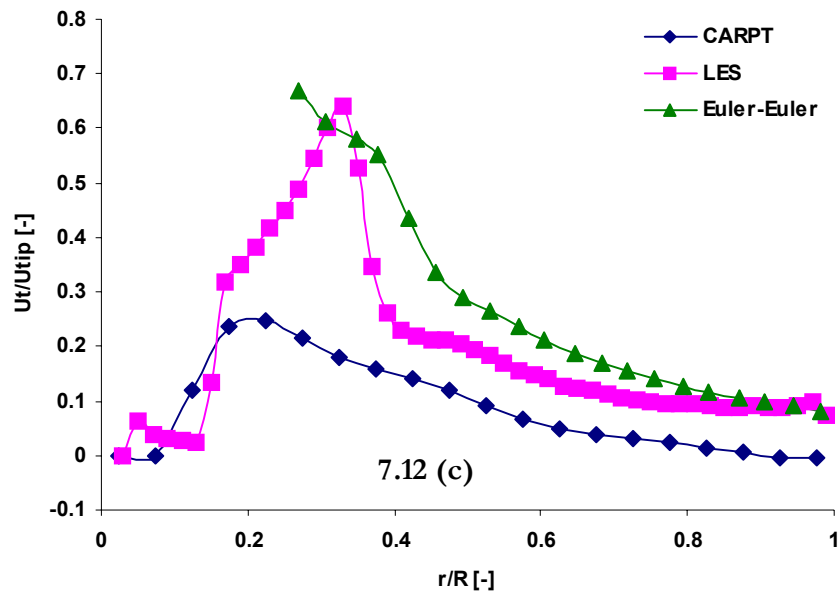


Figure 7.12 Comparison of CARPT and CFD predictions at planes midway between the baffles for $z/T = 0.34$ (a) radial velocity, (b) axial velocity and (c) tangential velocity

processing. The number of compartments in the angular direction is 36 and hence, perfect demarcations of the angular planes are not possible. The numerical simulations, however, shows the presence of the baffles as the velocities turn out to be zero after $r/R = 0.8$. Apart from this, no other significant differences in the trends are observed between the solids velocity component data at baffled and un-baffled planes.

7.4.7. Solids Sojourn Time Distributions

The Lagrangian information obtained from the CARPT experiment and large eddy simulation is used to calculate the probability density function (PDF) of solids sojourn times in different axial regions in the tank. The concept of solids sojourn time distribution (STD) has been discussed in detail in Chapter 4, where it was used to evaluate the Zwietering's correlation for the "just-suspension" speed for incipient solid suspension in the tank. Based on the mean sojourn time obtained experimentally for two impeller speeds

at the bottom zone of the tank, it was confirmed that the Zwietering's correlation significantly over-predicts the just suspension speed and incipient suspension can be achieved at speeds lower than the “just-suspension” speed predicted by the correlation. Similar observation has been reported by Brucato and Brucato (1998) who concluded that practically all particles get suspended at speeds of about 80% of that predicted by the correlation. Reasonable predictions of solids sojourn time distributions in the tank will eventually lead to improved predictions of just-suspension condition for slurry reactors. From an operational point of view, such optimization of operating condition can result in significant reduction in energy requirement, since the power required scales as the cube of the impeller speed.

In order to obtain the solids sojourn time distributions (STD), the total height of the tank is divided into 10 equal axial regions (zones) each 2cm in height and the movement of the tracer particle is monitored across each of these zones. The STD curve in each zone is generated from the particle position versus time data by recording the time when the particle is found in the zone of interest. Tracking the particle until it exits the zone of interest provides the time the particle spends in the axial zone under consideration from entry to exit. This yields the sojourn time of the particle in the zone of interest during that pass. This process is repeated each time the particle enters and leaves the zone under consideration, which then provides a distribution of sojourn times of the particle in that axial region. Therefore, the sojourn time distribution (STD) in any axial zone i can be defined as

$E_i(t_s)\Delta t_s$ = fraction of occurrences in zone i that has sojourn times between t_s and $t_s + \Delta t_s$

The moments of the STDs are calculated in order to characterize the obtained distributions. The first moment provides the mean of the distribution μ_i , which is defined as

$$\mu_i = \sum_{t_s=0}^{\infty} t_s E_i(t_s) \Delta t_s \quad (7.5)$$

The second central moment gives the variance of the distribution σ_i^2 , which is defined as

$$\sigma_i^2 = \sum_{t_s=0}^{\infty} (t_s - \mu_i)^2 E_i(t_s) \Delta t_s \quad (7.6)$$

The positive square-root of the variance is the standard deviation of the distribution, which depicts how much the distribution spreads out with respect to the mean value.

The axial variation of the mean and standard deviation of the solids sojourn time distributions in the tank as obtained from the CARPT experiment and the large eddy simulation are reported in Table 7.1 and is compared in Figures 7.13 (a) and 7.13 (b). The fractional occurrences of the tracer particle at different axial locations are also reported in Table 7.1 and plotted in Figure 7.14, where each occurrence corresponds to one appearance of the particle in the zone of interest from entry to exit. The sojourn time distributions cannot be obtained with the Euler-Euler model since the dynamics of the solids phase is also solved in the Eulerian framework, unlike the large eddy simulation which tracks the individual particles through a Lagrangian approach. It can be seen that the fractional occurrences and the first and second moments of the distributions predicted by LES compare well with those from CARPT experiment, both qualitatively and quantitatively, in spite of the fact that significant mismatch between CARPT results and LES predictions of velocities are observed particularly around the impeller. This is somewhat surprising considering that one would expect the mismatch in the velocity profiles to be reflected in the sojourn time distributions as well. As a result it is worthwhile to compare the distribution functions obtained from CARPT data and the LES simulation at four axial slices containing the four axial locations where the velocity profiles are compared. Such a comparison is presented in Figures 7.15 (a) to 7.15 (d), where the slices considered are 0-2 cm (containing $z/T = 0.075$), 4-6 cm (containing $z/T = 0.25$), 6-8 cm (containing $z/T = 0.34$) and 12-14 cm (containing $z/T = 0.65$). The PDF obtained for the bottom slice by the two methods is characteristically different – CARPT shows a larger fraction having small sojourn time compared to LES prediction, and hence the mean sojourn time predicted by LES is larger for this slice. For the slice just below the impeller (4-6 cm), significant difference in the PDF can be observed qualitatively. The spike

predicted by the large eddy simulation is not observed by CARPT. However, this spike will have less impact on the first and second moments of the distribution since the spike occurs at very small t_s , which probably led to similar mean and standard deviation for the two cases. In the axial slice containing the impeller (6-8 cm) both CARPT and LES show two peaks but the peaks are slightly shifted towards the left with LES compared to that with CARPT. The range of sojourn time (t_s) covered by the distribution is, however, more or less equal. Significant difference in the PDF exists for the slice between 12 and 14 cm as well, but the two distributions lead to similar first moment (mean) although the second moment (standard deviation) obtained from CARPT is larger.

Table 7.1 Axial variation of solids fractional occurrence, mean sojourn time and standard deviation as obtained with CARPT and LES for 1% solids holdup at 1000 RPM

Axial Bounds (cm)	Fractional Occurrence CARPT	Mean CARPT (s)	Standard Deviation CARPT (s)	Fractional Occurrence LES	Mean LES (s)	Standard Deviation LES (s)
0 – 2	0.064	0.096	0.080	0.048	0.175	0.115
2 – 4	0.144	0.061	0.052	0.143	0.050	0.036
4 – 6	0.158	0.039	0.037	0.173	0.045	0.033
6 – 8	0.128	0.057	0.032	0.149	0.051	0.039
8 – 10	0.113	0.071	0.052	0.104	0.049	0.033
10 – 12	0.124	0.061	0.057	0.102	0.049	0.036
12 – 14	0.117	0.069	0.056	0.098	0.054	0.041
14 – 16	0.092	0.085	0.066	0.088	0.067	0.052
16 – 18	0.048	0.128	0.088	0.071	0.085	0.060
18 – 20	0.011	0.082	0.049	0.025	0.172	0.103

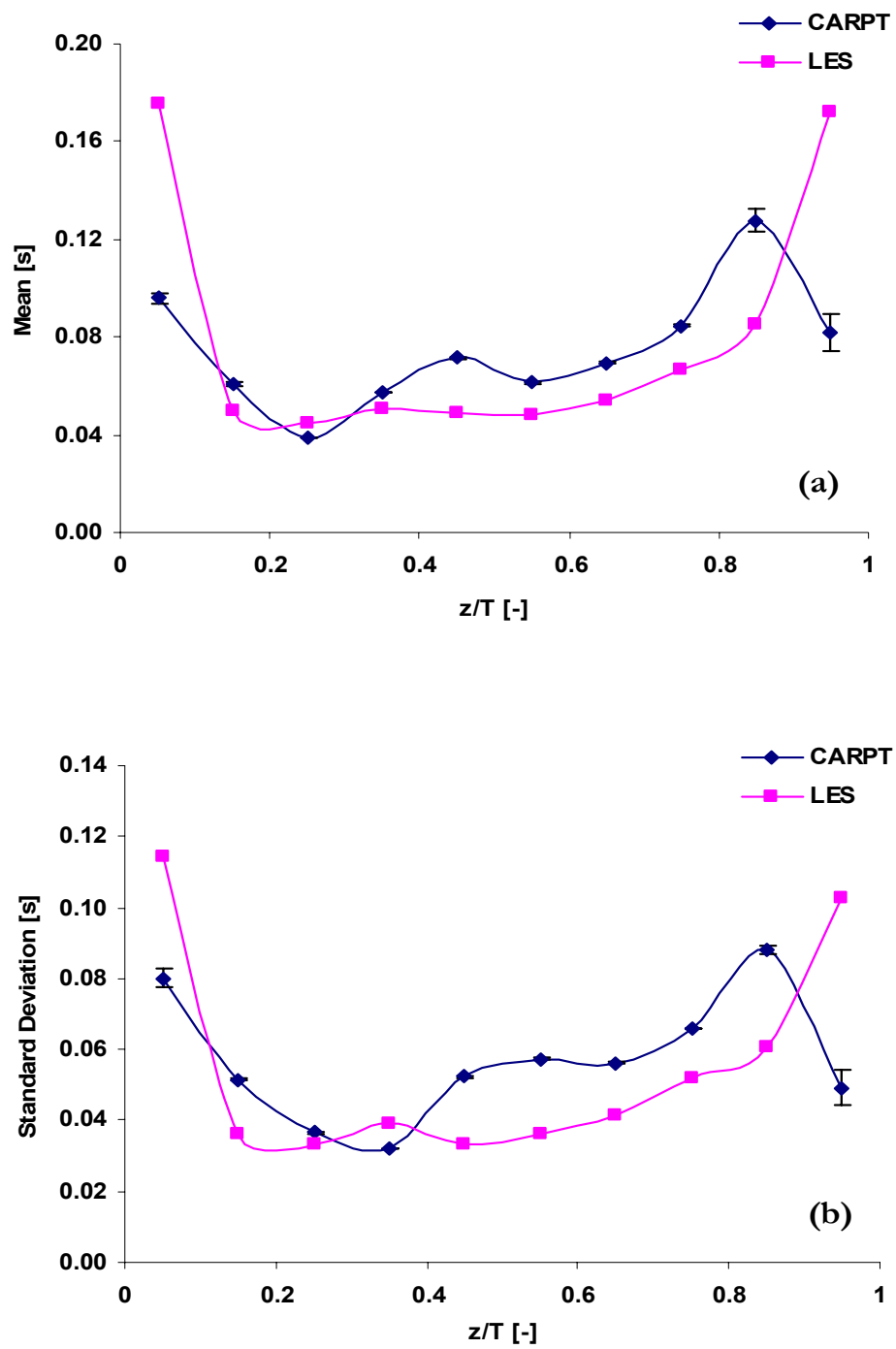


Figure 7.13 Axial variation of the moments of the solids sojourn time distribution in the tank

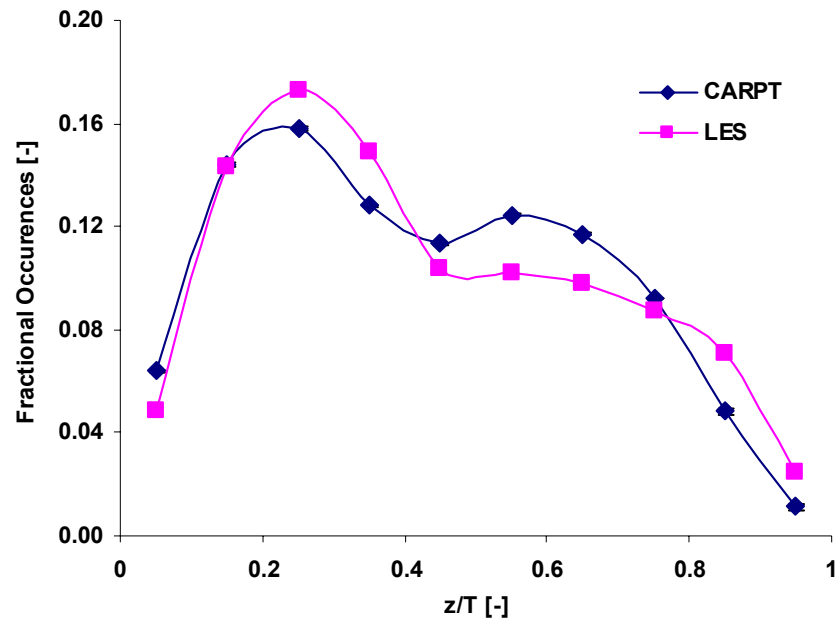


Figure 7.14 Solids fractional occurrences in different axial regions of the tank

7.5. Influence of Drag and Lift Closures on the Euler-Euler Predictions of Solids Flow Field

The comparison of the Euler-Euler and Large Eddy Simulation predictions to the CARPT data revealed significant discrepancy in the region in and around the impeller. The agreement is reasonable within engineering accuracy at other parts of the tank. The flow near the impeller is very complex characterized by large velocity gradients, high turbulence intensity and significantly higher fluid vorticity (Derksen, 2003) compared to other regions in the vessel. The particle-particle interaction at relatively higher solids loading and the interaction between the particle and the impeller add more complexity to the problem. These can have a significant effect on the phase interaction closure models, primarily presented in terms of the drag and lift coefficients. Significant insights might be obtained on this issue if a systematic evaluation is carried out with flows around a solid

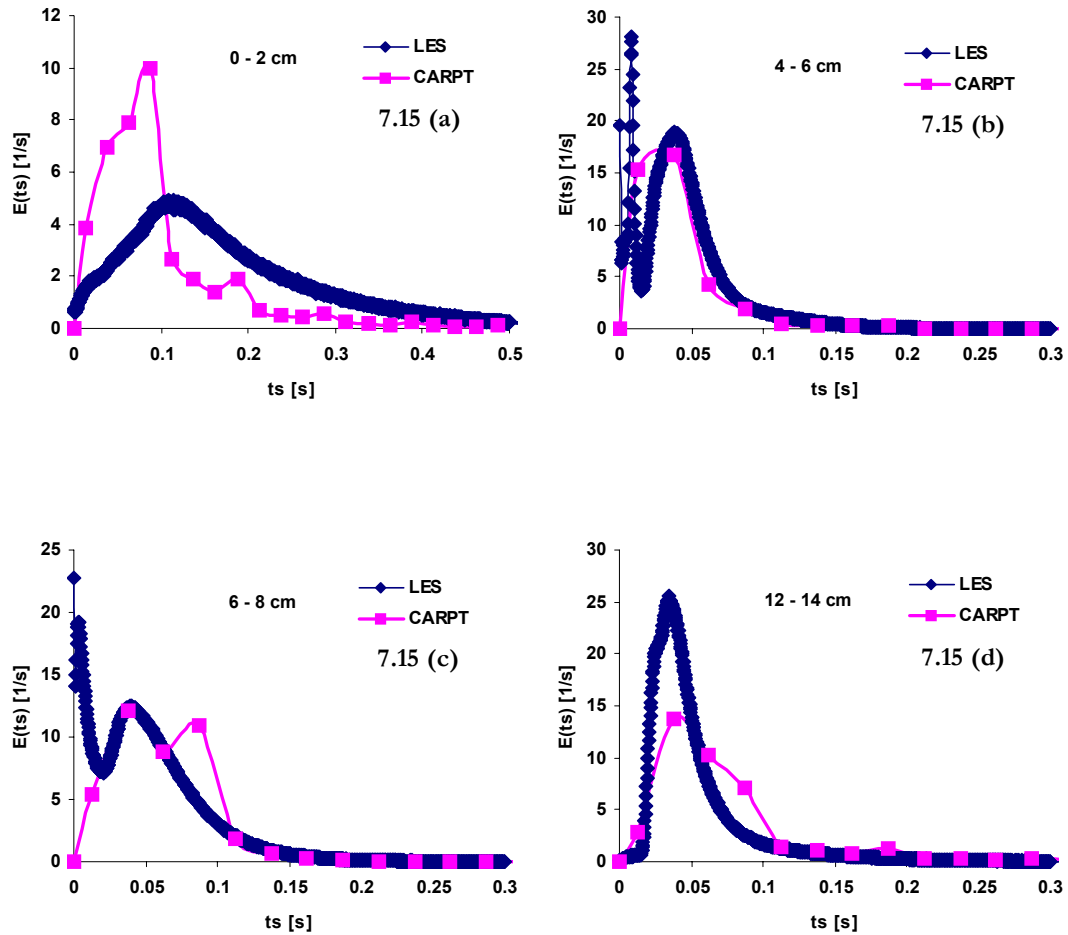


Figure 7.15 Solids sojourn time distributions at different axial slices in the tank

sphere, which then provide understanding about the effect of flow properties on the drag and lift forces experienced by the sphere.

There exists a difference in the literature about the importance of the lift forces for solid-liquid flow simulations in a stirred vessel. While Derksen (2003) argues that lift forces can be significant particularly near the impeller region, Ljungqvist and Rasmuson (2001) do not find much difference in the predictions obtained with and without the use of lift forces in their Euler-Euler simulation. The large eddy simulation performed in this work is

comprehensive with Saffman and Magnus forces, as well as the virtual mass force in addition to the drag force. The coefficients for the Saffman and Magnus forces are estimated using the correlations proposed by Mei (1992) and Oesterle and Bui Dinh (1998) respectively, which vary in the vessel depending on the local Reynolds number and other flow properties, the details of which are provided by Derksen (2003). On the other hand, the Euler-Euler simulations of Ljungqvist and Rasmuson use a constant lift coefficient of 0.5 that is truly valid for a rigid sphere in a weak shear flow of an inviscid fluid and when vorticity and unsteady effects are not strong (Auton et al., 1988). However, despite the rigor of the LES model used, the predictions are not acceptable in the impeller region and agreement is poor when compared to the CARPT data. This suggests that it is necessary to understand the effect of the flow features prevailing in the impeller region on the drag and lift forces acting on the solid particles. This section aims to provide an extensive review of the literature that addresses such effects and then evaluate the influence of the available closure models on the Euler-Euler flow predictions.

7.5.1. Effect of Flow Properties on the Forces on a Solid Sphere – Literature Review

As already mentioned, the presence of high levels of turbulence, fluid vorticity and high shear rates with a radial flow impeller, and the possibility of free rotation of the solid particles are the characteristic flow features that can be expected to prevail around the impeller in a stirred vessel. For example, the fluid vorticity around the impeller region can be significantly higher compared to other parts of the tank as shown in Figures 7.16 (a) and 7.16 (b) that presents the distribution of liquid vorticity in $r-\theta$ and $r-z$ planes respectively. Drag and lift closures that are typically used for numerical simulations in the literature do not account for any of these complex flow effects which might have an influence on the forces experienced by the solids. It is, therefore, worthwhile to review the experimental and modeling efforts in the open literature that have been focused to understand the impact of these flow properties on the inter-phase forces. This might shed

some light on the possible causes that led to poor model predictions particularly around the impeller region.

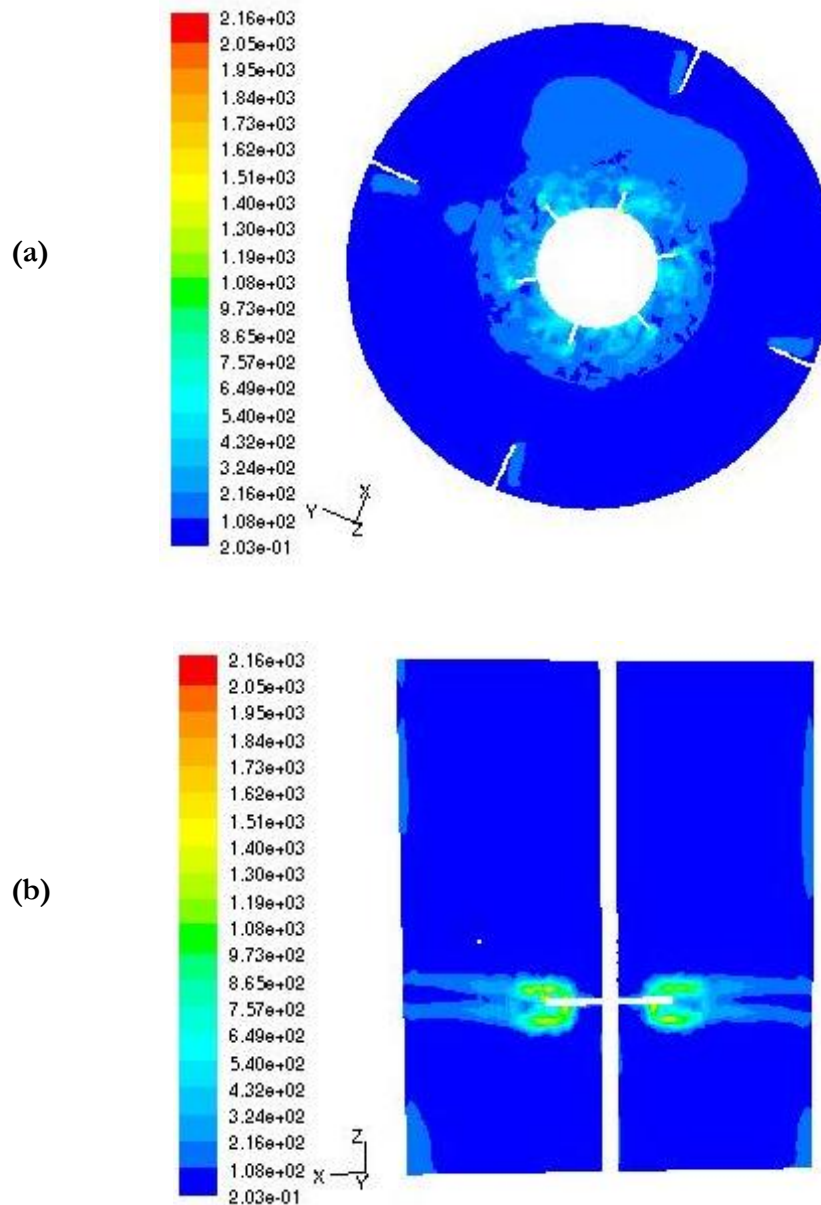


Figure 7.16 Distribution of liquid phase vorticity (s^{-1}) in the tank obtained from the Euler-Euler simulation (a) r - θ plane (b) r - z plane

Effect of Free Stream Turbulence

Magelli et al. (1990) observed that free stream turbulence in the liquid phase could have a significant effect on the drag experienced by the solids in the reactor. In their work, they measured the axial profiles of solids concentration in multiple-impeller vessels, which were then interpreted by a simple two-parameter sedimentation-dispersion model. The parameters involved in their model were an effective axial turbulent dispersion coefficient of the solid phase and the average settling velocity of the particles. Using the dispersion coefficient that was obtained in an independent study (Magelli et al., 1986), the settling velocity of the particles was predicted by best fitting of the model predictions to the experimental data. It was assumed that the axial turbulent dispersion coefficient of the solid phase was equal to that of the liquid phase following the findings of Magelli et al. (1986). They found that the ratio between particles settling velocity in the turbulent fluid and that in the stagnant fluid was in the range between 0.4 and 1.0. Based on their results, Magelli et al. (1990) correlated the ratio of the settling velocity in turbulent liquid and the settling velocity in still liquid to the ratio of the particle diameter d_s and the Kolmogorov length scale l_k . They also showed that when particle diameter is smaller than $5-10l_k$, particles settling velocity remain unaffected by turbulence and the same settling velocity as in a quiescent fluid is obtained. They argued that in this case the interaction between energy dissipating eddies and the particles is negligible and hence the drag coefficient is practically unaffected by turbulence. On the other hand, if $d_s > 10l_k$ the interactions become significant causing large changes in both particle drag and settling velocity. However, it should be noted that the results presented by Magelli et al. (1990) were not based on direct measure of the particle settling velocity, but were rather obtained using a simplistic model with the assumption that dispersion coefficients for both the phases were equal. Brucato et al. (1998) attempted to improve on the results of Magelli et al. (1990) and made direct measurements of the settling velocity exhibited by a cloud of particles using a suitable residence time technique. The technique consists of injecting a small quantity of solid particles at the top of a tall column containing a fluid in turbulent flow and measuring the solids concentration at two axial sections in the column. The “mean crossing time” is

computed for each section from the concentration dynamics obtained, and assuming that the vessel is unbounded and that axial dispersion model applies, the settling velocity is calculated as the ratio of the distance between the two sections to the difference in the “mean crossing time” at the two sections. Their data also show that free stream turbulence can increase the particle drag coefficients significantly. They observed that the normalized increase in the drag coefficient can be directly correlated with the ratio d_s/l_k , and proposed a correlation where the normalized increase in the drag coefficient is proportional to the cube of the ratio d_s/l_k with the proportionality constant being 8.76×10^{-4} . Ljungqvist and Rasmuson (2001) carried out Euler-Euler simulations in a solid-liquid stirred tank using different closures for the drag coefficient and concluded that the closures studied led to very similar results. They also implemented the drag correction provided by Brucato et al. (1998) thereby taking into account the fluid phase turbulence, but no significant changes in the model predictions was observed. In order to understand the effect of turbulence on the drag coefficient more systematically, Khopkar et al. (2006) performed two-dimensional simulations of flow through regularly arranged cylindrical objects using the finite volume technique. They used the Euler-Euler approach with the standard k - ε model for turbulence in their simulations that were carried out in the range of particle Reynolds numbers between 0.54 to 69.4 and solids holdup between 5 and 20%. Their results indicate that in addition to the ratio d_s/l_k , the fractional increase in drag coefficient is also influenced by the particle Reynolds number and the solids volume fraction. However, due to lack of data points they ignored the possible effect of solids volume fraction and particle Reynolds number and correlated the predicted results only to the ratio d_s/l_k . They observed that the correlation proposed by Brucato et al. (1998) holds under the range of conditions simulated, but suggested a proportionality constant that is one order of magnitude smaller than that presented by Brucato et al. (1998). More fundamental simulations were carried out by Bagchi and Balachandar (2003), who performed direct numerical simulations of a particle in a frozen isotropic turbulent flow to address the effect of free stream turbulence on the drag force acting on the particle. In their simulations the particles Reynolds number was in the range 50 to 600 while the

diameter of the particle was varied from about 1.5 to 10 times that of the Kolmogorov length scale. They compared the DNS results obtained for the mean and time-dependent drag to the predictions of the standard drag correlation proposed by Schiller and Neumann (1933), and observed that the free stream turbulence does not have a systematic and substantial effect on the mean drag. They also mentioned that the Schiller-Neumann correlation based on the instantaneous or mean relative velocity yields a reasonably accurate prediction of the mean drag that were obtained from the DNS. However, such an observation can be the outcome of their particle size being of the order of $10l_k$ for which turbulence might not have an influence on the drag as mentioned by Magelli et al. (1990). Hence, it seems that the drag force experienced by larger particles ($>10l_k$) can be significantly influenced by the free stream turbulence present.

Effect of Shear Rate and Sphere Rotation

Several numerical investigations can be found in the open literature that studies the drag and lift forces acting on a rigid sphere either fixed or rotating in a linear shear flow (Salem and Oesterle, 1998; Kurose and Komori, 1999; Bagchi and Balachandar, 2002). Salem and Oesterle (1998) used the finite volume formulation for their simulations that were carried out at low Reynolds number (based on the sphere radius) of up to 20. Their simulation results for the drag coefficients on a non-rotating particle in a uniform flow agree well with those predicted by the correlation proposed by Morsi and Alexander (1972). The drag coefficients in their study are found to increase slightly with increasing shear rate but remain unaffected by the sphere rotation. Kurose and Komori's (1999) work expands the understanding further as they performed extensive numerical investigation of the drag and lift forces acting on a solid sphere in a homogeneous linear shear flow. The influence of the fluid shear and the rotational speed of the sphere on the drag and lift forces were estimated for particle Reynolds numbers up to 500. The computed drag coefficients for a stationary sphere in a uniform unsheared flow again agreed well with those obtained from Morsi and Alexander's (1972) correlation for the range of particle Reynolds number studied. Their results demonstrate that the drag force on a stationary sphere in a linear shear flow and that

on a rotating sphere in a uniform unsheared flow increases marginally with increasing fluid shear and particle rotational speed, but the maximum increase observed is only about 10% at high Reynolds number around 500. This is probably in line with the predictions of Salem and Oesterle (1998) who did not find any difference in the drag coefficients at low Reynolds numbers due to the rotation of the particle. Kurose and Komori (1999) also reported that for a stationary sphere in a linear shear flow the lift force acts from the low-fluids-velocity side to the high-fluids velocity side when the particle Reynolds number is smaller than 60, while at higher Reynolds numbers greater than 60 it acts from the high-velocity-side to the low-velocity side. This implies that the computed lift coefficients are negative at larger Reynolds numbers. But for a rotating sphere in a uniform unsheared flow the direction of the lift force is independent of particle Reynolds numbers and the computed lift coefficients are always positive, which for a fixed rotational speed tends to approach a constant value at Reynolds number greater than 200. In their work Kurose and Komori (1999) also investigated whether the drag and lift forces acting on a rotating sphere in a linear shear flow can be estimated from the drag and lift forces calculated for a stationary sphere in a linear shear flow with the same shear rate and that for a rotating sphere with the same rotational speed in a uniform unsheared flow. This is of interest because if the superposition principle holds the effects of fluid shear and particle rotation on the drag and lift coefficients can be treated independently. Their results show that the superposition does hold at smaller Reynolds numbers, while the discrepancy increases as the particle Reynolds number increases. Based on their numerical investigation, they proposed correlations for the estimation of drag and lift coefficients for a rotating rigid particle in a shear flow. More recently Bagchi and Balachandar (2002) also studied the effect of the sphere rotation on the drag and lift forces in a linear shear flow by performing direct numerical simulations in the range of Reynolds numbers between 0.5 and 200. The computed drag coefficients on a non-rotating and rotating sphere in a shear flow and those obtained using the correlation of Schiller and Naumann (1933) do not show any difference in the range of variables simulated. This suggests that the external shear and the rotation of the sphere have little influence on the drag coefficient, which is in agreement with the results of Salem and Oesterle (1998) obtained at low particle Reynolds numbers. The

computed lift coefficients reported by Bagchi and Balachandar (2002) for a non-rotating sphere in a shear flow become negative at higher Reynolds numbers and agree well with those observed by Kurose and Komori (1999). The lift due to the rotation of the sphere (Magnus effect) has a significant contribution to the total lift force at intermediate range of Reynolds number between 5 and 100. Their work also confirmed that the superposition of the Saffman and Magnus effects hold in the range of parameters they studied and hence, the total lift force acting on the solid sphere can be calculated as the sum of the lift force on a non-rotating sphere in shear flow and the lift force on a sphere rotating in a uniform flow field. To summarize, the ambient shear rate and particle rotation seem to have no significant influence on the drag force exerted on a solid sphere and standard drag laws like Schiller-Neumann (1933) and Morsi-Alexander (1972) work reasonably well in predicting the mean drag on a particle in a turbulent flow field. However, shear rate and particle rotation can affect the lift force strongly through the Saffman and Magnus effects experienced by the particle.

Effect of Ambient Vorticity

Sridhar and Katz (1995) experimentally investigated the influence of liquid phase ambient vorticity in the flow on the drag and lift forces experienced by bubbles. The forces acting on the bubbles entrained in a vortex were measured using particle image velocimetry. The pressure, buoyancy and inertia forces were directly calculated from the data obtained, while the drag and lift forces were then determined from a force balance on each bubble. In the range of bubble diameters (500 to 800 μm) and Reynolds numbers (20 to 80) they considered, the drag on a bubble was found to be similar to that on a solid body. Their experimental measurements for the drag coefficients in the range of parameters studied are quite close to that predicted using the Schiller Naumann (1933) correlation, which suggests that ambient vorticity does not have any significant influence on the drag coefficient. However, the lift coefficients are affected strongly by the ambient vorticity, and their quantitative and qualitative results did not agree with those predicted by any of the theoretical models. Their lift coefficients were significantly larger than any other estimates.

Depending on the magnitude of vorticity, the observed differences can be more than an order of magnitude. They also observed that the lift coefficients are independent of the particle Reynolds number. They used a least square fit of their data to propose a correlation for the lift coefficient which is independent of the Reynolds number and is proportional to the fourth root of the local vorticity. Bagchi and Balachandar (2002) followed similar lines and studied the effect of vorticity on the lift force acting on a solid sphere numerically by means of direct numerical simulations. The sphere Reynolds number is in the range of 10 to 100. They compared the computed lift coefficients for a rigid sphere in a vortex with those predicted for a solid sphere in a linear shear flow and demonstrated that the vortex-induced lift force is significantly higher than that observed in shear flow. The magnitude of the lift coefficient increases almost linearly with the magnitude of the ambient vorticity at a given Reynolds number. In contrast to the experimental results of Sridhar and Katz (1995), their lift coefficients decrease monotonically with increasing Reynolds number. They mentioned that such quantitative disagreement with Sridhar and Katz's (1995) data is primarily because of the idealized solid body rotation used in the simulation for the undisturbed ambient flow, which essentially is an approximation of the experimentally generated vortex ring. The experimental uncertainties associated with tracking the bubble location, size and sphericity can also give rise to possible differences between experimental and numerical data. Based on their simulation results, Bagchi and Balachandar (2002) also proposed a correlation for the vortex-induced lift coefficient that depends on the Reynolds number and is proportional to the ambient vorticity. They also noticed that the drag force is insensitive to the ambient shear and ambient vorticity. The free rotation of the sphere has some contribution to increase the lift force due to Magnus effect, but its contribution is found to be only 4-14% of the total lift for the conditions simulated, which can be considered to be of secondary importance when vortex-induced lift is experienced by the sphere. The vorticity in the flow, therefore, have a strong influence on the lift force experienced by a solid sphere and this can have the maximum contribution to the total lift if the ambient vorticity is large.

7.5.2. Closure Models Tested

The closure models evaluated in this study with the Euler-Euler simulation of Fluent 6.2 are summarized in Table 7.2. Based on the extensive review presented in the previous section it seems that the standard drag models should be reasonable in predicting the drag force acting on the solid particles and hence, for the drag coefficient C_D , the models of Schiller-Neumann (1933), Morsi-Alexander (1972), Syamlal-O'Brien (1989) and Gidaspow (1992) are tested. The correction factor to the drag coefficient prescribed by Brucato (1998) in order to account for the effect of free stream turbulence is also incorporated and assessed. The base value of the drag coefficient C_{D0} is calculated using the Schiller-Neumann (1933) model and the Kolmogorov length scale is computed as

$$l_k = \left(\frac{\nu^3}{\varepsilon} \right)^{1/4} \quad (7.7)$$

ν is the kinematic viscosity and ε is the kinetic energy dissipation rate.

The model of Bagchi and Balchandar (2002) is used to calculate the lift coefficient C_L apart from the constant value of 0.5 described earlier. This model accounts for the effect of the ambient vorticity on the lift coefficient. The local liquid phase vorticity ϖ is computed through a User Defined Function (UDF) as $\varpi = \nabla \times \vec{u}_l$, since the vorticity equation is not explicitly solved in the Euler-Euler model. The dimensionless vorticity in this correlation is defined as

$$\varpi^* = \frac{\varpi d_s}{|\vec{u}_s - \vec{u}_l|} \quad (7.8)$$

The Magnus force experienced by the particles could not be included in the Euler-Euler simulation because the rotation of the particles cannot be quantified in this approach, although the rotational effect might have an important contribution to the total lift force as the literature review indicates.

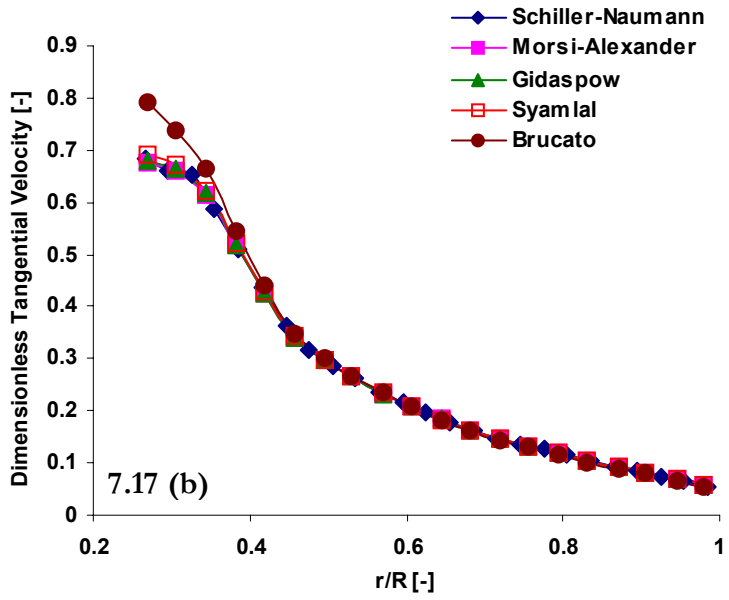
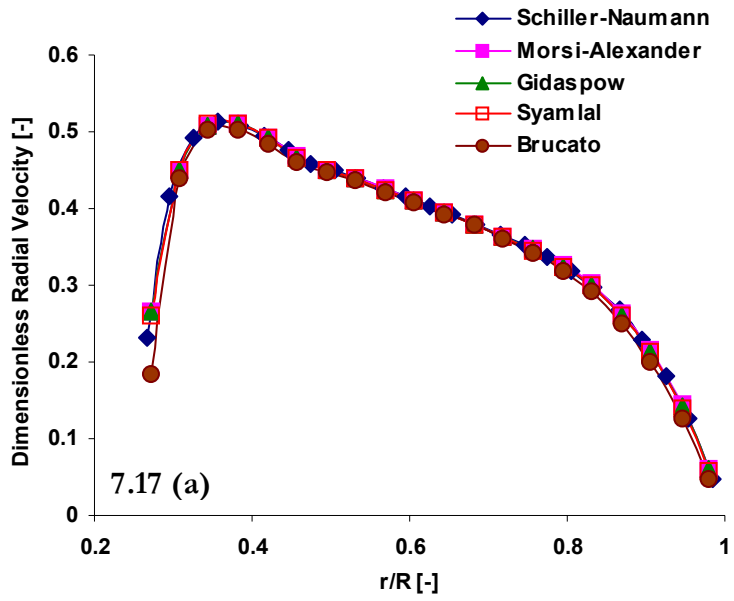
Table 7.2 Drag and lift closures evaluated with the Euler-Euler model

Schiller-Neumann (1933)	$C_D = \begin{cases} \frac{24}{\text{Re}_s} (1 + 0.15 \text{Re}_s^{0.687}) & \text{Re}_s \leq 1000 \\ 0.44 & \text{Re}_s > 1000 \end{cases}$
Morsi-Alexander (1972)	$C_D = a_1 + \frac{a_2}{\text{Re}_s} + \frac{a_3}{\text{Re}_s^2}$ $a_1, a_2, a_3 = \begin{cases} 0, 24, 0 & 0 < \text{Re}_s < 0.1 \\ 3.69, 22.73, 0.0903 & 0.1 < \text{Re}_s < 1 \\ 1.222, 29.1667, -3.8889 & 1 < \text{Re}_s < 10 \\ 0.6167, 46.50, -116.67 & 10 < \text{Re}_s < 100 \\ 0.3644, 98.33, -2778 & 100 < \text{Re}_s < 1000 \\ 0.357, 148.62, -47500 & 1000 < \text{Re}_s < 5000 \\ 0.46, -490.546, 578700 & 5000 < \text{Re}_s < 10000 \\ 0.5191, -1662.5, 5416700 & \text{Re}_s \geq 10000 \end{cases}$
Syamlal-O'Brien (1989)	$C_D = \left[0.63 + \frac{4.8}{\sqrt{\text{Re}_s / v_{r,s}}} \right]^2$ $v_{r,s} = 0.5(A - 0.06 \text{Re}_s + \sqrt{(0.06 \text{Re}_s)^2 + 0.12 \text{Re}_s (2B - A) + A^2})$ $A = \alpha_l^{4.14} \text{ and } B = \begin{cases} 0.8 \alpha_l^{1.28} & \alpha_l \leq 0.85 \\ \alpha_l^{2.65} & \alpha_l > 0.85 \end{cases}$
Gidaspow (1992)	$C_D = \frac{24}{\alpha_l \text{Re}_s} \left[1 + 0.15 (\alpha_l \text{Re}_s)^{0.687} \right] \quad \alpha_l > 0.8$
Brucato (1998)	$\frac{C_D - C_{D0}}{C_{D0}} = 8.76 \times 10^{-4} \left(\frac{d_s}{l_k} \right)^3$
Bagchi-Balachandar (2002)	$C_L = \frac{24}{\text{Re}_s} (1 + 0.597 \text{Re}_s^{0.593}) \overline{\omega}^*$

7.5.3. Observations

The azimuthally averaged radial profiles of solids radial, tangential and axial velocities at the plane of the impeller ($z/T = 0.34$) as obtained using the various drag models in the Euler-Euler framework are compared in Figures 7.17 (a) to 7.17 (c). The lift coefficient is kept constant at the default value of 0.5 for all the simulations. The predictions remain exactly the same with all the models other than the Brucato (1998) model which exhibits some differences close to the impeller. The predicted solids tangential velocity near the impeller tip increases with this model since the correction factor enhances the drag thereby reducing the slip velocity between the phases. This, however, results in even more over-prediction of the solids tangential velocity when compared to the CARPT data. Figures 7.18 (a) and 7.18 (b) shows the comparison of the radial profiles of the azimuthally averaged solids holdup at two axial locations in the tank given by $z/T = 0.075$ and $z/T = 0.65$. Similar to the earlier observation, the model predictions are more-or-less the same other than the Brucato's model that tends to improve the solids suspension in the vessel because of the enhanced drag. The observation that should be given careful consideration here is that the Brucato (1998) model suspends more solids in the tank but also causes larger over-prediction of the tangential velocity near the impeller compared to those predicted by the other models. Although this increase in drag force has been shown to provide improved predictions of axial solids concentration profile in the tank (Micale et al., 2000; Khopkar et al., 2006), larger errors in the solids velocity predictions will obviously result. Therefore, reasonable predictions of both solids velocities and holdup can never be obtained at the same time with this model.

The influence of the model of Bagchi and Balachandar (2002) for the lift coefficient C_L on the predictions of solids velocities in the impeller plane ($z/T = 0.34$) are shown in Figures 7.19 (a) to 7.19 (c). The Schiller-Neumann (1933) model is used to calculate the drag coefficient. The velocity components remain unaffected by the lift model used for the simulation. However, small differences can be observed in the solids holdup profiles



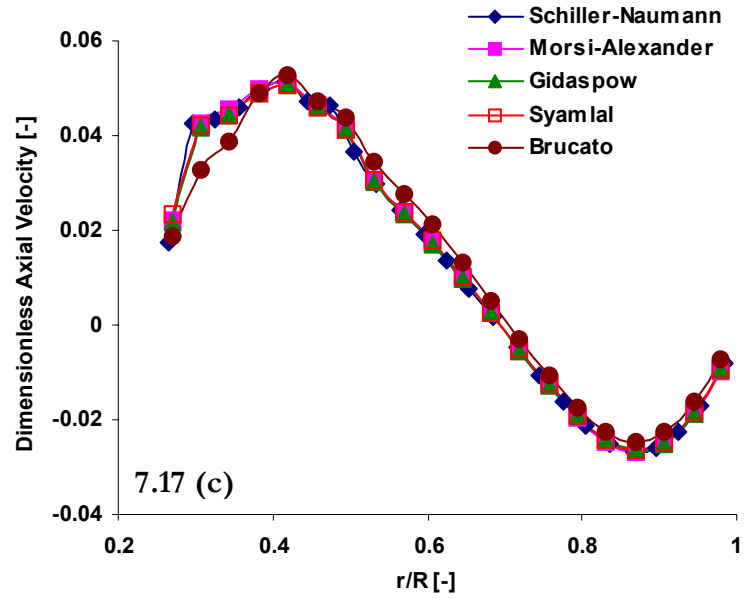
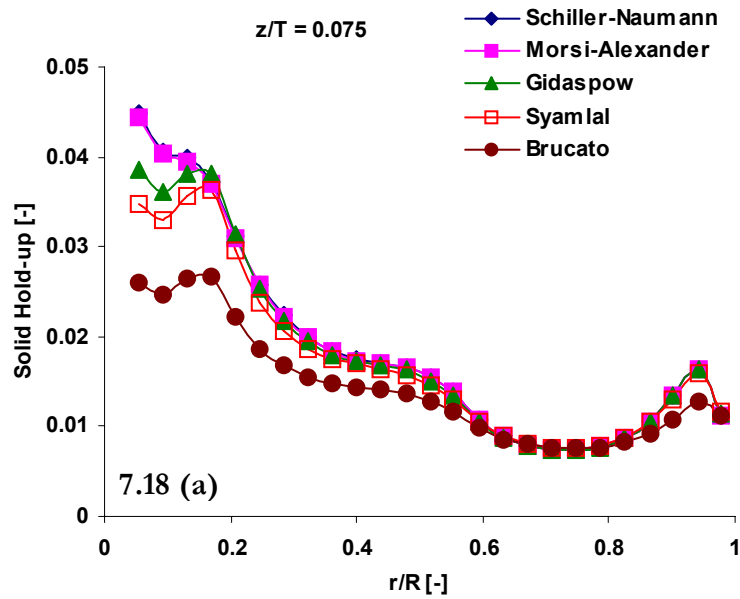


Figure 7.17 Influence of drag closure model on the Euler-Euler predictions of solids velocity components at $z/T = 0.34$



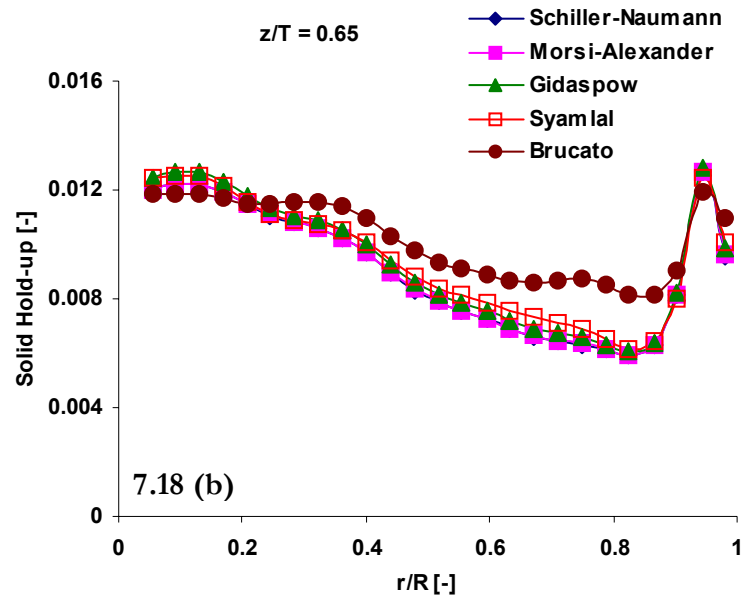
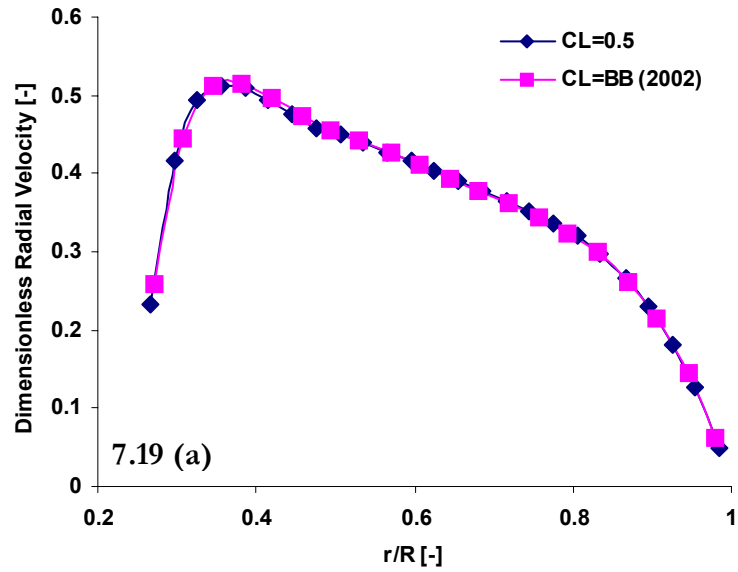


Figure 7.18 Influence of drag closure model on the Euler-Euler predictions of solids holdup



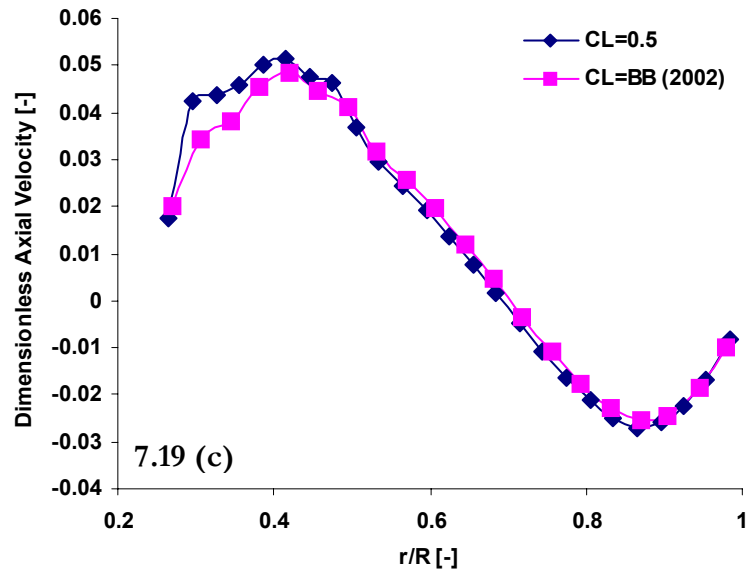
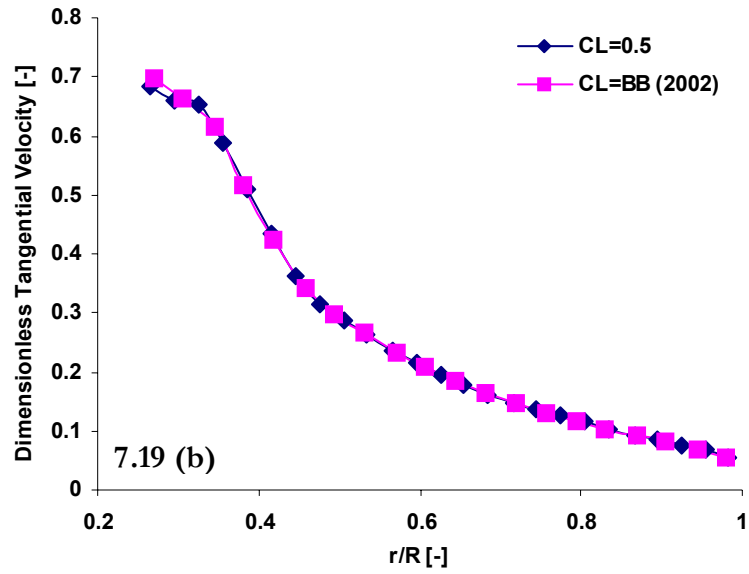


Figure 7.19 Influence of lift closure model on the Euler-Euler predictions of solids velocity components at $z/\Gamma = 0.34$

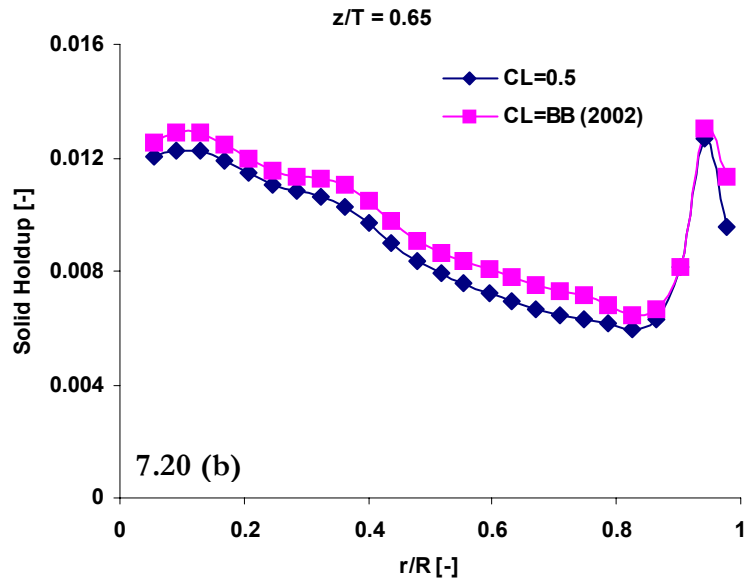
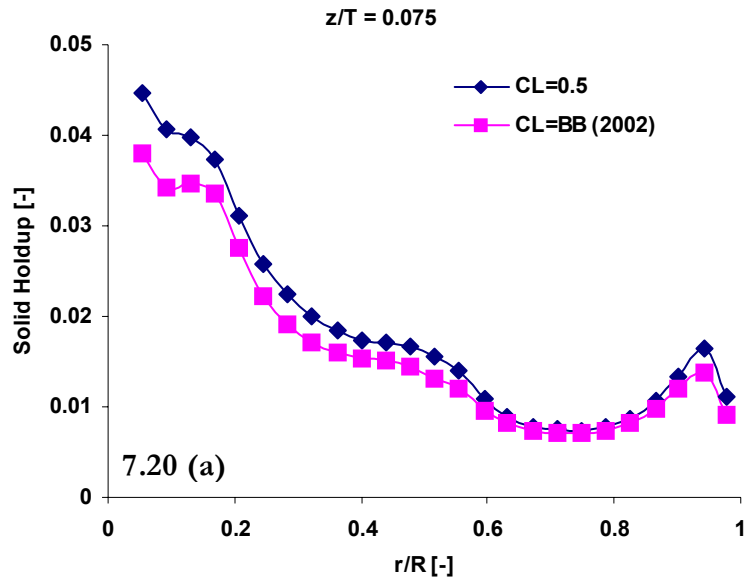


Figure 7.20 Influence of lift closure model on the Euler-Euler predictions of solids holdup

predicted at the two axial locations mentioned earlier. These are presented in Figures 7.20 (a) and 7.20 (b). The increase in lift force due to the ambient vorticity reduces the solids holdup at the bottom ($z/T = 0.075$) and increases it at the top plane ($z/T = 0.65$) marginally.

7.6. Summary

In this work, the ability of the large eddy simulation (LES) and the Euler-Euler CFD model in predicting the solids dynamics in a solid-liquid stirred tank reactor is evaluated through an extensive qualitative and quantitative comparison of the solids phase velocities, turbulent kinetic energy and sojourn time distributions (STD) with those obtained using Computer Automated Radioactive Particle Tracking (CARPT) experiment. The overall flow pattern obtained using the CARPT technique shows the bottom re-circulation loop to be significantly stronger than the top one, which is not captured by either the large eddy simulation or the Euler-Euler model. The predictions of the azimuthally averaged velocity components, particularly the tangential component, at different axial locations in the reactor are improved when LES is used as compared to the Euler-Euler model. Major discrepancies in the prediction of solids velocities by the numerical models can be seen in and around the impeller plane. In spite of the observed mismatch in time-averaged velocity predictions compared to CARPT data, the large eddy simulation provides reasonably good agreement for the mean and standard deviation of the solids sojourn times in the reactor with the experimentally determined values. Based on the observations presented in this work, it can be concluded that more fundamental understanding of the flow field and the associated interactions close to the impeller are necessary in order to resolve and predict the complex two-phase flow in a solid-liquid stirred tank reactor. However, reasonable predictions of LES for the mean and variance of the sojourn time distributions in various zones of the tank provides additional encouragement for extending the compartmental model for the stirred tank reactor developed in Chapter 3 to liquid-solid systems.

Literature review suggests that the ambient shear rate, vorticity and particle rotation do not have any influence on the drag force experienced by the solids. The effect of free stream turbulence on the drag, however, seems to be strong particularly for larger particle sizes $>10l_k$. Ambient vorticity, if large, can have a significant impact on the lift force acting on the solids. Several available drag and lift closures that are commonly used in the literature have been tested in the Euler-Euler framework in order to understand their influence on the model predictions. It turns out that most of these closure models have hardly any influence on the results obtained for the solids velocities and holdup. The correction factor suggested by Brucato (1998) to account for the free-stream turbulence causes improved solids suspension in the vessel compared to those obtained from the other models, but at the cost of larger over-prediction of the tangential velocity near the impeller. As a result, it is unlikely that this model will be able to provide reasonable predictions of both solids velocities and holdup at the same time in different regions of the tank.

Chapter 8

Conclusions and Future Work

The influence of mixing on reactor performance has been well known for decades, and the quantification of such effect has been known to provide improved control over reaction selectivity. This can subsequently lead to reduction in waste production, thereby resulting in environmentally and economically beneficial operation. In a stirred tank reactor, the convective flow generated by the impeller rotation dictates the macromixing behavior of the system, while mesomixing occurs due to the dispersion caused by turbulence. As a result it is imperative to understand and account for the flow and turbulence in the reactor in order to predict the effect of mixing on the reactor performance. Although CFD has emerged as a promising tool in this regard, it suffers from the disadvantage of high computation cost when complex chemistries with large number of species are involved. In view of such a limitation, the CFD-based compartmental model is proposed in this work to quantify and predict the impact of mixing on the performance of stirred tank reactors. In this approach, the flow field is first solved using CFD, and the averaged flow and turbulence (in terms of eddy diffusivity) information is transferred to the compartmental framework in order to solve the reactive flow problem. A proper framework for this CFD-based approach has been successfully developed in this work for single phase system, and the model has been tested with experimental data available in the open literature. The results are in reasonable agreement (within 7-8%) and the effect of varying feed location is nicely captured at significantly reduced computation cost (Guha et al., 2006). Comparison with a full blown CFD simulation is also carried out demonstrating that such a simulation did not provide significant additional improvement in the predicted yields. Thus, the compartmental model is a promising alternative to quantify the mixing effects in large-scale industrial reactors at a lower computational expense. However, it should be recognized that

this model can only account for macromixing and mixing due to turbulent dispersion (mesomixing), but ignores the micromixing effects on reactor performance. The condition for which micromixing effects can be ignored depends on the relative magnitudes of the micromixing and the reaction time scales.

It is expected that the number and locations of the compartments necessary to represent a given system would depend on the flow and kinetics of the system, and a methodology for the a priori determination of the same has been developed in this work based on a time-scale analysis of the two processes (Guha et al, 2006). The compartments in the framework are created utilizing the flow field such that the overall residence time in each compartment is less than the characteristic reaction time scale, i.e. locally Da is less than unity for each compartment. $Da \leq 1$ ensures low conversion per pass through the compartments and hence, the compartments can be assumed to be macroscopically well mixed. This methodology, approach and algorithm developed can be used for industrial reactors for any reaction type provided rate terms and kinetic constants are known.

In order to extend the CFD-based compartmental approach to solid-liquid stirred tanks it is necessary to evaluate the CFD predictions extensively before using them as input to the compartmental model. The dearth of available experimental data in dense suspensions necessitated the use of Computer Automated Radioactive Particle Tracking (CARPT) in this work to quantify the solids dynamics in a stirred tank. CARPT is a completely non-intrusive technique for the investigation of dense multiphase flows and provides Lagrangian description of the flow being studied. Various Eulerian measures of the flow in terms of ensemble-averaged solids velocity components and solids turbulent kinetic energy are calculated from the Lagrangian information obtained from the CARPT experiments. The solids dynamics at high solids loading show significant difference compared to those observed at low solids loading in the existing literature studies indicating the importance of solid-solid interactions in dense slurry flows. The solids sojourn time distributions in various axial regions in the tank are also calculated from the CARPT data, and the mean and standard deviations of the distributions obtained are computed. The mean sojourn

time at the bottom section of the tank at the conditions of the experiments clearly indicate that incipient solids suspension based on Zwietering's "one second" rule is achieved at an impeller speed lower than that predicted by the Zwietering correlation (Guha, Ramachandran and Dudukovic, 2007). Such reduction in the operating impeller speed can lead to significant energy savings for large industrial processes, since the power required scales as the cube of the impeller speed.

To quantify the solids distribution at different axial locations in the tank, the gamma-ray Computed Tomography (CT) technique is used in this work. The data currently obtained using CT, however, has an anomaly for overall solids holdup of 1% where improved solids suspension is observed at the lower impeller speed of 850 RPM. Also, the current data show low solids presence near the tank wall in most of the cases, although the high solids concentration close to the shaft seems to be captured. Higher solids holdup near the wall is expected because of the characteristic flow pattern with a radial flow impeller in a stirred vessel. To evaluate the data further, a solids mass balance in the tank is carried out by interpolating the solids holdup in the entire tank based on the experimental data at the three axial levels obtained using CT. The interpolation error is quantified by performing the same exercise using CFD data at the three axial levels. This error is typically of the order of 10%, while a mass balance error of about 60-70% is observed with the current CT data at all the experimental conditions. A numerical investigation with a synthetic phantom having solids holdup in the range 1% to 10% suggests that solids are not distinguished clearly from water when solids holdup is low (1% or less) while the reconstruction result is associated with increased errors as the solids holdup increases in the range of holdup studied.

The ability of the large eddy simulation (LES) and the Euler-Euler CFD model in predicting solid-liquid stirred tank flow is evaluated in this work utilizing the experimental data obtained. Knowing the shortcoming of the CT data, only the CARPT data is used for this assessment. The overall flow pattern obtained using the CARPT technique shows the bottom re-circulation loop to be significantly stronger than the top one, which is not

captured by either the large eddy simulation or the Euler-Euler model. The predictions of the azimuthally averaged velocity components, particularly the tangential component, at different axial locations in the reactor are improved when LES is used as compared to the Euler-Euler model. Major discrepancies in the prediction of solids velocities by the numerical models can be seen in and around the impeller plane, while improved predictions are obtained in regions away from the impeller (Guha et al., 2007). In spite of the observed mismatch in time-averaged velocity predictions compared to CARPT data, the large eddy simulation provides reasonably good agreement for the mean and standard deviation of the solids sojourn times in the reactor with the experimentally determined values, thereby providing some hope for CFD models in predicting the complex solid-liquid flow in stirred tanks.

Several available drag and lift closures have been tested in the Euler-Euler framework based on an extensive review of the open literature in order to understand their influence on the model predictions. It turns out that most of these closure models have hardly any influence on the results obtained for the solids velocities and holdup. The correction factor suggested by Brucato (1998) to account for the free-stream turbulence causes improved solids suspension in the vessel compared to those obtained from the other models, but at the cost of larger over-prediction of the tangential velocity near the impeller. As a result, it is unlikely that this model will be able to provide reasonable predictions of both solids velocities and holdup at the same time in different regions of the tank.

8.1. Future Work

Although the predictions of the CFD-based compartmental model can be considered reasonable, the discrepancy from experimental data can be seen to be larger when the reactant feeding is far from the impeller where the dispersion term (mesomixing) in the model equation becomes important (Guha et al., 2006). This term is closed through the turbulent eddy diffusivity which is computed using the k and ε values obtained from the CFD simulation of the flow with the standard k - ε model. The discrepancy observed might

be related to the predictions of the turbulence quantities by the standard k - ε model, and therefore, it is worthwhile to investigate if the k and ε values obtained from the large eddy simulation (LES) leads to improved predictions of the reactor performance. Such an attempt was made in this work in the Fluent 6.2 framework using the sliding mesh formulation. Some improvement in the quantification of the mean flow field was observed but the turbulent quantities were not captured well in the present simulation and were severely under-predicted compared to the experimental data. This might have been caused by the lower grid and time resolution used for the simulation, further refinement of which should result in better predictions of the turbulent kinetic energies and energy dissipation rates. Simulation with finer grid and time step can be carried out in the future and the results obtained can be used to compute the closure for the compartmental model. Although computationally very expensive, this will clearly demonstrate if the predictions of the k - ε model caused the discrepancy observed when the feeding is far from the impeller and hence, will provide a bench-mark to the compartmental model prediction.

The compartmental model developed can be further refined to account for micromixing effects in the compartments when micromixing time scale is large compared to the characteristic reaction time scale. This can be done by implementing a suitable micromixing model in each of the compartments and solving them simultaneously with the macroscopic compartment level equations. Micromixing models that might be looked into in detail include the interaction by exchange with the mean (IEM) model (David and Villermaux, 1987) and the population balance model (Madras and McCoy, 2004). For the IEM model, the transient model for un-premixed feed should be used since the steady state model that is commonly known will not capture the temporal effects and might result in a sort of 'steady' result unaffected by time. However, solution of the transient IEM model might be cumbersome and time consuming, and the determination of the micromixing time constant in each compartment will be an issue that needs to be addressed. On the other hand, for the population balance approach, the primary challenge might be closing the moment equations when the moment method is used for solution. Possible solutions to this problem include either assuming a distribution a priori, or to solve for the distribution

completely. The former approach will be approximate while the later one will be computationally intensive when applied in the compartmental framework since the number of equations will increase significantly. Also, quantification of the breakage and coalescence constants in each compartment will be a challenge in using the population balance model.

Computational Fluid Dynamics (CFD) efforts for solid-liquid stirred tank flow should focus on the development and use of fundamentally-based models for interphase exchange coefficients. Currently available closure models are not sufficient in predicting the flow close to the impeller region. Experimental and numerical investigations should be performed to understand the effects of flow features and phase interactions close to the impeller region. The interactions of the particles with the rotating impeller might also be important and should be looked into carefully. Solids phase distribution measurements using tomography should be performed in the future and should also be compared with those predicted by the CFD models. Such evaluation is necessary to make sure if the closure models developed can reasonably predict both the solids flow field and phase distribution at the same time.

The reliability of the CFD predictions should be confirmed at a larger scale by comparing with experimental data. This would require CARPT and CT experiments being performed with a tank of larger dimensions and using the data for CFD assessment. Once CFD simulations are established to be reasonable and reliable, the CFD-based compartmental model currently developed for single phase system can be extended to solid-liquid reactive flows in stirred tanks. The closures for double and triple products of fluctuating components arising from the Reynolds averaging will be the challenge involved in this step. However, such an extension, if successfully carried out, will provide an efficient tool to quantify mixing effects in large scale solid-liquid stirred tanks.

References

- Akiti, O. and Armenante, P.M., 2004. *Experimentally-validated micromixing-based CFD model for fed-batch stirred tank reactors*, AIChE J., 50, 3, 566.
- Alcamo, R., Micale, G., Grisafi, F., Brucato, A. and Ciofalo, M., 2005. *Large eddy simulation of turbulent flow in an unbaffled stirred tank driven by a Rushton turbine*, Chemical Engineering Science, 60, 2303.
- Alexopoulos, A.H., Maggioris, D. and Kiparissides, C., 2002. *CFD analysis of turbulence non-homogeneity in mixing vessels: a two-compartment model*, Chemical Engineering Science, 57, 1735.
- Altway, A., Setyawan, H., Margono and Winardi, S., 2001. *Effect of particle size on simulation of three-dimensional solid dispersion in stirred tank*, Trans IChemE, 79, Part A, 1011.
- Armenante, P.M., Nagamine, E.U. and Susanto, J., 1998. *Determination of correlations to predict the minimum agitation speed for complete solid suspension in agitated vessels*, Canadian Journal of Chemical Engineering, 76, 413.
- Assirelli, M., Bujalski, W., Eaglesham, A. and Nienow, A.W., 2002. *Study of micromixing in a stirred tank using a rushton turbine: comparison of feed positions and other mixing devices*, Trans I ChemE, 80(A), 855.
- Auton, T.R., Hunt, J.C.R. and Prud'homme, M., 1988. *The force exerted on a body in inviscid unsteady non-uniform rotational flow*, J. of Fluid Mechanics, 197, 241.
- Bagchi, P. and Balachandar, S., 2002. *Effect of free rotation on the motion of a solid sphere in linear shear flow at moderate Re* , Physics of Fluids, 14, 8, 2719.
- Bagchi, P. and Balachandar, S., 2002. *Shear versus vortex-induced lift force on a rigid sphere at moderate Re* , J. of Fluid Mechanics, 473, 379.
- Bagchi, P. and Balachandar, S., 2003. *Effect of turbulence on the drag and lift of a particle*, Physics of Fluids, 15, 11, 3496.
- Bakker, A. and Oshinowo, L.M., 2004. *Modeling of turbulence in stirred vessels using large eddy simulation*, Chemical Engineering Research and Design, 82, A9, 1169.
- Baldi, G., Conti, R. and Alaria, E., 1978. *Complete suspension of particles in mechanically agitated vessels*, Chemical Engineering Science, 33, 21.
- Baldyga, J. and Bourne, J.R., 1984a. *A fluid mechanical approach to turbulent mixing and chemical reaction: II: micromixing in the light of turbulence theory*, Chem. Eng. Commun., 28, 243.

- Baldyga, J., 1989. *Turbulent mixer model with application to homogeneous instantaneous chemical reactions*, Chemical Engineering Science, 44, 5, 1175.
- Baldyga, J., Bourne, J.R. and Walker, B., 1998. *Non-isothermal micromixing in turbulent liquids: theory and experiment*, Canadian Journal of Chemical Engineering, 76, 641.
- Barresi, A. and Baldi, G., 1987. *Solid dispersion in an agitated vessel*, Chemical Engineering Science, 42, 12, 2949.
- Barrue, H., Bertrand, J., Cristol, B. and Xuereb, C., 2001. *Eulerian simulation of dense solid-liquid suspension in multi-stage stirred vessel*, Journal of Chemical Engineering of Japan, 34, 5, 585.
- Bauer, T., Roy, S., Lange, R. and Al-Dahhan, M.H., 2005. *Liquid saturation and gas-liquid distribution in multiphase monolith reactors*, Chemical Engineering Science, 60, 11, 3101.
- Bezzo, F., Macchietto, S. and Pantelides, C.C., 2003. *General hybrid multi-zonal/CFD approach for bioreactor modeling*, AIChE J., 49, 8, 2133.
- Bhusarapu, S., Al-Dahhan, M.H. and Dudukovic, M.P., 2006. *Solids flow mapping in a gas-solid riser: mean holdup and velocity fields*, Powder Technology, 163, 1-2, 98.
- Bhusarapu, S., Al-Dahhan, M.H., Dudukovic, M.P., Trujillo, S. and O'Hern, T.J., 2005. *Experimental study of the solids velocity field in gas-solid risers*, Industrial and Engineering Chemistry Research, 44, 25, 9739.
- Bird, R.B., Stewart, W.E. and Lightfoot, E.N., 1994. *Transport phenomena*, John Wiley and Sons, New York.
- Boltersdorf, U., Deerberg, G. and Schluter, S., 2000. *Computational studies of the effects of process parameters on the product distribution for mixing sensitive reactions and on distribution of gas in stirred tank reactors*, Recent Res. Devel. Chemical Engg., 4, 15.
- Boyer, C., Koudil, A., Chen, P. and Dudukovic, M.P., 2005. *Study of liquid spreading from a point source in a trickle bed via gamma-ray tomography and CFD simulation*, Chemical Engineering Science, 60, 22, 6279.
- Brucato, A. and Brucato, V., 1998. *Unsuspected mass of solid particles in stirred tanks*, Canadian Journal of Chemical Engineering, 76, 420.
- Brucato, A., Ciofalo, M., Grisafi, F. and Micale, G., 1994. *Complete numerical simulations of flow fields in baffled stirred vessels: the inner-outer approach*, I.Chem.E Symposium Series no. 136, 155.
- Brucato, A., Ciofalo, M., Grisafi, F. and Tocco, R., 2000. *On the simulation of stirred tank reactors via computational fluid dynamics*, Chemical Engineering Science, 55, 291.

- Brucato, A., Grisafi, F. and Montante, G., 1998. *Particle drag coefficients in turbulent fluids*, Chemical Engineering Science, 53, 18, 3295.
- Bujalski, J.M., Jaworski, Z., Bujalski, W. and Nienow, A.W., 2002. *The influence of the addition position of a tracer on CFD simulated mixing times in a vessel agitated by a Rushton turbine*, Trans IChemE, 80, Part A, 824.
- CARPT User Manual, 2007. *Introduction to radioactive particle tracking for potential users*, Chemical Reaction Engineering Laboratory (CREL), Washington University in St. Louis, St. Louis.
- Chaouki, J., Larachi, F. and Dudukovic, M.P., 1997. *Non-invasive monitoring of multiphase flows*, Elsevier, Amsterdam.
- Chen, J., Rados, N., Al-Dahhan, M.H. and Dudukovic, M.P., 2001. *Particle motion in packed/ebullated beds by CT and CARPT*, AIChE J., 47, 5, 994.
- Chen, M., Kontomaris, K. and McLaughlin, J.B., 1998. *Direct numerical simulation of droplet collisions in a turbulent channel flow. Part I: collision algorithm*, Int. J. Multiphase Flow, 24, 1079.
- Chen, S. and Doolen, G.D., 1998. *Lattice Boltzmann method for fluid flows*, Annu. Rev. Fluid Mech., 30, 329.
- David, R. and Villiermaux, J., 1987. *Interpretation of micromixing effects on fast consecutive-competing reactions in semi-batch stirred tanks by a simple interaction model*, Chem. Eng. Commun., 54, 333.
- Davidson, P.A., 2004. *Turbulence – an introduction for scientists and engineers*, Oxford University Press, New York.
- Decker, S. and Sommerfeld, M., 1996. *Calculation of particle suspension in agitated reactors with the Euler-Lagrange approach*, IChemE Symp Series, 140, 71.
- Degaleesan, S., 1997. *Fluid dynamic measurements and modeling of liquid mixing in bubble columns*, D.Sc. Thesis, Washington University in St. Louis, St. Louis.
- Degaleesan, S., Dudukovic, M.P. and Pan, Y., 2001. *Experimental study of gas-induced liquid-flow structures in bubble columns*, AIChE J, 47, 9, 1913.
- Degaleesan, S., Duduković, M.P., Toseland, B.A. and Bhatt, B.L., 1997. *A two-compartment convective-diffusion model for slurry bubble column reactors*, Ind. Eng. Chem. Res., 36, 4670.
- Deglon, D.A. and Meyer, C.J., 2006. *CFD modeling of stirred tanks: numerical considerations*, Minerals Engineering, 19, 1059.
- Derksen, J.J. and Van den Akker, H.E.A., 1999. *Large eddy simulations on the flow driven by a Rushton turbine*, AIChE J., 45, 2, 209.

- Derksen, J.J., 2003. *Numerical simulation of solids suspension in a stirred tank*, AIChE J., 49, 11, 2700.
- Devanathan, N., 1991. *Investigation of liquid hydrodynamics in bubble columns via computer automated radioactive particle tracking (CARPT)*, D.Sc. Thesis, Washington University in St. Louis, St. Louis.
- Devanathan, N., Moslemian, D. and Dudukovic, M.P., 1990. *Flow mapping in bubble columns using CARPT*, Chemical Engineering Science, 45, 8, 2285.
- El-Hamouz, A.M. and Mann, R., 1998. *Effect of micromixing on the yield of intermediates in triplet consecutive/competitive reactions*, Canadian Journal of Chemical Engineering, 76, 650.
- Fasano, J.B., Bakker, A. and Penney, W.R., 1994. *Advanced impeller geometry boosts liquid agitation*, Chemical Engineering, 101, 8, 110.
- Fishwick, R., Winterbottom, M., Parker, D., Fan, X., Stitt, H., 2005. *The use of positron emission particle tracking in the study of multiphase Stirred tank reactor hydrodynamics*, Canadian Journal of Chemical Engineering, 83, 1, 97.
- Fluent User Manual, Fluent Inc. (http://www.fluentusers.com/fluent6326/doc/doc_f.htm).
- Fox, R.O., 1996. *Computational methods for turbulent reacting flows in the chemical process industry*, Revue De L' Institut Francais Du Petrole, 51, 2, 215.
- Fox, R.O., 2003. *Computational models for turbulent reacting flows*, Cambridge University Press, Cambridge.
- Gidaspow, D., Bezburuah, R. and Ding, J., 1992. *Hydrodynamics of circulating fluidized beds: kinetic theory approach*, Proceedings of the 7th Engineering Foundation Conference on Fluidization, 75.
- Godfrey, J.C. and Zhu, Z.M., 1994. *Measurement of particle-liquid profiles in agitated tanks*, AIChE Symposium Series, 299, 181.
- Gosman, A.D., Lekakou, C., Politis, S., Issa, R.I. and Looney, M.K., 1992. *Multidimensional modeling of turbulent two-phase flows in stirred vessels*, AIChE J., 38, 12, 1946.
- Guha, D., Derksen, J.J., Ramachandran, P.A. and Dudukovic, M.P., 2007. *Evaluation of large eddy simulation and Euler-Euler CFD models for solids flow dynamics in a stirred tank reactor*, in review, AIChE J.
- Guha, D., Dudukovic, M.P., Ramachandran, P.A., Mehta, S. and Alvare, J., 2006. *CFD-based compartmental modeling of single phase stirred-tank reactors*, AIChE J., 52, 5, 1836.

- Guha, D., Ramachandran, P.A. and Dudukovic, M.P., 2007. *Flow field of suspended solids in a stirred tank reactor by Lagrangian tracking*, in press, Chemical Engineering Science.
- Harris, C.K., Roekaerts, D., Rosendal, F.J.J., Buitendijk, F.G.J., Daskopoulos, P.H., Vreenegoor, A.J.N. and Wang, H., 1996. *Computational fluid dynamics for chemical reactor engineering*, Chemical Engineering Science, 51, 1569.
- Hartmann, H., Derksen, J.J. and Van den Akker, H.E.A., 2006. *Mixing times in a turbulent stirred tank by means of LES*, AIChE J., 52, 11, 3696.
- Hartmann, H., Derksen, J.J., Montavon, C., Pearson, J., Hamill, I.S. and Van den Akker, H.E.A., 2004. *Assessment of large eddy and RANS stirred tank simulations by means of LDA*, Chemical Engineering Science, 59, 2419.
- Holden, P.J. and Mann, R., 1996. *Turbulent 3-D mixing in a stirred vessel: correlation of a networks-of-zones image reconstruction approach with pointwise measurements*, IChemE Symposium Series, 140, 167.
- Jian, M. and Zhengming, G., 2006. *Large eddy simulations of mixing time in a stirred tank*, Chinese J. Chem. Eng., 14, 1, 1.
- Jones, R.M., Harvey III, A.D. and Acharya, S., 2001. *Two-equation turbulence modeling for impeller stirred tanks*, Journal of Fluids Engineering, 123, 640.
- Karim, K., Varma, R., Vesvikar, M. and Al-Dahhan, M.H., 2004. *Flow pattern visualization of a simulated digester*, Water Research, 38, 17, 3659.
- Kemoun, A., Cheng Ong, B., Gupta, P., Al-Dahhan, M.H. and Dudukovic, M.P., 2001. *Gas holdup in bubble columns at elevated pressure via computed tomography*, International Journal of Multiphase Flow, 27, 5, 929.
- Kemoun, A., Rados, N., Li, F., Al-Dahhan, M.H., Dudukovic, M.P., Mills, P.L., Leib, T.M. and Lerou, J.J., 2001. *Gas holdup in a trayed cold-flow bubble column*, Chemical Engineering Science, 56, 3, 1197.
- Khopkar, A.R., Kasat, G.R., Pandit, A.B. and Ranade, V.V., 2006. *Computational fluid dynamics simulation of the solid suspension in a stirred slurry reactor*, Ind. Eng. Chem. Res., 45, 12, 4416.
- Kougoulos, E., Jones, A.G. and Wood-Kaczmar, M.W., 2006. *A hybrid CFD compartmentalization modeling framework for the scaleup of batch cooling crystallization processes*, Chem. Eng. Comm., 193, 1008.
- Kresta, S.M. and Wood, P.E., 1991. *Prediction of the three-dimensional turbulent flow in stirred tanks*, AIChE J., 37, 3, 448.

- Kumar, S.B., 1994. *Computer tomographic measurements of void fraction and modeling of the flow in bubble columns*, Ph.D. Thesis, Florida Atlantic University, Boca Raton.
- Kurose, R. and Komori, S., 1999. *Drag and lift forces on a rotating sphere in a linear shear flow*, J. of Fluid Mechanics, 384, 183.
- Limtrakul, S., Chen, J., Ramachandran, P.A. and Dudukovic, M.P., 2005. *Solids motion and holdup profiles in liquid fluidized beds*, Chemical Engineering Science, 60, 1889.
- Ljungqvist, M. and Rasmuson, A., 2001. *Numerical simulation of the two-phase flow in an axially stirred vessel*, Trans IChemE, 79, Part A, 533.
- Lumley, J.L., 1978. *Two-phase and non-Newtonian flows in turbulence*, Springer Topics in Applied Physics, 12, 289.
- Luo, H., Kemoun, A., Al-Dahhan, M.H., Sevilla, J.M.F., Sanchez, J.L.G., Camacho, F.G., Grima, E.M., 2003. *Analysis of photobioreactors for culturing high-value microalgae and cyanobacteria via an advanced diagnostic technique: CARPT*, Chemical Engineering Science, 58, 12, 2519.
- Madras, G. and McCoy, B.J., 2004. *Kinetics and reactive mixing: fragmentation and coalescence in turbulent fluids*, AIChE J., 50, 4, 835.
- Magelli, F., Fajner, D., Nocentini, M. and Pasquali, G., 1986. *Solids concentration profiles in slurry reactors stirred with multiple impellers*, World Congress III of Chemical Engineering, Tokyo, Vol. 3, 362.
- Magelli, F., Fajner, D., Nocentini, M. and Pasquali, G., 1990. *Solids distribution in vessels stirred with multiple impellers*, Chemical Engineering Science, 45, 615.
- Mann, R. and El-Hamouz, A.M., 1995. *A product distribution paradox on scaling up a stirred batch reactor*, AIChE J., 41, 4, 855.
- Mann, R. and Hackett, L.A., 1988. *Fundamentals of gas liquid mixing in a stirred vessel: an analysis using network of back-mixed zones*, 6th European Conference on Mixing, Pavia.
- Mann, R., 1985. *Gas liquid mixing in stirred vessels*, I.Chem.E. Symposium Series No. 94, 335.
- Marshall, E., Haidari, A. and Subbiah, S., 1996. Presented at AIChE Annual Meeting, Chicago.
- Mei, R., 1992. *An approximate expression for the shear lift force on a spherical particle at finite Reynolds numbers*, Int. J. of Multiphase Flow, 18, 145.
- Micale, G., Grisafi, F., Rizzuti, L. and Brucato, A., 2004. *CFD simulation of particle suspension height in stirred vessels*, Trans IChemE, 82, Part A, 1204.

Micale, G., Montante, G., Grisafi, F., Brucato, A. and Godfrey, J., 2000. *CFD simulation of particle distribution in stirred vessels*, Trans IChemE, 78, Part A, 435.

Middleton, J.C., Pierce, F. and Lynch, P.M., 1986. *Computations of flow fields and complex reaction yield in turbulent stirred reactors, and comparison with experimental data*, Chem. Eng. Res. Des., 64, 18.

Mohd-Yusof, J., 1998. *Development of immersed boundary methods for complex geometries*, Annual Research Briefs, Center for Turbulence Research, Stanford University, Stanford (<http://ctr.stanford.edu/ResBriefs98/myusof.pdf>).

Montante, G. and Magelli, F., 2005. *Modeling of solids distribution in stirred tanks: analysis of simulation strategies and comparison with experimental data*, International Journal of Computational Fluid Dynamics, 19, 3, 253.

Montante, G., Micale, G., Magelli, F. and Brucato, A., 2001. *Experiments and CFD predictions of solid particle distribution in a vessel agitated with four pitched blade turbines*, Trans I Chem E, 79(A), 1005.

Morsi, S.A. and Alexander, A.J., 1972. *An investigation of particle trajectories in two-phase flow systems*, J. of Fluid Mechanics, 55 (2), 193.

National Institute of Standards and Technology (NIST) Database for X-ray and gamma-ray data (<http://physics.nist.gov/PhysRefData/contents-xray.html>).

Ng, K., Fentiman, N.J., Lee, C.K. and Yianneskis, 1998. *Assessment of sliding mesh CFD predictions and LDA measurements of the flow in a tank stirred by a Rushton impeller*, Trans I Chem E, 76(A), 737.

Nienow, A.W., 1968. *Suspension of solid particles in turbine-agitated baffled vessels*, Chemical Engineering Science, 23, 1453.

Nouri, J.M. and Whitelaw, J.H., 1992. *Particle velocity characteristics of dilute to moderately dense suspension flows in stirred reactors*, Int. J. Multiphase Flow, 18, 1, 21.

Oesterle, B. and Bui Dinh, T., 1998. *Experiments on the lift of a spinning sphere in the range of intermediate Reynolds numbers*, Exp. in Fluids, 25, 16.

Oshinowo, L., Jaworski, Z., Dyster, K.N., Marshall, E. and Nienow, A.W., 2000. *Predicting the tangential velocity field in stirred tanks using the multiple reference frames (MRF) model with validation by LDA measurement*, 10th European Mixing Conference, Amsterdam, Elsevier, 281.

Paul, E.L. and Treybal, R.E., 1971. *Mixing and product distribution for a liquid-phase, second-order, competitive-consecutive reaction*, AIChE J., 17, 3, 718.

- Paul, E.L., Atiemo-Obeng, V.A. and Kresta, S.M., 2004. *Handbook of industrial mixing – science and practice*, John Wiley and Sons, New Jersey.
- Peskin, C.S., 1972. *Flow patterns around heart valves: a numerical method*, Journal of Computational Physics, 10.
- Peskin, C.S., 2002. *The immersed boundary method*, Acta Numerica, 1.
- Placek, J., Tavlarides, L.L., Smith, G.W. and Fort, I., 1986. *Turbulent Flow in stirred tanks*, AIChE J., 32, 11, 1771.
- Rados, N., Shaikh, A., Al-Dahhan, M.H., 2005. *Solids flow mapping in a high pressure slurry bubble column*, Chemical Engineering Science, 60, 22, 6067.
- Rammohan, A., Kemoun, A., Al-Dahhan, M., Dudukovic, M. and Larachi, F., 2001. *CARPT dynamic bias studies: evaluation of accuracy of position and velocity measurements*, Recents Progres en Genie des Procedes, 15, 59.
- Rammohan, A.R., 2002. *Characterization of single and multiphase flows in stirred tank reactors*, D.Sc. Thesis, Washington University in St.Louis, St. Louis.
- Rammohan, A.R., Kemoun, A., Al-Dahhan, M.H. and Dudukovic, M.P., 2001. *A Lagrangian description of flows in stirred tanks via computer automated radioactive particle tracking (CARPT)*, Chemical Engineering Science, 56, 2629.
- Rammohan, A.R., Kemoun, A., Al-Dahhan, M.H. and Dudukovic, M.P., 2001. *Characterization of single phase flows in stirred tanks via computer automated radioactive particle tracking (CARPT)*, Trans IChemE, 79(A), 831.
- Ranade, V.V., 2002. *Computational flow modeling for chemical reactor engineering*, Academic Press, New York.
- Ranade, V.V., Perrard, M., Xuereb, C., Le Sauze, N. and Bertrand, J., 2001b. *Trailing vortices of Rushton turbine: PIV measurements and CFD simulations with snapshot approach*, Chem. Eng. Res. Des., 79A, 3.
- Revstedt, J., Fuchs, L. and Tragardh, C., 1998. *Large eddy simulations of the turbulent flow in a stirred reactor*, Chemical Engineering Science, 53, 24, 4041.
- Rigopoulos, S. and Jones, A., 2003. *A hybrid CFD-reaction engineering framework for multiphase reactor modeling: basic concept and application to bubble column reactors*, Chemical Engineering Science, 58, 3077.
- Roy, S. and Al-Dahhan, M.H., 2005. *Flow distribution characteristics of a gas-liquid monolith reactor*, Catalysis Today, 105, 3-4, 396.

- Roy, S., Chen, J., Kumar, S.B., Al-Dahhan, M.H. and Dudukovic, M.P., 1997. *Tomographic and particle tracking studies in a liquid-solid riser*, Industrial and Engineering Chemistry Research, 36, 11, 4666.
- Roy, S., Kemoun, A., Al-Dahhan, M.H. and Dudukovic, M.P., 2005. *Experimental investigation of the hydrodynamics in a liquid-solid riser*, AIChE J, 51, 3, 802.
- Salem, M.B. and Oesterle, B., 1998. *A shear flow around a spinning sphere: numerical study at moderate Reynolds numbers*, Int. J. of Multiphase Flow, 24, 4, 563.
- Sano, Y. and Usui, H., 1985. *Interrelations among mixing time, power number and discharge flow rate number in baffled mixing vessels*, Journal of Chemical Engineering of Japan, 18, 47.
- Sbrizzai, F., Lavezzo, V., Verzicco, R., Campolo, M. and Soldati, A., 2006. *Direct numerical simulation of turbulent particle dispersion in an unbaffled stirred-tank reactor*, Chemical Engineering Science, 61, 2843.
- Schiller, L. and Neumann, A., 1933. *Über die grundlegenden berechnungen bei der schwerkraftaufbereitung*, Verein Deutscher Ingenieure, 77, 318.
- Sha, Z., Palosaari, S., Oinas, P. and Ogawa, K., 2001. *CFD simulation of solid suspension in a stirred tank*, Journal of Chemical Engineering of Japan, 34, 5, 621.
- Shaikh, A. and Al-Dahhan, M.H., 2005. *Characterization of the hydrodynamic flow regime in bubble columns via computed tomography*, Flow Measurement and Instrumentation, 16, 2-3, 91.
- Shamlou, P.A. and Koutsakos, E., 1989. *Solids suspension and distribution in liquids under turbulent agitation*, Chemical Engineering Science, 44, 3, 529.
- Smagorinsky, J., 1963. *General circulation experiments with the primitive equations: 1. The basic experiment*, Mon. Weather Rev., 91, 99.
- Smith III, F.G., 1997. *A model of transient mixing in a stirred tank*, Chemical Engineering Science, 52, 9, 1459.
- Spidla, M., Mostek, M., Sinevic, V., Jahoda, M. and Machon, V., 2005. *Experimental assessment and CFD simulations of local solid concentration profiles in a pilot-scale stirred tank*, Chem. Pap., 59 (6a), 386.
- Sridhar, G. and Katz, J., 1995. *Drag and lift forces on microscopic bubbles entrained by a vortex*, Physics of Fluids, 7, 2, 389.
- Syamlal, M. and O'Brien, T.J., 1989. *Computer simulation of bubbles in a fluidized bed*, AIChE Symp. Series, 85, 22.

- Takahashi, K. and Fujita, H., 1995. *A study of the agitation speed to just cause complete suspension for non-spherical particles*, Journal of Chemical Engineering of Japan, 28, 2, 237.
- Tyagi, M., Roy, S., Harvey III, A.D. and Acharya, S., 2007. *Simulation of laminar and turbulent impeller stirred tanks using immersed boundary method and large eddy simulation technique in multi-block curvilinear geometries*, Chemical Engineering Science, 62, 1351.
- Varma, R., Bhusarapu, S., O'Sullivan, J.A. and Al-Dahhan, M.H., 2007. *Comparison of alternating minimization and expectation maximization algorithms for single source gamma ray tomography*, in review, Measurement Science and Technology.
- Verschuren, I.L.M., Wijers, J.G. and Keurentjes, J.T.F., 2002. *Mean concentrations and concentration fluctuations in a stirred-tank reactor*, AIChE J., 48, 7, 1390.
- Verzicco, R., Fatica, M., Iaccarino, G. and Orlandi, P., 2004. *Flow in an impeller-stirred tank using an immersed boundary method*, AIChE J., 50, 6, 1109.
- Vicum, L., Ottiger, S., Mazzotti, M., Makowski, L. and Baldyga, J., 2004. *Multi-scale modeling of a reactive mixing process in a semibatch stirred tank*, Chemical Engineering Science, 59, 1767.
- Wells, G.J. and Harmon Ray, W., 2005. *Methodology for modeling detailed imperfect mixing effects in complex reactors*, AIChE J., 51, 5, 1508.
- Wittmer, S., Vivier, H., Falk, L. and Villiermaux, J., 1997. *Characterization of mixing by analysis of particle trajectories*, Récents Progrès en Génie des Procédés, 11, 35.
- Wu, H. and Patterson, G.K., 1989. *Laser-doppler measurements of turbulent-flow parameters in a stirred mixer*, Chemical Engineering Science, 44, 10, 2207.
- Wu, J., Zhu, Y. and Pullum, L., 2001. *Impeller geometry effect on velocity and solids suspension*, Trans I Chem E, 79(A), 989.
- Wu, J., Zhu, Y., Bandyopadhyay, P.C., Pullum, L. and Shepherd, I.C., 2000. *Solids suspension with axial-flow impellers*, AIChE J., 46, 3, 647.
- Yakhot, V., Orszag, S.A. and Yakhot, A., 1987. *Heat transfer in turbulent fluids – I. pipe flow*, International Journal of Heat and Mass Transfer, 30(1), 15.
- Yamazaki, H., Tojo, K. and Miyanami, K., 1986. *Concentration profiles of solids suspended in a stirred tank*, Powder Technology, 48, 205.
- Yang, Y.B., Devanathan, N. and Dudukovic, M.P., 1993. *Liquid backmixing in bubble columns via computer-automated radioactive particle tracking (CARPT)*, Experiments in Fluids 16, 1, 1.

Yeoh, S.L., Papadakis, G., Lee, K.C. and Yianneskis, M., 2004. *Large eddy simulation of turbulent flow in a Rushton impeller stirred reactor with sliding-deforming mesh methodology*, Chem. Eng. Technol., 27, 3, 257.

Yoon, H.S., Balachandar, S., Ha, M.Y. and Kar, K., 2003. *Large eddy simulation of flow in a stirred tank*, Journal of Fluids Engineering, 125, 486.

Zhang, X. and Ahmadi, G., 2005. *Eulerian-Lagrangian simulations of liquid-gas-solid flows in three-phase slurry reactors*, Chemical Engineering Science, 60, 5089.

Zhang, Y., Yang, C. and Mao, Z., 2006. *Large eddy simulation of liquid flow in a stirred tank with improved inner-outer iterative algorithm*, Chinese J. Chem. Eng., 14, 3, 321.

Zwietering, Th.N., 1958. *Suspending of solid particles in liquid by agitators*, Chemical Engineering Science, 8, 244.

Vita

Debangshu Guha

Date of Birth	April 27, 1976
Place of Birth	Durgapur, India
Degrees	B.E., Chemical Engineering, May 1999 M.E., Chemical Engineering, January 2002 D.Sc., Chemical Engineering, August 2007
Professional Societies	American Institute of Chemical Engineers (AIChE) Indian Institute of Chemical Engineers (IIChE)

Publications

Guha, D., Derksen, J.J., Ramachandran, P.A. and Dudukovic, M.P., 2007. *Evaluation of large eddy simulation and Euler-Euler CFD models for solids flow dynamics in a stirred tank reactor*, in review, AIChE J.

Guha, D., Ramachandran, P.A. and Dudukovic, M.P., 2007. *Flow field of suspended solids in a stirred tank reactor by Lagrangian tracking*, in press, Chemical Engineering Science.

Guha D., Jin, H., Dudukovic, M.P., Ramachandran, P.A. and Subramaniam, B., 2007. *Mass transfer effects during homogeneous 1-octene hydroformylation in CO₂-expanded solvents: Modeling and experiments*, in press, Chemical Engineering Science.

Guha, D., Dudukovic, M.P., Ramachandran, P.A., Mehta, S. and Alvare, J., 2006. *CFD-based compartmental modeling of single phase stirred-tank reactors*, AIChE J., 52, 5, 1836.

August 2007

Short Title: Flow and Mixing in Stirred Tanks

Guha D., D.Sc., 2007